



van der Putten, Marieke Anne (2018) Deep tissue in vivo quantitative optical biopsy. PhD thesis.

<https://theses.gla.ac.uk/8947/>

Copyright and moral rights for this work are retained by the author

A copy can be downloaded for personal non-commercial research or study, without prior permission or charge

This work cannot be reproduced or quoted extensively from without first obtaining permission in writing from the author

The content must not be changed in any way or sold commercially in any format or medium without the formal permission of the author

When referring to this work, full bibliographic details including the author, title, awarding institution and date of the thesis must be given

Enlighten: Theses

<https://theses.gla.ac.uk/>  
[research-enlighten@glasgow.ac.uk](mailto:research-enlighten@glasgow.ac.uk)

# DEEP TISSUE *IN VIVO* QUANTITATIVE OPTICAL BIOPSY

**Marieke Anne van der Putten**

**MSc, BSc (Hons)**

Submitted in fulfilment of the requirements for the degree of  
Doctor of Philosophy

School of Physics & Astronomy,  
College of Science & Engineering,  
University of Glasgow

December 2017



University  
of Glasgow

## Abstract

The study of vascular oxygen saturation has important implications in a range of diseases with which inflammation and hypoxia are associated. This thesis details advancements in multispectral imaging systems for *in vivo* optical biopsy, relating to new applications primarily for the localised measurement of blood oxygen saturation *in vivo*, and also fluorescence cellular imaging. A calibration-free oximetry technique, based on previous work in retinal oximetry, was developed for the purposes of microvascular oximetry analysis in deep tissue. A novel multispectral microscope was developed for imaging of the microvasculature, with annular back-illumination providing glint-free images and simplification of the optical oximetry model. This system was successfully employed for proof-of-concept oximetry in the mouse tendon, resulting in the first localised measurements of vascular hypoxia associated with acute inflammation. The tendon is of interest as it is affected by auto-immune inflammatory diseases such as rheumatoid arthritis. A further application of the oximetry algorithm to inflammation in the spinal cord of rats is described in this thesis, in which hypoxia associated with a rat model for multiple sclerosis was successfully quantified. The latter part of the thesis describes advancements made towards incorporating microendoscopic probes to the imaging system, extending the calibration-free oximetry technique to applications where minimally-invasive imaging is required. Preliminary *ex vivo* validation experiments in the mouse tendon are described. Finally, the minimally-invasive system was modified for multispectral fluorescence microscopy, and a novel technique for localised delivery of fluorophore-conjugated antibodies is described. Localised interventions and observations of immunological events is of interest to biologists as a greater understanding of immune-related disease can potentially be gained. Preliminary *ex vivo* experiments observing the binding of antibodies to T cells in the lymph node are described.

---

## Declaration

The work presented in this thesis is based on research carried out at the Imaging Concepts Group (ICG), School of Physics & Astronomy, University of Glasgow, Scotland. All procedures involving the use of living animals were carried out in accordance with UK Home Office guidelines. No part of this thesis has been submitted elsewhere for any other degree or qualification and is the sole work of the author apart from the following exceptions or where explicitly stated:

- The vessel-tracking software described in section 2.6.2 was written by A. Gorman, previously of the ICG.
- The data used for analysis in chapter 5 was acquired by Lewis E. Mackenzie (previously of the ICG) in collaboration with Kenneth Smith, Andrew Davies and Roshni Desai of the Department of Neuroinflammation, University College London.

Some of the work presented in chapters 4, 5 and 6 has been published. The relevant publications are listed below.

1. M.A. van der Putten, J. M. Brewer, and A. R. Harvey (2017). "Minimally invasive optical biopsy for oximetry," *Proc. SPIE* 10040, Endoscopic Microscopy XII, 1004009. doi: 10.1117/12.2253645
2. M.A. van der Putten, J. M. Brewer, and A. R. Harvey (2017). "Multispectral oximetry of murine tendon microvasculature with inflammation," *Biomedical Optics Express*, vol.8, no.6, p.2896. doi: 10.1364/BOE.8.002896
3. M.A. van der Putten, L.E. MacKenzie, A.L. Davies, J. Fernandez-Ramos, R.A. Desai, K.J. Smith, A.R. Harvey (2017). "A multispectral microscope for in vivo oximetry of rat dorsal spinal cord vasculature," *Physiological Measurement*, vol.38, p.205-18. doi: 10.1088/1361-6579/aa5527

## Acknowledgements

I would like to express my sincerest gratitude to my research supervisor, Professor Andy Harvey. Andy's guidance and advice over these past years has been greatly appreciated. I would also like to thank my second supervisor, Professor Jim Brewer of the Institute of Infection, Immunity and Inflammation (III). Jim has also been very supportive and encouraging during this research. Both Andy and Jim have been instrumental to the completion of my PhD and I feel very fortunate to have had such great supervisors. I am grateful to the University of Glasgow's Lord Kelvin Adam Smith scholarship scheme for providing the funding which made this project possible.

Many thanks are owed to both Dr. Hannah Scales and Dr. Robert Benson of III. I am very grateful for their help with the various biology aspects of this research, without which I could not have accomplished any of the *in vivo* experiments. I would also like to thank the staff of the Central Research Facility for their support, and for accommodating my imaging equipment during the *in vivo* experiments.

I would like to thank all my colleagues in the Imaging Concepts Group (ICG). The ICG has been a very pleasant place to work, and I have been fortunate to work with very helpful, kind and supportive colleagues. In particular, I would like to thank Dr. Javier Fernandez-Ramos and Dr. Lewis MacKenzie for their collaboration and discussions regarding the oximetry work in this thesis.

I would also like to thank our collaborators at University College London's Department of Neuroinflammation, particularly Professor Ken Smith and Dr. Andrew Davies, for their support in the completion and publication of the spinal cord oximetry work.

I would like to thank my mum Deirdre, and my sisters Sophie and Emma, for their unconditional support and belief in me over the past few years. I am also very grateful to Duncan for his support and companionship.

Finally, I would like to acknowledge my father Wil, who sadly passed away during the course of this research. As a fellow physicist, he was always interested in hearing about my work, and I always appreciated his advice and encouragement. I continue to miss his support (and frequent suggestions of papers I should read!), but his positive influence remains with me and has been very motivating for the completion of this work. This thesis is dedicated to him.

# Contents

<b>List of Figures</b>	<b>viii</b>
<b>List of Abbreviations</b>	<b>xi</b>
<b>1. Introduction and Background</b>	<b>1</b>
1.1. Aims and outline of thesis . . . . .	1
1.2. Motivation: inflammatory disease . . . . .	5
1.3. Interactions of light with tissue . . . . .	8
1.3.1. Absorption . . . . .	8
1.3.2. Scattering . . . . .	11
1.3.3. Fluorescence . . . . .	15
1.4. Overview of the vasculature and oxygen transport . . . . .	16
1.5. Oximetry: theory and background . . . . .	21
1.5.1. Electrochemical oxygen sensing . . . . .	21
1.5.2. Optical oximetry . . . . .	23
1.6. Multispectral imaging . . . . .	32
1.6.1. Basic concept . . . . .	32
1.6.2. Techniques . . . . .	34
1.6.3. Current Applications . . . . .	38
1.7. Microendoscopes for optical biopsy . . . . .	39
1.7.1. Introduction to microendoscopy . . . . .	39
1.7.2. GRIN lenses: Theory . . . . .	41
1.7.3. Review of applications . . . . .	44
1.8. Summary . . . . .	46
<b>2. Development and characterisation of calibration-free oximetry algorithm</b>	<b>47</b>
2.1. Introduction . . . . .	47
2.2. Derivation of basic analytical model . . . . .	49
2.3. Consideration of light paths . . . . .	51
2.4. Review of previous methods . . . . .	53
2.5. Development of optical model for microvasculature oximetry . . . . .	56
2.6. Implementation of algorithm with multispectral data . . . . .	61
2.6.1. Preliminary data processing . . . . .	61
2.6.2. Vessel tracking . . . . .	62
2.6.3. Calculation of experimental transmission values . . . . .	62
2.6.4. Diameter estimation . . . . .	65
2.6.5. Implementation of oximetry algorithm . . . . .	65

2.7.	Oximetry error . . . . .	69
2.7.1.	Photometric error . . . . .	69
2.7.2.	Propagation of error . . . . .	71
2.7.3.	Errors in extinction coefficients and other parameters . . . . .	72
2.8.	Assessment of performance . . . . .	73
2.8.1.	Blue wavelengths . . . . .	75
2.8.2.	Waveband-associated error . . . . .	75
2.8.3.	Green-Red wavelengths . . . . .	81
2.9.	Conclusions . . . . .	85
<b>3.</b>	<b>Multispectral imaging system for <i>in vivo</i> microcirculation oximetry</b>	<b>86</b>
3.1.	Development of imaging setup . . . . .	86
3.1.1.	Complete configuration for multispectral imaging . . . . .	87
3.1.2.	Illumination . . . . .	87
3.1.3.	Reflective objective . . . . .	92
3.2.	Graphical user interface for multispectral data acquisition . . . . .	99
3.3.	Assessment of image quality . . . . .	101
3.4.	<i>In vitro</i> validation . . . . .	105
3.5.	<i>Ex vivo</i> validation . . . . .	111
3.6.	Conclusions . . . . .	117
<b>4.</b>	<b><i>In vivo</i> oximetry study of hypoxia associated with acute inflammation</b>	<b>120</b>
4.1.	Background . . . . .	120
4.2.	Methods . . . . .	121
4.2.1.	Acute model for inflammation . . . . .	121
4.2.2.	Setup for imaging of tendon microvasculature . . . . .	122
4.3.	Results and discussion . . . . .	125
4.3.1.	Multispectral images . . . . .	125
4.3.2.	Comparison of control and inflamed tendon vasculature . . . . .	129
4.3.3.	Assessment of vessel diameter . . . . .	130
4.3.4.	Oximetry validation <i>in vivo</i> . . . . .	134
4.3.5.	Kinetic study of SO <sub>2</sub> . . . . .	134
4.4.	Potential for diagnostic classification . . . . .	137
4.5.	Conclusions . . . . .	140
<b>5.</b>	<b>Oximetry study of vasculature in the rat dorsal spinal cord <i>in vivo</i></b>	<b>142</b>
5.1.	Background . . . . .	142
5.2.	Experimental setup . . . . .	144
5.3.	Image acquisition . . . . .	148
5.4.	Oximetry analysis . . . . .	150
5.5.	Results and discussion . . . . .	152
5.5.1.	Multispectral images . . . . .	152
5.5.2.	Changes in inspired oxygen . . . . .	153
5.5.3.	Repeatability of measurements . . . . .	157
5.5.4.	Comparison of control and EAE vasculature . . . . .	158

5.5.5. Assessment of vessel diameter . . . . .	161
5.5.6. Experimental oximetry validation . . . . .	163
5.6. Conclusions . . . . .	166
<b>6. Minimally invasive oximetry</b>	<b>169</b>
6.1. Introduction . . . . .	169
6.2. Incorporation of microendoscope to multispectral imaging system .	171
6.2.1. Triplet fibre illumination . . . . .	172
6.3. Assessment of image quality . . . . .	177
6.3.1. Basic Zemax model . . . . .	177
6.3.2. Resolution and contrast modulation . . . . .	181
6.4. <i>Ex vivo</i> minimally invasive oximetry . . . . .	184
6.5. <i>In vitro</i> validation . . . . .	187
6.5.1. FEP phantoms with green-red wavelengths . . . . .	189
6.6. Conclusions . . . . .	191
<b>7. Fluorescence microendoscopy for experiments in immunology</b>	<b>195</b>
7.1. Introduction . . . . .	195
7.2. Background and motivation . . . . .	197
7.3. Experimental setup for minimally invasive fluorescence microscopy	201
7.3.1. Adaptations from oximetry setup . . . . .	201
7.4. Validation of system . . . . .	206
7.5. Visualisation of T cells <i>ex vivo</i> . . . . .	207
7.5.1. Demonstration of fluorescence microendoscopy - T cells . .	208
7.5.2. Demonstration of localised delivery of fluorophore-conjugated antibody . . . . .	209
7.6. Validation of localised AB labelling . . . . .	212
7.7. Two-photon microscopy . . . . .	217
7.8. Conclusions . . . . .	220
<b>8. Conclusions and future work</b>	<b>222</b>
8.1. Multispectral imaging system for oximetry . . . . .	223
8.2. Minimally invasive <i>in vivo</i> oximetry . . . . .	225
8.3. Fluorescence microendoscopy for immunology . . . . .	226
8.4. Concluding remarks . . . . .	227
<b>Bibliography</b>	<b>229</b>

# List of Figures

1.1.	Simplified illustration of atomic absorption of light . . . . .	9
1.2.	Simplified illustration of macroscopic absorption of light . . . . .	10
1.3.	Illustration of Mie and Rayleigh scatter geometry . . . . .	13
1.4.	Illustration of elastic and inelastic optical scattering processes . . .	14
1.5.	Jablonski diagram depicting fluorescence process . . . . .	16
1.6.	Extinction spectra of oxygenated and deoxygenated haemoglobin .	19
1.7.	Oxygen-haemoglobin dissociation curve . . . . .	19
1.8.	Illustration of vessel intensity line profile . . . . .	26
1.9.	Illustration of multispectral imaging concept . . . . .	34
1.10.	Illustration of Bayer filter mosaic . . . . .	35
1.11.	Microendoscopy publications over time . . . . .	40
1.12.	Illustration of light paths in GRIN lenses . . . . .	42
1.13.	Illustration of triplet GRIN lens microendoscope . . . . .	43
2.1.	Illustration of light paths in vascular oximetry . . . . .	52
2.2.	Illustration of line profile analysis in MATLAB . . . . .	64
2.3.	Examples of oximetry analysis: fit of model to raw data . . . . .	67
2.4.	Example of oximetry analysis: fit of model to raw data . . . . .	68
2.5.	Relative analysis error with respect to optical transmission. . . . .	70
2.6.	Depiction of chord length across artificial blood vessel . . . . .	74
2.7.	Example images of theoretical vessels from artificial data sets . . . .	75
2.8.	Example of cross-sectional line profiles of theoretical blood vessel .	76
2.9.	Errors associated with finite waveband . . . . .	77
2.10.	Example of theoretical vessel with additive noise . . . . .	78
2.11.	Recovered SO <sub>2</sub> for theoretical data with additive noise (blue) . . . .	78
2.12.	Recovered SO <sub>2</sub> with waveband-specific contrast reduction (blue) . .	79
2.13.	Recovered K with waveband-specific contrast reduction (blue) . . .	80
2.14.	Recovered SO <sub>2</sub> for theoretical data with additive noise (green-red) .	82
2.15.	Recovered SO <sub>2</sub> with waveband-specific contrast reduction (green-red) red) . . . . .	83
2.16.	Recovered K with waveband-specific contrast reduction (green-red)	84
3.1.	Schematic of MSI system for oximetry . . . . .	88
3.2.	Photo of MSI system for oximetry . . . . .	88
3.3.	Transmission profiles of theoretical 10 $\mu$ m blood vessel . . . . .	89
3.4.	Corrected AOTF output as measured by spectrometer . . . . .	91
3.5.	Illustration of laser speckle reducer effect . . . . .	92
3.6.	Configuration of mirrors for reflective objective . . . . .	93

## List of Figures

---

3.7. Comparison of images with and without beam block . . . . .	94
3.8. Simulated transmission pupils . . . . .	95
3.9. Simulated modulation transfer functions . . . . .	96
3.10. Zemax model of annular illumination configuration . . . . .	98
3.11. Zemax illumination images . . . . .	99
3.12. AOTF GUI and MDR connector pin diagram . . . . .	100
3.13. Software flow chart for multispectral image acquisition . . . . .	102
3.14. Resolution test of imaging system (USAF 1951 target) . . . . .	104
3.15. Edge spread function of imaging system . . . . .	105
3.16. Modulation transfer system of imaging system . . . . .	106
3.17. Illustrative diagram and raw image of tendon microvasculature . . . . .	107
3.18. Line profiles of blood-filled 50 $\mu\text{m}$ FEP at blue wavelengths . . . . .	108
3.19. Retrieved phantom $\text{SO}_2$ for varying oxygenation . . . . .	110
3.20. Illustrative image of exposed tendon tissue . . . . .	111
3.21. ODR analysis of <i>ex vivo</i> tendon vessel . . . . .	112
3.22. Setup of chamber for nitrogen flow experiment . . . . .	113
3.23. Multispectral images of murine tendon microvasculature <i>ex vivo</i> . . . . .	115
3.24. ODR as function of time for <i>ex vivo</i> oximetry validation - 1 . . . . .	116
3.25. ODR as function of time for <i>ex vivo</i> oximetry validation - 2 . . . . .	116
3.26. Reported $\text{SO}_2$ for <i>ex vivo</i> oximetry validation . . . . .	117
4.1. Comparison of footpad thickness before and after inflammation . . . . .	123
4.2. Photograph of mouse prepared for imaging . . . . .	125
4.3. Multispectral images of murine tendon microvasculature <i>in vivo</i> . . . . .	127
4.4. Illustrative images of tendon microvasculature results . . . . .	128
4.5. Comparison of $\text{SO}_2$ from control and inflamed microvasculature . . . . .	130
4.6. Comparison of $\text{SO}_2$ from all microvasculature . . . . .	131
4.7. Reported $\text{SO}_2$ as function of measured diameter . . . . .	133
4.8. Measurement of $\text{SO}_2$ post mortem . . . . .	135
4.9. Kinetic analysis of $\text{SO}_2$ as a function of increasing inflammation . . . . .	136
4.10. Confusion matrix for trained classification model (all data) . . . . .	138
4.11. Confusion matrix for trained classification model (cross validation) . . . . .	139
5.1. Comparison of transmission profiles for 80 $\mu\text{m}$ vessel . . . . .	146
5.2. Schematic of basic multispectral microscope . . . . .	147
5.3. Multispectral images of control rat . . . . .	154
5.4. Example of optical transmissions $T(\lambda)$ and $\text{SO}_2$ along vessel . . . . .	155
5.5. Results for control venous $\text{SO}_2$ . . . . .	156
5.6. Average control arterial and venous $\text{SO}_2$ . . . . .	157
5.7. Results for EAE venous $\text{SO}_2$ . . . . .	159
5.8. Comparison of average dorsal venous $\text{SO}_2$ . . . . .	160
5.9. Reported $\text{SO}_2$ as function of measured diameter . . . . .	162
5.10. Example images of vascular phantoms at 546 nm and 600 nm . . . . .	164
5.11. Comparison of intensity profiles over blood vessel at 30% and 100% $\text{SO}_2$ . . . . .	165

---

5.12. Validation of SO <sub>2</sub> results for basic MSI system . . . . .	166
6.1. Illustration of microendoscope coupled to objective . . . . .	172
6.2. Setup for minimally invasive oximetry . . . . .	174
6.3. Geometry of individual fibre illumination output . . . . .	174
6.4. Photograph of assembled fibre triplet, at both proximal and distal ends . . . . .	176
6.5. Illustration of Zemax microendoscope model . . . . .	179
6.6. Expected chromatic focal shift for triplet lens microendoscope . . .	180
6.7. Zemax plot of spot diagram through focus . . . . .	181
6.8. Image of USAF resolution target through microendoscope . . . . .	182
6.9. Image of grid target through microendoscope for two illumination schemes . . . . .	183
6.10. Line profile of grid target microendoscope image . . . . .	184
6.11. Example image of <i>ex vivo</i> microvasculature through microendoscope	185
6.12. Intensity profiles (raw and normalised) of vessel through microen- doscope . . . . .	187
6.13. Image of pulled micropipette . . . . .	188
6.14. Image of 50 µm FEP phantom through microendoscope . . . . .	190
6.15. Normalised intensity profiles of phantom imaged through mi- croendoscope . . . . .	190
6.16. Obtained SO <sub>2</sub> for microendoscopic imaging of <i>in vitro</i> phantom . .	191
7.1. Fluorescent microendoscopy with localised delivery of antibodies .	200
7.2. Transmission spectra of multi-channel optical fluorescence filters .	202
7.3. Adaptations to minimally invasive microscope for fluorescence imaging . . . . .	202
7.4. AOTF channels for fluorescence excitation . . . . .	203
7.5. Flow chart for multi-channel fluorescence acquisition . . . . .	204
7.6. Fluorescent excitation channel spectra . . . . .	205
7.7. [Multi-channel images of fluorescent beads through microendoscope	208
7.8. Preliminary image of DsRed T cells . . . . .	210
7.9. Intensity profiles of labelled DsRed T cells at fluorescent channels .	211
7.10. Negative control of intensity profiles from cell-free area . . . . .	211
7.11. Flow cytometry data showing DsRed and eFluor Channels . . . . .	214
7.12. Gated flow cytometry data showing DsRed and PE-Cy7 Channels .	215
7.13. Gated flow cytometry data showing DsRed and AF647 Channels .	216
7.14. Flow cytometry data showing DsRed and AF647 Channels . . . . .	218
7.15. Composite two-photon image of DsRed LN . . . . .	219

# List of Abbreviations

<b>2P</b>	Two-photon
<b>ACPA</b>	Anti-citrullinated protein antibody
<b>AOTF</b>	Acousto-optic tuneable filter
<b>BGA</b>	Blood gas analyser
<b>CIA</b>	Collagen-induced arthritis
<b>DOS</b>	Diffuse optical spectroscopy
<b>EAE</b>	Experimental autoimmune encephalomyelitis
<b>EM</b>	Electromagnetic
<b>FEP</b>	Fluorinated ethylene propylene
<b>FOV</b>	Field of view
<b>fps</b>	Frames per second
<b>GRIN</b>	Gradient refractive index
<b>Hb</b>	Haemoglobin
<b>HbO<sub>2</sub></b>	Oxyhaemoglobin
<b>HSI</b>	Hyperspectral imaging
<b>IR</b>	Infrared
<b>IRIS</b>	Image-replicating imaging spectrometer
<b>LCTF</b>	Liquid crystal tuneable filter
<b>LN</b>	Lymph node
<b>MM</b>	Multi-mode
<b>MSI</b>	Multispectral imaging
<b>MTF</b>	Modulation transfer function
<b>NA</b>	Numerical aperture
<b>NIR</b>	Near-infrared
<b>NIRS</b>	Near-infrared spectrometry
<b>OCT</b>	Optical coherence tomography
<b>OD</b>	Optical density

## List of Figures

---

<b>ODR</b>	Optical density ratio
<b>OTF</b>	Optical transfer function
<b>PBS</b>	Phosphate buffered saline
<b>PSD</b>	Power spectral density
<b>PSF</b>	Point spread function
<b>RBC</b>	Red blood cell
<b>RF</b>	Rheumatoid factor
<b>SLOT</b>	Sagittal laser optical tomography
<b>SNR</b>	Signal-to-noise ratio
<b>SO<sub>2</sub></b>	Blood oxygen saturation
<b>StO<sub>2</sub></b>	Tissue oxygen saturation
<b>TNR</b>	True negative rate
<b>TPR</b>	True positive rate
<b>UV</b>	Ultraviolet
<b>MS</b>	Multiple sclerosis
<b>PO<sub>2</sub></b>	Partial pressure of oxygen
<b>RA</b>	Rheumatoid arthritis

# 1. Introduction and Background

---

**Summary:** In this chapter, the aims of and motivation for the thesis are presented. An outline of the thesis is also given. A brief background is presented on the relevant physics concepts, as well as a review of associated literature throughout, including: interactions of light with biological tissue, an overview of the vasculature and oxygen transport, the theory behind vascular optical oximetry and multispectral imaging, and finally an introduction to the theory and application of microendoscopic probes for minimally invasive imaging.

## 1.1. Aims and outline of thesis

The main aim of the interdisciplinary research described in this thesis is the development of a novel imaging system for deep tissue *in vivo* optical biopsy. "Optical biopsy" is a broad term referring to a range of techniques which employ the interaction of light with biological tissue to provide qualitative or quantitative information, usually regarding the health of the tissue [1]. Optical biopsy incorporates a range of absorption and fluorescence spectroscopic techniques, as well as optical coherence and photo-acoustic tomography, for numerous applications in medical diagnostics. These have included the diagnosis of multiple cancers such as breast, lung and skin cancer [2], as well as other conditions such as Barrett's

## 1. Introduction and Background

---

oesophagus [3]. Optical biopsy is possible due to the optical spectrum of a tissue sample containing information regarding its biochemical composition [4].

Performing *in vivo* optical biopsy presents many advantages over conventional biopsy techniques which typically require a section of tissue to be excised for histological analysis. Surgical excision of tissue is invasive and can cause delays in diagnoses and the potential for sampling errors. Optical biopsy attempts to minimise these problems by allowing for real-time, non-destructive *in situ* analyses of tissue. The aim of this thesis is the development of a novel system for optical biopsy *in vivo*, with a view to extending the technique to “minimally invasive” imaging for access to deep tissue. As described later in this chapter, minimally invasive imaging is facilitated by miniature microendoscopic lenses.

The specific focus of this work is the application of oximetry (quantitative blood oxygen saturation measurement) in immune-related inflammatory disease, involving the development of new minimally-invasive imaging capability. Oximetry is based on sensing the optical properties of haemoglobin (Hb), which change depending on how much oxygen is bound to it [5]. Multispectral imaging is employed in order to achieve this localised imaging oximetry, as well as fluorescence imaging techniques to allow for the observation of immune-related cellular events. In summary, the explicit objectives of this thesis and the reasons for these objectives are listed below:

1. Development of multispectral imaging system and oximetry algorithm for the specific application of oximetry in microvasculature.  
*Hypoxia is associated with inflammatory disease, and a robust technique for the localised oximetry of microvasculature will allow for the investigation of the relationship between vascular oxygenation and disease pathology.*
2. Proof-of-concept oximetry experiments *ex vivo* and *in vivo* using the above system to investigate hypoxia associated with inflammation.

## 1. Introduction and Background

---

*Validation experiments will verify the correct operation of the system, and preliminary in vivo experiments comparing controls and inflamed tendons in mice will demonstrate the ability of the system to resolve changes in microvascular oxygenation.*

3. Adaptation of multispectral imaging system for minimally invasive oximetry using microendoscopic probes, and associated proof-of-concept oximetry experiments *ex vivo*.

*For longitudinal experiments over a longer period of time, minimally invasive access to the tissue will be necessary. Microendoscopic probes are proposed as a means for achieving this goal.*

4. Development of minimally invasive fluorescence imaging system, and associated proof-of-concept experiments.

*In addition to oximetry, the ability to study immune-related cellular events in vivo, again using minimally invasive microendoscopes, may provide further insight into the etiology and progression of inflammatory diseases.*

The outline of the thesis is as follows: this chapter presents the background and motivation for the thesis, namely the study of inflammatory disease by means of oximetry and fluorescence microscopy. As a number of different areas are incorporated within this thesis, an introduction to the broad range of relevant concepts is described. The interaction of light with biological tissue is first presented, followed by an overview of the vasculature and a brief description of oxygen transport. The principles of oximetry are then described, including a review of previous relevant studies. Finally, an introduction to multispectral imaging is given, followed by a review of microendoscopic probes for minimally invasive imaging.

In chapter 2, a derivation of the analytical model used to perform oximetry analysis is given, along with a review of both similar and disparate calibration-free oximetry techniques. The practical implementation of the model in MATLAB is described in detail, as well as the intermediary data processing steps. A method

## 1. Introduction and Background

---

for generating “theoretical” oximetry data is also described, and used for assessment of the performance of the analysis technique in the presence of additive noise and contrast loss.

Chapter 3 contains a description of the multispectral imaging system which was developed as part of this thesis, and describes a consideration of its constituent parts. A validation of the oximetry capability of the system is also given in this chapter, both *in vitro* and *ex vivo*.

In chapter 4, *in vivo* oximetry studies are presented, in which blood oxygen saturation of mouse tendon microvasculature is investigated, in both controls and those with acute localised inflammation. The extent to which the oximetry system can detect hypoxia *in vivo* is investigated.

In chapter 5, a collaborative study with the Department of Neuroinflammation at University College London is described. In this study, a basic multispectral imaging system was used to study the vasculature of the rat dorsal spinal cord. An investigation is presented into the oxygen state of this vasculature in rats affected by a model for multiple sclerosis.

Chapter 6 presents the progress made towards extending the multispectral oximetry technique to minimally invasive imaging using microendoscopic probes. The modifications made to the original system are detailed, including a custom-made triplet optical fibre illumination source. An *in vitro* validation of this newer minimally invasive system is described, as is preliminary *ex vivo* imaging.

In chapter 7, the final experimental work of the thesis is presented. Distinct from vascular oximetry, this chapter describes a fluorescence microendoscopy system combined with the capability to deliver small amounts of fluid in the vicinity of the field of view. The system was used to observe binding of fluorophore-conjugated antibodies with antigen-presenting T cells in the lymph node. The work was validated by flow cytometry; the “gold-standard” for cell classification.

## 1. Introduction and Background

---

Finally, chapter 8 details the potential future work and conclusions drawn from completion of the thesis.

### **1.2. Motivation: inflammatory disease**

Oxygen is of fundamental importance to the health and function of all living cells and tissue. A state of inadequate oxygenation, known as hypoxia, can occur either due to increased demand by the tissue, or by insufficient supply from the vasculature, and occurs in a range of diseases. At a physiological level of hypoxia, cells do not receive adequate oxygen required to function correctly, leading to metabolic issues and damage to tissue. In particular, auto-immune inflammatory diseases such as rheumatoid arthritis (RA) and multiple sclerosis (MS) result in a hypoxic environment around the affected tissue which is generally inflamed [6, 7].

RA is a chronic, immune-related disease causing painful swelling and inflammation of the tendons and joints. RA can lead to destruction of synovial joints through bone erosions, severe disability and premature mortality. RA affects approximately 0.5 - 1 % of the population, and is more prevalent in women than in men [8]. There is no known cure for RA, but remission is possible if diagnosed and treated early. Early treatment can also prevent irreversible tissue damage and bone erosion [9]. However, RA is difficult to diagnose at an early stage, with no single laboratory test confirming its diagnosis [10]. A blood test for auto-antibodies such as "rheumatoid factor" (RF) and "anti-citrullinated protein antibodies" (ACPA) are often performed in suspected cases of RA, as elevated levels are associated with autoimmune disease [11]. However, they are not solely conclusive of a diagnosis, with elevated levels occasionally present in healthy individuals. Further, RF is frequently absent in early stages of the disease. At present, physicians assess whether the patient exhibits a number of clinical features, for each of which they are given a score [12]. The patient is given a positive diagnosis of RA if their

## 1. Introduction and Background

---

total score exceeds a certain threshold. These classification criteria, originally published in 1987 by the American College of Rheumatology, were originally not considered useful for detecting early forms of RA. The criteria were shown to have specificity of little improvement over random probability [13]. In 2010, the classification criteria were updated in order to address the issues with early disease diagnosis [14]. However, the sensitivity of these newer criteria remains relatively low in early RA, at 72.3 % [15]. In classification, the sensitivity of a diagnostic test is the probability or rate of making a correct, positive diagnosis. The specificity of a test is the rate of correctly making a negative diagnosis. Sensitivity and specificity are also known as true positive rate (TPR) and true negative rate (TNR) respectively. There is still clear motivation for studying the early stages of the disease in order to further improve capability for early diagnoses. In this thesis, the blood oxygen saturation of the vasculature in inflamed tendons is investigated as a preliminary study into whether hypoxia may be viable as a proxy biomarker for early stage RA.

The link between hypoxia and RA is well established. It has previously been reported that RA synovitis (an inflammation of the synovial membrane within the joint) is associated with angiogenesis; the creation of new blood vessels [16]. However, the joint remains hypoxic as a result of a dysfunctional neovascular network. It has also been reported that levels of partial pressure of oxygen ( $PO_2$ ) are lower in the synovial fluid of knee joints in patients suffering from RA [17].  $PO_2$  levels influence the binding affinity of haemoglobin to oxygen, and hence the oxygen saturation of blood; described in detail in section 1.4. Although the association between hypoxia and RA is clear, the specific role that hypoxia plays in the progression of the disease is not fully understood [18]. It is also not known when and where hypoxia originates in affected joints, and whether hypoxia may be suitable as a proxy biomarker for RA and associated inflammation. A primary goal of this work was the development of an optical biopsy system capable of investigating these questions by allowing for quantitative, localised oximetry *in*

## 1. Introduction and Background

---

*in vivo*.

To date, there have been a small number of studies reporting optical tests for the classification of RA *in vivo*. In 2004, Hielscher et al published a study demonstrating sagittal laser optical tomography (SLOT) of finger joints [19]. The same group performed a first clinical evaluation using this technology the following year in 2005 [20]. The technique involves acquiring a 3-dimensional representation of a joint by trans-illumination of distal finger joints using an NIR laser at 675 nm. The resulting absorption coefficients  $\mu_a$  were investigated, and shown to be elevated in patients with RA compared to healthy subjects. For 675 nm, an increase in  $\mu_a$  indicates a reduction in oxygenation, as at this wavelength, the extinction coefficient of deoxygenated haemoglobin,  $\epsilon_{Hb}$ , is greater than that of oxygenated haemoglobin  $\epsilon_{HbO_2}$ . The 2005 study achieved specificity and sensitivity of 0.71. A subsequent study reported that sensitivity and specificity of 0.76 and 0.78 respectively were achieved if further optically derived parameters were combined in the classification process [21]. More recently in 2011, the technique was further improved by the introduction of “frequency domain” optical tomography [22]. The technique utilises phase information to improve separation of scattering and absorption effects - hence improving sensitivity and specificity values to 0.85 or higher. Whilst clearly a promising technique for the optical classification of arthritic joints, the resolution of SLOT is limited, with many single measurements taken in order to build a 3-dimensional image. This results in data which lacks fine anatomical detail, with the smallest resolvable feature reported to be 0.4 mm. Additionally, as multiple measurements are required and processed, there is a lengthy reconstruction time.

There has been a recent study published by Rajaram et al (2016), in which it is claimed that measurement of joint blood flow is “more sensitive to inflammatory arthritis than oxyhaemoglobin, deoxyhaemoglobin, and oxygen saturation” [23]. In this paper, the results were achieved using diffuse optical spectroscopy (DOS), and measurements involved an optical contrast agent. The oxygen saturation the

## 1. Introduction and Background

---

authors measured was of the tissue in its entirety ( $StO_2$ ), and they claimed to have found no statistically significant reduction in  $StO_2$  when comparing arthritic rabbit knees to controls. However, as in SLOT, spatial resolution is an issue with this technique. It may be the case that localised oxygen saturation of the vasculature is more sensitive to inflammation than  $StO_2$  of the joint as a whole.

Vascular oximetry is the quantitative measurement of blood oxygen saturation ( $SO_2$ ), the basic theory of which is presented in section 1.5. Vascular oximetry provides measurements localised to individual capillaries. It is possible that measurement of localised  $SO_2$  will not provide improved sensitivity or specificity in terms of classification for inflammation. However, the localised nature of these measurements will allow, at the very least, for exploration of the link between hypoxia and the causes and progression of RA and inflammation on a microscopic scale.

### 1.3. Interactions of light with tissue

#### 1.3.1. Absorption

Central to the concept of spectroscopy and oximetry is the absorption of light by matter. On a molecular level, absorption is a resonant interaction which occurs between a photon and a medium it encounters. A photon carries energy  $E = h\nu$ , where  $h$  is Planck's constant, and  $\nu$  the frequency of the light. If this energy matches a specific transition energy, a free ground state molecule may absorb the photon and enter an excited state as depicted in figure 1.1. These transitions have distinct energy levels, and the incident photon must exactly match this transition energy to be absorbed. However, real media such as biological tissue are complex and contain multiple energy states, resulting in continuous absorption over a range of optical frequencies. Consequently, biological tissues possess characteristic absorption spectra.

## 1. Introduction and Background

---

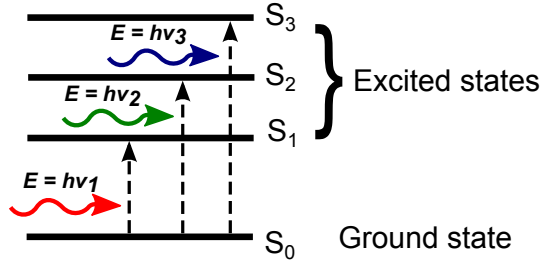


**Figure 1.1.** Simplified illustration of atomic absorption of light

On the macroscopic level, this atomic absorption manifests as an attenuation of light impinging upon a material, reducing its intensity as photons are absorbed by the constituent molecules. This physical principle, known widely as the Lambert-Beer law, is a fundamental concept to this thesis and will now be derived. The derivation is based on that presented in Ingle & Crouch (1988) [24].

Consider a beam of light, parallel to the  $z$  axis, incident on an infinitesimal slab of material of area  $A$  and thickness  $\delta z$  as illustrated in Figure 1.2. The slab contains absorbing molecules of concentration  $N$  (molecules/cm<sup>3</sup>), and cross section  $\sigma$  of light being absorbed by a single molecule. The fraction of incident photons absorbed by the slab will be a ratio of the total absorbing area over the overall area:

$$\frac{\sigma AN \delta z}{A} = \sigma N \delta z \quad (1.1)$$

If the total number of photons incident on the slab is  $I_z$ , we can therefore define the number of photons absorbed as  $\delta I_z$ , multiplying the incident number of photons by the above fraction:

$$\delta I_z = -I_z \sigma N \delta z \quad (1.2)$$

We wish to obtain  $I_z$  as a function of  $z$ . Rearranging and then integrating both sides of 1.2, we get

$$\int \frac{\delta z}{I_z} = - \int \sigma N \delta z \quad (1.3)$$

$$\ln(I_z) = -\sigma N z + C \quad (1.4)$$

Considering now a real slab of thickness  $l$ , we can define the incident intensity at

## 1. Introduction and Background

---

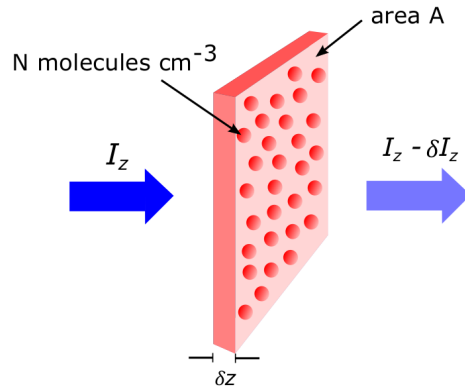


**Figure 1.2.** Simplified illustration of macroscopic absorption of light by molecules in an infinitesimal slab of thickness  $\delta z$ . Incident photon intensity  $I_z$  is attenuated through absorption by  $\delta I_z$ .

$z = 0$  as  $I_0$ , and as  $I$  at  $z = l$ . Substituting these values into equation 1.4 we get the following:

$$\ln(I) - \ln(I_0) = (-\sigma l N + C) - (-\sigma(0)N + C) = -\sigma N l \quad (1.5)$$

and rearranging for optical transmission  $T$ ,

$$\ln\left(\frac{I}{I_0}\right) = -\sigma l N \quad (1.6)$$

$$T = \frac{I}{I_0} = \exp(-\sigma l N) \quad (1.7)$$

and finally, we substitute  $N$  and  $\sigma$  for the molar concentration  $c$  (mol/litre) and molar attenuation coefficient  $\epsilon$  ( $\text{Mol}^{-1}\text{cm}^{-1}$ ) respectively. The absorbance  $A$  of the sample can then be expressed as

$$A = -\log_{10} \frac{I}{I_0} = \left(\frac{\sigma l N}{2.303}\right) = \epsilon c l \quad (1.8)$$

The molar attenuation coefficient is dependent on the energy of the incident photons (related to the wavelength of light by  $E = \frac{hc}{\lambda}$ ), such that  $A(\lambda) \propto \epsilon(\lambda)$ .

The above equation 1.8 is the Lambert-Beer law, and it relates the attenuation of

## 1. Introduction and Background

---

light through a medium to its properties such as molar attenuation coefficient and molar concentration. It is worth noting that an equivalent descriptor for the optical absorption characteristic of a material is often given in terms of its absorption coefficient  $\mu_a$  (in units of  $\text{cm}^{-1}$ ). It is defined as the sum of absorbing molecules within the tissue [25]:

$$\mu_a = \ln(10) \sum_i c_i \varepsilon_i \quad (1.9)$$

such that  $T = \exp -\mu_a l = 10^{-\varepsilon c l}$ .

The Lambert-Beer law is not a complete description of light interaction with tissue; most biological tissues exhibit significant optical scatter which also influences the intensity of transmitted light. Modifications to the Lambert-Beer law can be made to include such considerations of optical scatter, and this is known as the “modified Lambert-Beer” law. Additionally, at high incident light intensities, nonlinear optical processes can occur within material which also affect the properties of transmitted light. In the field of oximetry (and throughout this thesis), absorbance is referred to as optical density.

### 1.3.2. Scattering

Optical scattering occurs when light is incident on optically inhomogeneous material such as biological tissue [26]. It results in a deviation of light from its original path. Unlike absorption in which the number of photons decreases, optical scattering leaves the number of incident photons unchanged, however the number of photons transmitted through a material may decrease due to the re-direction of these photons. It therefore also contributes to attenuation of light transmitted between a source and receiver, and its consideration is necessary in analytical models for oximetry, as described in chapter 2.

## 1. Introduction and Background

---

Optical scattering may be an *elastic* or *inelastic* process. The scattering is said to be elastic if the frequency of the scattered light remains unchanged from the original frequency. Inelastic optical scattering results in a change (either an increase or decrease) in optical frequency of the scattered light. In this case, such as in Raman scattering, the energy either gained or lost by the light is transferred to the scattering molecules.

### **Elastic scattering**

There are two principal regimes of elastic optical scattering, known as *Rayleigh* scattering and *Mie* scattering. Rayleigh scattering occurs if the size of the scattering centre is much smaller than the wavelength of the light ( $r \ll \lambda$ ), in which case the scattering cross-section  $\sigma_s(\lambda)$  will depend strongly on wavelength, where  $\sigma_s(\lambda) \propto \lambda^{-4}$  [27]. This rule implies that shorter wavelengths are generally scattered more strongly than longer wavelengths. The intensity of Rayleigh scattering is also proportional to the polarisability of the material. Mie scattering refers to optical scattering by particles of comparable or larger size than the wavelength of light ( $r \approx \lambda$ ), and is not as strongly wavelength-dependent. Technically, Mie theory does include scattering by particles of all sizes, but for small particles the solution approximates that of Rayleigh scattering [28]. The scattering dependence of both regimes is illustrated in figure 1.3. Mie scattering is highly anisotropic, resulting in light which is strongly forward-scattered. In contrast, Rayleigh scattering, whilst not isotropic, results in light being both forward- and back-scattered; the Rayleigh-scattered light intensity at right angles is half the forward and backward scattered intensity. Light which is multiply scattered by a material is said to be diffuse.

The optical scattering properties of a material are described by its scattering coefficient  $\mu_s$  ( $\text{cm}^{-1}$ ) and the scattering function  $p(\theta, \psi)$  ( $\text{sr}^{-1}$ ), where  $\theta$  and  $\psi$  are the deflection and azimuthal angles of scatter respectively [25]. The scattering

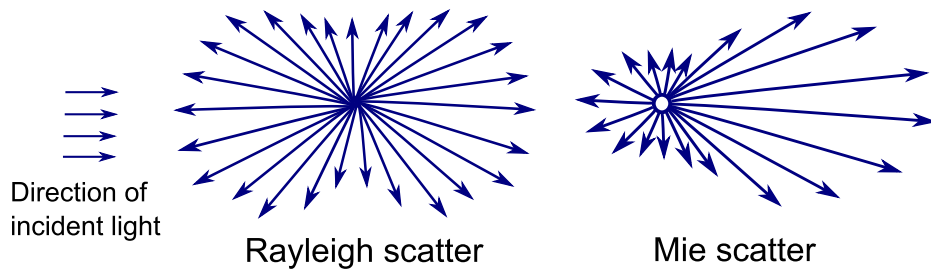


**Figure 1.3.** Illustration of Mie and Rayleigh scatter geometry. Highly forward scatter is associated with Mie scattering, whereas Rayleigh scatter exhibits both forward- and back-scatter.

function  $p(\theta, \psi)$  is appropriate for single or few scattering events. In thicker sections of material where many scattering events occur such as in biological tissue, there is an averaging of  $\psi$  due to the random orientation of scattering structures, thus  $\psi$  can be ignored. Multiple scattering also results in an averaging of  $\theta$ , resulting in a parameter  $g = \langle \cos \theta \rangle$  known as the anisotropy function. This function defines the degree of forward scatter;  $g$  is 0 for isotropic scatter, and 1 for completely forward scatter. For most biological tissue, the Mie regime of scatter dominates, and  $g$  is usually 0.8 - 1 [29]. The reduced scattering coefficient  $\mu'_s$  can then be defined, with  $\mu'_s = \mu_s(1 - g)$ . This accounts for the directional dependence of the scatter. Considering both absorption and elastic scattering, we can define a total transport loss by a total attenuation coefficient  $\mu_t = \mu_a + \mu'_s$ . It is known that scattering coefficients of haemoglobin are wavelength dependent, however it has recently been shown that they are also dependent on oxygenation [30]. This is taken into consideration in the oximetry model described in chapter 2.

### Inelastic optical scattering

In certain cases, optical scattering may result in a transfer of energy from the scattering molecule to the photon, or vice versa. This is known as Raman scattering. Incident light of a single frequency interacts with a molecule and may be scattered with a frequency shift equal to the loss or gain of energy to a molecular vibration. If a molecule absorbs energy from the incident light, it will be promoted from the

## 1. Introduction and Background

---

ground vibrational energy state to a higher excited state which results in Stokes Raman scattering. In this case, the scattered photon will have lower energy and hence frequency than the incident light. Anti-Stokes Raman scattering occurs if some molecules are already in an excited vibrational state. In this case the scattered light gains energy and will have higher frequency. This process is depicted in figure 1.4, as well as a comparison with elastic Rayleigh scattering. Raman scattering only occurs if nuclear motion is induced in the scattering process and it is therefore quite a weak process, with only one in every  $10^6 - 10^8$  scattered photons undergoing Raman scatter [31].

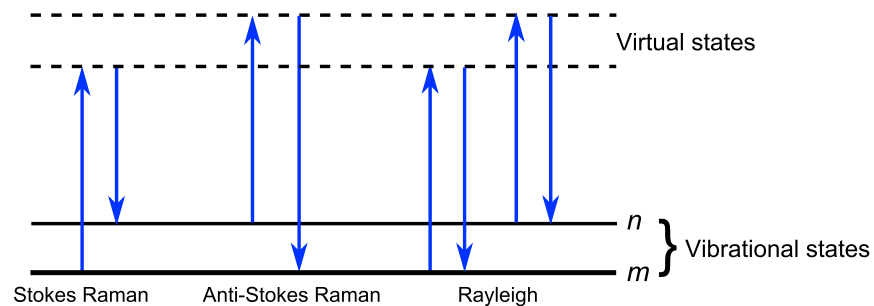


**Figure 1.4.** Illustration of vibrational energy states and transfer from ground state  $m$  to excited vibrational state  $n$  and vice versa as a result of Stokes and Anti-Stokes Raman scattering. Elastic Rayleigh scattering is also depicted.

As different molecular species will exhibit different molecular vibrations and hence Raman peaks, Raman spectroscopy is often employed for quantification of the chemical composition of material. Raman spectra are typically presented as a function of wavenumber shift ( $\text{cm}^{-1}$ ) from the original frequency:

$$\text{Raman shift (cm}^{-1}\text{)} = \frac{1}{\lambda_0} - \frac{1}{\lambda_s} \quad (1.10)$$

where  $\lambda_0$  is the incident wavelength, and  $\lambda_s$  the wavelength of the Raman-scattered light.

Raman scattering is not of particular relevance to vascular optical oximetry. How-

## 1. Introduction and Background

---

ever, Raman spectroscopy has previously demonstrated that differences exist between the Raman spectra of oxygenated and deoxygenated haemoglobin [32] [33]. It has been employed *ex vivo* in various optical biopsy techniques, and is capable of distinguishing between healthy and cancerous tissues *ex vivo*, including breast cancer [34], and brain cancer [35]. In recent years, the application of Raman spectroscopy *in vivo* has been investigated, such as in the diagnosis of skin cancer [36]. However, it presents significant challenges due to the relatively low intensity of the Raman signal, coupled with background tissue autofluorescence.

### 1.3.3. Fluorescence

The final optical interaction to be briefly discussed is fluorescence. Fluorescence is a form of photoluminescence, in which an atom or molecule emits light following excitation by absorption of photons of specific wavelengths. Figure 1.5 is a simplified depiction of this process. A molecule in a singlet electronic state  $S_0$  may be promoted to an excited state  $S_n$ . The molecule returns to ground state by means of internal conversion of energy and fluorescent radiative emission. This process is almost instantaneous and occurs on the order of  $10^{-8}$  seconds. As demonstrated in the figure, the energy of the emitted photon is lower than that of the absorbed photon, and hence the wavelength of fluorescent emission will be longer than that of the excitation. The difference between wavelengths of the absorbed and emitted photons is known as the Stokes shift.

The fluorescent emission spectrum of a material can be used for both qualitative and quantitative analysis; fluorescence microscopy presents many biological applications. The cloning of green fluorescent protein (GFP) in 1992 facilitated the development of fluorescent genetic probes, allowing for imaging of single cells and bacteria and the study of cellular activity [37]. Fluorescence microscopy has been utilised for distinguishing cancerous cells from healthy cells including in lung cancer [38] and breast cancer [39], and for guiding neuro-surgical tissue resection

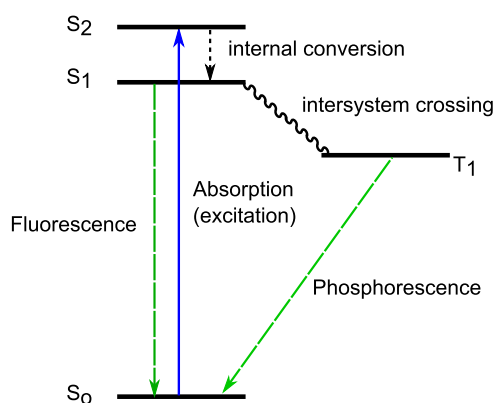


**Figure 1.5.** Simplified Jablonski diagram depicting fluorescence and phosphorescence processes. A molecule which has been excited can return to ground state via internal conversion, fluorescence or phosphorescence emissions.

in brain cancer [40]. It has also been employed as a diagnostic test for diseases such as pulmonary tuberculosis [41]. In recent years, fluorescence microscopy has also been combined with microendoscopic probes for numerous applications in mice. These have included cellular imaging within the brain [42, 43], in skin tissue [44] and within the kidney [45].

In this thesis, fluorescent microendoscopy is employed for the observation of immune cells in the lymph node of transgenic mice, and for the observation of localised binding of fluorescently-conjugated antibodies. This work is presented in detail in chapter 7.

### 1.4. Overview of the vasculature and oxygen transport

It is well known that oxygen is transported throughout the body by blood. The lungs are responsible for intake of oxygen, and the heart pumps blood throughout the body, with arteries and veins carrying oxygenated and deoxygenated blood respectively. A microvascular network of small blood vessels then deliver oxygen directly to local tissue. The oxygen is transferred to parenchymal cells, where it

## 1. Introduction and Background

---

is utilised through mitochondrial respiration. The structure of the vasculature is such that each cell in need of oxygen is close enough to a capillary for successful diffusive exchange [46]. This is the general function of the cardiovascular system.

The diameter of blood vessels, as well as the thickness of the vessel wall, varies significantly throughout the body. In humans, larger arteries and veins (such as the femoral or jugular) can have inner diameter of over 10 mm, however the actual size is dependent on age and height [47]. Branching arteries and veins, known as arterioles and venules, have smaller inner diameter, reducing to less than 300  $\mu\text{m}$ . The microvasculature is comprised of the smallest blood vessels, and these capillaries have diameters as small as 5 - 10  $\mu\text{m}$  [48]. In general, veins and venules tend to be slightly larger than arteries and arterioles respectively. The diameters of blood vessels are auto-regulated, meaning they can change in response to the metabolic demands, either systemic or localised. Expansion of a blood vessel is known as vasodilation, whereas vasoconstriction is a narrowing of the blood vessel. Vasodilation occurs in situations where there is increased metabolic demand, such as in cases of hypoxia [49].

The main carrier of oxygen in the blood is haemoglobin, which are molecules found in red blood cells (RBCs). It was first reported by George Stokes in 1863 that haemoglobin is capable of existing in two states of oxidation, meaning that oxygen can bind to it reversibly [50]. Oxygen binds to the ferrous iron contained in the haem group of a subunit of haemoglobin. There are four of these subunits per haemoglobin molecule, meaning that each haemoglobin molecule can carry up to four oxygen molecules and thus has finite capacity [5]. The oxygen saturation of the vasculature ( $\text{SO}_2$ ) is generally expressed as a percentage value, representing the fraction of oxygenated haemoglobin ( $[\text{HbO}_2]$ ) compared to the total haemoglobin. The total haemoglobin is the sum of both the oxygenated and

## 1. Introduction and Background

---

deoxygenated haemoglobin ([Hb]) concentrations.

$$SO_2(\%) = \frac{[HbO_2]}{[HbO_2] + [Hb]} \times 100 \quad (1.11)$$

Normal arterial oxygen saturation in a healthy human can vary from between 97 % and 100 %, with oxygen saturation in the veins decreasing to approximately 70 %. Oxygen levels in the smaller vessels of the microvasculature are often much lower than this [51].

A fundamental aspect of haemoglobin is that it possesses distinct extinction spectra depending on whether it is in an oxygenated or deoxygenated state. This is due to the structural changes that occur within the molecule as it binds to or releases oxygen [52]. This was also first reported in Stokes' 1863 paper, where he compared the distinct absorption bands of oxygenated blood, and blood which had been deoxygenated by a reducing agent [50]. The extinction coefficients of oxygenated and deoxygenated haemoglobin have since been empirically quantified and the spectra are shown in figure 1.6. They are a fundamental aspect of optical models for measurement of blood oxygen saturation, as will be described in chapter 2.

The affinity of oxygen to haemoglobin is determined by the partial pressure of oxygen ( $PO_2$ ), usually described in units of mmHg or kPa [54]. The relationship between the actual oxygen saturation of a vessel and its oxygen partial pressure is by the sigmoidal "oxygen-dissociation curve", which itself is dependent on factors such as pH, temperature and  $CO_2$ . A typical example of the curve is shown in figure 1.7. Normal values for arterial  $PO_2$  range from 75 to 100 mmHg (10.5 to 13.5 kPa). The oxygen-dissociation curve also specifies parameters such as  $P_{50}$ , the partial pressure at 50 % oxygen saturation. In humans, this is typically about 26.6 mmHg [55].

The partial pressure of oxygen in the vasculature plays a role in the transport and diffusion of oxygen. For example, in the alveoli of the lungs, the oxygen

## 1. Introduction and Background

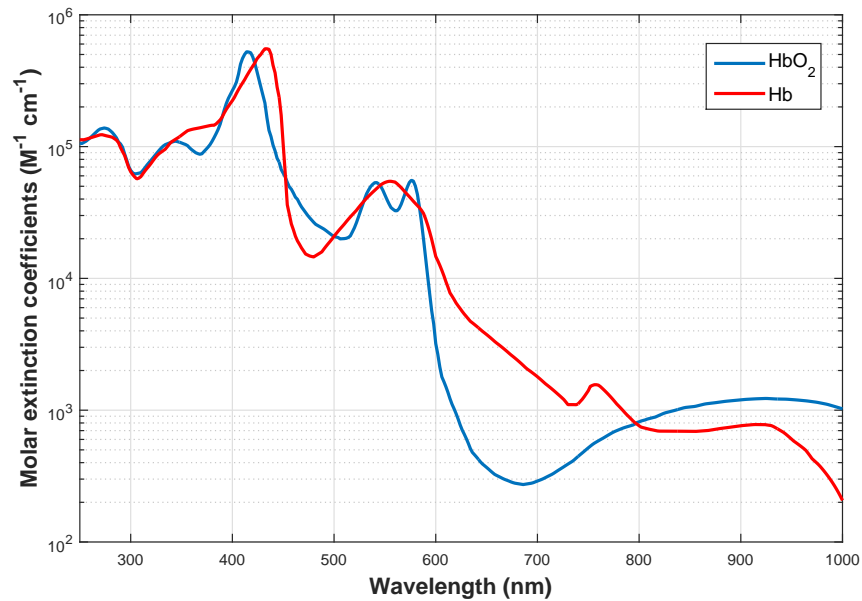


**Figure 1.6.** Extinction spectra of oxygenated (Hb) and deoxygenated haemoglobin (HbO<sub>2</sub>). Note the logarithmic y axis. Data from [53].

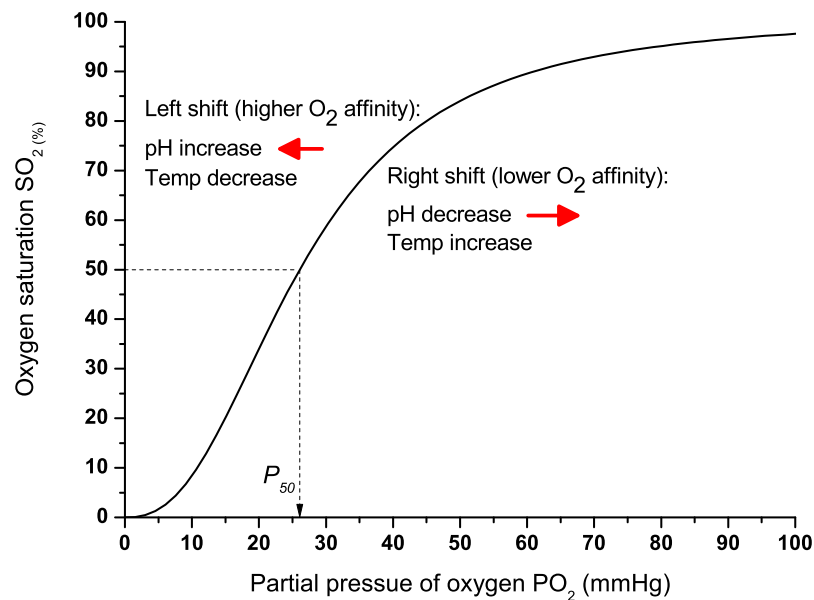


**Figure 1.7.** Example of a standard oxygen-dissociation curve for haemoglobin. Right and left shift of this curve occurs with changes in pH and temperature, as indicated, and also with levels of CO<sub>2</sub>.

## 1. Introduction and Background

---

partial pressure is higher in the alveoli than the adjacent capillaries, which results in diffusion of oxygen from the alveoli into the blood vessels. Conversely, in peripheral vessels, the partial pressure of oxygen is higher than that of adjacent tissue, leading to diffusion of oxygen from the microvasculature and into the tissue itself. The macroscopic rate of diffusion of oxygen is governed by Fick's first law, which in its one-dimensional form is:

$$J = -D \frac{d\psi}{dx} \quad (1.12)$$

where  $J$  is the "diffusion flux" in units of  $\text{mol m}^{-2}\text{s}^{-1}$ ;  $D$  is a diffusivity constant ( $\text{m}^2/\text{s}$ );  $\psi$  is the concentration of oxygen ( $\text{mol}/\text{m}^3$ ) and  $x$  is dimension (m) [56]. The quantity  $-\frac{d\psi}{dx}$  is known as the concentration gradient, which in the case of oxygen transport will be proportional to the  $\text{PO}_2$  gradient. It also indicates that diffusion is inversely proportional to dimension, meaning that oxygen will diffuse at a higher rate from the microvasculature than from large arteries, due to the difference in vessel wall thickness.

The concept of partial pressure of oxygen is important to consider, as several oximetry techniques (described in section 1.5) do not measure  $\text{SO}_2$  directly, but instead measure  $\text{PO}_2$ , from which oxygen saturation is inferred. Further, it is also important to consider that for vessels with low  $\text{PO}_2$ , oxygen diffusion can occur from exposure to the oxygen in air [57]. A detailed analysis of microvascular oxygen transport, whilst of relevance to the understanding of physiological function and microvascular disease, is not strictly necessary for the understanding of optical oximetry techniques and as such is not explored in depth in this thesis. There are many detailed theoretical models of microvascular oxygen transport, a review of which can be found in Goldman, 2008 [58].

The measurement and monitoring of oxygen saturation in both the tissue and vasculature is important in a wide range of situations. Hypoxia in retinal vessels may be indicative of a number of disorders including glaucoma and retinopathy [59].

## 1. Introduction and Background

---

In trauma patients, monitoring wound oxygenation provides a strong indicator of healing viability and can support the prevention of infection [60]. Also, as previously mentioned, hypoxia is implicated in a range of inflammatory disease such as multiple sclerosis and rheumatoid arthritis [6, 7, 18]. The study of oxygen saturation in models of disease thus has the potential to provide new information regarding aetiology and pathology. The following section introduces techniques which have been utilised for the measurement of oxygen saturation.

### 1.5. Oximetry: theory and background

Oximetry is a term used for the quantitative measurement of oxygen saturation, however it encompasses a wide range of techniques and modalities. Some oxygen-sensing techniques utilise the electrochemical properties of noble metals in order to measure the oxygenation of tissues; other techniques utilise the optical properties of haemoglobin to measure vascular haemoglobin saturation [61]. Further, oximetry may be applied to bulk or point measurements in tissue, or localised to individual blood vessels. In this section, a brief introduction to the various methods of oximetry are introduced, with a particular focus on the latter technique of optical vascular oximetry. Calibration-based two-wavelength and three-wavelength oximetry techniques are described, along with a brief review of previous studies. A further review of calibration-free multispectral oximetry algorithms, which are employed in this thesis, is found in chapter 2.

#### 1.5.1. Electrochemical oxygen sensing

The first oxygen sensing technique to be described is the Clark electrode. So called after its inventor Leland Clark, it was first described in 1956 [62] and can measure the ambient oxygen concentration in a liquid or tissue. It comprises a reference electrode (anode) and measuring electrode (cathode), as well as an

## 1. Introduction and Background

---

oxygen-permeable and electrically insulating membrane. The membrane ensures that the electrodes themselves do not come into contact with the tissue, whilst still allowing oxygen to reach the area behind the membrane.

The mode of operation of the Clark electrode is that the positive cathode is depolarized by oxygen, which is transported from surrounding tissue (which has relatively high  $PO_2$ ) into the membrane where the  $PO_2$  is near zero. In practice, this means that the amount of oxygen can be quantified by the change in voltage between the cathode and the anode. The voltage is proportional to the number of oxygen molecules being reduced. In order to acquire accurate readings of tissue  $PO_2$ , the electrode must first be calibrated in a solution of known oxygen tension. The Clark electrode found its first application in cardiovascular surgery, for the monitoring of extracted arterial blood during pulmonary by-pass [63]. Today, this has been largely superseded by non-invasive pulse oximetry which accurately monitors arterial blood oxygen saturation. However, there have been an extensive number of other applications for polarographic needle electrodes. These include, for example, the monitoring of  $PO_2$  in porcine models of haemorrhage and endotoxaemia [64]; the study of  $PO_2$  in the skeletal muscular tissue of patients affected by sepsis [65]; and study of the spatial distribution of  $PO_2$  in tumours [66].

Needle-tip oxygen sensors are useful for continuous real-time measurements, with response times under 500 ms [61]. However, they are only capable of measuring  $PO_2$  at a specific point. Therefore, any local variations of oxygen level may not be detected. Repeated measurements over an area are required in order to study spatial variations of  $PO_2$ . Further, only superficial measurements are possible. It has been reported that the "catchment area" of oxygen electrodes is approximate to the size of their tip area, effectively limiting measurements to depths of 15-20  $\mu\text{m}$  [64]. It is also possible that electrode penetration may cause  $PO_2$  disturbance and alter the environment. For localised oxygen saturation measurements, optical oximetry techniques will be preferable, as an optical imaging system will clearly allow for higher spatial resolution than can be achieved with

needle-tip electrodes.

### 1.5.2. Optical oximetry

The measurement of oxygen saturation using optical techniques is possible due to the distinct extinction spectra of oxygenated and deoxygenated haemoglobin, as previously presented in figure 1.6.

#### NIRS and tissue oximetry

A prominent optical technique for the measurement of tissue oxygen saturation is near-infrared spectrometry (NIRS). First reported by Jöbsis in 1977 [67], NIRS has been widely utilised for the study of cerebral, myocardial, and general tissue oxygen saturation *in vivo* [68]. The NIR region of the spectrum is utilised due to the “optical window” between 650 and 900 nm. In this region, absorption of light by haemoglobin and water are minimal, as can be observed for haemoglobin in figure 1.6. The lower absorption allows light to penetrate up to several centimetres in biological tissue [69].

NIRS is based on detection of light which has been transmitted through biological tissue, using transmitter and detector optodes. For most NIRS measurements, reflectance spectroscopy is performed, with the detector placed ipsilateral to the transmitting optode (e.g. the same side of the body). For certain applications such as in neonates, transmission spectroscopy is possible, in which areas such as the skull are trans-illuminated [70]. The ratio of emergent to incident light is related to the thickness of the tissue, the concentration and extinction coefficient of the absorbing chromophore (haemoglobin in this case), as given by the Lambert-Beer law previously derived in section 1.3.1. Measurements at multiple wavelengths allow for determination of haemoglobin concentration and hence oxygen saturation.

## 1. Introduction and Background

---

Central to the concept of NIRS, however, is that the effective optical path length will increase as the light is multiply scattered within the tissue. For example, in a normal adult head, the optical pathlength is approximately 6.3 times the physical length [70]. For measurements of oxygen saturation, this additional pathlength must be accounted for in the analysis. The calibration arises as multiplication of the optical path length between the illumination and detector, by what is known as the “differential pathlength factor” (DPF) [71], which itself is dependent on wavelength. In this case, the Lambert-Beer law is modified for NIRS as follows:

$$I(\lambda) = I_o(\lambda)e^{-\mu_a(\lambda)d(\text{DPF})(\lambda)+G(\lambda)} \quad (1.13)$$

where  $I(\lambda)$  is the diffuse reflected light intensity,  $I_o(\lambda)$  is the incident light intensity,  $\mu_a$  is the absorption coefficient of the tissue, and  $G(\lambda)$  is a constant dependent on wavelength, medium and geometry.

The DPF has been characterised for a multitude of different tissues and wavelengths, allowing for quantification of total haemoglobin concentration within tissue. However, it is suggested that the DPF may vary in certain situations such as in the presence of ischaemia or cerebral oedema [70]. For accurate NIRS measurements, it is necessary to first quantify the actual DPF using time-of-flight measurements as opposed to using estimated DPF values [72].

Although NIRS allows for the measurement of oxygen saturation for a range of applications *in vivo*, it is not well suited to the study of small heterogeneities in oxygen saturation within tissue. The highest resolution possible with NIRS is approximately 5 mm [60], meaning that the measurements will not resolve the oxygen saturation of individual blood vessels such as in the microvasculature. When localised measurements are desired, vascular oximetry is preferable to NIRS.

In addition to NIRS, various other techniques have been explored for the calculation of tissue oxygenation (StO<sub>2</sub>). Diffuse reflectance spectrophotometry at visible

## 1. Introduction and Background

---

wavelengths is also possible. In 1981, Sato et al. [95] introduced an oximetry algorithm based on these measurements, acquired of liver tissue in rat models, at wavelengths between 450 and 650 nm. Haemoglobin concentrations were first determined by spectrophotometry over the entire wavelength range. The authors then calculated the optical density difference ( $\Delta A_{569-586}$ ) at two isobestic points (569 and 586 nm), which was found to be proportional to haemoglobin concentration. The  $\Delta A_{569-586}$  value at zero haemoglobin concentration was the optical density of a blood-free liver. In this way, the  $StO_2$  could be determined.

Harrison et al. (1992) also introduced a tissue oximetry method applied to non-invasive measurements of the human skin [96]. This technique involved the preliminary calculation of a “haemoglobin index” (HbI) based on five isobestic points between 500 and 620 nm, allowing for accurate calculation of an “oxygenation index” (OXI), given by the following equation:

$$OXI = [(E_{571.8} - E_{560.1})/11.7 - (E_{560.1} - E_{548.5})/11.6] \times 100/HbI \quad (1.14)$$

where  $E_x$  is the extinction at wavelength  $x$  calculated from the absorbance ( $A_x$ ) according to  $E_x = -\log(1 - A_x)$ . This technique was used to assess oxygenation changes occurring during the course of a tuberculin reaction in human skin, which involves an induction of erythema and oedema. The results were validated with transcutaneous oxygen measurements.

In 1994, Knoefel et al. introduced another algorithm, also based on diffuse reflectance spectrophotometry measurements, of pancreatic tissue in rats [98]. The study introduced a correction for tissue scatter, by using least-squares regression on measurements acquired between 640 and 820 nm - a region where the extinction coefficients of haemoglobin are 50 times smaller than in the range between 540 and 580 nm. By extrapolation to an intercept at 550 nm, scattering at oximetry wavelengths could be estimated and compensated for. The technique was validated *in vitro*, showing successful measurement of pure  $HbO_2$  as having  $SO_2$  of

## 1. Introduction and Background

---

$99.2 \pm 0.9\%$ , and pure Hb an  $\text{SO}_2$  of  $0.5 \pm 1.4\%$ . These diffuse reflectance techniques were all calibration-based methods, and determined calibration parameters such as scatter and tissue contribution varied between tissue and subject.

### Vascular oximetry

Vascular oximetry is the measurement of oxygen saturation in the blood vessels. Like NIRS, the extinction spectra of oxygenated and deoxygenated haemoglobin allows for quantification of oxygen saturation. However, unique to vascular oximetry is the method with which optical transmission is calculated. In vascular oximetry, the optical transmission or optical density (OD) of specific blood vessels is determined. This is performed using a ratio of image intensity values within the blood vessel ( $I$ ) as compared to the “background intensity” directly adjacent to the blood vessel ( $I_o$ ), giving optical transmission  $T = \frac{I}{I_o}$ . This is achieved by taking an intensity line profile transverse to the vessel, and usually applying a series of fits in order to extract values for  $I$  and  $I_o$ . This idea is depicted in in figure 1.8. Optical density (OD) can then be calculated using the relationship  $\text{OD} = -\log_{10}(T)$ . This method was first reported in 1959 by Hickam and Fraser [73], and is now ubiquitous to vascular imaging oximetry [59].

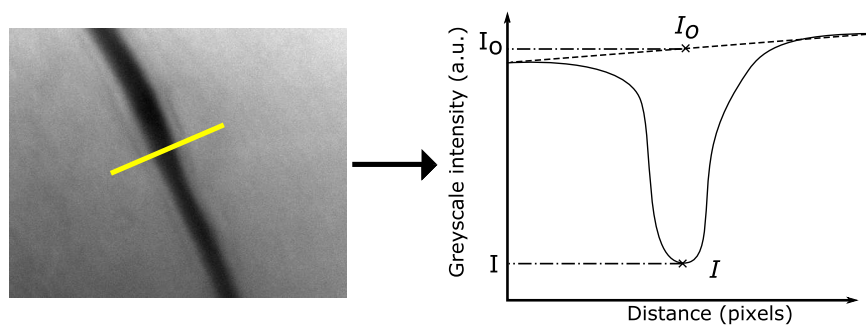


**Figure 1.8.** Illustration of vessel line profile, shown in yellow in the image on the left, depicting how intensity values  $I$  and  $I_o$  are extracted from image data for vascular oximetry.

## 1. Introduction and Background

---

### *Two-wavelength oximetry*

The simplest form of vascular oximetry is known as two-wavelength oximetry, and has been carried out predominantly for applications in retinal oximetry. Retinal oximetry is typically performed using modified fundus cameras, slit lamps or scanning laser ophthalmoscopes (SLOs) [74]. Once optical density has been determined at two distinct wavelengths, a ratio of these values gives the “optical density ratio” (ODR):

$$\text{ODR} = \frac{\text{OD}_{\lambda 1}}{\text{OD}_{\lambda 2}} \quad (1.15)$$

The wavelengths used for two-wavelength oximetry have traditionally been one oxygen-sensitive wavelength, and one wavelength at which there is no difference in the OD at oxygenated or deoxygenated vessels. This is known as an isosbestic wavelength. In this case, there is a linear relationship between this ratio and blood oxygen saturation, first reported also by Hickam and Fraser [73].  $\text{SO}_2$  may thus be inferred from measurements of ODR. If both wavelengths are oxygen-sensitive, the relationship may still be used for oximetric purposes but is no longer linear [59]. In its simplest form, this relationship can be expressed as:

$$\text{SO}_2 = 100\% - \text{ODR}/\text{OS} \quad (1.16)$$

where OS is a constant known as “oxygen sensitivity”. In practice, several factors affect the accuracy of two-wavelength oximetry. These include vessel diameter, and fundus pigmentation in the eye for retinal vessel measurements. Both of these factors introduce systematic error, introducing additional linear dependences with measured  $\text{SO}_2$ . The “gold-standard” calibration-based two-wavelength oximetry technique was introduced by Beach et al. in 1999 [75]. In 2008, further corrections by Hammer et al. were proposed in order to increase the accuracy of two-wavelength oximetry [76]:

$$\text{SO}_2 = 100\% - (\text{ODR} - \text{ODR}_{a,100})/\text{OS} - (a - VD) \times b + \left( c - \log \frac{I_{\text{out}}^{610 \text{ nm}}}{I_{\text{out}}^{548 \text{ nm}}} \right) \times d \quad (1.17)$$

## 1. Introduction and Background

---

where  $VD$  is vessel diameter measured from the image;  $\left(\log \frac{I_{610\text{ nm}}}{I_{548\text{ nm}}}\right)$  represents fundus pigmentation;  $ODR_{a,100}$  is arterial ODR measured during inhalation by the subject of pure oxygen; and constants  $a, b, c$  and  $d$  were determined experimentally using a number of healthy subjects. Using this technique, Hammer et al. were able to perform retinal oximetry with high reproducibility.

The predominant application of two-wavelength oximetry to the study of retinal oxygenation has been aided by the development of commercial retinal oximeters such as Oxymap and Imedos [77]. Retinal oximetry studies have shown decreased arterial saturation in glaucoma [78]; abnormal venous saturation in people with age-related macular degeneration [79] as well as diabetic retinopathy [80]. Retinal oximetry has also been applied to functional studies of the vasculature by asking subjects to breath hypoxic air. For example, in 2013, Choudhary et al. presented a study of the effect of acute mild hypoxia on retinal oxygen saturation [81]. Two-wavelength oximetry has also recently revealed physiological information regarding oxygen dynamics in the bulbar conjunctival and episcleral vessels of the eye [82].

### *Three-wavelength oximetry*

In addition to two-wavelength oximetry, the use of an additional third wavelength for measurement of oxygen saturation has also been explored. This three-wavelength oximetry technique was introduced in 1975 by Pittman et al [83]. It employed one  $SO_2$ -sensitive wavelength (555 nm) and an additional two isosbestic wavelengths (546 nm and 520 nm), relatively close in proximity to each other. These two isosbestic bands were used in order that contribution of scatter to the OD measurements could be determined by means of a modified form of the Lambert-Beer law. The  $SO_2$  could then be determined by the following expression:

$$SO_2 = m \frac{OD_{555\text{ nm}} - B}{OD_{546\text{ nm}} - B} + b \quad (1.18)$$

## 1. Introduction and Background

---

where 555 nm was the oxygen-sensitive wavelength, and 546 nm one of the isosbestic wavelengths;  $B$  is the scattering contribution determined using both isosbestic wavelengths; and  $m$  and  $b$  are constants. The technique is only valid for a range of three wavelengths in which the optical scattering is considered to be constant. It was shown that for wavelengths in the visible blue region of the EM spectrum, the wavelength dependence of the scattering contribution is “not negligible”. Three-wavelength oximetry has been applied to retinal oximetry by Delori [84, 85]. However, due to the restrictions placed on suitable wavebands, three-wavelength oximetry has not found extensive use, with two-wavelength oximetry proving more popular for clinical studies in the field of retinal oximetry [74].

### *Green-blue spectral shift*

An additional vascular oximetry technique was introduced by Denninghoff et al (2006) [86]. It is based on the principle that the optical density of a blood vessel  $OD(\lambda)$ , for a given value of  $SO_2$ , represents a parabolic curve in the visible green region of the EM spectrum (between 475 nm and 510 nm). The technique utilises a red shift in the minimum of this optical density curve with increasing  $SO_2$ . This allows for oximetry that is reportedly insensitive to path length, pH or concentration changes.

First reported in Hb solution, it was next extended to measurements of whole blood [87] and *in vivo* measurements were made in retinal oximetry of swine in 2008 [88]. This study reported a high correlation of measured arterial  $SO_2$  values with those measured by a co-oximeter ( $r^2 = 0.8$ ,  $SO_2$  residual error =  $\pm 3.4\%$ ). Whilst a promising technique, it is not without limitations. Reflected light or ‘glints’ are an issue for many oximetry techniques, as they can alter the measurements of optical density and hence oxygen saturation. For this *in vivo* study, intra-vitreous illumination was provided by an optical fibre inserted directly into the eye such that the retina was illuminated at an angle. Due to the highly

## 1. Introduction and Background

---

invasive nature of the technique, it is not proposed as a widely applicable retinal oximetry test in humans.

### **Deep tissue localised oximetry**

In addition to retinal oximetry, a number of oximetry studies related to other applications in deep tissue have previously been performed. These have included both vascular and general tissue oximetry.

In 1987, Ellsworth et al. demonstrated two-wavelength vascular oximetry of the microvasculature in hamster cheek retractor muscles [51]. In 1990, the same group published a further paper reporting the additional capability of recording video-rate optical density data, with both wavelengths captured simultaneously instead of sequentially [89]. Although specifically applied to the cheek retractor muscles, the authors state that the technique should have “wide applicability to other tissues”. The limitation of this technique, however, is the calibration-based nature of two-wavelength oximetry as previously discussed. Calibrations determined *in vitro* and for this specific *in vivo* application will not be appropriate for other applications. For *in vivo* calibration in this case, optical densities at both 0 % and 100 % had to be defined by the application of sodium dithionite and sodium cyanide directly to the tissue, respectively. The toxicity of both compounds renders this two-wavelength oximetry technique impracticable outside animal models.

The application of vascular oximetry to non-retinal applications is relatively limited. However, oxygen saturation in overall tissue may be generated by spectral analysis of reflected absorbance images. In 1997, Shonat et al. introduced a basic optical model for multispectral oximetry of the mouse brain, with data acquired using an acousto-optic tuneable filter (AOTF) microscope [90]. The AOTF is described in section 1.6. Shonat et al. generated two-dimensional maps of oxygen saturation in cortical tissue. These results were validated with PO<sub>2</sub> data generated simultaneously using a phosphorescence lifetime imaging technique. This

## 1. Introduction and Background

---

initial model did not include the wavelength-dependent scattering of light by haemoglobin, which was instead assumed to be wavelength-independent. Additionally, the reflectance intensity across the entire surface was assumed to be uniform, which contributed to a  $\pm 10\%$  variation in  $\text{SO}_2$  values.

In 2005, Sorg et al. demonstrated measurement of haemoglobin saturation in tumour microvasculature [91], using a liquid crystal tuneable filter (LCTF) for spectral discrimination. The LCTF is also described in section 1.6. For this study, localised oxygen saturation maps were produced using the same model previously described by Shonat et al., with a modification made to include the wavelength-dependence of light scattering by haemoglobin. Palmer et al. (2010) also studied tumour hypoxia dynamics [92], reporting localised hypoxia within the tumour. For both studies, a dorsal skin-fold window-chamber model was also utilised in order to access the tissue.

The studies discussed above all required highly invasive surgeries in order to access the targeted tissue. This is a limitation for longitudinal studies, which are not possible using invasive techniques where the animals are often terminated under anaesthesia after imaging. In the case of Palmer et al. and Sorg et al., optical transmission could be accurately quantified due to the implanted skin flap window through which light could propagate - allowing for transillumination microscopy [91, 92]. For most other tissues this is not possible and a more sophisticated optical model is required.

Overcoming the invasive nature of the above oximetry studies is a motivating factor for extending two-dimensional localised oximetry to microendoscopic techniques. The minimally invasive nature of these probes, described in section 1.7.1, would allow for longitudinal oximetry over an extended time frame of weeks or even months. There are scarce reports of vascular optical oximetry with microendoscopy in the literature. Kaneko et al. (2014) reported optical oximetry using a commercial endoscope system ( $\sim 10$  mm diameter) in combination with

three spectral imaging channels in order to generate maps of  $\text{StO}_2$  [93]. In a first human clinical study, the authors could distinguish between areas of neoplasia and non-neoplasia in the esophagus and colorectum. As the technique utilises commercial endoscopes, the tissues which can be imaged are limited. For oximetry of deep tissue within the joint, for example, microendoscopic systems show more promise. A summary of the various techniques and oximetry algorithms presented in this chapter is shown in table 1.1. For the sake of completeness, additional multispectral algorithms presented in chapter 2 are also included in this summary table.

### 1.6. Multispectral imaging

#### 1.6.1. Basic concept

In this thesis, multispectral imaging (MSI) is employed for quantification of localised oxygen saturation. Multispectral imaging combines digital imaging and microscopy with additional information provided by spectroscopy. A spectral imaging system involves the acquisition of two-dimensional spatial information  $(x, y)$ , as well as a third dimension in wavelength,  $\lambda$ , resulting in a spectral datacube  $(x, y, \lambda)$  as illustrated in figure 1.9. This allows for the capture of both spatial and spectral information of a particular scene of interest. Depending on the imaging system, the spectral information may be acquired either in turn (sequential MSI) or simultaneously (snapshot MSI). Although the concept is similar, the difference between multispectral and hyperspectral imaging (HSI) is related to the number of spectral bands acquired. For multispectral imaging systems, several distinct wavebands may be captured; for hyperspectral imaging systems, hundreds of spectral images may be captured over a continuous spectrum.

## 1. Introduction and Background

**Table 1.1.** Summary of oximetry techniques presented in this thesis, including vascular and tissue oximetry.

Study	Technique	Wavelengths	Key points
Pittman et al. (1975) [83]	Three-wavelength <i>in vitro</i> oximetry of whole blood	520, 546, 555 nm	1.4% error in SO <sub>2</sub> <i>in vitro</i>
Cohen & Laing (1976) [94]	Calibration-based photographic eye <i>in vivo</i> oximeter (multiple-scattering analysis)	470, 515 nm	Technique was accurate for high SO <sub>2</sub> but deviated at lower oxygenations
Sato et al (1981) [95]	Reflectance spectrophotometry for tissue oximetry	450-650 nm	Hb concentrations and StO <sub>2</sub> changes determined during aerobic to anoxic transitions.
Harrison et al. (1992) [96]	Calibration-based, non-invasive spectrophotometry for <i>in vivo</i> oximetry of human skin	500-620 nm	Results agreed with transcutaneous O <sub>2</sub> validation measurements (linear fit r=0.97) but were pigment dependent
Schweitzer et al. (1995) [97]	Model-based vascular oximetry technique (including compensation for Hb scatter)	510-586 nm	SO <sub>2</sub> measurements in human retina demonstrated ( $\pm 4\%$ agreement with <i>in vitro</i> measurements)
Knoefel et al. (1996) [98]	Reflective spectrophotometer for assessment of Hb concentration and StO <sub>2</sub> in pancreatic microcirculation <i>in vivo</i>	400-820 nm	Scattering intensity determined using range of spectral measurements, achieving values of $99.2 \pm 0.9\%$ SO <sub>2</sub> for pure HbO <sub>2</sub> and $0.5 \pm 1.4\%$ for Hb.
Beach et al. (1999) [75]	Calibration-based Two-wavelength vascular oximetry technique for application to the retina	560,600 nm	Retinal venous SO <sub>2</sub> determined to be $55 \pm 3.37\%$ , increasing by $19.2 \pm 2.9\%$ when subject inhaled 100% O <sub>2</sub> .
Smith et al. (2000) [99]	Model-based scanning laser multispectral <i>ex vivo</i> oximetry	629, 678, 821, 899 nm	Accurate SO <sub>2</sub> calculated <i>in vitro</i> , as well as path-length contribution factors.
Denninghoff et al. (2006) [86]	Calibration-free oximetry technique utilising blue-green transmission spectra shift with SO <sub>2</sub>	450-850 nm, 2 nm increments	SO <sub>2</sub> changes determined and found to be independent of Hb concentration.
Hammer et al. (2008) [76]	Calibration-based two-wavelength vascular oximetry technique with compensation for scattering and fundus pigmentation	548,610 nm	Arterial and venous SO <sub>2</sub> for retinal vessels determined at normoxia, and validated by an increase when subjects breathed 100% O <sub>2</sub> .

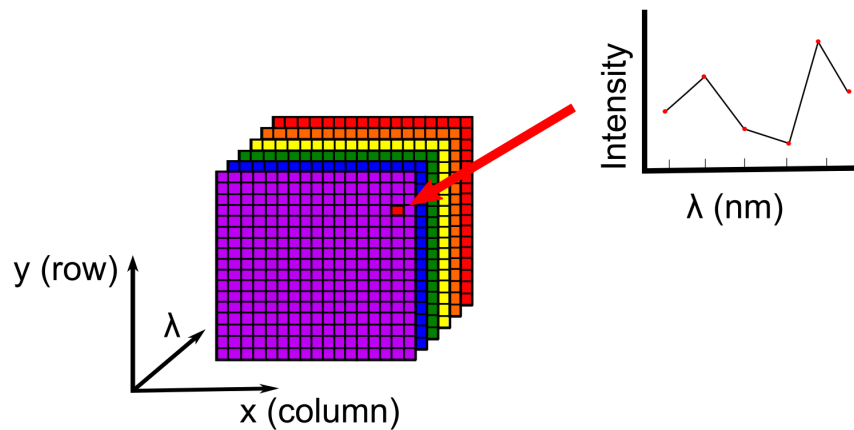


**Figure 1.9.** Illustration of multispectral imaging concept which involves acquisition of three-dimensional spectral datacube ( $x, y, \lambda$ ). As illustrated, the detected intensity at a given pixel will be a function of not only the spatial coordinates, but also its spectral band.

### 1.6.2. Techniques

#### Bayer filters

Perhaps the most ubiquitous multispectral filter is the Bayer filter mosaic. In its standard form, it is an array of RGB filters predominantly used with digital image sensors for digital cameras. Each filter corresponds to an individual image pixel. Although RGB Bayer filter mosaics are capable of providing spectral images in a single snapshot, the limited spatial resolution and number of wavebands makes them impractical for many spectroscopic applications. However, versions of the Bayer filter exist whereby additional filters are introduced to the matrix, allowing for further spectral resolution at the cost of spatial resolution. For example, Kaluzny et al. have presented a 16-band Bayer filter mosaic for hyperspectral imaging in the eye for retinal oximetry [100].

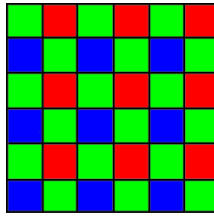


**Figure 1.10.** Bayer RGB filter mosaic. There are two times as many green filters in order to more closely replicate the spectral response of the human eye.

### Liquid crystal tuneable filters

A common technique for the spectral filtering of white light is the liquid crystal tuneable filter (LCTF). It is an electronically controlled optical filter, allowing for transmission of a single waveband which can be switched.

The basic principle of the LCTF is based on the Lyot filter, which is a polarising interference filter consisting of sequential pairs of polarisers and retarding birefringent waveplates [101]. In a Lyot filter, the optical axes of the polarisers must be oriented at  $45^\circ$  with respect to the fast and slow axes of the waveplate crystal. The incident light can thus be considered as consisting of two linear polarisation components, which, upon transmission through the birefringent waveplate, will emerge with different phase. The light then travels through another polariser, the output of which will be:

$$T(\lambda) = \cos^2\left(\frac{\pi d(n_o(\lambda) - n_e(\lambda))}{\lambda}\right) \quad (1.19)$$

where  $n_o$  and  $n_e$  are the ordinary and extraordinary (fast and slow) refractive indices of the waveplate at a particular wavelength, and  $d$  is the thickness of the waveplate. If each waveplate is twice the thickness of the preceding waveplate, a specific wavelength with a narrow bandwidth is transmitted.

The most common type of LCTF, the Lyot-Öhman type, is based on the Lyot filter. However, in place of the birefringent waveplates, it instead uses neumatic

## 1. Introduction and Background

---

liquid crystals [102]. In this case, the liquid crystal molecules are aligned at an angle of  $45^\circ$  with respect to the polarisers. These liquid crystals are electronically controllable and their retardation can be tuned by applying a voltage over the cell. The LCTF is versatile and can switch between transmitted wavelengths in 50 m sec. The nominal passband of the LCTF used in chapter 5 of this thesis (*Varispec* VIS-7-HC-20) transmits a waveband of approximately 10 nm. The LCTF has been previously employed in multispectral imaging studies of oxygen saturation in animal models of tumour development [91, 103].

### **Acousto-optic tuneable filters**

The acousto-optic tuneable filter (AOTF) operates using a different principle to the LCTF, but also allows for easily switchable waveband transmission for sequential multispectral imaging using a white light source. The AOTF is based on acousto-optic interactions; a high frequency GHz acoustic (RF) wave is produced by a constituent piezoelectric transducer. This wave is propagated through an anisotropic birefringent optical medium, resulting in periodic variation of refractive index. This produces an effective diffraction grating in the material upon which light is then incident. A polarised, collimated beam incident at the Bragg angle will be diffracted, and in this way, specific wavelengths of choice can be transmitted. The period of the virtual diffraction grating, and hence the transmitted wavelength, can be changed by changing the frequency of the RF wave.

The resolution of the AOTF, as given by the full width half maximum of transmitted light at wavelength  $\lambda_0$ , is defined as follows

$$\Delta\lambda = \frac{\lambda_0^2}{2l\Delta n \sin^2\theta_i} \quad (1.20)$$

where  $l$  is the length of the optical material, and  $\Delta n = n_e - n_o$ , the birefringence of

## 1. Introduction and Background

---

the material [104]. The bandwidth of the transmitted wavelength thus increases with increasing wavelength, however is narrower than that transmitted by an LCTF. The AOTF used for the majority of oximetry and fluorescence imaging in this thesis (*Gooch & Housego*) transmits a nominal waveband of just 2 nm. The AOTF also allows for much faster switching of wavelengths, on the order of ms. Thus, for sequential multispectral imaging, the AOTF is generally preferable to the LCTF. The AOTF has previously been employed for multispectral imaging oximetry, such as mapping oxygen tension in the mouse brain [90].

### IRIS

The final technique for multispectral imaging to be discussed is the “Image Replicating Imaging Spectrometer”, or IRIS [105]. This image-replicating filter allows for simultaneous acquisition of a number of spectral bands - this is known as snapshot multispectral imaging. The advantage of a snapshot system is that temporal phenomena may be observed; sequential capture of a number of wavebands means that changes in e.g. oxygen saturation over a short period of time can't be resolved. IRIS is effectively a snapshot alternative to the LCTF. Similar to the LCTF, the mechanism behind IRIS also employs the use of the Lyot filter. However, instead of regular birefringent waveplates within the filter system, IRIS employs Wollaston prisms.

Wollaston prisms are birefringent polarising beamsplitters, which allows for the “image-replication” aspect of the system. Light incident on IRIS is first polarised by an initial input polariser, and then separated both spectrally and spatially into two orthogonally polarised beams by the Wollaston prism. These beams are further separated by subsequent pairs of waveplates and Wollaston prisms. For an N-stage IRIS (that is, N pairs of polarisers and Wollaston prisms) there will be  $2^N$  spectral images produced at the detector. The images can then be co-registered in order to construct the spectral datacube. Although allowing

## 1. Introduction and Background

---

for video-rate multispectral imaging, one disadvantage of IRIS is that since the image is replicated multiple times at the detector, the spatial resolution of each individual image is thus limited.

Although not employed in the experimental work of this thesis, IRIS has been used for a multitude of ocular oximetry studies in the past, in conjunction with a modified Fundus camera [74, 81, 82]. IRIS is discussed in chapter 8 as a potential technique for minimally invasive oximetry in future.

### 1.6.3. Current Applications

Multispectral and hyperspectral imaging are widely used due to the additional information that is available with spectral discrimination. MSI is primarily known for its use in a range of remote sensing applications for military and civilian purposes. These have included environmental imaging for determination of forest species [106], vegetation, soil and terrain mapping [107, 108].

In recent years, spectral imaging techniques have been translated towards bio-imaging and biomedical diagnostic applications - often with oximetry applications due to the spectral properties of oxy- and deoxy-haemoglobin [48]. These have included applications in diabetes [109], retinal imaging [110] and tissue oximetry in sickle-cell disease [111]. Calin et al., (2014) provides an extensive review of the use of spectral imaging in the medical field [112]. As previously discussed, spectral imaging has also been utilised for studies in retinal oximetry and tumour oxygenation [91, 100, 103].

Hyperspectral imaging has also been combined with endoscopes for minimally invasive imaging. In 2011, Kester et al. reported a spectral imaging system called 'the image mapping spectroscopy endoscope' [113]. The system combined a GRIN lens microendoscope in conjunction with a spectrometer, and allowed for high-throughput spectral imaging at 5.2 frames per second (fps). A multispectral

## 1. Introduction and Background

---

$(x,y,\lambda)$  datacube of  $(350 \times 350 \times 48)$  was acquired. The authors report  $100 \mu\text{m}$  spatial resolution at the working distance of 10 mm from the endoscope surface. It is stated that this resolution was chosen to resolve vascularisation, however the system's ability to resolve the microvasculature, with capillaries of less than  $10 \mu\text{m}$  diameter, would be insufficient. Lim and Murukeshan (2016) also recently presented a hyperspectral fibre-bundle endoscope system capable of video-rate snapshot acquisition [114]. The proposed technique could be used for a variety of bio-imaging applications, with a large range of 756 spectral bands available. However, the spatial resolution of the system was likely to be limited by the diameter of the individual fibres at  $125 \mu\text{m}$  (the authors did not report the actual value). In this thesis, a combination of high resolution multispectral imaging is pursued in order to quantify vascular oxygen saturation in capillaries of the microvasculature.

### 1.7. Microendoscopes for optical biopsy

#### 1.7.1. Introduction to microendoscopy

Microendoscopy is a relatively recent term used for a range of minimally invasive optical probes, providing minimally invasive access for optical sensing and imaging of deep tissue. Microendoscopes are distinct from conventional endoscopy systems in that they are inherently less invasive, and as such, can be used to penetrate through tissue for localised optical access. Conventional endoscopes, such as those used in gastroenterology, have diameters typically larger than 10 mm [115], and as such are limited to use in orifices such as the oesophagus. In contrast, diameters as small as  $350 \mu\text{m}$  have been reported for *in vivo* microendoscopy applications [116]. Although there is no official definition regarding what makes an endoscope *micro*-endoscopic, most reports in the literature which refer to microendoscopy employ probes of diameter no larger than 1 mm. The use

## 1. Introduction and Background

---

of microendoscopes in various modes of microscopy has been increasing over recent years; figure 1.11 displays the marked growth in the number of publications directly related to microendoscopy per year since 1987.

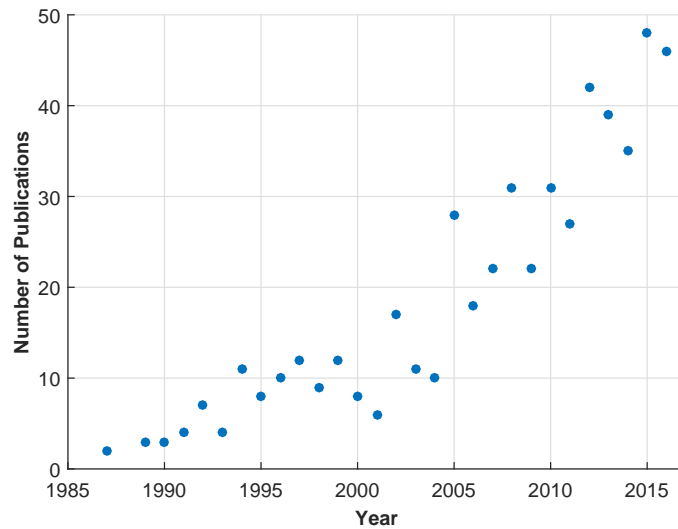


**Figure 1.11.** Increase in number of publications in microendoscopy over time (data from Web of Science search for titles directly including “microendoscopy,” “microendoscope” or “microendoscopic”)

Microendoscopes have been composed of a variety of materials. Optical fibre bundles have been used for minimally invasive imaging, however the associated diameters tend to be large relatively large, and there are associated performance issues which limit resolution [117]. In 2013, Shahmoon et al. presented a report describing a polymer based microendoscopic system with outer diameter of only 200  $\mu\text{m}$  [118]. Predominantly, however, microendoscopy techniques employ small gradient refractive index (GRIN) lenses which act as miniature optical relays to access deep tissue and these can provide high NA and associated imaging resolution and quality [119]. A useful review of fabrication and operation of such probes was published by Kim et al. in 2012 [120].

### 1.7.2. GRIN lenses: Theory

A conventional lens has a single refractive index (the index of refraction simply being the ratio of velocity of light in a vacuum to the light velocity in the medium) and light will travel in straight lines through this material. Unlike conventional lenses, GRIN lenses have a central refractive index  $N_o$ , with a parabolic refractive index gradient according to

$$N(r) = N_o[1 - (k/2)r^2] \quad (1.21)$$

where  $k$  is the gradient constant of the GRIN lens, and  $N(r)$  is the refractive index at radius  $r$  from the centre of the lens [121]. This means that light will travel in curved paths rather than straight lines; characteristic of a GRIN lens is that light will travel a sinusoidal path along its length. A complete sinusoidal period, known as the pitch, is defined as

$$p = \frac{2\pi}{\sqrt{k}} \quad (1.22)$$

If a GRIN lens has pitch equal to 1, or integer multiples, an upright image of an object at one surface will be formed with 1:1 magnification at the other surface. GRIN lenses with pitch 0.25 will collimate a point source or focus an object at infinity. For incorporation into microendoscopes, often a pitch of slightly less than 0.25 (such as 0.22 or 0.23) is utilised at the ends of the probe, such that a short working distance is produced from the surface of the probe to the object or image plane. This concept is illustrated in figure 1.12. In contrast to optical fibres, the light paths do not reach the walls of the material, and therefore do not rely on cladding of lower refractive index in order to confine the propagating rays [121]. In practice, gradient refractive indices are achieved in GRIN lenses by the exchange of silver or lithium ion-exchange in the glass.

It is possible to use a single GRIN lens for imaging in deep tissue, however there

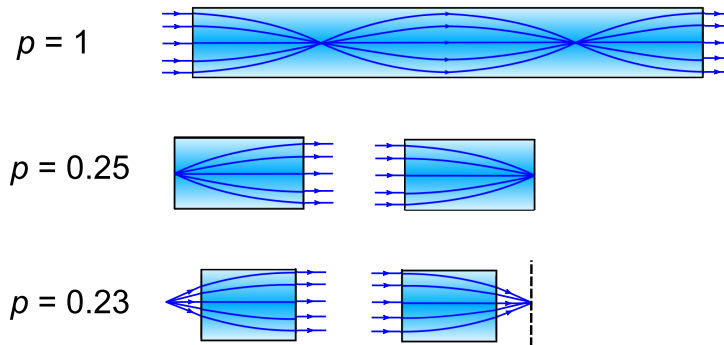


**Figure 1.12.** Illustration of sinusoidal light paths in GRIN lenses, with imaging properties of lenses with varying pitch depicted.

are practical issues relating to the physical length achievable with one single lens. In 1987, Acosta et al. demonstrated that the numerical aperture of a GRIN lens is inversely proportional to its pitch length [122]. It is also known that poorer optical resolution is associated with longer probes due to the accumulation of spherical aberration over multiple half-pitch lengths [123]. For ‘optical-relay’ imaging, a triplet-lens system is generally utilised, with two shorter high-NA imaging and coupling lenses on each end respectively, and a longer, lower-NA relay lens (of integer multiple of 0.5 pitch) in between them. The coupling and imaging lenses generally utilise pitch lengths of just under 0.25, such that a short working distance is achieved. A triplet GRIN lens microendoscope is depicted in figure 1.13. For incorporation into a standard optical microscope, it is necessary to ensure that the focal plane of the objective lens and the focal plane of the microendoscope are coincident. It is also preferable that the NA of the objective is at least as high as the NA of the GRIN coupling lens; which ensures that the microscope objective captures the complete NA of light exiting the microendoscope, minimising signal loss. The transmission efficiency is an important consideration, particularly if both the illumination and imaging path are propagated through the lens. Previous studies have reported that the throughput is between approximately 60-70% [124].

## 1. Introduction and Background

---

Another important characteristic of a GRIN lens is its field of view (FOV); the diameter of the observable area through the probe. The precise FOV is difficult to quantify for a specific lens, as it will vary with the distance between the image plane of the microendoscope and the focal plane of the objective lens. In Kim et al. (2012), the FOV for a triplet-lens is defined as:

$$\text{FOV} \approx \varnothing \left( \frac{\text{NA}_{RL}}{\text{NA}_{IL}} \right) \quad (1.23)$$

where  $\text{NA}_{RL}$  and  $\text{NA}_{IL}$  are the numerical apertures of the relay lens and coupling/imaging lens respectively. However in Li et al. (2008), the authors define the FOV as:

$$\text{FOV} \approx \varnothing \left( \frac{l_{IL}}{l_{RL}} \right) \quad (1.24)$$

where  $l_{IL}$  and  $l_{RL}$  are the pitch lengths of the imaging lens and relay lenses. As the numerical aperture is inversely proportional to pitch length, it is clear that both the pitch and NA influence the FOV. Consider a triplet lens such as that shown in figure 1.13, with a diameter of  $350 \mu\text{m}$  and NA of 0.5 and 0.2 for the imaging and relay lenses respectively. The first definition gives a  $\text{FOV} \approx 140 \mu\text{m}$ , whereas the second definition gives a value of just  $80 \mu\text{m}$ . The ambiguity of this definition in the literature suggests that it will be necessary to empirically quantify the FOV for each application.

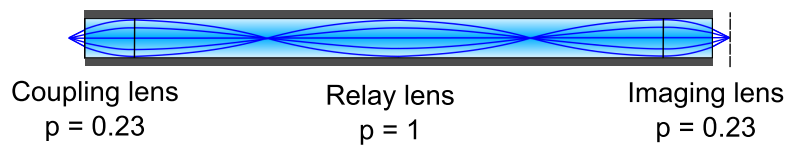


**Figure 1.13.** Illustration of triplet GRIN lens microendoscope with two high-NA lenses at each end (imaging and coupling lens respectively) and longer, lower-NA relay lens.

For off-axis illumination (illumination away from the radial centre of the GRIN lens), vignetting effects occur. For a point source displaced from the optical axis by a distance  $x_1$ , the bundle of rays incident on the GRIN lens are confined

## 1. Introduction and Background

---

to an ellipse within the lens, degenerating towards a line as  $x_1$  increases until no image is transmitted [125]. This results in images that decrease in intensity radially, and the presence of off-axis astigmatism. For wide-field illumination, this radial intensity fall-off can be minimised by a simple flat-fielding technique [126]. Similar to standard microscopy, the optical penetration depth of GRIN lenses is limited to approximately  $100\ \mu\text{m}$ , which can be extended with the use of two-photon imaging or the use of NIR wavelengths [120]. However, GRIN lenses allow for deeper insertion into tissue, provided care is taken to avoid excessive tissue damage. Finally, an important issue to be considered with the use of GRIN lenses is chromatic aberration, which arises due to the wavelength dependence of refractive indices  $N_o$  and gradient constant  $k$  [127]. In the context of sequential multispectral imaging, in which images are acquired at a range of wavebands, consideration must be given to the focal shift associated with chromatic aberration introduced by the GRIN lens microendoscope.

### 1.7.3. Review of applications

The applications of microendoscopy are many. Two-photon fluorescence microscopy through microendoscopes has been particularly prevalent, and have been applied to the imaging of various tissues *ex vivo* and *in vivo*. These have included neuronal imaging within the mouse brain [43, 128, 129]; mouse and human sarcomeres in muscle tissue [116]; and mouse kidney tissue [45]. For all of these studies, a variant of a GRIN lens microendoscopic probe was employed in conjunction with a commercial two-photon microscope.

Li et al. (2008) reported the application of two-photon fluorescence microendoscopy to imaging of the mouse kidney *in vivo*, using a fluorescent cell nuclear dye. In this paper, a high-NA triplet microendoscope ( $\text{NA} = 0.6$ ,  $\varnothing = 350\ \mu\text{m}$ ) of length  $16.25\ \text{mm}$ . Whilst successfully reporting images of live kidney, the authors

## 1. Introduction and Background

---

note that the increased number of pitches associated with a relatively long probe results in autofluorescence within the lens itself.

Whilst studies relating to the application of microendoscopy have predominantly employed two-photon fluorescence microscopy, standard single photon fluorescence has been pursued. In 2011, Pillai et al. described confocal fluorescence microscopy combined with a GRIN microendoscope [130]. Using fluorescent labels and an excitation laser of 488 nm, a bovine muscle tissue sample was imaged *ex vivo*. By axial translation of the probe, a high-resolution, three-dimensional image stack was acquired. Saunter et al. (2012) reported widefield (non-confocal) fluorescence microendoscopy ( $\varnothing = 0.5$  mm, length = 30 mm) of GFP-expressing zebra heart tissue *ex vivo*, as well as the pituitary gland in a rat model *in vivo* [126]. The low levels of excitation as compared to two-photon excitation were reported as being used to minimise any potential photo-toxic damage. Whilst image quality was inferior to many two-photon and confocal studies, this microendoscopy technique provided a larger field of view than in two-photon systems, and further, did not require laser scanning.

Finally, as well as fluorescence microendoscopy, efforts have been made into the application of optical coherence tomography (OCT) to microendoscopic imaging. OCT is an optical imaging technique which uses low-coherence interferometry of NIR light in order to generate three-dimensional images [131]. The application of OCT with microendoscopy was first reported in 1996 by Tearney et al., in which a microprism at the distal end of the GRIN lens was used in order to direct the imaging beam perpendicular to the probe [132]. A rotation motor then allowed for acquisition of three-dimensional OCT images in a human vein *in vitro*. In 1997, the same research group reported *in vivo* microendoscopic OCT, reporting images of rabbit gastrointestinal and respiratory tracts [133].

More recently in 2014, Quirk et al. reported development of an optofluidic OCT probe, in which a coaxial fluid-filled channel was implemented adjacent to the

imaging lens [134]. Localised focal injection of saline into a sheep lung was performed *ex vivo*, in order to perform localised index-matching for improvement of OCT penetration depth. The concept of coaxial localised fluid delivery is one that has not been extensively explored, and is a basis for work reported in chapter 7 of this thesis.

### 1.8. Summary

In this chapter, an introduction to the thesis has been presented. The topics that have been presented form the basis upon which the research in this thesis was undertaken. In summary, this thesis deals with the development of a novel multi-spectral imaging system and calibration-free oximetry technique. Although many potential applications are possible as the system is highly transferable, the specific motivation for this system was the application of oximetry to the study of hypoxia in inflammation and associated diseases. Further, longitudinal oximetry studies will be possible with the incorporation of minimally invasive microendoscopes to the imaging system. With microendoscopic capability, fluorescence imaging in addition to oximetry is explored in this thesis as a means for cellular imaging of inflammation, through the introduction of cell-specific, fluorescently labelled antibodies. It is hoped that development of a robust technique for localised oximetry of the microvasculature, as well as localised, minimally-invasive fluorescence imaging will ultimately provide a greater understanding of immune-related disease progression.

## 2. Development and characterisation of calibration-free oximetry algorithm

---

**Summary:** In this chapter, the analytical model employed for microvascular oximetry is described in detail, as well as a review comparing previous methods and algorithms employed for vascular oximetry. Modifications made from this previous work are highlighted. The implementation of the oximetry algorithm in MATLAB is described, as well as the necessary data processing steps. Finally, the performance of the algorithm is characterised by producing sets of artificial multispectral data with additive noise and contrast loss. Multiple sources of error are also considered and discussed.

### 2.1. Introduction

In order to derive oxygen saturation values from multispectral data, it was first necessary to develop a suitable algorithm. As discussed in the previous chapter, two-wavelength and three-wavelength oximetry techniques generally make use of empirical measurements, such that the system may be calibrated to allow for measurement of correct oxygen saturation values. In the case of two-wavelength oximetry, the optical density ratios (ODRs) for oxygenated and deoxygenated vessels are determined through calibration; a linear fit of ODR as a function of  $SO_2$  can then be used to determine the oxygenation of an unknown vessel. Calibration-based oximetry has found applications predominantly in the retina [59], and has

## 2. Development and characterisation of calibration-free oximetry algorithm

---

also been demonstrated in the microvasculature of striated muscle tissue [89]. Calibration of ODR in the retina is possible due to the presence of arterial vessels, the oxygenation of which can be validated using *ex vivo* blood gas measurement, or non-invasively using pulse oximetry [135]. Variations in pigment density occur across the retina and between individuals, and ODR is also known to be influenced by vessel diameter, predominantly due to scattering effects: both of these factors require further calibration for accurate two-wavelength oximetry [76]. Additionally, the linear relationship between ODR and  $\text{SO}_2$  only holds if one wavelength is isosbestic. This requirement is difficult to achieve, as an illuminating waveband with finite spectral width will not be perfectly isosbestic, even if its central wavelength is isosbestic [59].

For imaging of the microvasculature, the constituent capillaries are not easily distinguishable as either arterioles or venules, and so arterial pulse oximetry can not provide external calibration as is achieved in the retina. For previous two-wavelength oximetry of hamster muscle capillaries, calibration was achieved by determining two ODR end-points, for  $\text{SO}_2$  of 0% and 100%. These oxygenations were achieved by placing solutions of sodium dithionite and sodium cyanide over the muscle respectively, as well as having the animal breath varying levels of oxygen [89]. The aforementioned compounds are both toxic, and as such, repeated calibration is unlikely to be feasible for longitudinal studies in animals. For imaging of the microvasculature where the optical environment is expected to change locally (due to changes in overlying tissue, for example), a global ODR calibration would be ineffective. For these reasons, calibration-free models of optical transmission are a more appropriate choice for transferable, localised oximetry applicable in a range of tissues.

Optical transmission of light through a blood vessel is dependent on several factors, such as blood vessel diameter, the wavelength of illuminating light, the effective extinction and scattering coefficients of haemoglobin, and other scattering losses. The standard Lambert-Beer law describes absorption only, but may be

## 2. Development and characterisation of calibration-free oximetry algorithm

---

modified to include further considerations such as wavelength-dependent scattering and loss of contrast. By employing a realistic, analytical model in this manner, it is possible to perform calibration-free vascular oximetry to a high degree of accuracy.

In section 2.2, the basic analytical model used for oximetry analysis is derived and explained. The following section 2.4 covers a review of similar methods which have previously been employed for vascular oximetry, and illustrates how the algorithm used in this thesis has been adapted from this previous work. The emphasis of this chapter is placed on the application of a model for microvascular deep tissue oximetry. By configuring the optical imaging setup, the physical model can be partially simplified.

### 2.2. Derivation of basic analytical model

As introduced in section 1.3.1, the basic Lambert-Beer law can be expressed as

$$\text{OD}(\lambda) = \varepsilon(\lambda)cl \quad (2.1)$$

where OD is the optical density of a medium,  $\varepsilon(\lambda)$  is the molar extinction coefficient of the absorbing molecule,  $c$  is the molar concentration and  $l$  is the length over which light has been absorbed. For vascular oximetry where the optical transmission of light through blood vessels is assessed, this can be rewritten as:

$$\text{OD}(\lambda) = \varepsilon(\lambda)C_{HbT}d \quad (2.2)$$

where  $d$  is vessel diameter, and  $C_{HbT}$  is the molar concentration of total haemoglobin in the blood vessel (in units of  $\text{mol L}^{-1}$ ). The molar concentration of haemoglobin can be determined by dividing its mass concentration [ $\text{g L}^{-1}$ ] by the molecular weight of haemoglobin ( $64458 \text{ g mol}^{-1}$  [25]). The molar concentration of haemoglobin varies depending on haematocrit (the volume of red blood cells

## 2. Development and characterisation of calibration-free oximetry algorithm

---

compared to total blood volume), which itself is influenced by numerous factors such as age and gender. For the research in this thesis, the default value is prescribed as  $160 \text{ g L}^{-1}$ , although it is allowed to vary during the analysis as later described in section 2.6.5.

In equation 2.2,  $\varepsilon(\lambda)$  is the effective extinction coefficient of haemoglobin, dependent on oxygen saturation and the extinction coefficients of both oxygenated and deoxygenated haemoglobin:  $\varepsilon_{HbO_2}(\lambda)$  and  $\varepsilon_{Hb}(\lambda)$ . These extinction coefficients have been well defined in the literature [53], and were previously depicted in figure 1.6. The proportional concentration of  $\varepsilon_{HbO_2}(\lambda)$  and  $\varepsilon_{Hb}(\lambda)$  can be defined as  $c_1$  and  $c_2$  respectively, such that  $c_1 + c_2 = C_{HbT}$  and hence 2.2 can be rewritten as:

$$\text{OD}(\lambda) = (\varepsilon_{HbO_2}(\lambda)c_1 + \varepsilon_{Hb}(\lambda)c_2)d \quad (2.3)$$

The value for oxygen saturation ( $\text{SO}_2$ ), is equivalent to the proportion of oxygenated haemoglobin in the total solution of haemoglobin within the blood, thus we can define  $c_1 = C_{HbT}\text{SO}_2$  and  $c_2 = C_{HbT}(1 - \text{SO}_2)$ . Substituting, equation 2.3 then becomes

$$\text{OD}(\lambda) = C_{HbT}d[(\varepsilon_{HbO_2}(\lambda) - \varepsilon_{Hb}(\lambda))\text{SO}_2 + \varepsilon_{Hb}(\lambda)] \quad (2.4)$$

Finally, we know that  $\text{OD}(\lambda) = \log_{10}(T)$ , where  $T(\lambda)$  is the fractional optical transmission of light through the vessel. Equation 2.4 can simply be rewritten as:

$$T(\lambda) = 10^{-C_{HbT}d[(\varepsilon_{HbO_2}(\lambda) - \varepsilon_{Hb}(\lambda))\text{SO}_2 + \varepsilon_{Hb}(\lambda)]} \quad (2.5)$$

By experimental determination of  $T(\lambda)$  by multispectral imaging, and knowledge of vessel diameter,  $C_{HbT}$  and empirical coefficients  $\varepsilon_{HbO_2}(\lambda)$  and  $\varepsilon_{Hb}(\lambda)$ , a value for  $\text{SO}_2$  can be determined. Clearly the above model accounts for absorption of light by haemoglobin only and will not provide accurate results in most real imaging situations. It does not take into consideration the effect of optical scatter by haemoglobin or red bloods as a whole, nor the influence of the imaging ge-

ometry or any systemic loss of contrast (due to the MTF, for example). The next section describes previous models which have been developed for calibration-free vascular oximetry.

### 2.3. Consideration of light paths

Before an introduction of previous optical models for oximetry, an introduction to the concept of light-paths in vascular oximetry is necessary. For full-field illumination, the light intensity imaged at the centre of a blood vessel is instead considered to be a combination of three components as depicted in figure 2.1. These components include back-scattered light, light which has been absorbed by the blood in a single pass of the vessel (single-pass light) and light which has travelled through the blood vessel and back in a second pass (double-pass light). Single-pass absorption occurs in the case of transmission illumination, in which the vessel is back-illuminated. Double-pass absorption occurs when light is reflected back towards the detector from behind the blood vessel, resulting in additional absorption. The proportional contribution of these light paths to overall detected light intensity is an important consideration in the implementation of calibration-free optical models for oximetry.

The concept of light-paths in oximetry have been previously explored with Monte Carlo modelling. In 2001, Hammer et al. published a report regarding the light paths in retinal vessel oximetry, considering a spherical model of the eye which consisted of six concentric layers with different optical properties [136]. The authors determined from this study that for wavelengths between 520 nm and 586 nm, back-scattered light dominates, with single-pass absorption contributing to a greater extent than double-pass absorption over a range of vessel diameters (25  $\mu\text{m}$  to 200  $\mu\text{m}$ ). More recently, Rodmell et al. (2014) performed an investigation into the distribution of light paths within the retina [137]. The distribution of path lengths in each layer of the model was investigated by assessing the number of

## 2. Development and characterisation of calibration-free oximetry algorithm

photons detected as a function of travelled path-length for blood vessels of varying diameter. Examining these distributions, peaks were found at a path-length equal to the vessel diameter, representing single-pass absorption; and a secondary peak at twice the diameter, representing double-pass absorption. In agreement with Hammer et al., the contribution of single-pass outweighed that of double-pass, and it was demonstrated that the proportion of double-pass to single-pass photons increases with decreasing vessel size. This suggests that for oximetry of the microvasculature, the contribution of double-pass transmission becomes more prominent. The authors concluded that the contribution of double-pass light to the transmitted intensity is significant and should be considered in oximetry analysis. However, an important concept also validated by Rodmell et al. was that illumination of the edge of a vessel, and detection of light directly above it resulted in isolated single-pass light, with a distribution tightly constrained around the vessel diameter. This was an important consideration for the development of the illumination configuration of multispectral imaging system described in chapter 3 of this thesis.

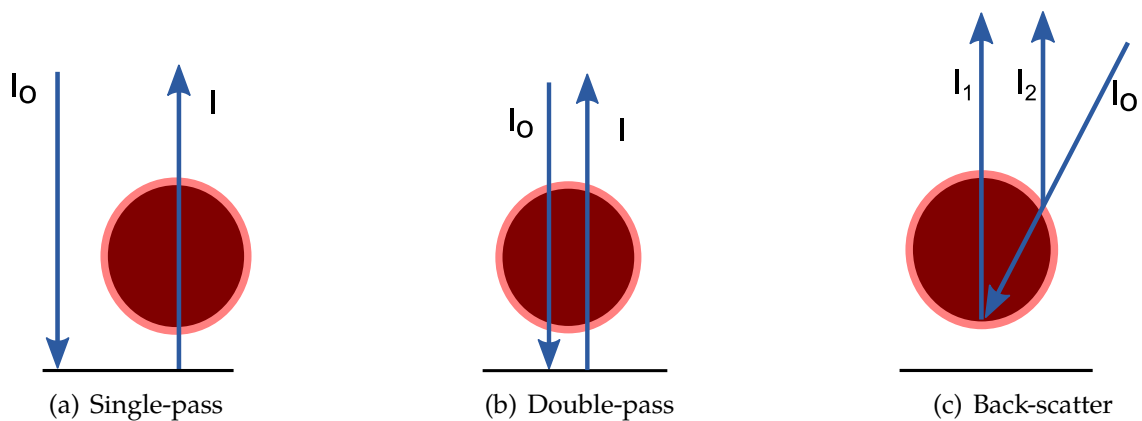


**Figure 2.1.** Illustration of light paths in vascular oximetry. Three possible interactions of incident light  $I_o$  with blood vessel shown: single-pass and double-pass absorption; and back-scattered paths depicted.

In chapter 1, a brief introduction to NIRS oximetry was presented. It was stated that the differential pathlength factor (DPF) is crucial in the analysis of NIRS data,

## 2. Development and characterisation of calibration-free oximetry algorithm

---

as the optical path length is much greater than source-detector distance. This greatly influences the observed values of optical transmission. However, this is not an issue for vascular oximetry. The path lengths involved in vascular oximetry are on the order of microns, and are hence much smaller than those in NIRS. It is therefore not necessary to incorporate the previously mentioned DPF in vascular oximetry analysis.

### 2.4. Review of previous methods

Due to the transparency of the ocular media, vascular oximetry has predominantly been applied to study of the retina. Consequently, the majority of calibration-free optical models for vascular oximetry have been developed specifically with consideration of optics within the retina. This section presents a brief review of previous models that have been applied to retinal oximetry, which form a basis for a specific model described in this thesis for deep-tissue microvascular oximetry.

The first attempt to develop an optical model for retinal oximetry was in 1976 by Cohen & Laing [94]. This study involved image acquisition of a large retinal artery in the rabbit, at 470 nm and 515 nm simultaneously using a beamsplitter and two interference filters for spectral filtering. The authors calculated ratios of vessel optical density, similar to two-wavelength oximetry. However, instead of performing a linear calibration as is standard in two-wavelength oximetry, the optical density ratio was related to a modified form of the Lambert-Beer law, taking into consideration the macroscopic scattering cross-section of the constituent red blood cells (RBCs). The oxygen saturation  $S$  could then be determined with the following:

$$S = \frac{R\epsilon_{Hb}(470 \text{ nm}) - \epsilon_{Hb}(515 \text{ nm}) + \frac{1}{2cd} [\log(1 - 1.32(515 \text{ nm})^2) - R \log(1 - 1.32(470 \text{ nm})^2)]}{[\epsilon_{HbO_2}(515 \text{ nm}) - \epsilon_{Hb}(515 \text{ nm})] - R[\epsilon_{HbO_2}(470 \text{ nm}) - \epsilon_{Hb}(470 \text{ nm})]} \quad (2.6)$$

## 2. Development and characterisation of calibration-free oximetry algorithm

---

where  $R = OD(\lambda_1)/OD(\lambda_0)$ . The parameter  $(1 - 1.32\lambda_1^2)$  is equivalent to  $q(\lambda)$ , the fraction of the total flux scattered by an RBC into the detector, and arises from the consideration of RBC scattering according to Twersky's theory of scattering by biological suspensions [138]. The model employed in this study by Cohen & Laing neglected the contribution of single-pass light transmission, instead assuming that all detected light had undergone double-pass absorption due to specular reflection of light from the fundus. Further, the authors neglected to consider directly back-scattered light, basing this assumption on Twersky's model for light reflected by an infinitely thick layer of blood [138]. These assumptions were later revealed to be invalid in the retina; as discussed in the previous section 2.3, back-scattered light and single-pass absorption actually dominate significantly over double-pass absorption [136, 137].

In 1995, Schweitzer et al. introduced a simple correction for optical scattering in whole blood [97], which modified the previously described equation 2.4 into the following:

$$OD(\lambda) = S + n \cdot \log\left(\frac{1}{\lambda}\right) + c \cdot d \cdot s(SO_2(\varepsilon_{HbO_2} - \varepsilon_{Hb}) + \varepsilon_{Hb}(\lambda)) \quad (2.7)$$

where  $S$  is a wavelength-independent scattering contribution;  $n$  is a scattering exponent; and  $s$  is a factor accounting for the influence of the detector geometry ( $0 \leq s \leq 1$ ). The parameters of this model which then have to be optimized are the oxygen saturation  $SO_2$ , the concentration-thickness-geometry product  $c \cdot d \cdot s$ , wavelength-independent scatter  $S$ , and scattering exponent  $n$ . The images were acquired at multiple wavelengths between 520 nm and 620 nm using a retinal camera adapted with a spectrograph ( $\Delta\lambda \leq 2$  nm). Using this model, good agreement was found between  $SO_2$  values in superficial arterioles and venules in the porcine brain; and measurements acquired with a laboratory blood gas analyser (deviation  $\sim 4\%$ ). No attempts were made to apply the model to retinal vessels in this case due to low SNR associated with the imaging system, resulting from the lower reflectivity of the fundus compared to the brain. The authors also stated

## 2. Development and characterisation of calibration-free oximetry algorithm

---

that consideration of the direct back-reflection of light from retinal vessels would be necessary for future application of this model to the retina.

Smith et al. (2000) were the first to implement the concept of multiple light paths to retinal oximetry [99]. The authors defined the total flux detected from the centre of a retinal vessel,  $\Phi_v$ , as  $\Phi_v = \Phi_{sp} + \Phi_{dp} + \Phi_{bs}$ ; the summation of flux from single-pass, double-pass and back-scattered photons respectively. The flux reflected from the fundus (e.g. adjacent tissue) was defined as  $\Phi_f = R_f \Phi_o$ , where  $R_f$  is the fundus reflectance and  $\Phi_o$  is the incident flux. Defining the transmittance then as  $T_v = \frac{\Phi_v}{\Phi_o}$ , the following general multi-pass transmittance model was derived:

$$T_v = \left( \alpha + \frac{a_2}{R_f} \right) \exp\{-[\text{SO}_2 \varepsilon_{\text{HbO}_2} + (1 - \text{SO}_2) \varepsilon_{\text{Hb}}] cd\} + \beta \exp\{-2[\text{SO}_2 \varepsilon_{\text{HbO}_2} + (1 - \text{SO}_2) \varepsilon_{\text{Hb}}] cd\} + \frac{a_1}{R_f}. \quad (2.8)$$

In this expression,  $\alpha$  and  $\beta$  are coefficients representing the fractions of light transmitted in a single and double pass, respectively. The coefficients  $a_1$  and  $a_2$  are constants arising from the assumption of a linear relationship between the reflectance  $R$  of a blood sample and its transmittance ( $R = a_1 + a_2 \exp(-\varepsilon cd)$ ) [138]. Equation 2.8, whilst providing a complete description of all light-paths, requires the determination of seven variables:  $\alpha$ ,  $\beta$ ,  $a_1$ ,  $a_2$ ,  $R_f$ ,  $cd$ , and  $s$ . It was determined to be unlikely that all parameters could be determined from least-squares regression, particularly as some were expected to be wavelength-dependent. The authors then considered two approximations which could be made in certain situations, in order to simplify the general model: 1) negligible back-scatter and 2) negligible double-pass.

For the first approximation, the back-scatter is negligible if  $\frac{a_1}{R_f} \ll 1$  and  $\frac{a_2}{R_f} \ll 1$ ; such as may be applicable for measurements made at lower wavelengths (blue or green) where haemoglobin absorption is higher, resulting in less backscattering; or for measurements made at high reflectance background (such as the optic disk) where  $R_f$  is high. The alternative approximation, where double-pass light may

## 2. Development and characterisation of calibration-free oximetry algorithm

---

be considered negligible, is based on the previously discussed Monte Carlo work by Hammer et al. [136]. This work predicted that the double-pass contribution to flux is the smallest component of retinal vessel oximetry, and so  $\Phi_{dp}$  is negligible for vessels larger than  $\sim 160 \mu\text{m}$ . For both approximations, the following equation was derived:

$$T_v = T_s(\lambda) \exp(\chi(\lambda)cd\varepsilon(\lambda)) \quad (2.9)$$

where  $T_s$  and  $\chi$  have different definitions for both approximations. For approximation 1) where back-scatter is neglected,  $T_s = \alpha + \beta$  and  $\chi = (\alpha + 2\beta)/(\alpha + \beta)$ , with limits  $0 \leq T_s \leq 1$  and  $1 \leq \chi \leq 2$ . For approximation 2) where double-pass is neglected,  $T_s = \alpha + \frac{a_1+a_2}{R_f}$  and  $\chi = \frac{a_2+\alpha R_f}{a_1+a_2+\alpha R_f}$ , with  $T_s > 0$  and  $\chi < 1$ . The wavelengths utilised were 629 nm, 678 nm, 821 nm, and 899 nm.

This model by Smith et al. is perhaps one of the most comprehensive in the literature, as it explicitly accounts for the individual light-paths in retinal vessel oximetry. Initial results with this technique showed good agreement between calculated and actual  $\text{SO}_2$  in a model eye [121]. However, it did not account for the reduced scatter coefficients of haemoglobin, nor allow for any contrast loss on the vessels for reasons other than oxygen saturation. For accurate results, it was also necessary for the authors to perform *ex vivo* calibration in swine, in order to first determine values for  $\chi cd$  and  $T_s$  [99].

### 2.5. Development of optical model for microvasculature oximetry

For the purposes of the research described in this thesis, it was desired to implement an optical model which would be appropriate for general vascular oximetry in the microvasculature. It was necessary to take into consideration the relevant light-paths as described previously, as well as the contribution of optical scatter by the haemoglobin in addition to its extinction coefficients. Further, additional considerations of geometric influence and scatter of light by the tissue, resulting

## 2. Development and characterisation of calibration-free oximetry algorithm

---

in loss of contrast, was required. Particularly for localised oximetry, where the optical environment is likely to be inhomogeneous, a model which could compensate for changes in loss of optical density associated with small layers of tissue overlying vessels, for example, would be hugely beneficial. In this section, specific considerations made for this research are detailed and the final implemented optical model described.

### **Simplification of light-paths with illumination configuration**

As discussed in the review of previous optical models, consideration of light-paths is crucial to vascular oximetry. Expressions such as equation 2.8, are impractical and difficult to analyse due to the number of variables. In order to simplify the optical model as much as possible, consideration was given to the illumination configuration of the imaging system itself. Previous methods have focused on the application of retinal oximetry which usually involves acquisition of data using a modified fundus camera. For vascular oximetry elsewhere, there are fewer restraints on the illumination scheme. It was detailed in Rodmell et al. that if illumination of a vessel is provided adjacent to the vessel itself, single-pass transmission can be isolated from double-pass and back-scattered light [137]. The method for achieving this illumination configuration is described in chapter 3. With this configuration, it is possible to assume that *both* double-pass and back-scattered light are negligible - resulting in a simplification of the required model for optical transmission. For this case, we have the following general equation:

$$T(\lambda) = s \cdot 10^{-C_{HbT}\eta d[\epsilon_{HbO_2}(\lambda) - \epsilon_{Hb}(\lambda)]SO_2 + \epsilon_{Hb}(\lambda)} \quad (2.10)$$

where  $s$ , the factor accounting for the influence of detector geometry is retained ( $0 \leq s \leq 1$ , previously described by Schweitzer [97]); and  $\eta$  is the path length contribution. For the illumination configuration where only single-pass transmission is significant,  $\eta = 1$ .

### Incorporation of wavelength- and SO<sub>2</sub>-dependent scatter coefficients

It has previously been noted by Smith (1999) that scattering effects of whole blood are not constant over the wavelength range [139]. Consideration of the wavelength-dependence on the optical scatter by whole blood is necessary for a complete consideration of optical transmission. In addition to wavelength-dependence, Faber et al. (2004) reported a theoretical study which purported that the scattering coefficient of blood  $\mu_s$ , as well as its anisotropy factor  $g$ , is also dependent on oxygen saturation [140]. These claims were based on calculation of the complex refractive indices of Hb and HbO<sub>2</sub>, in combination with Mie scattering theory. More recently in 2009, Friebel et al. published an empirical study which largely confirmed this theory [30]. In this paper, a concise empirical analysis of parameters  $\mu_s$  and  $g$  as a function of SO<sub>2</sub> was described for blood of standard haematocrit (33.2%), with measurements acquired using integrating sphere measurements of light transmittance. The data confirmed that  $\mu_s$  and  $g$  are significantly influenced by changes in SO<sub>2</sub>. In particular, Friebel et al. reported that the differences in  $g$  are strongest in the range of 410 - 430 nm, with a maximal decrease of 12%; and that there is a 15% change in  $\mu_s$  at 400 nm. This suggests that the scattering coefficients are most strongly affected in the blue wavelength regime, which is utilised for imaging of the microvasculature throughout this thesis. To date, this consideration appears not to have been implemented in any models for vascular oximetry. For the research in this thesis,  $\mu'_{Hb}(\lambda)$  and  $\mu'_{HbO_2}(\lambda)$  were introduced to the model, using values from Friebel et al. (2009) [30]. Treating  $\mu'_{Hb}(\lambda)$  and  $\mu'_{HbO_2}(\lambda)$  in the same way as  $\varepsilon_{Hb}(\lambda)$  and  $\varepsilon_{HbO_2}(\lambda)$ , equation 2.10 is then modified in the following form:

$$\begin{aligned}
 T(\lambda) = s \cdot 10^{-C_{HbT}\eta d} & \left[ (\varepsilon_{HbO_2}(\lambda) - \varepsilon_{Hb}(\lambda)) \text{SO}_2 + \varepsilon_{Hb}(\lambda) \right] \\
 & + \eta d \left[ (\mu'_{HbO_2}(\lambda) - \mu'_{Hb}(\lambda)) \text{SO}_2 + \mu'_{Hb}(\lambda) \right]
 \end{aligned} \tag{2.11}$$

## 2. Development and characterisation of calibration-free oximetry algorithm

---

Unlike  $\varepsilon(\lambda)$ , which are molar extinction coefficients in units of  $\text{cm}^{-1}\text{mol}^{-1}$ , the values for  $\mu_s(\lambda)$  represent the number of scattering events per unit length ( $\text{cm}^{-1}$ ). Consequently,  $\mu'_s(\lambda)$  needs to be multiplied by  $\eta d$  only.

### Compensation for reductions in contrast

As previously discussed, vascular oximetry is performed by first determining optical transmission through the blood vessel of interest. This transmission changes predictably with oxygen saturation and illumination wavelength. However, a critical issue with this technique is that the optical density of the vasculature may change independently of oxygen saturation, due to other factors such as tissue overlaying the blood vessels, for example. This tissue results in optical scattering which can reduce the contrast of the underlying vessels, resulting in higher inferred transmission than the “true” value as predicted by the modified Lambert-Beer law. Additionally, the MTF of the imaging system itself may introduce a systemic loss of contrast due to scatter by optical components. In this section, a simple factor is described which was introduced to the oximetry model in order to compensate for minor losses of contrast introduced by the local environment or the imaging system. This concept was previously developed by A. Gorman of the ICG, however to date has only been employed for retinal oximetry applications [141]. The performance of this factor is assessed in section 2.8.

The implementation of this “contrast factor” is based on the idea that we can interpret a loss of contrast as an additive component to both the background and transmitted light intensities as measured from the image. So, originally where transmission  $T$  is defined as  $T = \frac{I_v}{I_o}$ , we can define a modified transmission  $T'$ , where

$$T' = \frac{I_v + I_c}{I_o + I_c} \quad (2.12)$$

in which  $I_c$  is a constant value ( $I_c = 0$  for perfect contrast). It was necessary to derive a factor which could be incorporated to the oximetry model in order to

## 2. Development and characterisation of calibration-free oximetry algorithm

---

relate  $T'$  to  $T$ . To begin, the numerator and denominator in equation 2.12 are multiplied by  $I_o$ , giving

$$T' = \frac{I_o(I_v + I_c)}{I_o(I_o + I_c)} \quad (2.13)$$

Expanding the numerator we get

$$T' = \frac{I_o I_v + I_o I_c}{I_o(I_o + I_c)} \quad (2.14)$$

The following steps are then performed in order to isolate the original term for transmission  $T = \frac{I_v}{I_o}$ :

$$T' = \frac{I_o I_v + I_v I_c - I_v I_c + I_o I_c}{I_o(I_o + I_c)} \quad (2.15)$$

$$T' = \frac{I_v(I_o + I_c)}{I_o(I_o + I_c)} - \frac{I_v I_c}{I_o(I_o + I_c)} + \frac{I_o I_c}{I_o(I_o + I_c)} \quad (2.16)$$

$$T' = \frac{I_v}{I_o} - \frac{I_v I_c}{I_o(I_o + I_c)} + \frac{I_c}{(I_o + I_c)} \quad (2.17)$$

$$T' = \frac{I_v}{I_o} \left(1 - \frac{I_c}{(I_o + I_c)}\right) + \frac{I_c}{(I_o + I_c)} \quad (2.18)$$

Finally, we can define a ‘‘contrast factor’’  $K$ , allowing  $K = \frac{I_c}{I_o + I_c}$ . Equation 2.18 then becomes

$$T' = T(1 - K) + K. \quad (2.19)$$

Thus for an ideal image with no contrast reduction,  $K = 0$  and  $T' = T$ . As contrast image decreases,  $K$  will increase, with  $0 \leq K \leq 1$ . Incorporation of this factor allows the oximetry model to make minor adjustments for contrast and hence transmission, whilst still producing the true value for oxygen saturation.

Taking all the previous considerations into account, a final version of the optical model is given:

$$T(\lambda) = s(1 - K) \cdot 10^{-\left(C_{Hb} \eta d \left[ (\epsilon_{HbO_2}(\lambda) - \epsilon_{Hb}(\lambda)) \text{SO}_2 + \epsilon_{Hb}(\lambda) \right] + \left[ (\mu'_{HbO_2}(\lambda) - \mu'_{Hb}(\lambda)) \text{SO}_2 + \mu'_{Hb}(\lambda) \right] \eta d \right)} + K \quad (2.20)$$

## 2. Development and characterisation of calibration-free oximetry algorithm

---

For the research applications described in this thesis, this optical model was applied in conjunction with a custom multispectral imaging system. An *in vitro* and *ex vivo* validation of the complete oximetry technique is described in chapter 3.

### 2.6. Implementation of algorithm with multispectral data

In this section, the implementation of the analytical model for oximetry analysis is described. A number of basic data processing steps must be performed on raw multispectral images before they can be input to the oximetry analysis code which runs the analytical model described in the previous sections. To summarise, the entire processing and analysis method was as follows:

1. Background subtraction and multispectral image registration
2. Vessel tracking for determination of vessel coordinates
3. Calculation of experimental transmission profiles
4. Determination of vessel diameter along vessel
5. Oximetry algorithm for retrieval of  $SO_2$  and other parameters

#### 2.6.1. Preliminary data processing

After acquisition by the imaging system (to be discussed in chapter 3), multispectral data was stored in six separate images; one acquired at each specified waveband. These images were first read into MATLAB (in “double” format) and acquired “dark” images are subtracted from each respective image. The dark images were acquired at each waveband with no imaging target, thus imaging the background signal only. Subtraction of background images is necessary in order to remove the intensity contribution of dark current and shot noise. Particularly for images with low signal, it is important that this step be performed in order to achieve accurate transmission values. A basic intensity-based image registration

## 2. Development and characterisation of calibration-free oximetry algorithm

---

technique (MATLAB function *imregister*) was then applied to the six images, ensuring that they are correctly spatially aligned using affine transformations. As there are no moving parts associated with the switching of wavebands or acquisition of images, the images are expected to be co-registered. However, for cases *in vivo* where there may be minor movement of the object, this registration step ensures that any minor discrepancy can be rectified. The subtracted, registered images are then rearranged into a three-dimensional matrix  $(x, y, \lambda)$ .

### 2.6.2. Vessel tracking

The next step is that the three-dimensional matrix be loaded into vessel tracking software, previously developed within the Imaging Concepts Group. This software reads in the three-dimensional multispectral datacube, and allows the user to input a start and end point along a blood vessel (or multiple blood vessels) and the tracking algorithm finds a path between these points, choosing minimum intensity values along the path in order to determine the spatial coordinates of the centre of the blood vessel. Any of the six images can be selected and viewed in order to do this - as the images are registered, the coordinates will be the same for all wavebands.

### 2.6.3. Calculation of experimental transmission values

With the previously determined spatial coordinates of the blood vessels to be analysed, the next step is to extract experimental transmission values. These transmissions are approximated as the ratio of light transmitted through the blood vessel (the image intensity  $I$  in the centre of the vessel) to light which has not been transmitted through the vessel (image intensity  $I_o$ , directly adjacent to the vessel). This simple method is a standard technique used in many vascular oximetry studies [59].

## 2. Development and characterisation of calibration-free oximetry algorithm

---

This “transmission algorithm” works by taking pairs of adjacent blood vessel coordinates - provided from the previous vessel tracking step - and reading in a line intensity profile along the direction perpendicular to these two coordinates. This is equivalent to taking a line profile across the blood vessel. An example of such a line profile is shown in figure 2.2, as analysed using MATLAB. Smoothing is performed on the line profile in order to minimise effects from noise in low SNR images. The central region is first analysed, with a 2nd order polynomial fit applied to the section of the line profile which encapsulates the blood vessel only. In the MATLAB code, this is achieved by a user input of the line profile length in pixels, which should be changed depending on the size of the blood vessel. Fractional lengths of the line profile at both of its ends are ignored (e.g.  $0.2 \times$  profile length - this can also be easily changed depending on the clearance either side of the vessel), leaving the central pixels only. The minimum value of the subsequent polynomial fit is then used to extract the  $I$  value - the intensity of light which has been transmitted through the vessel.

Next, a linear fit is then applied to the profile, this time ignoring the central pixels analysed previously. This fit is thus applied only to the “background” pixels adjacent to the blood vessel. The value of this fit in the centre of the vessel (e.g. at the same spatial location in  $x$  of the minimum of the previous polynomial fit, as shown in figure 2.2) is extracted as the  $I_o$  value. Effectively, this is the intensity of light that would have been detected from the location of the vessel centre, in the absence of the vessel. The ratio of  $\frac{I}{I_o}$  is then inferred as the optical transmission value for that particular location along the vessel. An example of a line profile across a blood vessel is illustrated in figure 2.2.

This algorithm is run along every sequential pair of coordinates in the vessel (or multiple vessels), and at every wavelength, resulting in experimental transmission values which will be further processed for oximetry analysis. The wavelength-dependent transmission values at a specific spatial coordinate are referred to as a “transmission profile”. An example of this is shown in figure 2.3.

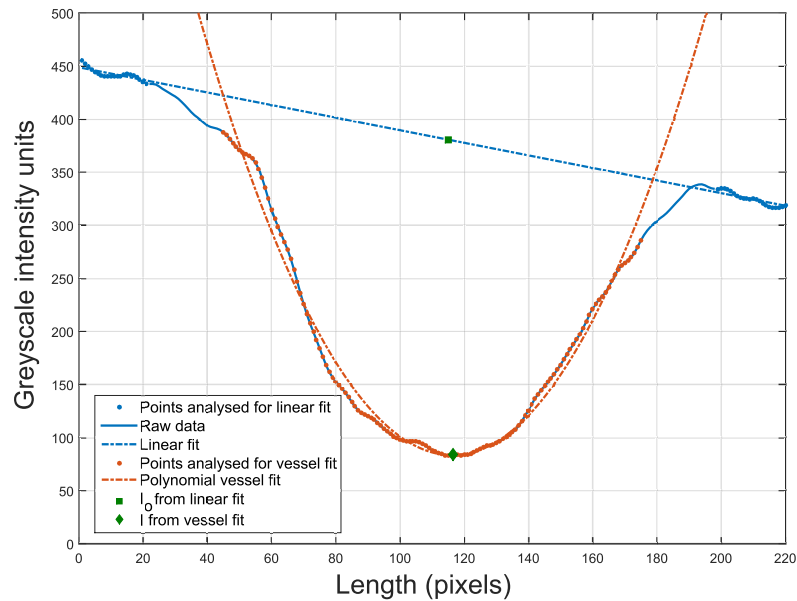


**Figure 2.2.** Illustration of blood vessel line profile as analysed in MATLAB, depicting the smoothed raw data; the linear and polynomial fits for  $I_0$  and  $I$  respectively; and the data points within the raw data that are used to generate the fits. The  $I$  and  $I_0$  values are also shown for this case, where  $I$  is chosen as the minimum value of the polynomial fit, and  $I_0$  is the value of the linear fit taken at the same pixel location as  $I$ .

## 2. Development and characterisation of calibration-free oximetry algorithm

---

### 2.6.4. Diameter estimation

The final “pre-processing” step to be run before the oximetry analysis code itself is to estimate the diameter of the blood vessel along its entire length. The average diameter value is used to input as an initial value of the diameter parameter of the oximetry analysis code, which reduces the number of free variables in the least-squares regression. The algorithm employed in this step was based on that described by Fischer et al. (2010) [142]. The same line profiles described for the transmission extraction step are also used for this step. In brief, the algorithm determines the precise vessel boundaries by finding the intersection of a linear fit (along the gradient at each side of the vessel) with threshold intensities. The diameter of the vessel is supplied in terms of pixels, however the pixel size of the detector is known ( $6.45 \mu\text{m} \times 6.45 \mu\text{m}$  in the case of the Hamamatsu detector used for all experimental work in this thesis, except for chapter 5) as is the magnification of the imaging system. There is a simple multiplicative factor applied to the “pixel diameter” in order to convert it to a real value in microns.

### 2.6.5. Implementation of oximetry algorithm

In order to run the oximetry analysis, the transmission profiles and diameter values determined in the previous step are input into MATLAB. The basic process of  $\text{SO}_2$  retrieval is optimisation of the optical model, which occurs when the difference between it and the experimental transmission profile is minimised. This is performed using a series of nonlinear least-squares regressions; specifically a trust-region reflective algorithm [143]. In order to calculate  $\text{SO}_2$ , a number of iterations of this fit were performed.

The initial iteration was performed by first averaging the experimentally obtained transmission profile  $T(\lambda)$  along the vessel, and using the average diameter value  $d$  along the vessel. An initial fit of the model to the data was run, giving preliminary

## 2. Development and characterisation of calibration-free oximetry algorithm

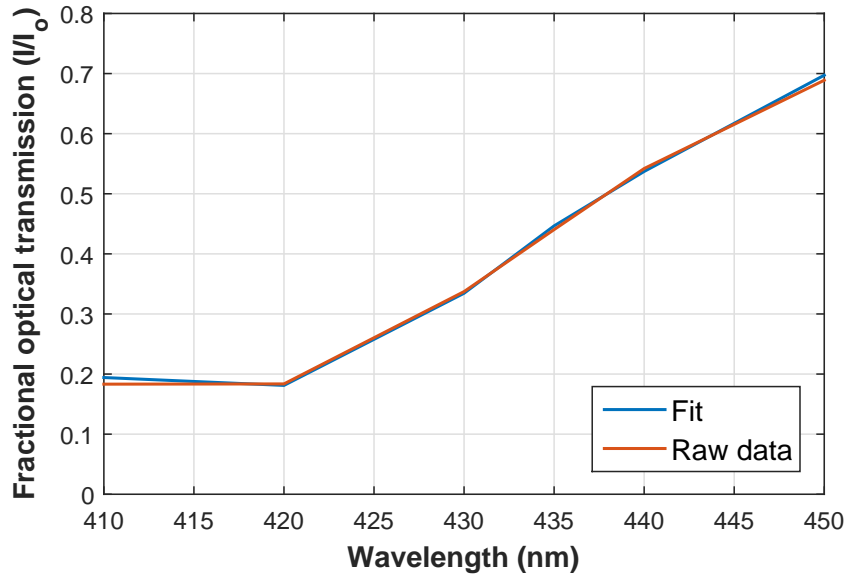
---

values for variable parameters  $s$ ,  $\text{SO}_2$ ,  $K$  and  $C_{Hb}$ . For single-pass transmission,  $\eta$  was set as a constant to 1. However for other analyses in which isolated single-pass illumination was not assumed,  $\eta$  could be allowed to vary if necessary. Three further fits were then run sequentially, allowing  $s$ ,  $K$  and  $\text{SO}_2$  to vary respectively along each point of the vessel, with all other parameters held constant to their most recently determined value. For each iteration of the fit, the model is optimised with respect to the experimental transmission profile. Both  $s$  and  $K$  were forced between boundary constraints 0 and 1. Due to potential errors in the determination of optical transmission, the upper boundary for the  $\text{SO}_2$  parameter was given as 1.2, corresponding to 120%. Clearly this would be an unphysical result. However, by increasing this upper limit, measurement errors and deviation of  $\text{SO}_2$  in oxygenated blood, about 100%, can be quantified; as opposed to “saturation” at 100%.

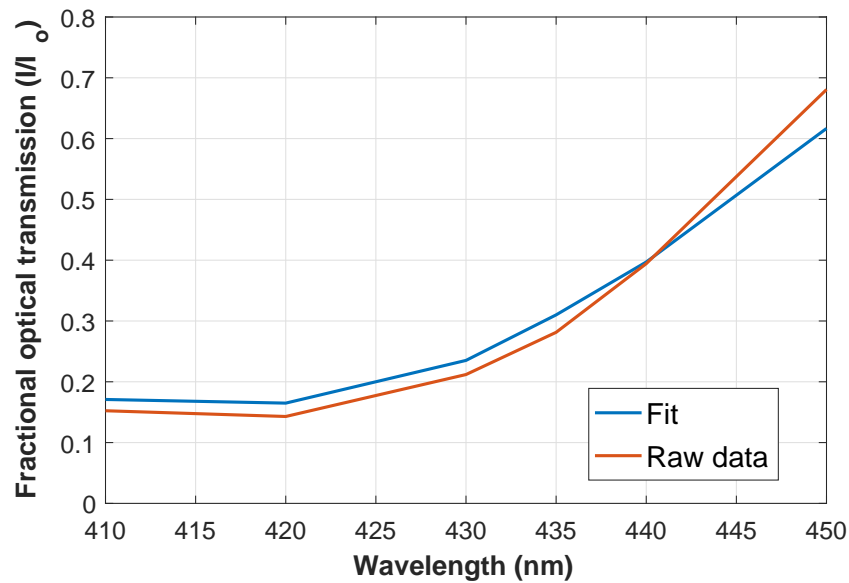
Two illustrative examples of the optimisation process at one particular coordinate are shown in figure 2.3. The experimentally determined transmission profiles are shown, as is the optical model which has been minimised with respect to the data, within the specified boundary constraints. During the analysis process, the profiles constantly update as the algorithm runs along each set of coordinates within every vessel to be analysed. As evident from figure 2.3(a) where  $R^2 = 0.99$ , for high quality fits there is minimal difference between the model and raw data. Figure 2.3(b) demonstrates a slightly poorer fit, but with an  $R^2$  value of 0.96 would still be acceptable. Larger mismatches between the optimised model and the raw data ( $R^2 < \sim 0.90$ ) tended to indicate the use of incorrect parameters, which would occasionally require further investigation (e.g. specifying  $\eta = 1$  for images that were not acquired with single-pass illumination configuration).

After the oximetry algorithm finished running, the results for determined parameters along each vessel were output, with the results for each individual vessel shown in a window such as that depicted in figure 2.4. The mean and standard deviation for each parameter along each vessel was also output for further analy-

## 2. Development and characterisation of calibration-free oximetry algorithm



(a) Good quality illustrative fit ( $R^2 = 0.99$ )



(b) Poorer quality illustrative fit ( $R^2 = 0.96$ )

**Figure 2.3.** Examples of oximetry analysis - least squares fit of analytical optical model to raw transmission profile data over blue wavelength regime; higher and poorer quality ( $R^2 = 0.99$  and 0.96 respectively) illustrative fits shown.

## 2. Development and characterisation of calibration-free oximetry algorithm

sis. For the analysis shown in the figure, the effective path length  $\eta$  was allowed to vary, however for imaging systems where the light configuration is known (e.g. imaging single-pass light only), this can be set to a constant such that there is one fewer free variable in the analysis. For the example shown in figure 2.4, the data was acquired with no back-scatter or double-pass, and the resulting value of  $\eta$  of 0. in this case confirmed This iterative algorithm proved to be a robust method of achieving smooth  $\text{SO}_2$  profiles along analysed vessels.

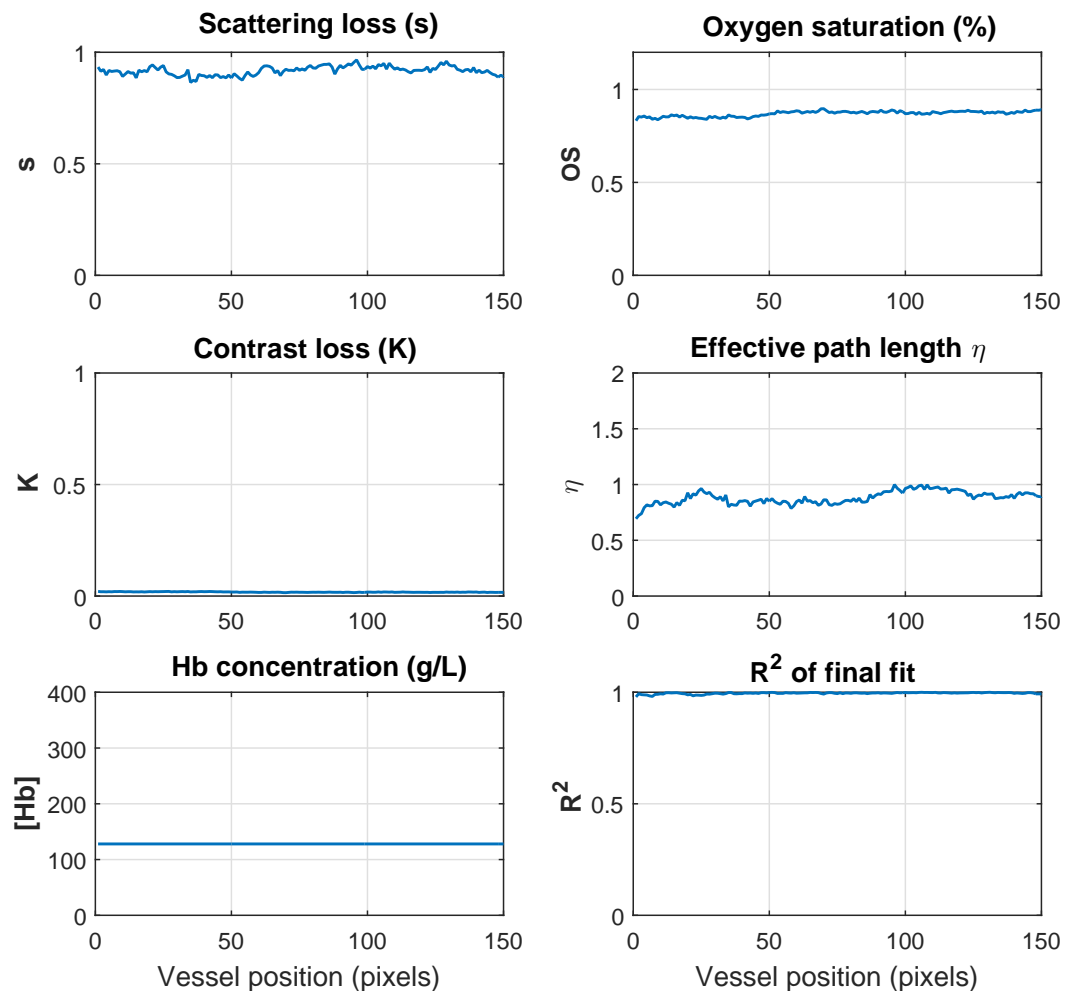


**Figure 2.4.** Example of oximetry analysis results outputs, with determined parameters along vessels shown.

## 2.7. Oximetry error

Due to the number of variables involved, the precise accuracy of an optical model for oximetry is difficult to quantify. In this section, several factors contributing to overall oximetry error are discussed.

### 2.7.1. Photometric error

Photometric errors arising from measurement of optical transmission will contribute to overall oximetry error. This issue has been previously considered by van Assendelft (1970) and Smith (1999) [144] [139]. The absolute error  $\Delta T$  of transmission will be dependent on the SNR of the imaging system, and generally independent of the magnitude of  $T$ . It is possible to assess the extent to which  $\Delta T$  will contribute to oximetry error by calculating the “relative analysis error”. For the simplest form of the Lambert-Beer law, this relative analysis error arises as  $\frac{\Delta c}{c}$ , where  $c$  is the molar concentration of haemoglobin, and  $\Delta c$  its associated error. Referring to this basic form of the Lambert-Beer law (Equation 1.8, derived in section 1.3.1), we have that

$$\log\left(\frac{1}{T}\right) = \epsilon c l \quad (2.21)$$

which can be rearranged for the molar concentration  $c$  as follows, also converting to natural logarithms:

$$c = \frac{\ln(1) - \ln(T)}{\epsilon \cdot l \cdot \ln(10)} \quad (2.22)$$

As detailed in van Assendelft (1970), the magnitude of  $\Delta T$  is such that the following approximation holds:

$$\Delta c = \left| \frac{dc}{dT} \right| \cdot \Delta T \quad (2.23)$$

which leads to

$$\Delta c = \frac{1}{T} \cdot \frac{1}{\epsilon \cdot l \cdot \ln(10)} \cdot \Delta T \quad (2.24)$$

## 2. Development and characterisation of calibration-free oximetry algorithm

and can be divided by  $c$  (equation 2.22) to give the relative analysis error,

$$\frac{\Delta c}{c} = \frac{\Delta T}{T} \cdot \frac{1}{\ln(1/T)} \quad (2.25)$$

This relative analysis error  $\frac{\Delta c}{c}$  is minimised when its derivative with respect to  $T$  is zero:

$$\frac{d\left(\frac{\Delta c}{c}\right)}{dT} = \frac{\Delta T}{T^2 \ln(1/T)} \cdot \left(\frac{1}{\ln(1/T)} - 1\right) = 0 \quad (2.26)$$

The above equation holds if either factor is zero; however as  $\Delta T = 0$  is physically unachievable, we can take the second solution which is  $\ln(1/T) = 1$ . It follows that the relative analysis error of the oximetry algorithm will be lowest for  $T = (1/e) = 36.8\%$ . Assuming  $\Delta T = 1\%$ ,  $\frac{\Delta c}{c} = 0.027$  at this value of  $T$ . However, the error remains acceptably low for  $10\% \leq T \leq 70\%$  [144]. This is demonstrated in figure 2.5, in which the relative analysis error is plotted with respect to  $T$ , and shown for varying  $\Delta T$ .

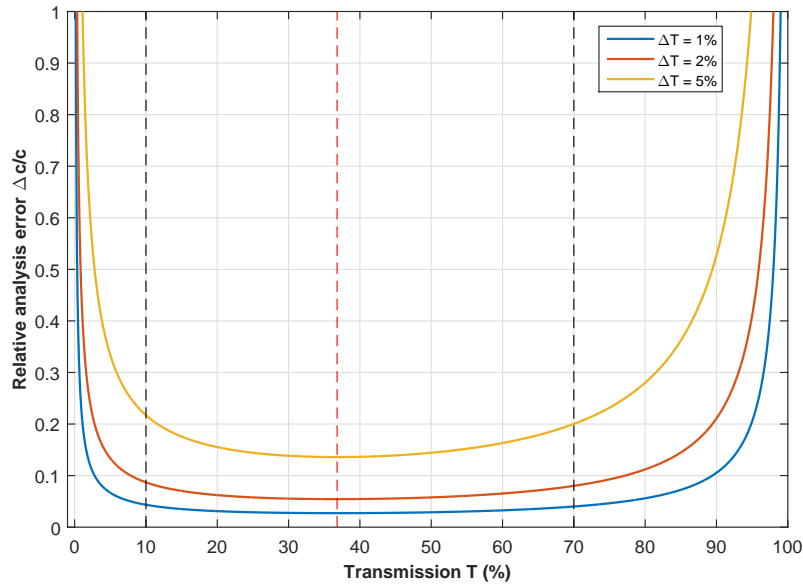


**Figure 2.5.** Relative analysis error with respect to optical transmission. The red dashed line represents the point of lowest error, with the black dashed lines representing the boundaries (10% to 70%) within which the error is considered to be acceptably low.

## 2. Development and characterisation of calibration-free oximetry algorithm

---

The optimal wavelength choice for oximetry will depend strongly on the application, taking into consideration the diameter of the vessels to be analysed and corresponding optical transmission. The data in figure 2.5 highlights the importance of choosing the correct wavelengths for a particular application. Practically, the size of blood vessels to be imaged has a large effect on optical transmission. The figure also highlights the importance for minimising  $\Delta T$  - as this is the fundamental error in measurement of transmission, it ultimately influences  $\frac{\Delta c}{c}$  and hence oximetry error.

### 2.7.2. Propagation of error

The error in  $SO_2$  with respect to measured transmission  $T(\lambda)$  can also be assessed qualitatively, by referring to equation 2.20. By rearranging the equation in terms of  $SO_2$ , the partial derivative of  $SO_2$  with respect to  $T(\lambda)$  can be calculated. Beginning with equation 2.20, of the complete model employed for oximetry, the following steps are performed in order to isolate  $SO_2$  and take the partial derivative. For simplicity, and due to the fact that  $\epsilon_{HbO_2}(\lambda)$  and  $\epsilon_{Hb}(\lambda)$  are expected to contribute to  $T(\lambda)$  to a greater extent than  $\mu'_{HbO_2}(\lambda)$  and  $\mu'_{Hb}(\lambda)$ , they are omitted from this analysis.

$$\log_{10}\left(\frac{T(\lambda) - K}{s(1 - K)}\right) = -(C_{Hb}\eta d [(\epsilon_{HbO_2}(\lambda) - \epsilon_{Hb}(\lambda)) SO_2 + \epsilon_{Hb}(\lambda)]) \quad (2.27)$$

$$SO_2 = \frac{\log_{10}(T(\lambda) - K) - \log_{10}(s(1 - K)) - C_{Hb}\eta d \epsilon_{Hb}(\lambda)}{C_{Hb}\eta d (\epsilon_{Hb}(\lambda) - \epsilon_{HbO_2}(\lambda))} \quad (2.28)$$

$$\frac{\delta(SO_2)}{\delta(T(\lambda))} = \frac{1}{\ln(10)} \frac{1}{(T(\lambda) - K)} \frac{1}{(C_{Hb}\eta d (\epsilon_{Hb}(\lambda) - \epsilon_{HbO_2}(\lambda)))} \quad (2.29)$$

A cursory assessment of equation 2.29 suggests that error increases with increasing contrast reduction; for the case of no observable vessel contrast, the measured image intensity values  $I$  and  $I_o$  will be equal, and so  $T = 1$ . Thus, as  $K$  approaches

## 2. Development and characterisation of calibration-free oximetry algorithm

---

1,  $\frac{1}{T-K}$  approaches infinity. Further, for wavelengths where  $\varepsilon_{Hb}(\lambda) - \varepsilon_{HbO_2}(\lambda)$  is small (e.g. for wavelengths that are close to being isosbestic), the error also increases. From this, we can conclude that wavelengths for which there is a large sensitivity to oxygen saturation ( $|\varepsilon_{Hb}(\lambda) - \varepsilon_{HbO_2}(\lambda)| \gg 0$ ), the error is expected to be minimised.

### 2.7.3. Errors in extinction coefficients and other parameters

It is worth noting that errors in oximetry may arise from errors in the employed extinction coefficients. The values used for these coefficients throughout this thesis were derived from human blood. The optical model was applied to both rat and mouse vasculature *in vivo*, and horse blood was used for phantom measurements *in vitro*. It has been shown that the differences between oxyhaemoglobin and deoxyhaemoglobin in human and murine blood are minimal [145]. It is also known that variations in reference values can occur due to changes in temperature. In 2007, Kim et al. published a report on the effect of coefficient variation on the determination of haemoglobin concentration [146]. The authors were specifically focused on the application of NIRS, so gave consideration predominantly to wavelengths in the near-IR. By increasing temperature by 20 °C, relative errors of 6.6% and 5.8% were found in  $\Delta[Hb]$  and  $\Delta[HbO_2]$  respectively. For *in vivo* oximetry performed in this thesis, the temperature of anaesthetised animals was kept stabilised at 37 °C, so deviations in temperature were avoided. Although further analysis is required, it is possible that such errors are more pronounced in two-wavelength oximetry than in multispectral oximetry utilising multiple wavebands.

For vascular oximetry, the spectra of oxyhaemoglobin and deoxyhaemoglobin only are assessed in order to determine  $SO_2$ . However, additional derivatives of haemoglobin such as methaemoglobin (HbMet) and carboxyhaemoglobin (HbCO) can be present in the blood and potentially contribute to optical absorption. In a previous study by Zijlstra et al., the error in measurements due to the presence of

HbCO was found to be “insubstantial” for two-wavelength oximetry [147], however it was noted that HbMet shows conspicuous differences. However, as the relative concentration of HbMet is much lower than Hb and HbO<sub>2</sub>, its influence on the extinction spectra of blood is generally assumed to be negligible in oximetry, and is the assumption made throughout this thesis.

### 2.8. Assessment of performance

In real imaging situations, it is unlikely that data acquired will agree perfectly with the theoretical model. Whilst the optical model takes into consideration the main elements which influence transmission such as wavelength, extinction and scatter coefficients, the real-life scenario is more complex. There may be minor changes in transmission as a result of low signal-to-noise ratio (SNR), for example, or additional absorption of light through small layers of overlaying tissue.

In order to characterise the performance of the algorithm, it was necessary to produce artificial spectral datasets representing the vasculature. It was desired to investigate the effect of loss of contrast and additive noise on the accuracy of the output parameters, specifically SO<sub>2</sub>. The analytical model previously described for fitting to the experimental data was used in this case to generate these artificial datasets. Two distinct sets of data were considered; those produced using the blue wavelengths (410 nm to 450 nm) as would be used for imaging of the microvasculature in the tendon; and also images produced at ‘green-red’ wavelengths, as would be used on larger vasculature in the rat spinal cord (chapter 5).

The artificial data sets were produced as follows. A simple case of one blood vessel on a white background was first considered. The transmission was defined as single pass Lambert-Beer absorption through a cylindrical vessel, taking into account the effective extinction and scatter coefficients for haemoglobin of user-specified oxygen saturation at each waveband of the data set. In order to generate

## 2. Development and characterisation of calibration-free oximetry algorithm

---

realistic transverse line profiles across these artificial vessels, the optical transmission was calculated by first defining a longitudinal chord of the cylinder for each distance  $d$  from the centre of the cylinder. The chord of a circle (e.g. cylinder cross-section) is equal to  $2\sqrt{r^2 - d^2}$ , where  $r$  is radius, calculated for  $d \leq r$ . This is depicted in figure 2.6.

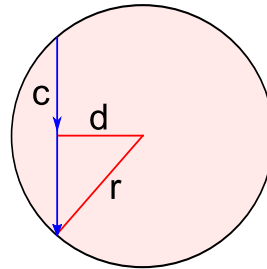


**Figure 2.6.** Depiction of chord length  $c$  across artificial blood vessel cross-section, over which absorption would be applied. Chord lengths were calculated at each distance  $d$  from the centre of the vessel, for  $d \leq r$ , the radius of the cylinder.

The modified Lambert-Beer law was then applied at each point across the vessel, using the chord length as the distance over which absorption and scatter by haemoglobin occurs. Clearly, the longest chord is at the centre of the vessel where absorption is greatest, and it was from this point that the theoretical optical transmission was calculated.

The data sets were generated with a blood vessel of  $10\ \mu\text{m}$  diameter for the case of blue wavelengths, and  $50\ \mu\text{m}$  diameter for green-red wavelengths. Further, the contrast of the produced images could be intentionally reduced by implementing the  $K$  factor previously described into the modified Lambert-Beer equation. For the initial case, there was no contrast reduction (e.g.  $K = 0$ ) and the geometric collection efficiency (' $s$ ' parameter) would be unity. The MATLAB code generated a series of images representing the blood vessel at each wavelength. A number of these are presented in figure 2.7 for reference, illustrating how the produced image changes with wavelength and contrast reduction  $K$ . The code also output cross-sectional line profiles of the vessel at each wavelength, as well as a transmission profile depicting minimum transmission as a function of wavelength. An example

## 2. Development and characterisation of calibration-free oximetry algorithm

---

of cross-sectional line profiles for a  $10\ \mu\text{m}$  theoretical blood vessel at  $\text{SO}_2 = 60\ \%$  is shown in figure 2.8.

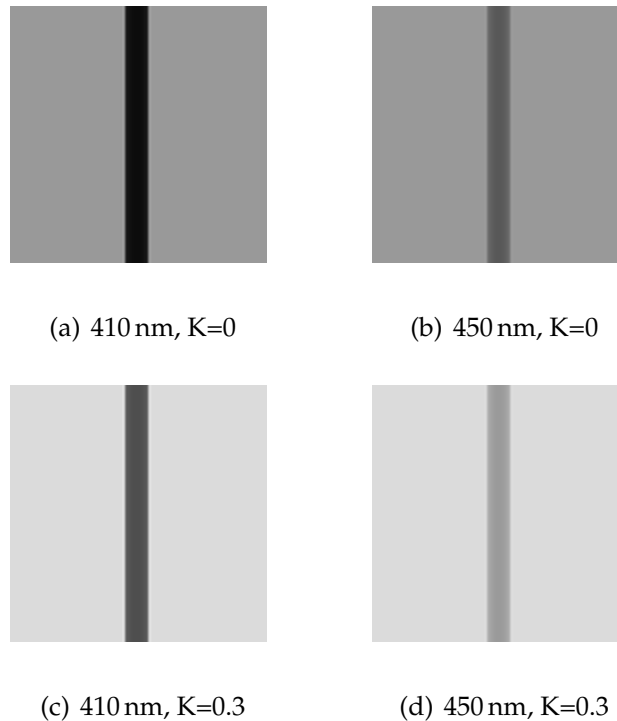


**Figure 2.7.** Example images of theoretical blood vessels from artificial data sets for a given  $\text{SO}_2$  of 60 %.

### 2.8.1. Blue wavelengths

The blue wavelengths are those used in the majority of the experimental work presented in this thesis, and are thus first to be considered. As previously mentioned, the blue wavelengths (410 nm, 420 nm, 430 nm, 435 nm, 440 nm and 450 nm) have sufficiently high extinction coefficients such that good contrast of the microvasculature is obtained.

### 2.8.2. Waveband-associated error

It is clear that for illumination of finite specified bandwidth, the effective extinction coefficient for a specific waveband will not be equal to that of its central

## 2. Development and characterisation of calibration-free oximetry algorithm

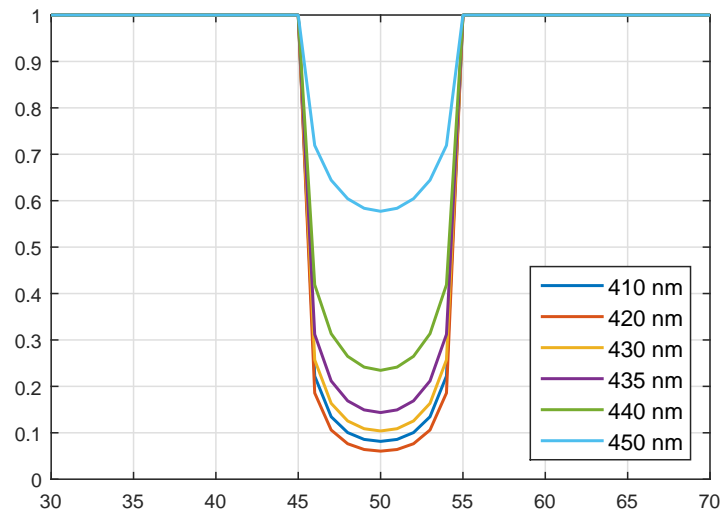


**Figure 2.8.** Cross-sectional line profiles of 10  $\mu\text{m}$  diameter theoretical blood vessel for  $\text{SO}_2 = 60\%$ ,  $K = 0$ .

wavelength, but in fact will be the integral of the illumination spectrum with all extinction coefficients over its wavelength range. The AOTF employed in this research has a nominal bandwidth of only 2 nm. The LCTF employed in chapter 5 exhibited a broader illumination spectrum, with bandwidth equal to approximately 10 nm. Figure 2.9 demonstrates the associated errors in  $\text{SO}_2$  which arise from using the extinction coefficient of the central wavelength only, for both of the aforementioned bandwidths. The data was generated by integrating a gaussian transmission spectrum (centred about a nominal wavelength, with FWHM equal to 2 nm and 10 nm respectively) with the extinction coefficients of its constituent wavelengths. The blue wavelength regime was employed for this test. The results showed, as evident from the figure, that for a bandwidth of 2 nm, the error remains acceptably low at less than 0.5% for  $\text{SO}_2$  of 30% upwards. However, a much increased error was demonstrated for a bandwidth of 10 nm. From these results, it was concluded that for analysis with AOTF data, integration across the illumination spectrum was not necessary. However, for those acquired with the LCTF (such as in chapter 5), this was necessary in order to minimise error.

## 2. Development and characterisation of calibration-free oximetry algorithm

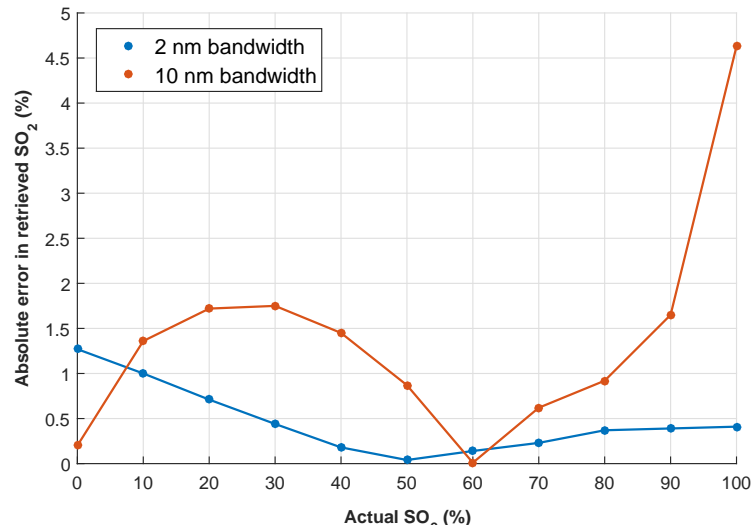


**Figure 2.9.** Errors associated with finite waveband, for FWHM of 2 nm and 10 nm.

### Additive noise

The first aspect to be considered is how robust the recovery of correct SO<sub>2</sub> is in the presence of noise. A set of images for varying oxygen saturations were produced using the process described previously. Random, artificial gaussian noise was applied to these images with increasing variance, and zero mean. The variance is the average squared deviation from mean image value; so for variances of 0.001, 0.002 and 0.005, the average deviation from the mean image value will be 3.16%, 4.4% and 7.07% respectively. Figure 2.10 shows an example image of a 10 μm diameter blood vessel with additive Gaussian noise. This is in comparison to the images shown in figure 2.7, for which no additive noise was implemented. Noise variance,  $\sigma^2$ , is inversely proportional to image signal-to-noise ratio (SNR); it can be defined as  $s^2/\sigma^2$ , where  $s$  is the signal (image intensity).

As evident from the results in figure 2.11, there is generally good agreement between original SO<sub>2</sub> and that recovered by the algorithm for the three levels of additive noise. This is demonstrated in the figure, for which a “perfect” linear fit was applied (1:1 ideal agreement). For this fit, all three data sets with varying noise

## 2. Development and characterisation of calibration-free oximetry algorithm

---

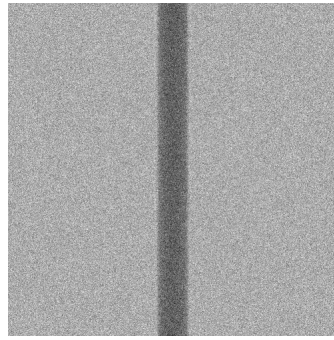


**Figure 2.10.** Example image at 450 nm of 10 µm diameter blood vessel with additive Gaussian noise (variance 0.005)

demonstrated an  $R^2$  value of  $\sim 0.99$ , suggesting that only very minor discrepancies existed between original and retrieved  $\text{SO}_2$ . The average standard deviation along the vessel was 2.28% for noise variance of 0.001. This value increased up to 3.33% and 4.9% for variances of 0.002 and 0.005 respectively. So, whilst the deviation in reported  $\text{SO}_2$  along the vessel seems to increase with increasing noise, the average value of the whole vessel remains constant. This suggests however that for noisy data,  $\text{SO}_2$  values at individual points along a blood vessel have a greater uncertainty than the vessel as a whole.

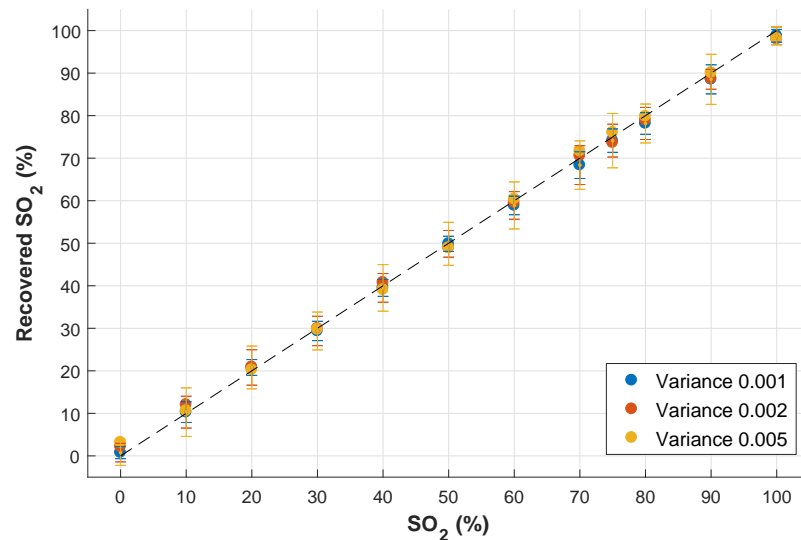


**Figure 2.11.** Recovered  $\text{SO}_2$  for theoretical data at blue wavelengths with additive Gaussian noise of increasing variance. Dashed line shows ideal linear fit (1:1 agreement, slope = 1).

### Waveband-specific contrast reduction

It was previously shown in section 2.7.2 that the error  $\delta(\text{SO}_2)/\delta(T(\lambda))$  increases with increasing  $K$ . For this assessment of algorithm performance, the error in retrieved  $\text{SO}_2$  associated with errors in contrast reduction factor  $K$  was investigated. Theoretical spectral images were generated with an initial  $K$  value of 0.3 and  $\text{SO}_2$  of 60%. An error in  $K$  was introduced for each waveband respectively, and  $\text{SO}_2$  was retrieved. Figure 2.12 demonstrates the significant error associated with increasing  $K$  of one waveband only, and also demonstrates how certain wavelengths contribute significantly more to error in  $\text{SO}_2$  than others; at 420 nm, 430 nm, 440 nm and 450 nm, the error in  $\text{SO}_2$  was shown to be  $\Delta(\text{SO}_2) \leq 5\%$  for a 50% error in  $K$ . This is in contrast to over 10% for 435 nm and over 15% for 410 nm.

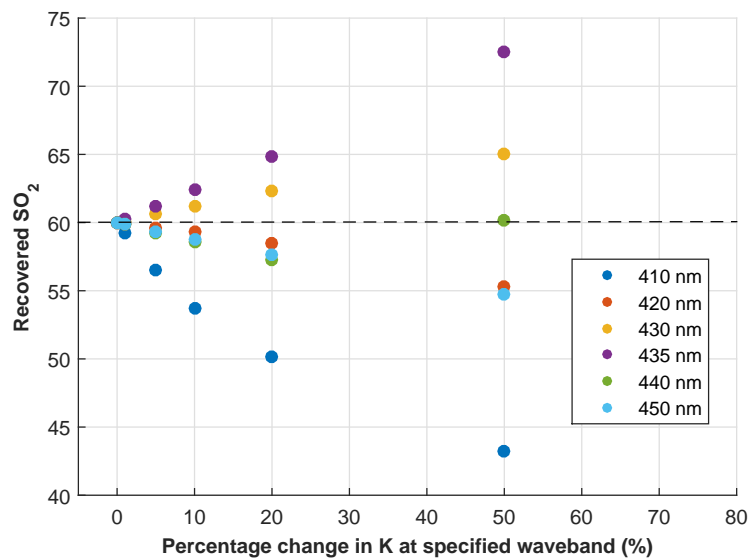


**Figure 2.12.** Recovered  $\text{SO}_2$  at blue wavelengths with waveband-specific contrast reduction

Figure 2.13 demonstrates the corresponding error in retrieved  $K$ , as output from the algorithm for a waveband-specific increase in  $K$ . Interestingly, the error in retrieved  $K$  is not as significant as the error in  $\text{SO}_2$ . Whilst relevant for a qualitative assessment of the contrast provided by the images (and the associated implications

## 2. Development and characterisation of calibration-free oximetry algorithm

regarding increased  $\text{SO}_2$  error with high values of  $K$ ), the precise value of  $K$  is not of particular importance compared to the  $\text{SO}_2$  parameter.

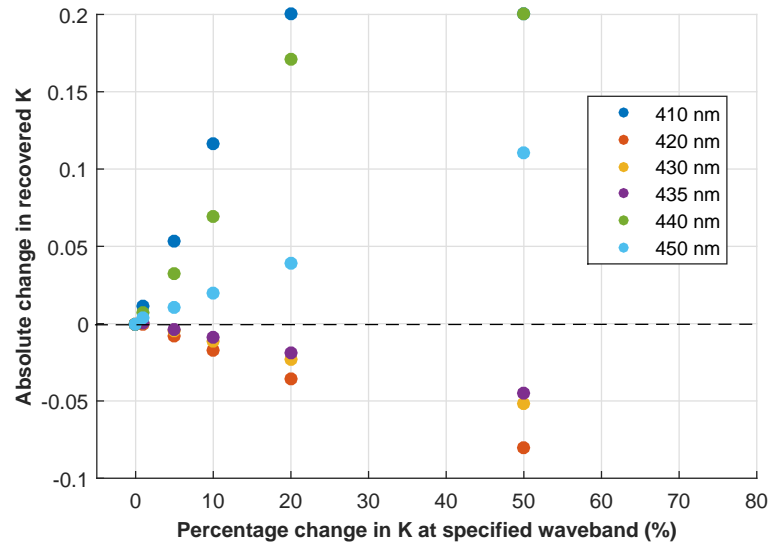


**Figure 2.13.** Change in recovered  $K$  at blue wavelengths with waveband-specific change

### $\text{SO}_2$ -dependent scatter

As earlier described in section 2.5, it has been reported that the optical scatter of light by haemoglobin is influenced not only by wavelength but by  $\text{SO}_2$  [30]. It was desired to quantify the effect that  $\text{SO}_2$ -dependence on reduced scatter coefficients has on oximetry. A data set was generated, using the blue wavelength regime, implementing the  $\text{SO}_2$  dependent coefficients as provided by Friebel et al. Oximetry analysis was then performed on this data, using a version of the model which did not take the  $\text{SO}_2$  dependence into consideration. The error resulting from omitting this consideration from the analysis is illustrated in table 2.1, in which a minor error ( $< 1.5\%$  for all oxygenations) was observed. This brief analysis confirms the influence of  $\text{SO}_2$  dependent scatter coefficients on oximetry, and provides motivation for its consideration in the previously described optical model.

## 2. Development and characterisation of calibration-free oximetry algorithm

---

**Table 2.1.** Oximetry error resulting from presence of SO<sub>2</sub> dependence of reduced scatter coefficients  $\mu'(\lambda)$ .

Original SO <sub>2</sub> (%)	Retrieved SO <sub>2</sub> (%)
100.00	101.07
85.00	85.44
70.00	69.83
50.00	49.21
25.00	24.16
00.00	00.45

### 2.8.3. Green-Red wavelengths

In chapter 5, an oximetry study is presented of the vasculature in the rat dorsal spinal cord. For this work, longer wavelength were utilised, as the vasculature was larger and more absorbing than the microvasculature to be studied in the murine tendon. The follow wavebands were employed: 546 nm, 560 nm, 570 nm, 584 nm, 590 nm and 600 nm. The theoretical tests applied to the blue wavebands were also carried out on artificial datasets which instead employ these wavelengths in the green and red visible region of the EM spectrum.

#### Additive noise

The same assessment was performed with the green-red wavelengths as with the blue. For a given SO<sub>2</sub> of 60%, increasing levels of gaussian noise were introduced to the generated multispectral images, and the retrieved SO<sub>2</sub> along the vessel was investigated. The results are shown in figure 2.14. Although the expected linear trend is evident, there are minor errors associated in the mean retrieved SO<sub>2</sub> value along the vessels for all levels of noise and given SO<sub>2</sub>. Further, the standard deviation of these values along the vessel were much increased with noise as compared to the blue wavelengths. For noise variance of 0.001, 0.002 and 0.005, the average standard deviations along the vessel for all oxygenations were 10.6%, 14.5% and 21.5% respectively. The potential reasons for this may be due

## 2. Development and characterisation of calibration-free oximetry algorithm

to the combination of Hb and HbO<sub>2</sub> extinction coefficients used within this green-red regime of the visible spectrum. Of the six wavelengths utilised in this regime, three are near isosbestic, meaning that  $\varepsilon_{Hb}(\lambda) - \varepsilon_{HbO_2}(\lambda)$  is small; as noted in section 2.7.2, this leads to an increase in  $\delta(\text{SO}_2)/\delta(T(\lambda))$ . This is in contrast to the blue regime where only one of the six wavebands are near isosbestic. Lower absolute values of extinction coefficients in the green-red region as compared to the blue regime also likely contribute to an increase in  $\delta(\text{SO}_2)/\delta(T(\lambda))$ . These results emphasise the importance of optimising SNR by minimising noise for experiments utilising this green-red wavelength regime.

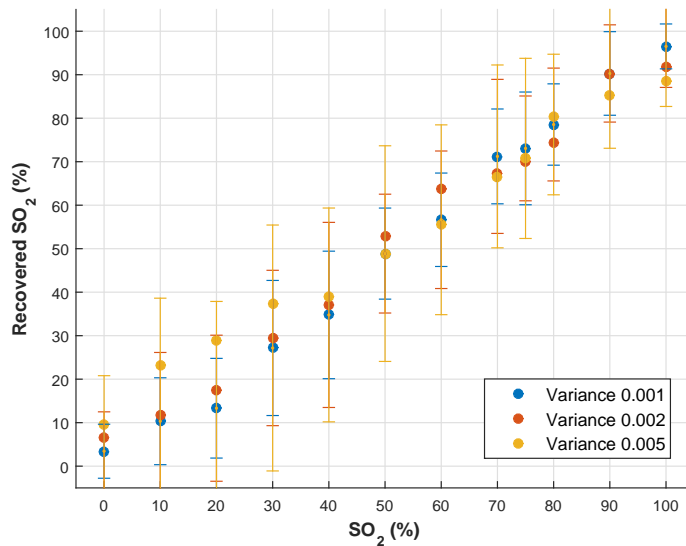


**Figure 2.14.** Recovered SO<sub>2</sub> for theoretical data at green-red wavelengths with additive Gaussian noise of increasing variance

### Waveband-specific contrast reduction

Finally, the assessment of SO<sub>2</sub> error related to waveband-specific errors in  $K$  was also performed for the green-red wavelength regime. For a given  $K = 0.3$  and SO<sub>2</sub> of 60%, figures 2.15 and 2.16 show the results of this investigation. As with the increased SO<sub>2</sub> error with additive noise, the error in SO<sub>2</sub> resulting from errors in  $K$  was also increased as compared to the blue regime. Specifically for wavebands

## 2. Development and characterisation of calibration-free oximetry algorithm

at 560 nm and 584 nm, at which an error in  $K$  of 50% results in retrieved  $\text{SO}_2$  of 100% and 0% respectively. The error in retrieved  $K$  is minimal, however as noted previously, this is of less importance than the  $\text{SO}_2$  parameter.

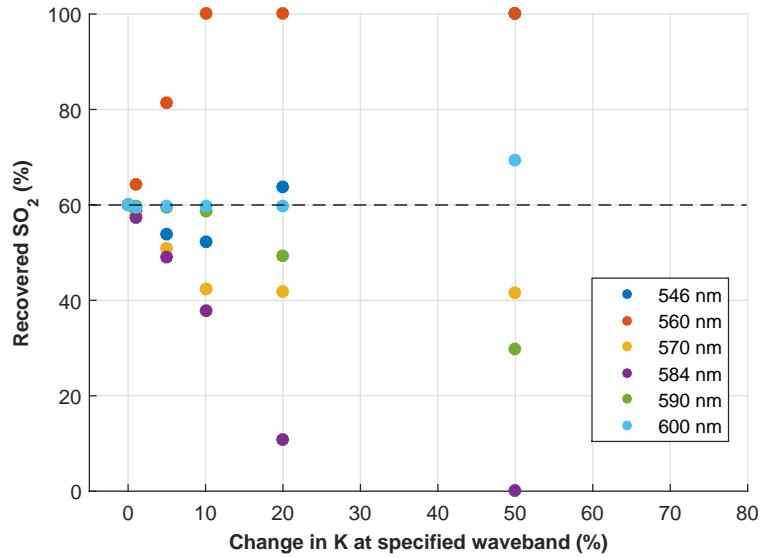


**Figure 2.15.** Recovered  $\text{SO}_2$  at green-red wavelengths with with waveband-specific contrast reduction

Table 2.2 displays the absolute extinction coefficients for both the blue and green-red wavelength regimes. It is clear that the values for  $|\varepsilon_{Hb} - \varepsilon_{HbO_2}|$  are much larger for the blue regime than for the green-red, which explains the increased error in  $\text{SO}_2$  arising from noise and contrast reduction at green-red wavelengths. These results suggest that the blue regime is preferable for oximetry, resulting in minimal  $\delta(\text{SO}_2)/\delta(T(\lambda))$  compared to the green-red regime. However, the high absolute values of the coefficients in the blue regime can result in total absorption of illumination for larger vessels (this is demonstrated experimentally later in figure 3.18). This means that for many applications beyond the microvasculature, the use of blue wavelengths is not feasible for vascular oximetry.

## 2. Development and characterisation of calibration-free oximetry algorithm

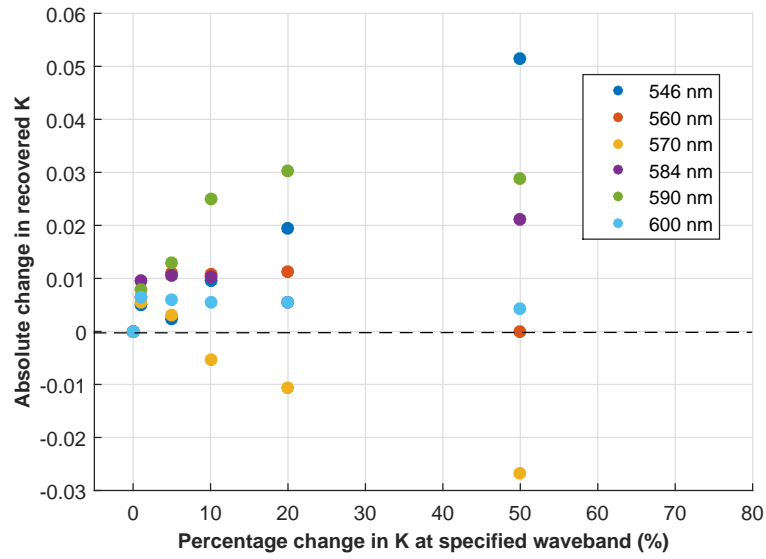


**Figure 2.16.** Change in recovered K at green-red wavelengths with waveband-specific change

**Table 2.2.** Values for extinction coefficients  $\epsilon_{Hb}$  and  $\epsilon_{HbO_2}$  ( $\text{cm}^{-1}\text{M}^{-1}$ ) for both blue and green-red wavelength regimes. Data from Prahl (1999) [53].

$\lambda$ (nm)	$\epsilon_{Hb}$	$\epsilon_{HbO_2}$	$ \epsilon_{Hb} - \epsilon_{HbO_2} $
410	303956	466840	162884
420	407560	480360	72800
430	528600	246072	282528
435	551552	145809	405743
440	413280	102580	310700
450	103292	62816	40476
546	51145	48527	2618
560	52893	33763	19130
570	45005	45164	159
584	33933	33977	44
590	27634	21940	5694
600	15421	3632	11789

### 2.9. Conclusions

In this chapter, an introduction to the oximetry algorithm employed in this thesis was described. By utilising models previously employed for retinal oximetry, consideration was given to adaptations for general microvascular oximetry in deep tissue. By considering the illumination configuration, a simplification of the optical model was derived by assuming single-pass absorption only. Chapter 3 will cover how this is achieved in an experimental setting. A simple factor accounting for reductions in contrast was introduced, allowing for correct  $SO_2$  to be achieved in the presence of additional optical scatter and loss. Further, whilst previous studies employed wavelength-dependent scatter coefficients only, the oxygen-saturation dependence of these coefficients was also introduced to the model.

An assessment of the associated errors was also discussed, in which different aspects contributing to oximetry error were introduced. Using theoretical, generated multispectral images, the performance of the algorithm was assessed. It is difficult to put a quantitative value on the absolute accuracy of the algorithm in all cases, as the oximetry error will depend on certain aspects such as contrast conditions and wavelengths utilised. However, taking all the above aspects and results into consideration, an error of approximately  $\pm 5\%$  in vessel  $SO_2$  seems reasonable. The issues related to experimental validation of the technique will be covered in chapter 3.

## 3. Multispectral imaging system for *in vivo* microcirculation oximetry

---

**Summary:** In this chapter, the development of the multispectral imaging system for oximetry is described. The choice of wavelengths and illumination source are detailed, as well as the objective lens and additional lenses and components. A preliminary assessment of image quality is first presented. This is followed by an *in vitro* validation using defibrinated whole horse blood. Finally, an *ex vivo* oximetry study of the microvasculature in an intact murine tendon is described.

### 3.1. Development of imaging setup

In the previous section, the data analysis algorithms developed for multispectral oximetry were introduced and described. In this section, the physical setup used to produce the multispectral data for analysis is described. Considerations such as required illumination specifications are discussed, as well as the software written in order to control multispectral image acquisition. Finally, *in vitro* and *ex vivo* experiments are presented, which were performed in order to demonstrate the capability of the imaging system to visualise the microvasculature, and to validate its sensitivity to oxygen saturation.

#### 3.1.1. Complete configuration for multispectral imaging

Before a detailed description of its constituent parts, the final configuration of the multispectral imaging system is shown in figure 3.1. In brief, the illumination was provided in the form of a collimated output from a supercontinuum laser source coupled to an AOTF. The illumination was propagated through a series of lenses, a speckle reducer and a beamsplitter before being delivered to the object by a reflective objective. The imaging light path travelled back towards the beamsplitter before being focused on a CCD by an imaging lens. A three-dimensional translation stage (MT3 XYZ Translation Stage, *Thorlabs*) was employed for correct placement of the object. The following sections describe each aspect of this microscope in detail. A photo of the assembled imaging system is presented in figure 3.2.

#### 3.1.2. Illumination

The primary consideration for the choice of illumination was the wavelengths which would be employed for multispectral imaging. As discussed in chapter 2, for the small capillaries of the microvasculature, the high extinction coefficients associated with visible blue wavelengths are necessary such that enough photons are absorbed across the vessel diameter to produce good contrast. The error arising from too high or too low an optical transmission was described in section 2.7.1. Previous retinal oximetry studies have predominantly employed wavelengths typically in the green and red region of the EM spectrum. For example, for various two-wavelength oximetry applications, Beach et al. (1999) employed 600 nm and 569 nm [75]; Hammer et al. (2008) utilised 610 nm and 548 nm [76]; and Choudhary et al. (2013) used 566 nm and 599 nm [81]. These studies were applied to oximetry of vessels approximately 100  $\mu\text{m}$  in diameter. For imaging of the microvasculature, blue wavelengths were selected: 410 nm, 420 nm, 430 nm, 435 nm,

### 3. Multispectral imaging system for *in vivo* microcirculation oximetry

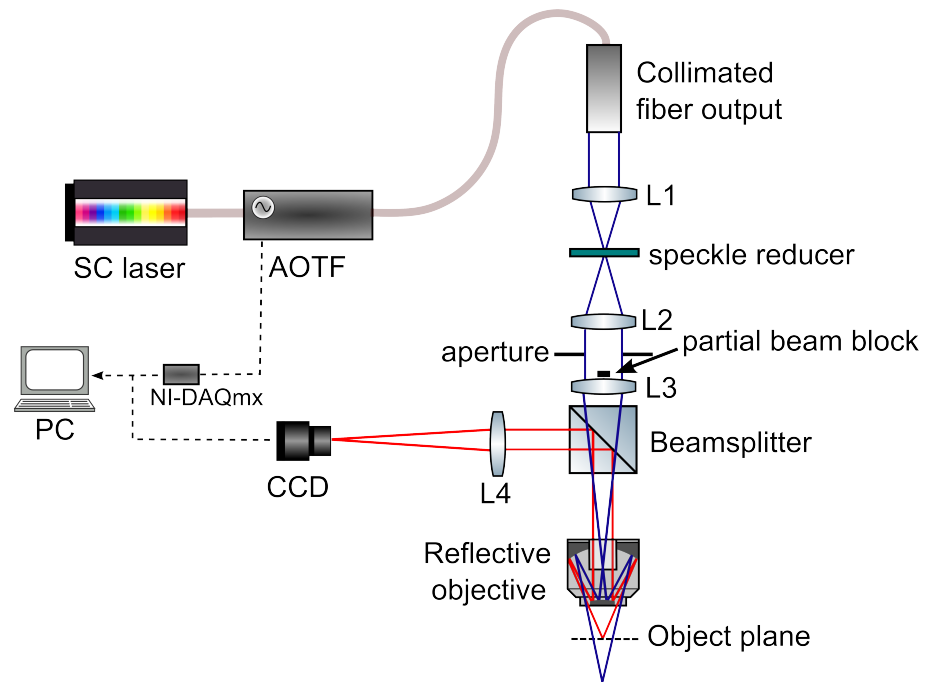


**Figure 3.1.** Diagram of multispectral imaging system for oximetry. Illumination path is shown in blue, and imaging path in red. Image acquisition and AOTF switching controlled with data acquisition toolbox (NI-DAQmx) and custom Labview interface. SC = supercontinuum; AOTF = acousto-optic tuneable filter; L1,L2,L3 = lenses 1, 2, 3 respectively; L4 = imaging lens.

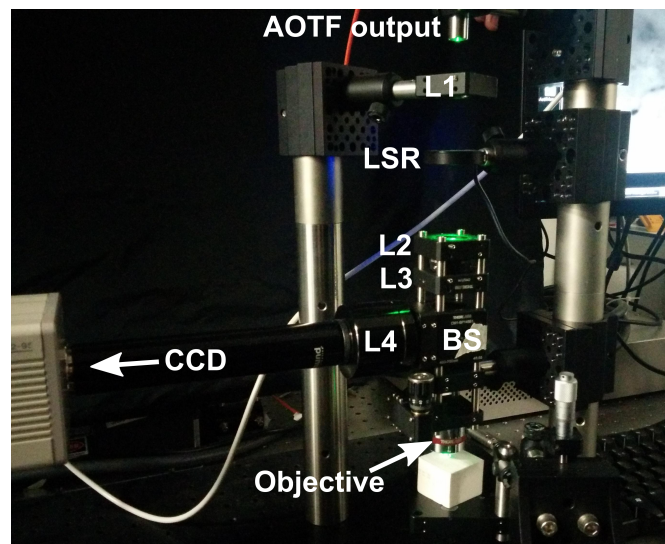


**Figure 3.2.** Photo of multispectral imaging system for oximetry. L1,L2,L3 = lenses 1, 2, 3 respectively; L4 = imaging lens; LSR = laser speckle reducer; BS = beamsplitter.

### 3. Multispectral imaging system for *in vivo* microcirculation oximetry

440 nm and 450 nm. Of these wavelengths, 420 nm is isosbestic; the rest provide sensitivity to  $\text{SO}_2$ .

In figure 3.3, theoretical transmission profiles are shown for a 10  $\mu\text{m}$  blood vessel. It is noted that for increasing  $\text{SO}_2$ , the transmission profiles over these six blue wavebands are distinct. Also, the transmission values for each waveband reside within the recommended transmission values for minimal photometric error ( $10\% \leq T \leq 70\%$ , as described in section 2.7.1).

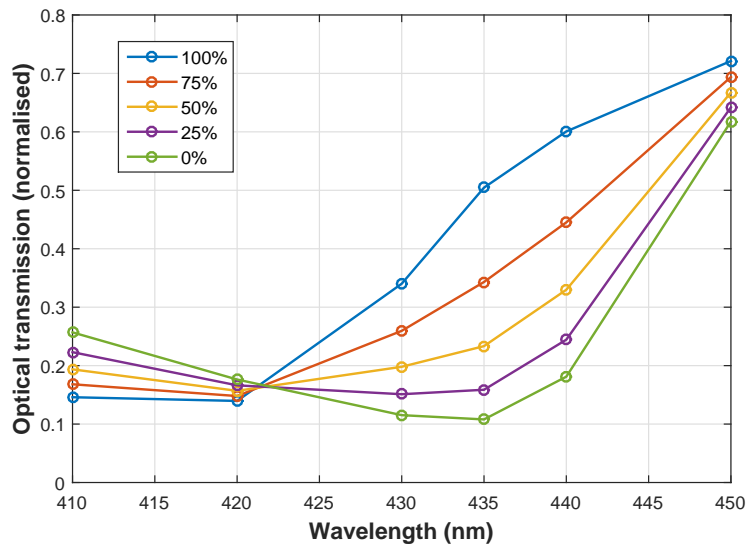


**Figure 3.3.** Transmission profiles of theoretical blood vessel of 10  $\mu\text{m}$  diameter at blue wavelengths.

Once the required wavelengths had been established, it was necessary to choose an appropriate light source to deliver such multispectral illumination. In chapter 1, the theory behind the AOTF was briefly described. Any white light source, such as a broadband LED, may be used in conjunction with an LCTF/AOTF for spectral filtering. However, it is necessary that there is sufficient intensity to begin with, specifically in the wavelength region of interest. It was necessary to choose a light source with sufficient intensity within the range of 410 nm to 450 nm, which closely borders the UV region of the EM spectrum.

For the purposes of this thesis, a supercontinuum white light source was used

### 3. Multispectral imaging system for *in vivo* microcirculation oximetry

---

(WhiteLase SC400-4, Fianium). A supercontinuum operates by taking the output of a pump laser, and propagating it through a nonlinear material such as photonic crystal fibre. This laser light undergoes spectral broadening through the medium as a result of nonlinear processes, resulting in a highly intense output which is spread over a broad wavelength range, with nominal output power of 4 W. The output is a collimated, unpolarised beam of  $\sim 2$  mm diameter. The supercontinuum is designated as a Class IV laser source, however coupled to an AOTF it is effectively class IIIb. Due to the fact that the total optical power is distributed across the optical spectrum, the power spectral density (PSD) of an illumination system refers to the optical power over a particular frequency or wavelength interval. The average PSD for the supercontinuum and AOTF over its entire wavelength range is 2 mW/nm. Before using for imaging spectrometry, it was important to confirm the correct spectral output of the supercontinuum-AOTF system. This was performed using a calibrated spectrometer (HR4000CG-UV-NIR, OceanOptics). The AOTF (Gooch & Housego) was supplied with calibration coefficients for the AOTF crystal, which relate input RF frequency to required output wavelength. Upon investigation, the original calibration appeared only to be valid for wavelengths approximately 450 nm upwards. For wavelengths  $< 450$  nm, there was an observable offset which increased with decreasing wavelength. In order to correct for this offset, the nominal wavelength (input to the AOTF GUI) which resulted in the correct, desired wavelength was determined for all six blue wavelengths to be used for multispectral imaging. In this manner, the correct spectra for the blue wavelengths could be obtained (e.g. for achieving 410 nm, a value of 405.5 nm was input into the GUI). The original and corrected wavebands are depicted in figure 3.4. In this figure, the output intensities of each individual waveband were normalised such that the peak intensity was unity. However, it is the case that transmitted optical intensity through the AOTF decreases with wavelength. For this reason, image exposures for longer wavelengths were generally shorter than for the shorter wavelengths.

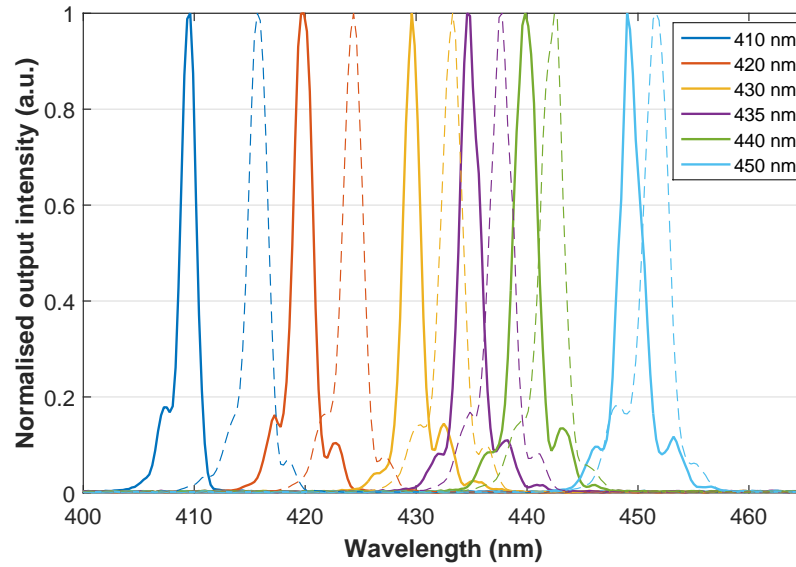


**Figure 3.4.** Corrected AOTF outputs for six blue wavebands, as measured by a spectrometer. The uncorrected wavebands originally output for the nominal wavelengths shown as dashed lines.

The supercontinuum and AOTF combination is a highly versatile illumination source for multispectral imaging. However, the user of laser light for microscopy purposes can have implications in terms of image quality. As the illumination is spatially coherent, laser speckle at the image plane is often observed. Laser speckle is a phenomenon due to the local constructive and destructive interference of light with itself, occurring when coherent light is incident on a “rough” surface [148]. Techniques such as rotating ground glass diffusers in the beam path can be used to minimise laser speckle by reducing beam coherence, however due to their thickness can introduce a large degree of scatter and divergence to the beam path. It was decided to use a “laser speckle reducer” (LSR 3005, *Optotune*), which dynamically diffuses the illumination. It consists of a narrow diffuser (330  $\mu\text{m}$ ) bonded to a thin elastic membrane; four independent electrodes then induce a circular oscillation of the diffuser in  $x$  and  $y$ . The LSR has the same decohering effect as a rotating diffuser however introduces a smaller degree of beam divergence ( $6^\circ$ ) than typical glass diffusers. This meant that it could be implemented at the focal spot of a “ $4f$ ” lens system as shown in figure 3.1. The

effect of using the LSR on image quality is demonstrated in figure 3.5.

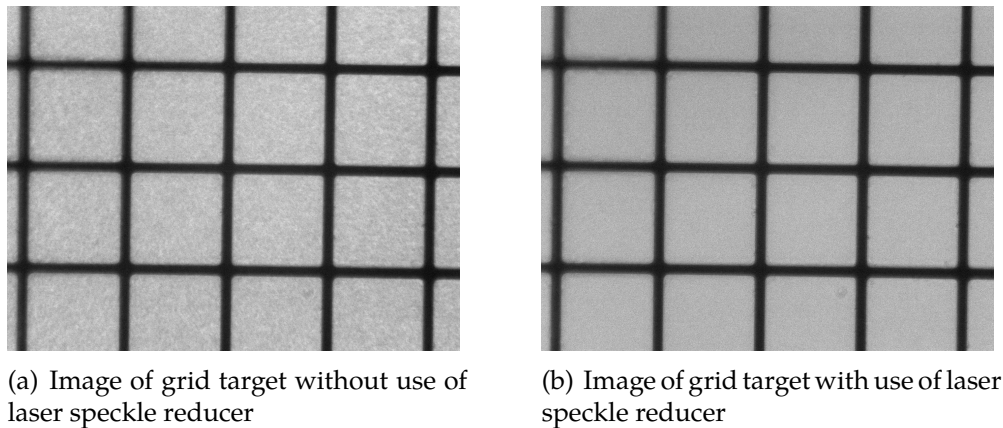


**Figure 3.5.** Comparison of image of grid target, obtained with and without the laser speckle reducer (Optotune LSR). While speckle is not entirely eliminated, there is clearly a marked improvement in image quality.

#### 3.1.3. Reflective objective

As described in chapter 1, multispectral imaging involves the acquisition of a range of images acquired at different wavebands. This can result in axial chromatic aberration over the spectral datacube, with images at certain wavebands being acquired slightly out of focus, depending on the range of wavelengths employed. In the interests of minimising chromatic aberration over the multispectral imaging system, it was decided to use a 40X reflective objective (LMM-40X-UVV, *Thorlabs*) with a numerical aperture (NA) of 0.5 and working distance of 7.8 mm. These objectives consist of two spherical mirrors, and unlike conventional objective lenses, introduce virtually no chromatic aberration [149]. Further, third order spherical aberration, coma and astigmatism can be eliminated if the two mirrors are concentric, and if the distance separating them is twice that of the objective focal length [150]. This configuration is depicted in figure 3.6.

Whilst using a reflective objective for imaging presents many advantages, there are also implications associated with its use. The smaller, primary mirror re-

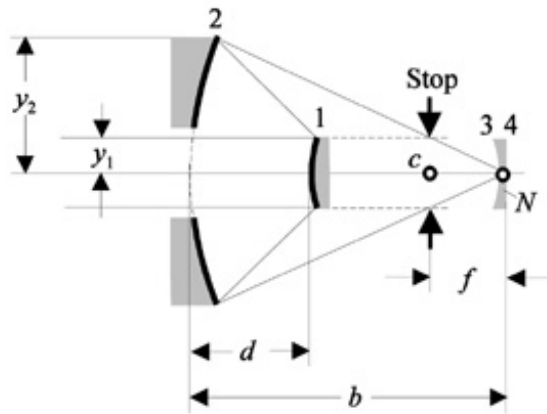
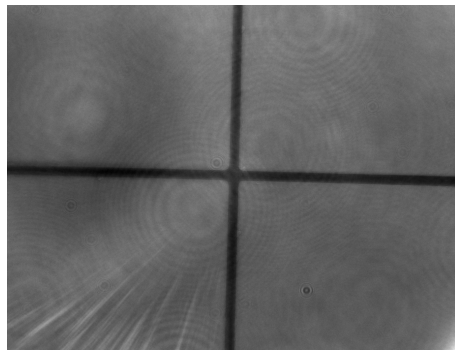


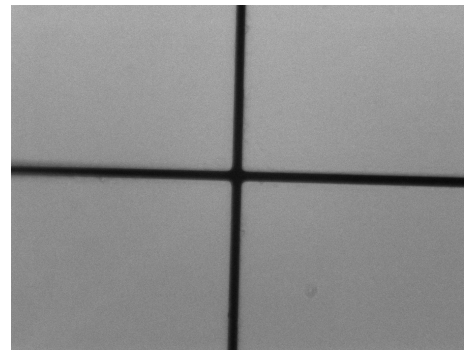
**Figure 3.6.** Configuration of two spherical mirrors for reflective objective.  $f$ : focal length,  $d$ : mirror separation,  $c$ : centre of curvature,  $y_1$  and  $y_2$ : semi-diameters of mirrors 1 and 2 respectively (from [150]).

sults in a central obscuration, resulting in a loss of throughput and a degradation of mid-frequencies of the modulation transfer function (MTF) (discussed in section 3.1.3). An additional issue was found to arise by using the reflective objective with an “epi-illumination” configuration, as with the setup shown in figure 3.1, where the illumination and imaging paths are coincident. As evident from figure 3.6, illumination rays impinging on the primary mirror are transferred to the secondary mirror before coming to a focus at the focal plane. However, a small portion of these rays at the centre of the reflective objective are reflected directly back towards to the beamsplitter and CCD, where they interfere with the imaging path. A consequence of this is severe degradation of image contrast and the presence of interference rings, as shown in figure 3.7(a).

In order to circumvent this issue, a partial beam block was placed in the illumination path. The beam block removed only the central portion of rays from the illumination, which resulted in a marked improvement of image quality and the removal of interference effects, depicted in figure 3.7(b).



(a) Image of grid target without beam block



(b) Image of grid target with beam block

**Figure 3.7.** Comparison of images of grid target, obtained with and without the beam block. Note the low contrast and interference rings visible in image (a) due to central reflection from primary mirror.

#### Assessment of MTF

It was desired to assess the implications of using the specific reflective objective lens that was chosen for this imaging system. The optical transfer function (OTF) of an optical imaging system,  $H(\nu, \eta)$ , is a complex function which describes the system's impulse response in the frequency domain; where  $\nu$  and  $\eta$  are the two-dimensional spatial frequency components respectively [121]. In real space, an image  $g(x,y)$  of an object  $f(x,y)$  is related by the convolution of the object by its impulse response  $h(x,y)$ . A convolution in the spatial domain is equivalent to multiplication in the Fourier domain, and this is represented as

$$G(\nu, \eta) = F(\nu, \eta) \times H(\nu, \eta) \quad (3.1)$$

where  $F$  denotes the object spectrum, and  $G$  denotes the image spectrum. By convention, it is assumed that the OTF is normalised to have a value of unity at zero spatial frequency. The modulation transfer function (MTF) of an imaging system describes the magnitude of the OTF (where  $\text{MTF} = |H(\nu, \eta)|$ ), and describes relative transmittance of image modulation (contrast) as a function of spatial

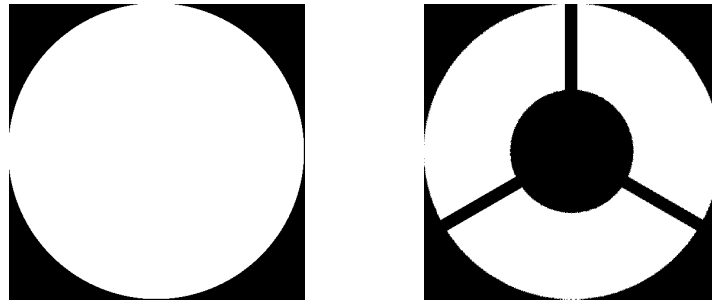
### 3. Multispectral imaging system for *in vivo* microcirculation oximetry

---

frequency  $\nu$ ;

$$\text{MTF}(\nu) = \frac{M_{\text{image}}(\nu)}{M_{\text{object}}} \quad (3.2)$$

It is known that obscuration of the exit pupil, as occurs with use of a reflective objective, can adversely affect the MTF of an imaging system [149]. The diffraction-limited MTF of an optical imaging system is defined as the autocorrelation of the exit pupil of the system [151]. The reflective objective has a nominal obscuration of 22%, including the spokes which hold the primary mirror in place. Its pupil transmission function was simulated in MATLAB, as shown in figure 3.8. An ideal, circular transmission pupil is also shown for comparison.



(a) Ideal pupil transmission function (b) Pupil transmission function with 22% obscuration

**Figure 3.8.** Simulated transmission pupils for ideal and obscured reflective objective lens

The theoretical MTF of the imaging system was determined by performing the autocorrelation of each of the transmission pupils. This gives the two dimensional MTF, from which a one-dimensional profile was taken and plotted in figure 3.9. The maximum “cut-off” frequency  $\nu_{\text{cut-off}}$  described will be, for a diffraction-limited case:

$$\nu_{\text{cut-off}} = \frac{2\text{NA}}{\lambda} \quad (3.3)$$

For an imaging system with NA 0.5 and  $\lambda = 450 \text{ nm}$ , this corresponds to a cutoff frequency of  $\sim 2.38 \mu\text{m}^{-1}$ . The simulated MTF from the obscured pupil must be normalised with respect to the maximum relative pupil transmission (0.78 in the

### 3. Multispectral imaging system for *in vivo* microcirculation oximetry

---

case of 22% obscuration). If this normalisation is not performed, the MTF at the higher spatial frequencies appear to exceed those for the ideal case, seemingly breaking the diffraction limit. In reality this is clearly impossible, and there is a physical reduction in light throughput as a result of the obscuration [149]. Regarding the oximetry algorithm, the contrast reduction factor  $K$  can be used to compensate for loss of contrast introduced by the imaging system itself, so it is expected that it should compensate for this zero-frequency reduction in MTF associated with use of the reflective objective. It is important to note that these simulated MTFs are for an ideal case with no additional aberrations. The real MTF of the imaging system was measured and is described in section 3.3.

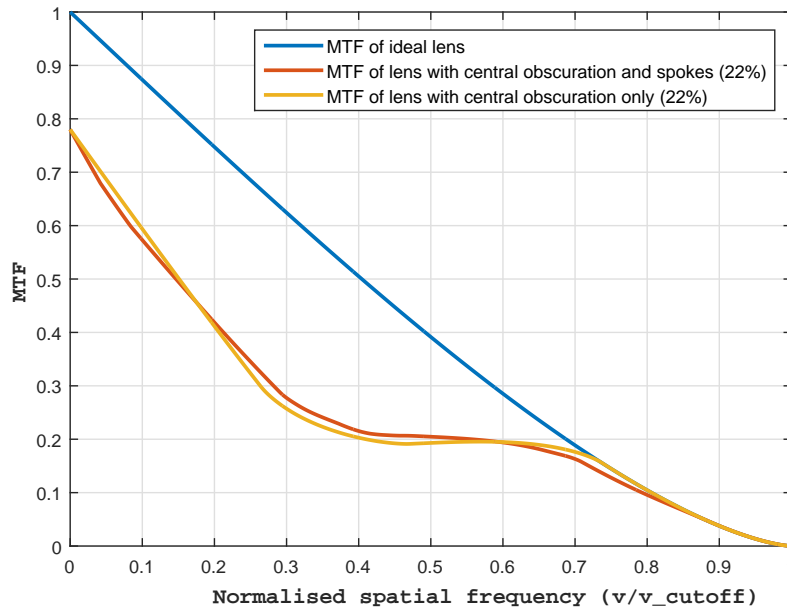


**Figure 3.9.** Simulated modulation transfer functions for ideal and obscured transmission pupils, indicating a reduction in the MTF for low and mid spatial frequencies in the obscured case

#### Annular illumination

As described in the previous chapter, simplification of the oximetry algorithm is possible if the light paths of the illumination are carefully considered. Single-pass

### 3. Multispectral imaging system for *in vivo* microcirculation oximetry

---

illumination of blood vessels through adjacent tissue can be assumed to occur if the adjacent tissue is illuminated in an annulus type pattern. Multiple scattering of diffuse light can propagate through tissue, effectively back-illuminating the microvasculature. In this case, back-reflected light from the blood vessels is also eliminated, further reducing the number of variables to be considered by the algorithm. In this section, the setup of an annular illumination pattern around the field of view is described. The use of the reflective objective has already been introduced as a means for multispectral imaging with minimal chromatic aberration. However, the reflective objective may also be utilised in order to generate the desired annulus at the focal plane of the imaging system. When collimated light is incident on the back-aperture of a Schwarzschild-type reflective objective, a focused spot is formed at the focal plane of the objective; as with any standard objective lens. If the illumination focus is offset from the focal plane, the defocused spot is approximately annular in shape, as a result of obscuration of light by the smaller primary mirror. The illumination focus can be offset by propagating a diverging beam through the back aperture of the objective, for example, as opposed to a collimated beam.

It was desired to model this setup in ray-tracing software (Zemax OpticStudio) in order to validate the concept. It was first necessary to know the parameters of the mirrors within the reflective objective, such as the radii of curvature of the two mirrors and the distance between them. For a reflective objective lens, third order spherical aberration, coma and astigmatism are eliminated if the two mirrors are concentric, and if the distance separating them is twice the objective focal length:  $d = 2f$  [150]. For purposes of optical modelling of the LMM-40X-UVV objective with a nominal 5 mm focal length, the two mirrors are separated by  $d = 2(5 \text{ mm}) = 10 \text{ mm}$ . We also have the following relations:

$$\begin{aligned} R1 &= (\sqrt{5} - 1)f \\ R2 &= (\sqrt{5} + 1)f \end{aligned} \tag{3.4}$$

### 3. Multispectral imaging system for *in vivo* microcirculation oximetry

---

where  $R_1$  and  $R_2$  are the radii of curvature of the primary and secondary mirrors respectively, determined to be 6.18 mm and 16.18 mm. Finally we have that the distance  $b$  between the secondary mirror and the focal plane is given by the following expression:

$$b = (\sqrt{5} + 2)f \quad (3.5)$$

such that  $b = 21.18$  mm. Using the above parameters, an optical model was assembled in Zemax. Zemax is a commonly used optical design software, which primarily uses ray tracing for modelling, design and analysis of illumination and imaging systems. The insertion of a planoconvex lens (focal length = 85 mm) was added to the model in order to offset the illumination focus as described above. The position of this lens with respect to the objective determines the size of the resulting annulus. A ray-trace of this setup is given in figure 3.10.

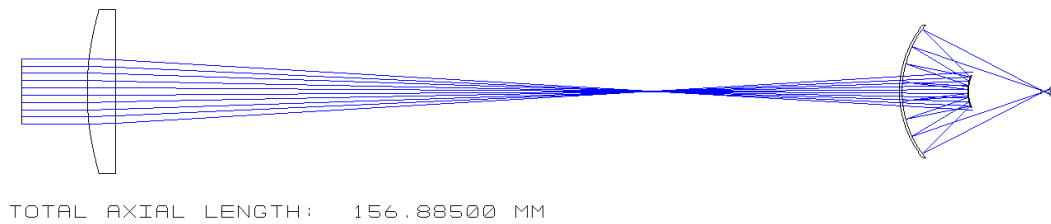


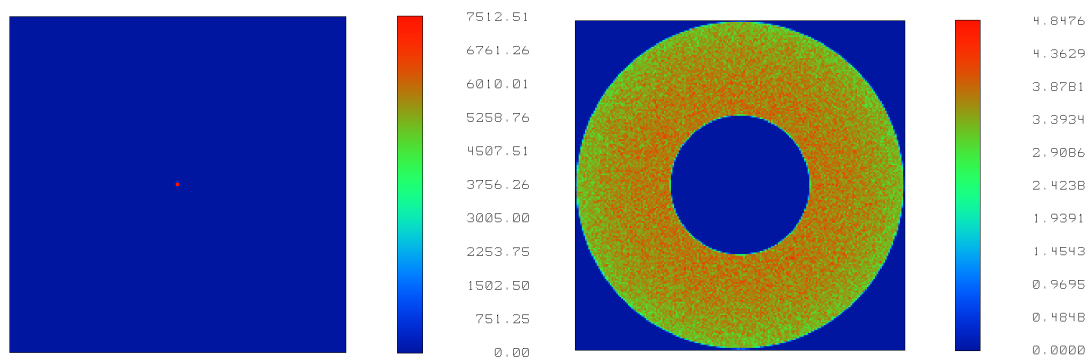
**Figure 3.10.** Zemax model depicting the setup for generation of annular illumination. A planoconvex lens of focal length 85 mm was used to offset the focus of the illumination from the focal plane of the objective.

Using the above model, simulated Zemax images were produced and these are given in figure 3.11. These are images of the illumination, with a detector placed precisely at the focal plane position. Figure 3.11(a) depicts the focal spot which would occur without the planoconvex lens. With the lens, annular illumination was generated as expected as shown in 3.11(b). The axial position of the planoconvex lens was optimised such that the inner diameter of the annulus was  $240 \mu\text{m}$ , just larger than the field of view of the imaging system. In this way, no direct illumination would be imaged, whilst the amount of light diffusing from nearby tissue would be maximised. The axial position determined from the model was

### 3. Multispectral imaging system for *in vivo* microcirculation oximetry

---

used to guide the physical setup of the imaging system.



(a) Focused spot at focal plane with collimated input (b) Annulus at focal plane with divergent input

**Figure 3.11.** Simulated Zemax images of focal plane ( $500\ \mu\text{m} \times 500\ \mu\text{m}$ , arbitrary intensity units).

### 3.2. Graphical user interface for multispectral data acquisition

As part of this thesis, custom software including a graphical user interface was designed and produced for multispectral data acquisition. This was achieved using LabVIEW 2014 SP1 (*National Instruments*). The main purposes of the code were as follows: to produce a live preview of the field of view; allow the user to switch on and off any multispectral wavebands as required; acquire a multispectral dataset with exposure times at each waveband defined by the user; and exportation of the individual images.

By default, the AOTF is controlled by a proprietary GUI, facilitated by a USB connection to the PC, allowing the user to select up to 8 waveband channels simultaneously. A screenshot of this GUI is presented in figure 3.12. In order to control the AOTF with LabVIEW, it was necessary that the AOTF was configured for external modulation. External modulation allows the AOTF to be modulated at  $1.24\ \mu\text{s}$ , much higher than speeds obtainable using the standard USB interface. External modulation was also necessary in order to incorporate AOTF control into

### 3. Multispectral imaging system for *in vivo* microcirculation oximetry

the multispectral imaging GUI. For future reference, the method for achieving this is presented here. A 40-way “MDR” plug, connected to the AOTF driver, was used to feed an analogue voltage signal across pins corresponding to individual AOTF channels, by means of the NI-DAQmx. This was facilitated by manually soldering connections according to the layout depicted in figure 3.12. The desired wavebands for all channels was first selected with the standard GUI, and switched on. The following command was then input into the AOTF console:

DAU DIS

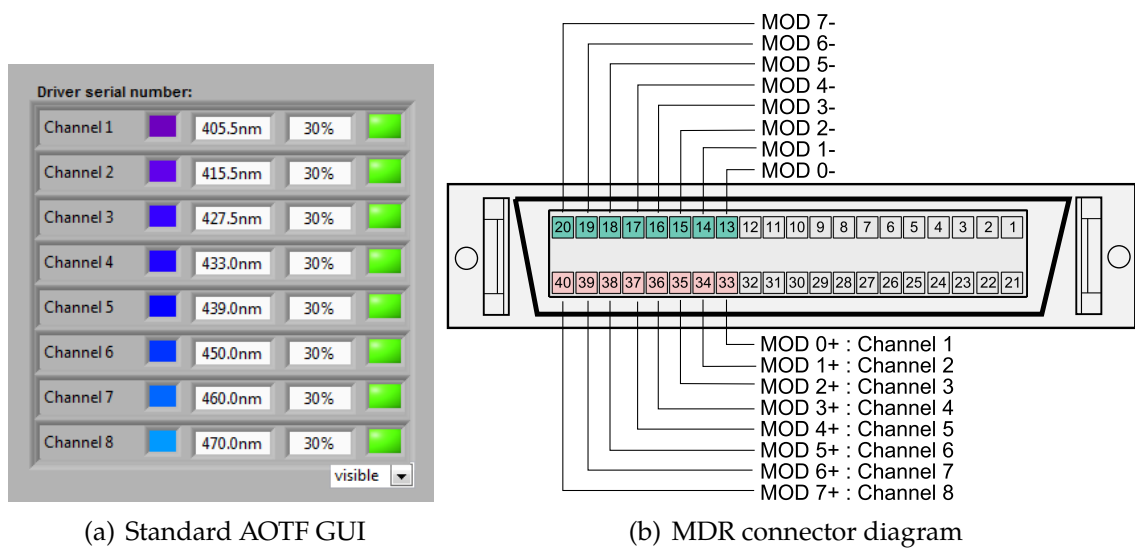


**Figure 3.12.** Illustration of the standard AOTF GUI, and the pin layout for the AOTF MDR connector with corresponding channels detailed.

The command disables the daughter card, at which point the RF power on each AOTF channel is controlled by the voltage applied across the corresponding pins on the MDR connector. The RF drive power (30% by default which corresponds to maximum efficiency) is then controlled by the voltage supplied across the pins. By default, the AOTF driver is analogue, and operates on a 0 to 10 V scale. As the NI-DAQmx supplies a voltage of +5 V, the driver gain must be set for this particular modulation scheme such that the RF drive power remains optimal. According to the *Fianium* AOTF manual, for modulation 0 - 5 V, the following

### 3. Multispectral imaging system for *in vivo* microcirculation oximetry

---

command should be used:

```
DAUGHTER GAIN * 72
```

Once this setup and control process was performed, it was possible to fully control the AOTF within LabVIEW, allowing the software to sequentially switch on and off wavebands as required during multispectral acquisition. For image preview and acquisition, a monochrome, cooled CCD detector was used (C4742-96-12G04, Hamamatsu). "DCAM" drivers were installed in order that LabVIEW could communicate with the CCD (by means of IEEE1394 FireWire interface). The appropriate sub-VIs for specific commands (e.g. camera initialisation, live image preview, image capture) were provided by Hamamatsu and incorporated into the multispectral system GUI. A simplified flow chart of the basic software logic employed to acquire the multispectral datasets is shown in figure 3.13. The basic concept of the acquisition was that an image was acquired of the scene at each specified waveband, ensuring that only the correct waveband was turned on and being transmitted for the appropriate image capture. Options were implemented into the software to allow the user to easily change the exposure time for each individual waveband, or to change the number of multispectral sequences that were captured for each acquisition.

#### 3.3. Assessment of image quality

Once the imaging system and associated software had been developed, it was desired to validate image quality. Preliminary imaging was performed with the assembled system in order to confirm the contrast, resolution and MTF of the microscope. The theoretical resolution  $R$  may be defined by the Abbe criterion, where:

$$R = \frac{\lambda}{2(\text{NA})}. \quad (3.6)$$

### 3. Multispectral imaging system for *in vivo* microcirculation oximetry

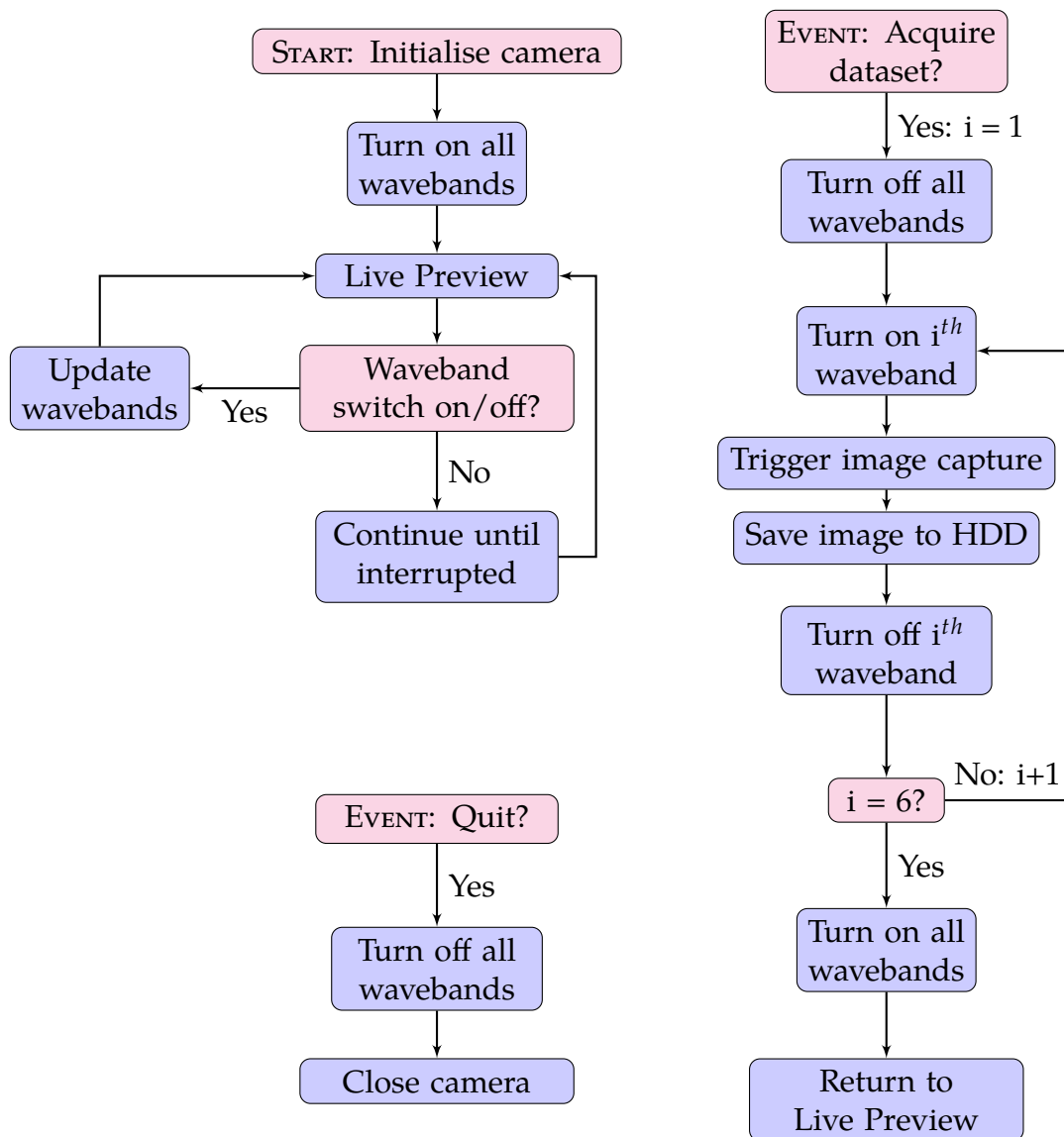


**Figure 3.13.** Simplified software flow chart for multispectral image acquisition in LabVIEW (6 waveband dataset)

### 3. Multispectral imaging system for *in vivo* microcirculation oximetry

---

For  $\lambda = 530 \text{ nm}$  and  $\text{NA} = 0.5$ , a diffraction-limited resolution of  $R = 0.53 \text{ }\mu\text{m}$ . The pixel size of the Hamamatsu detector was  $6.45 \text{ }\mu\text{m} \times 6.45 \text{ }\mu\text{m}$ . Considering that the magnification of the imaging system was 40X, the size of a diffraction-limited spot on the detector would be  $21.2 \text{ }\mu\text{m}$  in diameter. Nyquist's sampling theorem requires that to adequately sample a spatial frequency, the detector pixel size be less than half the size the smallest resolvable feature. At a diameter of  $21.2 \text{ }\mu\text{m}$ , the diffraction-limited spot is over three times the pixel size, and so the imaging system met this Nyquist sampling rate.

An image was acquired of a high resolution sample target (USAF 1951) in order to empirically quantify microscope resolution. With these targets, three parallel lines of decreasing size are assigned into groups and elements. For quantification of resolution, the smallest resolvable element is identified, and a look-up table of that specific group and element gives the width of the constituent lines. The resolution is defined as twice this width. The results of this test are shown in figure 3.14, in which the entire field of view is shown, as is a magnified image of the smallest groups. The smallest resolvable element was defined as that in which three distinguishable "dips" were still observable in a line profile. This element was established to be Group 10, Element 5. The width of each line in this element was  $0.308 \text{ }\mu\text{m}$ , leading to an empirically defined resolution of  $2(0.308 \text{ }\mu\text{m}) = 0.616 \text{ }\mu\text{m}$ . This was in good agreement with the previously defined diffraction-limited resolution. The presence of minor aberrations result in an empirical resolution which is slightly less than diffraction-limited.

For an image of a knife-edge acquired at  $450 \text{ nm}$ , the contrast modulation  $C_m$  was determined, where  $C_m = (I_H - I_L)/(I_H + I_L)$ ;  $I_H$  and  $I_L$  being high and low reference intensities respectively. "Perfect" contrast is defined as  $C_m = 1$  and total lack of contrast as  $C_m = 0$ . This is possible by first imaging a knife-edge target, in which there is a transition from "black" to "white" - e.g. from lowest to highest signal. Following subtraction of background image intensity, the average values on either side of the knife-edge give  $I_H$  and  $I_L$  respectively.

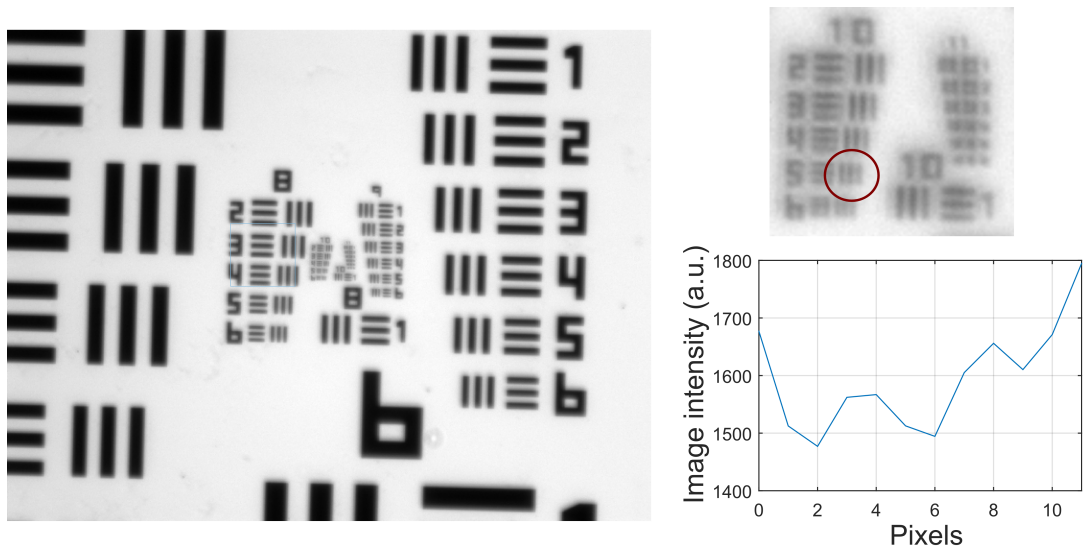


**Figure 3.14.** Resolution test of imaging system (USAF 1951 target). The image on the left is the entire field of view. The top right image shows the smallest groups, with the smallest resolvable element (Group 10 Element 5) highlighted. The corresponding line profile is displayed on the bottom right.

For the case of this imaging system, the contrast modulation was measured to be approximately 0.9. For a quantitative analysis of contrast modulation with spatial frequency, the modulation transfer function of the imaging system was also empirically determined. The intensity profile across the knife-edge is known as the edge spread function (ESF) of an imaging system; and its mathematical differentiation results in the line-spread function (LSF). It is the case then that the Fourier transform of the LSF yields a 1-dimensional MTF profile in  $x$ :

$$\mathfrak{F}\{\text{LSF}(x)\} = \text{MTF}(\nu, 0) \quad (3.7)$$

It was decided to perform this assessment at three distinct wavebands in the blue regime, to ascertain whether the MTF was influenced by wavelength. Figure 3.15 shows the edge spread function of the imaging system at 420 nm, 420 nm and 435 nm. The raw data is shown, as is a sigmoidal fit to the data which was used to then differentiate to generate the LSF. Due to noise in the signal across an individual line profile, differentiation of the raw data itself resulted in noisy LSFs,

supporting the use of the sigmoidal fit instead.

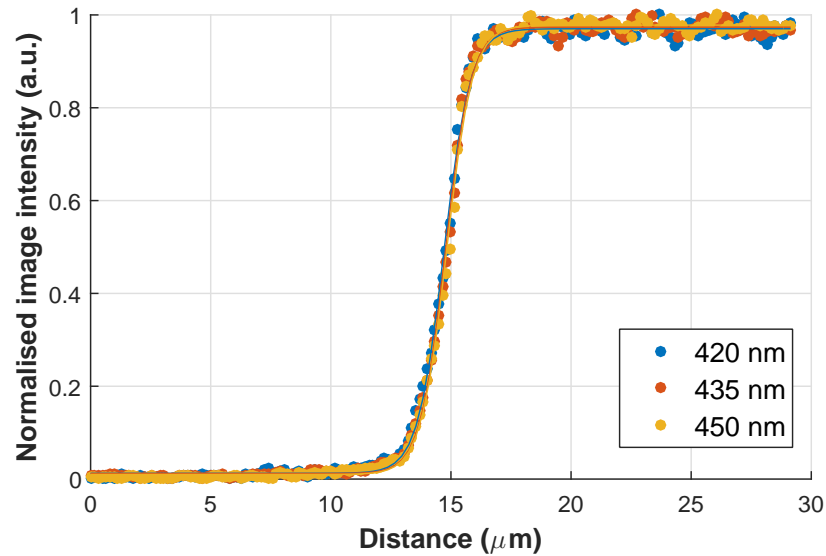


**Figure 3.15.** Edge spread function of imaging system, acquired by taking a profile across a knife-edge at 420 nm, 420 nm and 435 nm, with raw data and sigmoidal fits displayed.

The resulting MTFs are shown in figure 3.16, acquired by taking the Fourier transform of the LSF data. As evident from the figure, the experimentally determined cut-off frequency from the data is approximately  $1.2 \mu\text{m}^{-1}$ , which is less than the diffraction-limited theoretical case discussed previously, as expected. It is important to note that the contrast and MTF does not vary appreciably with wavelength. Regarding the oximetry algorithm, this result supports the argument for assigning the contrast reduction factor,  $K$ , as a constant independent of wavelength.

### 3.4. *In vitro* validation

#### Optical phantom for oximetry of vasculature

Before imaging the microvasculature *in vivo* or *ex vivo*, it was necessary to validate the sensitivity of the imaging system and oximetry algorithm to changes in oxygen saturation using real data. In order to perform oximetry *in vitro*, plastic tubes made

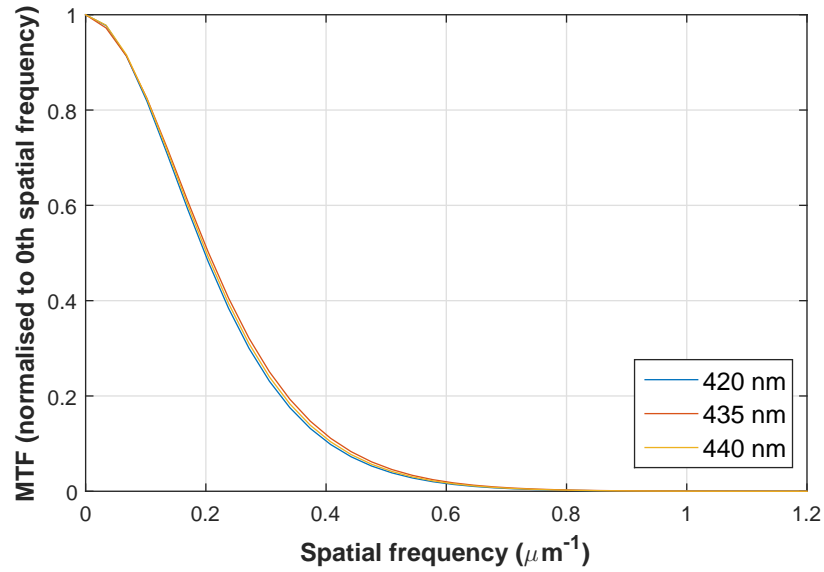


**Figure 3.16.** Modulation transfer system of imaging system, acquired by taking the Fourier transform of the LSF at 420 nm, 420 nm and 435 nm.

of “fluorinated ethylene propylene” (FEP) were chosen in order to simulate the blood vessel. FEP is useful in optical experiments owing to its transparency. It has refractive index 1.34, particularly close to that of water or saline, which is useful for index-matching. The FEP tubes chosen for the initial validation were the smallest available at an inner diameter of 50  $\mu\text{m}$ .

For all *in vitro* experiments, the FEP tubing is filled with “defibrinated” whole horse blood (*E&O Laboratories, UK*). This blood has had the fibrin removed; fibrin typically aids the clotting process and so defibrinated blood is necessary in experiments *in vitro* in order to ensure it does not coagulate. The blood is inserted into the tubing using a 1 mL syringe and ‘Luer-Lok’ ferrule connections, specific to the diameter of tubing being used.

In order to create a complete phantom of a blood vessel in the tendon, the filled FEP tubing was placed on a background of Spectralon (*Labsphere Inc., USA*), which is diffuse white reflective material and commonly used in optical phantoms [152]. It possesses uniform spectral reflectance across visible wavelengths. The opti-

### 3. Multispectral imaging system for *in vivo* microcirculation oximetry

cal properties of tendon tissue do not appear to have been characterised in the literature, however for the purposes of validation, Spectralon is assumed to be approximately similar. The albedo of Spectralon however will be much higher than real tissue, with a nominal reflectance of 99%. However, due to the ratio-metric nature in which optical transmission is estimated, this is not expected to affect the oximetry. Finally, the tubing is covered with a small amount of phosphate buffered saline (PBS) in order that the wall of the FEP is approximately index-matched to the background. An illustrative diagram of the simple vascular phantom of blood-filled FEP tubing on Spectralon is shown in figure 3.17(a). An example image of the phantom is shown in figure 3.17(b).

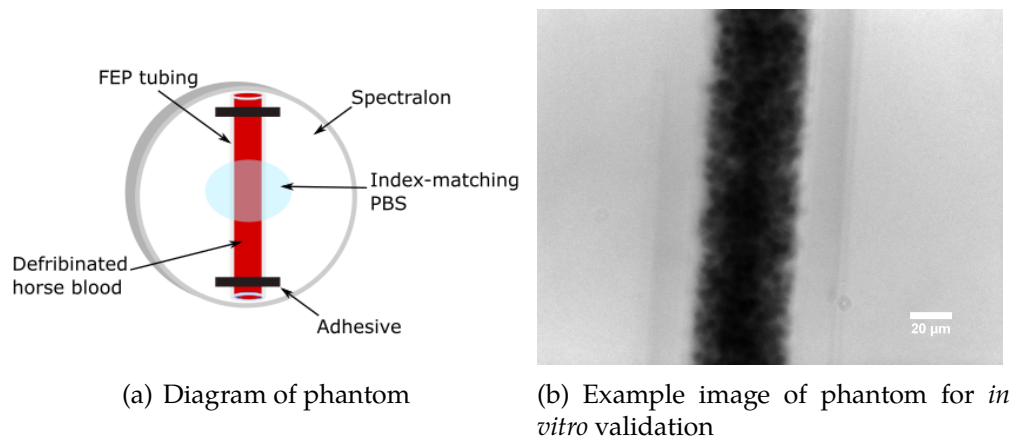


**Figure 3.17.** Illustrative diagram and example image acquired at 560 nm of optical vessel phantom consisting of 50 µm FEP tubing filled with defibrinated horse blood on Spectralon background.

#### Method

For validation of 100% oxygenation, the blood may be inserted into the tubing directly, as it is naturally oxygenated. For imaging of lower oxygenations, addition of a compound known as sodium dithionite is required. Sodium dithionite dissociates the oxygen from haemoglobin, and quickly de-oxygenates blood with which it comes into contact. For all validation experiments, the levels of sodium

### 3. Multispectral imaging system for *in vivo* microcirculation oximetry

---

dithionite added to volumes of whole horse blood were as described in Briley-Saebø & Bjørnerud (2000) [153]. A waiting period of 30 minutes was required after addition of sodium dithionite, to ensure that  $\text{SO}_2$  within the volume had reached equilibrium. Additionally, in order to ensure that the correct oxygen saturation had been achieved, the blood was checked with a clinical blood gas analyser (BGA) prior to insertion into the FEP tubing.

As the blue wavelength regime (410 nm to 450 nm) was to be predominantly used for experimental oximetry of the microvasculature, it was initially decided to perform the validation experiments with these wavelengths. A preliminary series of images of the phantom were acquired, and it became clear that at 50  $\mu\text{m}$ , the FEP phantom was too large for oximetry analysis; the high extinction coefficients of the blue wavelengths resulted in line profiles which were “saturated” due to total absorption at the majority of wavebands - an example of this is shown in figure 3.18. Due to the unavailability of smaller diameter FEP, it was instead decided to use the “green-red” regime of wavelengths for *in vitro* validation (546 nm to 600 nm). As the optical model and imaging system are the same, use of different wavelengths for this *in vitro* validation experiment is justifiable.

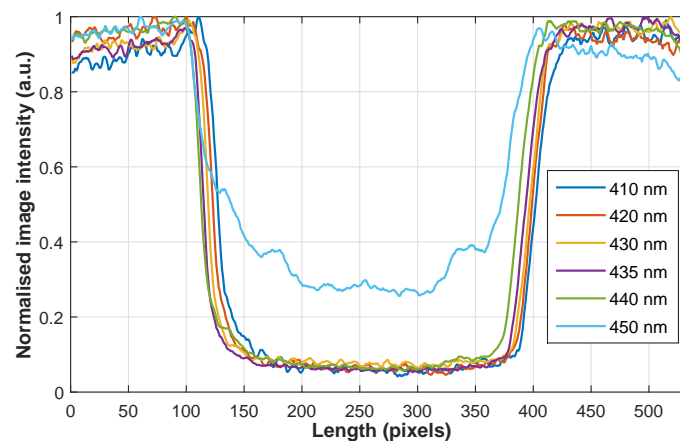


**Figure 3.18.** Line profiles of blood-filled 50  $\mu\text{m}$  FEP at blue wavelengths, demonstrating the total absorption of light at all wavelengths except 450 nm.

For this experiment, a basic validation of the response of the algorithm to phan-

### 3. Multispectral imaging system for *in vivo* microcirculation oximetry

---

toms of varying oxygenations was required. In addition, for validation of the contrast reduction factor  $K$  discussed in chapter 2, a semi-transparent scattering layer (lens cleaning tissue, *Thorlabs*) would be added above the phantom, between the FEP and the objective lens. It was expected that addition of this layer would result in an increase in  $K$  as reported by the algorithm. The effect of the added scattering layer on obtained values for  $SO_2$  was also investigated. The following configurations were imaged:

**Table 3.1.** Configurations of oxygen saturation (calculated as per Briley-Saebø & Bjørnerud (2000) [153]) investigated for *in vitro* validation

	$SO_2$ (%)	Added scatter layer?
1.	0	No
2.	50	No
3.	100	No
4.	0	Yes
5.	50	Yes
6.	100	Yes

## Results

The data were processed and analysed with the optical oximetry model described in chapter 2. The response of the algorithm to varying levels of oxygen saturation is shown in figure 3.19, for phantoms with and without the additional scatter. The numerical values obtained for  $SO_2$  and  $K$  along each phantom vessel are given in table 3.2, including the goodness of fit parameters  $R_2$ . As evident from both the graph and table, there was good agreement between the average  $SO_2$  reported by the algorithm and given  $SO_2$ . For vessels with no additional scatter layer, the average reported value of  $K$  was approximately zero. For the phantoms with the scatter layer, the value of  $K$  increased as expected, however to varying values of

### 3. Multispectral imaging system for *in vivo* microcirculation oximetry

0.42, 0.65 and 0.52 respectively. It was clear that the standard deviation of  $\text{SO}_2$  values along each vessel increased drastically for the phantoms with the scatter layer. As discussed in the previous chapter, an increase in  $K$  is expected to increase the error in  $\text{SO}_2$  with respect to error in transmission ( $\delta(\text{SO}_2)/\delta(T(\lambda))$ ). From analysis of these validation results, empirical evidence of this relationship was provided. A statistically significant correlation was found between the retrieved value of  $K$  and the observed standard deviation along the vessel, with Pearson correlation coefficient  $r = 0.97$ , and  $p = 0.02$ . Additionally, the goodness of fit  $R^2$  decreased from an average of 0.95 for phantoms with no scatter, to 0.86 for the phantoms with scatter. This was likely to be caused by the increased noise and hence reduced SNR associated with addition of the scatter layer. Later experiments *in vivo* demonstrated that the value of  $K$  obtained in microvasculature imaging was generally less than  $\sim 0.3$ , suggesting that the error in  $\text{SO}_2$  may not be as large *in vivo* as the *in vitro* results with additional scatter, which represented “worst-case” data in terms of image quality.

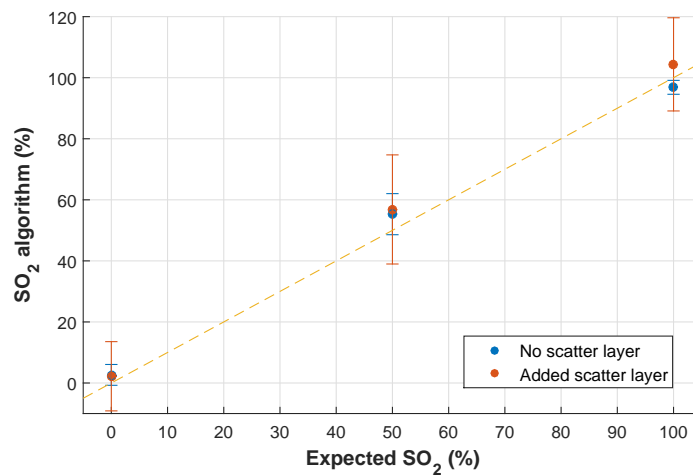


**Figure 3.19.** Retrieved  $\text{SO}_2$  for varying oxygenation in vessel phantom, for those with and without an additional layer of scatter. Linear 1:1 agreement depicted by dashed yellow line.

### 3. Multispectral imaging system for *in vivo* microcirculation oximetry

---

**Table 3.2.** Oximetry results of blood vessel phantom *in vitro*

	Calc. SO <sub>2</sub> (%)	Retrieved SO <sub>2</sub> (%)	K	R <sup>2</sup>
<i>No added scatter</i>	0	3 ± 3	0.00	0.96
	50	55 ± 7	0.04	0.92
	100	97 ± 2	0.00	0.97
<i>Added scatter</i>	0	2 ± 11	0.42	0.87
	50	57 ± 18	0.65	0.85
	100	104 ± 15	0.52	0.87

### 3.5. *Ex vivo* validation

#### Initial assessment of SO<sub>2</sub>

Following successful *in vitro* measurements of vascular SO<sub>2</sub>, validation *ex vivo* was necessary. For this, tendon microvasculature was imaged *in situ* in an intact mouse hind leg. The specific vasculature to be investigated was within the *peroneus longus* tendon, proximal to the *calcaneus* bone. Removal of superficial skin layers was performed in order to expose the microvasculature for imaging. This is illustrated in figure 3.20, with the specific tendon highlighted.



**Figure 3.20.** Illustrative photo of exposed tissue for multispectral imaging, with red arrow pointing to peroneus longus tendon. Superficial skin layers are surgically removed in order to expose the microvasculature.

Unlike whole blood *in vitro*, controlling or varying the oxygen saturation in an

### 3. Multispectral imaging system for *in vivo* microcirculation oximetry

*ex vivo* environment is particularly challenging. It is accepted that post mortem, blood vessels deoxygenate due to local metabolism of oxygen by cells [154]. However, if exposed to air, it is possible the oxygen will diffuse into the vasculature and re-oxygenated these deoxygenated vessels [57]. This has recently been demonstrated in vascular oximetry of the superficial episcleral blood vessels of the eye [82]. In order to first assess whether this was the case, multispectral data was acquired of exposed vasculature on tendon tissue in a mouse leg *ex vivo*. A range of wavelengths between 540 nm to 590 nm, in 5 nm increments, were used for imaging. Vessel tracking was performed along a section of vessel, and the transmission and hence optical density (OD) was determined along this section at each wavelength. The optical densities were then normalised with respect to the 545 nm OD. The resulting ODR values as a function of wavelength are plotted in figure 3.21. This initial qualitative check, showing the characteristic double-peak of the oxygenated spectrum, indicated that the exposed vessel was oxygenated.

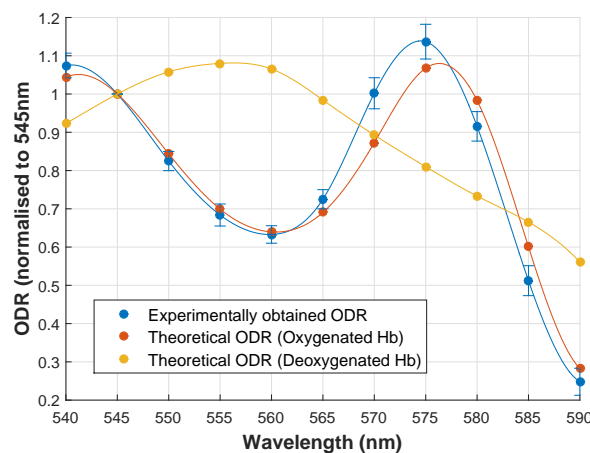


**Figure 3.21.** ODR analysis of *ex vivo* tendon vessel, normalised to 545 nm and showing theoretical ODR values for comparison

#### Nitrogen flow *ex vivo* validation

It was decided that in order for validation of the oximetry system in *ex vivo* microvasculature, a method for controlling the re-oxygenation of the vasculature

### 3. Multispectral imaging system for *in vivo* microcirculation oximetry

---

would be required. In this section, an experiment is described in which initially deoxygenated vasculature was imaged before and after re-oxygenation. A marked increase in  $\text{SO}_2$  was expected.

In order that the vasculature did not re-oxygenate upon exposure to room air, the intact mouse leg was placed within a small chamber through which a steady flow of nitrogen was delivered. The superficial layers of skin were then removed. This chamber, though not completely air-tight, was expected to vastly reduce the amount of oxygen in the immediate environment by continuous displacement of room air by nitrogen. The setup is illustrated in figure 3.22. The chamber was 3D-printed specifically for this purpose, with removable lid to allow for placing of the tendon, and small windows for the microscope objective, and for delivery of nitrogen flow in and out of the chamber. For safety purposes, the laboratory in which the experiment was performed was well ventilated.

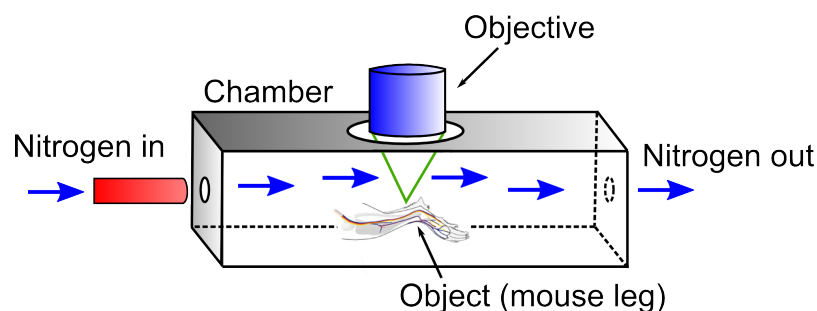


**Figure 3.22.** Illustration of setup for nitrogen flow experiment, with nitrogen delivered via tubing into a sealed chamber to prevent re-oxygenation of *ex vivo* blood vessels by oxygen in air.

## Results

The tendon was imaged numerous times over a period of over 35 minutes, at which point the nitrogen flow was switched off. An example multispectral dataset, acquired at wavelengths from 410 nm to 450 nm, is depicted in figure 3.23. A small number of different vessels were assessed. As evident in the figure, vessels of varying calibre were found, however those analysed were all in the region of

### 3. Multispectral imaging system for *in vivo* microcirculation oximetry

---

approximately 10  $\mu\text{m}$  diameter. Many vessels which were too large (and hence too absorbing for accurate optical transmission calculation) were omitted from analysis.

An initial analysis of vessel optical density was performed at intervals investigated its change over time, with respect to cessation of the flow of nitrogen through the chamber. An optical density ratio was taken of OD at 435 nm with respect to the isosbestic OD at 420 nm. As  $\epsilon_{Hb}(435 \text{ nm})$  is greater than  $\epsilon_{HbO_2}(435 \text{ nm})$ , the ODR is expected to be inversely proportional to  $\text{SO}_2$ . Figure 3.24 shows the result of this experiment, with ODR given as a function of time. The point of nitrogen cessation is highlighted. As evident from these results, allowing room air to permeate the chamber results in a decrease of ODR, assumed to be due to re-oxygenation of the vasculature by diffusion.

An additional experiment was then performed, in which the nitrogen flow was turned off, and then resumed after approximately 15 minutes. This was performed in order to investigate whether the nitrogen flow actively dissociates the oxygen present in *ex vivo* haemoglobin. It has previously been shown that bubbling a nitrogen gas mixture through whole blood can be used to control its oxygen saturation [155]. However, it was not clear whether flow of nitrogen across the tissue would affect *ex vivo* oxygen saturation in this case. The results of this experiment are shown in figure 3.25. From a qualitative analysis, the ODR does not increase again upon resuming of nitrogen flow through the chamber, after a period of several minutes. From these results, it was ascertained that the flow of nitrogen could be used only to prevent re-oxygenation of already deoxygenated haemoglobin; but not to actively de-oxygenate vasculature that is highly oxygenated.

Finally, the multispectral data acquired before and after cessation of nitrogen flow was run through the oximetry algorithm, in order to investigate the absolute oxygen saturation values  $\text{SO}_2$  for the constituent vasculature. For two individual tendon samples, the  $\text{SO}_2$  values were calculated at each time point, and averaged.

### 3. Multispectral imaging system for *in vivo* microcirculation oximetry

---

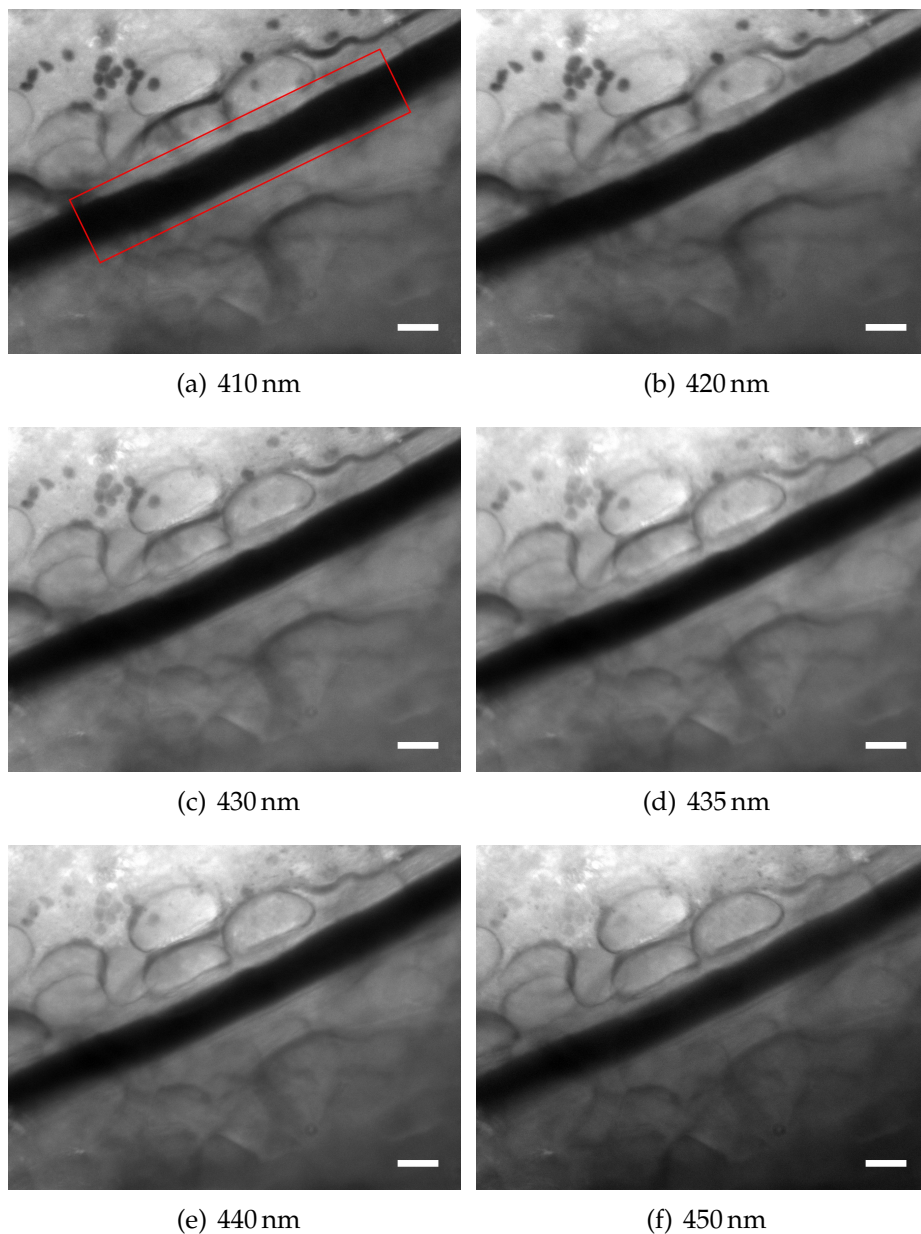


**Figure 3.23.** Illustrative raw multispectral images of murine tendon microvasculature *ex vivo*, at six wavelengths from 410 nm to 450 nm. The vessels become more transparent towards 450 nm due to the difference in haemoglobin extinction coefficients. The region of interest for  $\text{SO}_2$  analysis is indicated in red on figure 3.23(a). The scale bars represent 20  $\mu\text{m}$ .

### 3. Multispectral imaging system for *in vivo* microcirculation oximetry

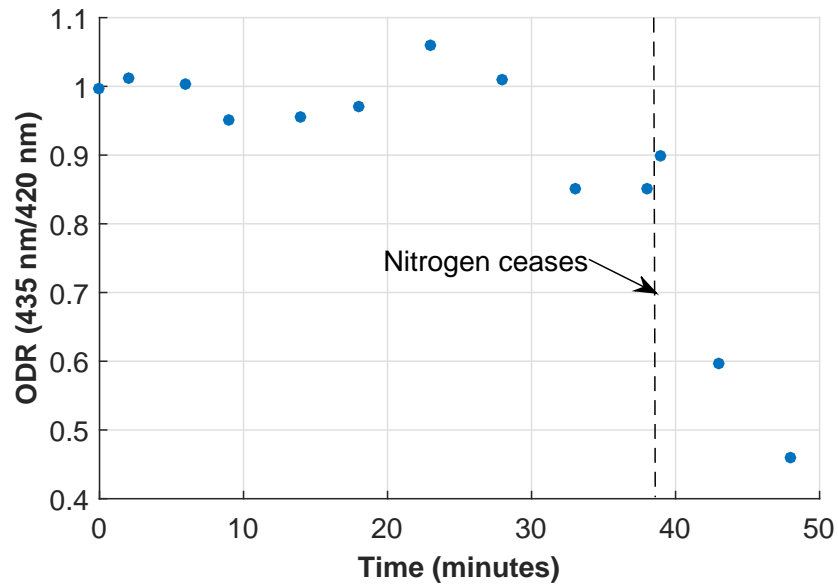


**Figure 3.24.** ODR as function of time for *ex vivo* oximetry validation, with decrease in ODR shown corresponding to cessation of nitrogen flow in chamber.

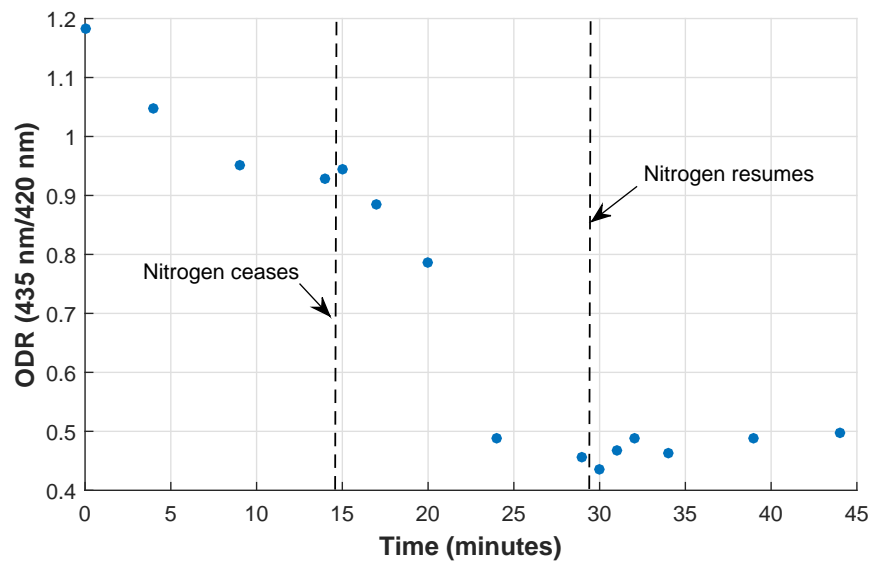


**Figure 3.25.** ODR as function of time for *ex vivo* oximetry validation. The expected decrease in ODR after nitrogen flow ceases is evident, associated with increasing oxygenation. Resuming the nitrogen flow does not appear to deoxygenate the vasculature.

### 3. Multispectral imaging system for *in vivo* microcirculation oximetry

---

The results are shown in figure 3.26. For both tendons, a statistically significant increase in oxygen saturation was observed upon cessation of nitrogen flow through the chamber, with  $p \ll 0.01$  in both cases. After ceasing the flow of nitrogen, the microvasculature of both tendons re-oxygenated to physiologically plausible values:  $92.6 \pm 4.2\%$  and  $96.3 \pm 1.9\%$  respectively. The absolute  $SO_2$  values indicate that the vasculature was not entirely de-oxygenated for initial imaging. It is plausible that a small degree of oxygen bound to the haemoglobin during short exposure of oxygen to the vessel before the flow of nitrogen was introduced.

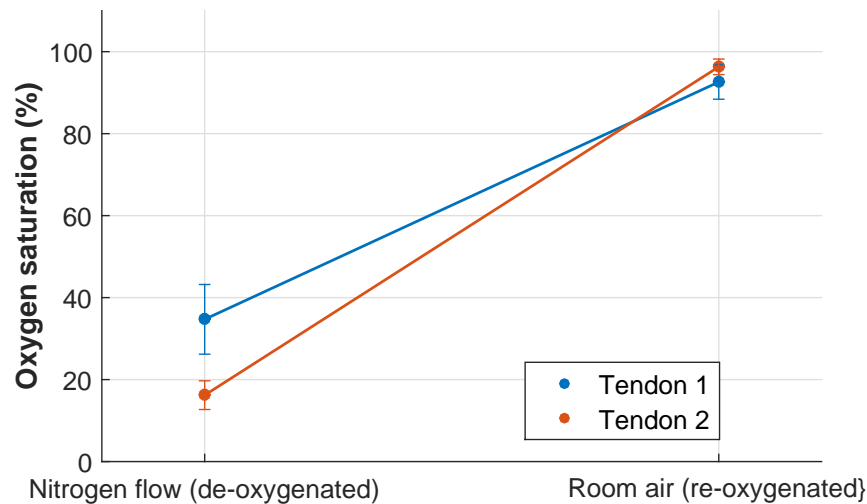


**Figure 3.26.** Reported  $SO_2$  for *ex vivo* oximetry validation, with a marked increase in  $SO_2$  after cessation of nitrogen flow, due to re-oxygenation by diffusion of oxygen in room air.

### 3.6. Conclusions

A novel multispectral imaging system was successfully developed and assembled. In this chapter, the issues and components considered throughout its development were presented and discussed. Image quality was assessed in both *in vitro* and *ex vivo* models. The system was determined to be adequate in terms of spatial and spectral resolution for the imaging of small vasculature, and subsequent determination of  $SO_2$ . The importance of minimising noise and contrast reduction

### 3. Multispectral imaging system for *in vivo* microcirculation oximetry

---

$K$  was demonstrated, with *in vitro* validation demonstrating that high amounts of optical scattering result in noisy images and high standard deviation between  $SO_2$  values determined along the vasculature.

The *in vitro* validation, while largely successful in terms of identification of extreme values of  $SO_2$  (e.g. 0% and 100%), displayed minor discrepancies between “actual”  $SO_2$  and that determined by the algorithm for mid-range values of  $SO_2$ . Due to a lack of other localised techniques for vascular oximetry, it is difficult to gauge whether discrepancies of several percent are caused by inaccuracies within the algorithm, or due to changing oxygenation within the vessel itself. Blood-gas analysers can be used to confirm the oxygenation of whole blood with an accuracy of  $\pm 2\%$ ; however it is unknown if blood oxygenation changes between this measurement and delivery into the narrow FEP capillaries. It is known that addition of sodium dithionite to whole blood changes its osmolarity, which in turn can influence scatter coefficients and scatter anisotropy factor [156]. This may also contribute to discrepancies between expected  $SO_2$  and experimental results. In future it may be desirable to pursue alternative methods for artificial deoxygenation of whole blood for validations. These include, as mentioned previously, the bubbling of nitrogen gas through whole blood, or by addition of yeast [157]. However, further research is required in order to ascertain whether the optical properties of blood are affected by these techniques, as with sodium dithionite.

One important conclusion of this chapter was that for *in vivo* vascular oximetry of superficial microvasculature, oxygen diffusion from air will result in re-oxygenated or deoxygenated blood vessels. The results of these preliminary validation experiments guided the use of oxygen-impermeable plastic film in the *in vivo* experiments. This technique has been used previously in order to isolate blood vessels from oxygen in the atmosphere [89]. This plastic film was placed in contact with exposed tissue to prevent oxygen diffusion - like nitrogen flow, it was found to be adequate in terms of preserving vascular oxygen saturation. However, unlike the flow of nitrogen described in this chapter, the use of plastic film reduces

### 3. Multispectral imaging system for *in vivo* microcirculation oximetry

---

contrast due to optical scatter. It is expected that this reduction in contrast can be compensated for in the oximetry algorithm by the contrast reduction factor  $K$ .

The following two chapters present *in vivo* applications of vascular oximetry using multispectral imaging. These chapters are effectively proof-of-concept studies which will demonstrate the suitability of multispectral imaging for vascular oximetry. Chapter 6 then presents modifications made to the imaging system in this chapter, such that it is adapted for minimally invasive oximetry.

## 4. *In vivo* oximetry study of hypoxia associated with acute inflammation

---

**Summary:** In this chapter, the preliminary experiments for *in vivo* deep tissue oximetry are described. Oxygen saturation was measured in the microvasculature within tendons of mice, comparing controls and those with acute inflammation. The methods for image acquisition are described, as well as results and following conclusions. The inflamed vasculature was found to be hypoxic as compared to the control vasculature. The work presented in this chapter was written up for publication in Biomedical Optics Express [158], from which a number of graphs presented in this chapter have been reproduced.

### 4.1. Background

It is well-known that auto-immune inflammatory diseases such as rheumatoid arthritis (RA) result in a hypoxic environment within affected tissue [6]. Molecular markers for hypoxia and associated angiogenesis are linked to these chronic diseases [18]. However, although the link between inflammation and tissue hypoxia is well established, further research is required in order to ascertain the exact causes and origins of hypoxia within the associated tissue and vasculature, as well as the role it plays in the progression of RA. With a deeper understanding

of the manifestation of hypoxia in immune-related inflammatory disease, the potential exists for earlier diagnoses and possible treatments. In RA, inflammation occurs primarily around affected tendon and joint areas, and associated hypoxia is localised to these areas. It is for this reason that the ability to measure localised vascular  $\text{SO}_2$  is highly desirable for the study of hypoxia in RA. Localised  $\text{SO}_2$  measurements within these areas would provide information currently inaccessible to bulk and probe-based oximetry techniques.

As previously discussed in section 1.2, studies involving diffuse optical spectroscopy (DOS) and sagittal laser optical tomography (SLOT) have been performed on finger joints affected by RA [19, 23]. Both of these studies report measurements of optical parameters such as absorption and scattering coefficients  $\mu_a$  and  $\mu_s$ . The tissue as a whole is considered for these studies, and whilst three-dimensional data is obtained, the spatial resolution is insufficient for the localisation of individual blood vessels. In this chapter, the multispectral imaging system and oximetry algorithms described in chapters 2 and 3 are applied to *in vivo* localised, vascular oximetry of tendon microvasculature in mice.

## 4.2. Methods

### 4.2.1. Acute model for inflammation

The experiments performed in this chapter involved the use of 13 female inbred BALB/c mice (18-25g, 6-8 weeks old, *Harlan*). Six of these mice were used as controls, and acute inflammation was induced in six further mice. The remaining mouse was used for a kinetic study of  $\text{SO}_2$  with increasing inflammation, presented in section 4.3.5. For all experiments in this chapter, inflammation was induced in the mice by using a compound known as  $\lambda$ -carrageenan. Carrageenan is a natural carbohydrate (polysaccharide), obtained through the extraction of certain species of red seaweed [159] (the word carrageenan is derived from the Irish

word “*carraigin*” meaning ‘moss’). The lambda ( $\lambda$ ) form of carrageenan is soluble in cold or hot aqueous solution, and is injectable, causing an acute inflammatory response which peaks approximately five hours post-inoculation [160]. This carrageenan-induced paw oedema has been widely reported as a test for a range of anti-inflammatory drugs, as well as to study the mechanisms associated with inflammation, including arthritis. The inflammation is produced by the operation of various mediators, such as histamine, prostaglandins and pro-inflammatory cytokines [159]. For the experiments in this chapter, 25  $\mu$ L of 1%  $\lambda$ -carrageenan in sterile phosphate buffered saline (PBS) was injected into the mouse footpad of the left hind leg. Due to the difficult nature of this injection, a temporary inhalable anaesthetic (isoflurane) was used in order to sedate the mice for footpad injection.

This localised inflammation was validated by measurement of footpad thickness prior to injection, and again five hours post-injection, at which point the inflammatory response had peaked. The paw thickness was measured in the dorsal-plantar axis at the metatarsal level, using calipers. Figure 4.1 shows the results of these measurements for all mice, with the control and inflamed groups highlighted. As evident from the graph, there was a marked increase in footpad thickness associated with those hind legs which were inoculated, and no significant change for control footpads, as expected. Footpad thickness for inflamed hind legs increased in these five hours from an average of  $1.6 \pm 0.1$  mm to  $3.0 \pm 0.1$  mm.

#### 4.2.2. Setup for imaging of tendon microvasculature

The imaging system described in the previous chapter was utilised for the experiments performed in this chapter. For this work, the specifications presented in table 4.1 were achieved.

In order to image the tendon microvasculature *in vivo*, it was necessary that the superficial skin layers be surgically exposed. Before this could be performed, the

#### 4. *In vivo* oximetry study of hypoxia associated with acute inflammation

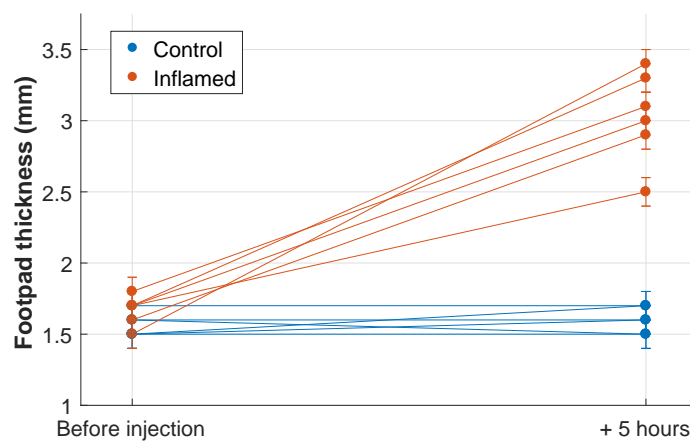


**Figure 4.1.** Comparison of footpad thickness before and after inoculation with  $\lambda$ -carrageenan, causing acute inflammation in the left footpad of each mouse

**Table 4.1.** Specifications of multispectral imaging system

	<b>Specifications</b>
<b>Mode</b>	Transmission
<b>Wavelengths</b>	410 nm, 420 nm, 430 nm, 435 nm, 440 nm, 450 nm
<b>Spectral resolution <math>\Delta\lambda</math></b>	2 nm
<b>Magnification</b>	40X
<b>Field of view</b>	240 $\mu\text{m}$ $\times$ 220 $\mu\text{m}$
<b>Spatial Resolution</b>	0.5 $\mu\text{m}$
<b>Sampling rate</b>	2 sec (6-waveband acquisition)

#### 4. *In vivo* oximetry study of hypoxia associated with acute inflammation

---

mice were anaesthetised. For the mice whose hind legs had been inflamed, five hours were allowed to elapse between inoculation and surgery/imaging, in order that maximum inflammation was achieved. For each case, the mouse was weighed in order to determine the appropriate dose of anaesthetic. An intraperitoneal injection of fentanyl-fluanisone (Hypnorm), midazolam (Hypnovel) and water (1:1:2 by volume) was then delivered at a dose of 10  $\mu\text{L/g}$ . This combination has been shown to produce good surgical anaesthesia which lasts over half an hour [161].

Following delivery of anaesthesia, the superficial layers of skin over the hind leg were surgically removed, exposing the peroneus longus tendon, proximal to the calcaneus bone. Preliminary imaging revealed significant motion artifacts, caused by movement of the animal during breathing. Consequently, it was necessary to secure the hind leg such that it was mechanically isolated from the torso of the mouse. The leg was secured to a small 3D printed block, which in turn was glued to the stage. The purpose of the block was to elevate the leg for ease of imaging. An additional bridge, placed between this block and the body of the mouse, was introduced to further isolate the leg and to reduce leg motion. A surgical adhesive glue known as Vetbond was utilised for this purpose, as was surgical tape. A photograph of the described setup is shown in figure 4.2. Setting up the mouse in this manner vastly reduced the observed motion artifacts, and allowed for the successful acquisition of time-sequential multispectral images. Minor motion between frames could be corrected for with pre-processing image registration, as described in chapter 2.

As mentioned in chapter 3, oxygen-impermeable plastic film was used for all *in vivo* imaging within this chapter. Once surgery and setup of the mouse on the stage had been completed, a small amount of film was placed directly on the exposed tissue. The film not only prevented oxygen in the air from diffusing into superficial vasculature, but it also helped to prevent the tissue from drying out over the course of the experiment. Previous studies have implemented a similar



**Figure 4.2.** Illustration of mouse prepared for multispectral imaging, with the hind leg secured to a raised 3D block with Vet-bond adhesive and surgical tape. An additional 3D-printed bridge piece mechanically isolated the hind leg for prevention of movement due to breathing.

technique in order to isolate superficial vasculature from the effects of oxygen diffusion from air [89]. Finally, a heat mat was placed beneath the mouse in order to maintain its body temperature over the course of the experiment, and was kept at approximately 37 °C. Due to the highly invasive nature of the surgery, the mice were euthanised under anaesthesia following the imaging session.

### 4.3. Results and discussion

#### 4.3.1. Multispectral images

For each of the mice imaged for the experiments in this chapter, several multispectral images of different scenes were obtained within an imaging period of approximately ten minutes. As previously mentioned, movement between frames was minimised due to robust securing of the hind leg being imaged. Localisation of the tendon tissue and microvasculature was performed during live preview of the FOV. Tendon tissue can be identified from its “plain” appearance; Figure 4.3 shows an example of one such dataset, acquired at each of the six wavebands

#### 4. *In vivo* oximetry study of hypoxia associated with acute inflammation

---

from 410 nm to 450 nm. The images highlight the change in contrast of these small vessels between wavebands due to the wavelength-dependence of the extinction coefficients constituent haemoglobin. As evident in figure 4.3(a) even single red blood cells are visible at 410 nm due to the high extinction coefficients. They become transparent at longer wavelengths as shown in figures 4.3(e) and 4.3(f).

Several multispectral images were analysed as described in chapter 2, with many images containing several vessels which were suitable for analysis. Figure 4.4 shows a number of resulting SO<sub>2</sub> maps from *in vivo* multispectral imaging, in which regions of vessels or several vessels were selected for analysis. Certain sections of vessels were unsuitable for analysis due to loss of focus caused by tapering, or travel deeper into the tissue. A clear example of this is shown in figure 4.4(a).

Before assessing the obtained SO<sub>2</sub> for each vessel, the “goodness of fit” R<sup>2</sup> values from the oximetry algorithm were assessed. The R<sup>2</sup> value is a statistical measure of how closely the data is fit to the model in regression analysis. A perfect fit results in R<sup>2</sup> = 1. Recalling there are four iterations fitting the optical model to the data per vessel (described in section 2.6.5), the R<sup>2</sup> value which was assessed was that of the final fit. Poor R<sup>2</sup> values were more common for images of scenes which were poorly illuminated - likely due to local tissue characteristics resulting in lower diffusion of light to the FOV - and hence demonstrated low SNR. These low quality images made oximetry analysis challenging as the resulting transmission profiles were noisy and did not agree well with the transmission profiles of the optical model. As there was likely significant error associated with such data, and as such were discarded. Those values of SO<sub>2</sub> which were generated with a final fit of R<sup>2</sup> less than 0.9 were discarded from further analysis. Using this method, the oximetry algorithm was robust, with SO<sub>2</sub> being approximately constant along each vessel; the standard deviation for all vessels was determined to be 2.3% on average.

#### 4. *In vivo* oximetry study of hypoxia associated with acute inflammation

---

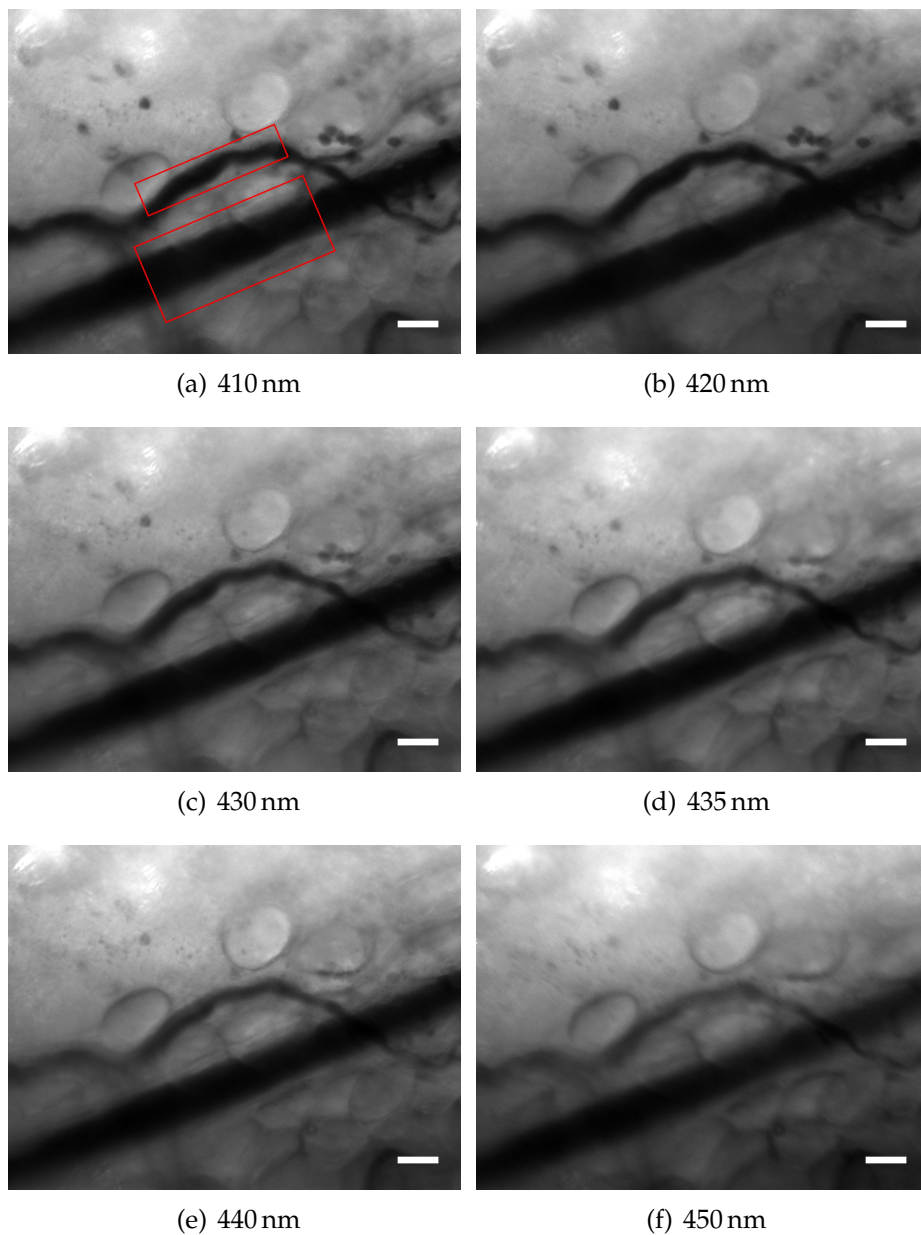


**Figure 4.3.** Illustrative raw multispectral images of murine tendon microvasculature *in vivo*, at six wavelengths from 410 nm to 450 nm. The vessels become more transparent towards 450 nm due to the difference in haemoglobin extinction coefficients. Regions of interest for SO<sub>2</sub> analysis are indicated in red on figure 4.3(a); in focus vessels with clearance on either side are required for determination of intensity profiles and SO<sub>2</sub>. The scale bars represent 20  $\mu$ m.

#### 4. *In vivo* oximetry study of hypoxia associated with acute inflammation

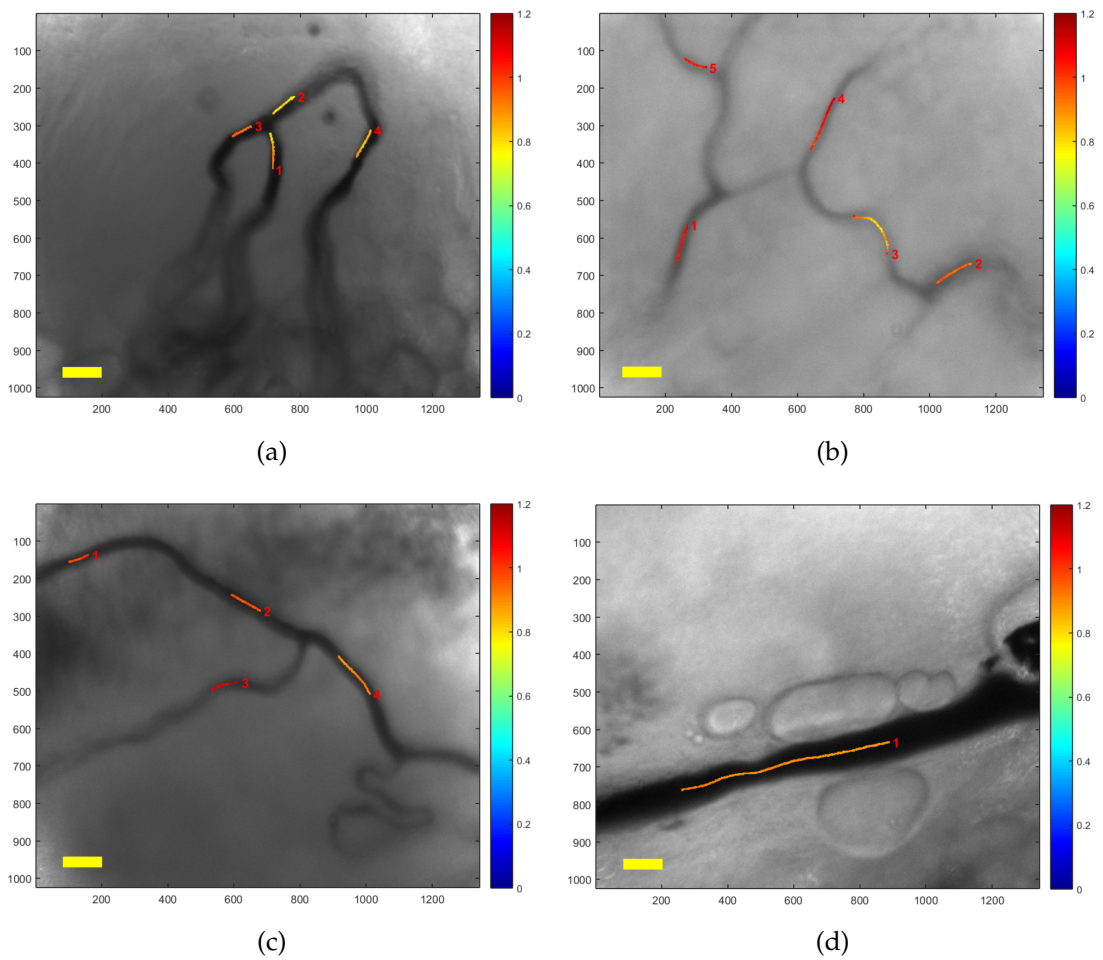


**Figure 4.4.** Illustrative images of tendon microvasculature results from *in vivo* measurements. The colour bars represent  $SO_2$ , and each vessel length analysed is numbered and labelled on each image. The scale bars represent 20  $\mu m$ .

### 4.3.2. Comparison of control and inflamed tendon vasculature

A number of vessels were analysed for each mouse, and the resulting values of SO<sub>2</sub> were collated. The SO<sub>2</sub> for each mouse (averaged over *N* vessels) is shown in table 4.2. Although the average standard deviation along each individual vessel was determined to be small, at 2.3%, the variation in SO<sub>2</sub> between vessels of the same mice result in higher standard deviations, as shown in the table and in figure 4.5. The overall average SO<sub>2</sub> was determined to be 94.8 ± 7.0% for control mice, and 84.0 ± 13.5% for inflamed mice respectively (mean ± standard deviation). Performing a paired t-test, this difference was found to be highly statistically significant (*p* < 0.001).

**Table 4.2.** Average SO<sub>2</sub> results from comparative oximetry study

Mouse ID # (Control)	SO <sub>2</sub> (%)	N vessels	Mouse ID # (Inflamed)	SO <sub>2</sub> (%)	N vessels
1	92 ± 7	13	7	74 ± 14	7
2	95 ± 6	23	8	84 ± 9	20
3	93 ± 7	16	9	88 ± 13	21
4	93 ± 9	20	10	86 ± 9	10
5	99 ± 5	24	11	87 ± 6	25
6	91 ± 5	7	12	87 ± 6	5
<i>N total (control):</i>		<b>103</b>	<i>N total (inflamed):</i>		<b>88</b>

These results suggest that average SO<sub>2</sub> levels are lower in the inflamed tendon microvasculature than for the controls. This result is not surprising, as the link between inflammation and hypoxia is well established. However, this is believed to be the first quantification of localised hypoxia in the vasculature of inflamed tendons. The results also demonstrate the sensitivity of the oximetry technique to changes in SO<sub>2</sub>, and detection of hypoxia *in vivo*. The increased standard deviation of SO<sub>2</sub> in inflamed vasculature is thought to be indicative of the dysfunctional neovascular network that is associated with inflammation [18]. This would result in a larger variation of SO<sub>2</sub> between vessels than would be expected in healthy controls, in agreement with the observations made here.

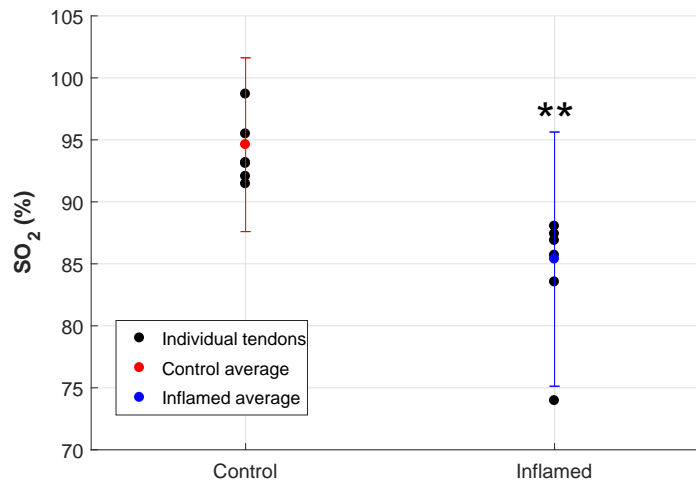


**Figure 4.5.** Comparison of measured  $\text{SO}_2$  from control and inflamed tendon microvasculature. Asterisks denote strong statistical difference in obtained values for inflamed data as compared to controls ( $p < 0.001$ ). Graph reproduced from [158].

It is also interesting to note that the change in average vascular  $\text{SO}_2$  with acute inflammation (approximately 11%) is very similar to that previously measured in the overall tissue oxygenation ( $\text{StO}_2$ ) of inflamed rabbit knees as determined by a DOS technique [23]. In that study by Rajaram et al.  $\lambda$ -carrageenan was also used to induce acute inflammation. The overall values were lower however, with baseline  $\text{StO}_2$  dropping from  $66 \pm 2\%$  to  $55 \pm 11\%$  post-inoculation. It is likely that the tissue itself is less oxygenated than the vasculature.

#### 4.3.3. Assessment of vessel diameter

Figure 4.6 presents all individual measurements made and the respective measured vessel diameters for those measurements. In order to investigate potential correlation between reported  $\text{SO}_2$  and measured vessel diameter, a linear fit was applied to the data, with slope of best fit = -0.33. This initially implied a negative correlation between  $\text{SO}_2$  and vessel diameter, however the goodness of fit was poor with  $R^2 = 0.026$ . To further investigate whether such a relationship exists, the Pearson correlation coefficient  $r$  was calculated for these measurements to be

#### 4. *In vivo* oximetry study of hypoxia associated with acute inflammation

$r = -0.1622$ . This coefficient is a descriptor of the degree to which one parameter is linearly correlated with another ( $r = 0$  for no correlation,  $r = \pm 1$  for total linear correlation). The statistical significance of this coefficient is related to the degrees of freedom of the measurements ( $df = \text{number of samples } N - 2$ ). Tables of “critical values” for Pearson’s correlation coefficients at specific degrees of freedom are readily found in the literature [162]. For  $df = 189$  for all measurements,  $p = 0.025$ , suggesting a statistically significant correlation (statistical significance determined as  $p < 0.05$ ).

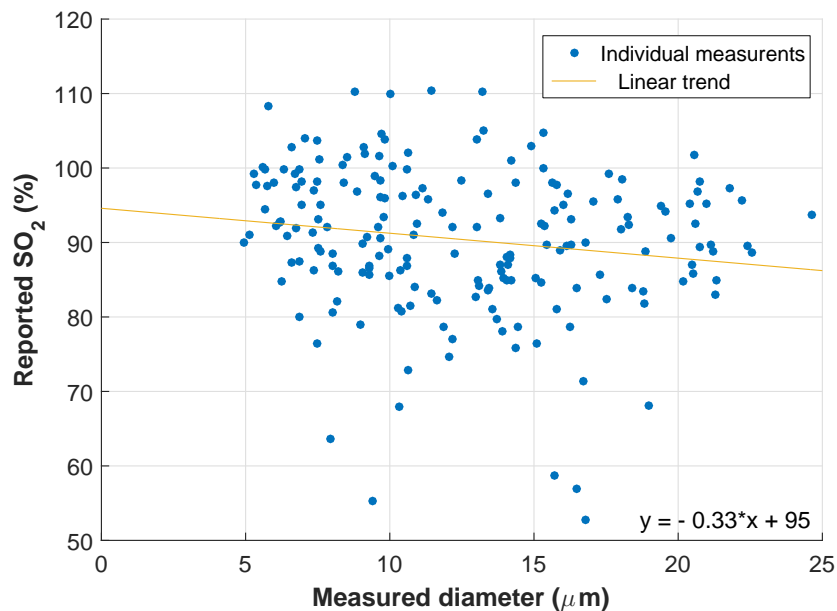


**Figure 4.6.** Comparison of measured  $\text{SO}_2$  from all tendon microvasculature.  $R^2 = 0.026$

In order to assess whether this correlation affects both control and inflamed vasculature (e.g. whether it may be systematic bias or a potential physiological effect), both sets of data were assessed individually. Figure 4.7 depicts all individual measurements for control and inflamed microvasculature respectively, with reported  $\text{SO}_2$  given as a function of measured vessel diameter. Linear fits were also applied to this data. For the control data, the slope of best fit was  $-0.35$ ; for the inflamed data it was  $-0.14$ , suggesting a potential negative correlation of  $\text{SO}_2$  with increasing diameter. However, the goodness of fit of these trends was very low:

#### 4. *In vivo* oximetry study of hypoxia associated with acute inflammation

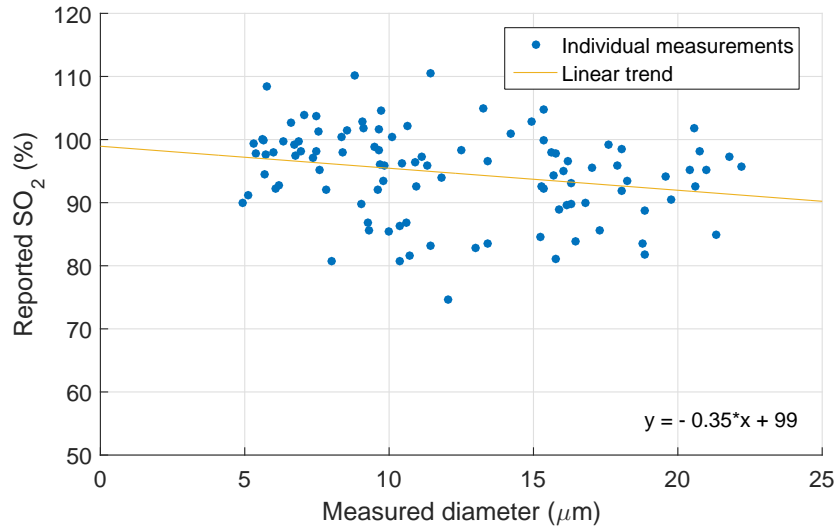
---

$R^2$  values of 0.058 and 0.004 respectively were reported for these linear trends. The Pearson correlation coefficient  $r$  was also calculated for both individual sets of control and inflamed data. For control data,  $r = -0.24$ . For the control data ( $df = 101$ ), the correlation was statistically significant, with  $p < 0.01$ . However, for inflamed data,  $r = -0.065$  and  $df = 88$ , which is not statistically significant ( $p > 0.05$ ).

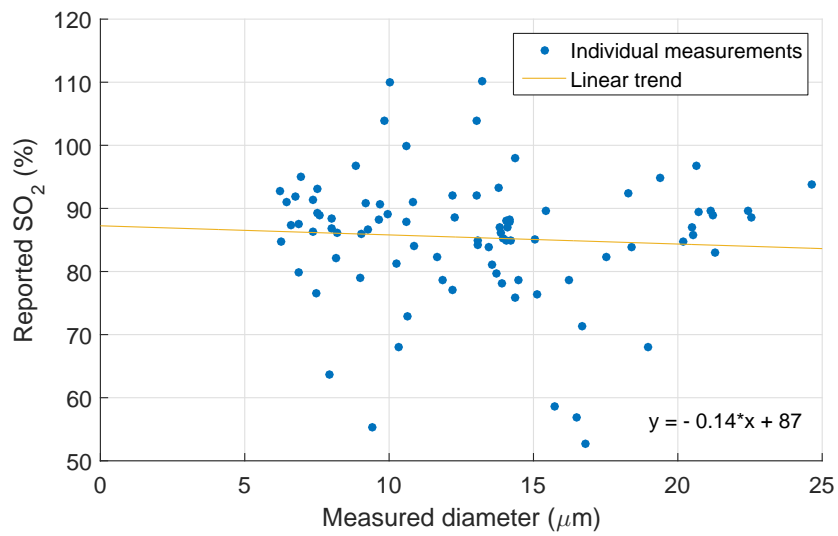
It is difficult to interpret the precise nature of this correlation - particularly as it is only significant for healthy control vasculature. Hickam et al. (1963) first noted that for two-wavelength oximetry, a dependence exists between ODR (and hence  $SO_2$ ) and vessel diameter [163]. The nature of this bias is suggested to be caused by deviations from the basic Lambert-Beer law due to scattering of light, resulting in optical densities that do not increase linearly with path length, as predicted by the Lambert-Beer law [164]. In Hammer et al. (2008) [76], an approximately linear negative correlation was demonstrated between two-wavelength oximetry results and vessel diameter. The authors proposed a correction factor in order to compensate for this effect.

However, for multispectral oximetry as has been performed here, a modified Lambert-Beer law was implemented. The consideration of wavelength- and  $SO_2$ -dependent scatter by haemoglobin, as well as implementation of the contrast reduction factor  $K$ , should in theory compensate for the bias which is introduced in two-wavelength oximetry. It is known that regulation of blood vessels by means of vasodilation can occur in response to hypoxia [49], and this physiological effect is potentially the cause of the weak negative correlation between  $SO_2$  and vessel diameter. If so, the dysfunctional vascular network associated with inflammation may be the reason why this correlation is not evident for the inflamed vasculature. As such, it was decided not to implement a linear calibration on the data.

4. *In vivo* oximetry study of hypoxia associated with acute inflammation



(a) Control vasculature:  $R^2 = 0.058$



(b) Inflamed vasculature:  $R^2 = 0.004$

**Figure 4.7.** Reported  $\text{SO}_2$  as function of measured diameter, with individual vessel measurements depicted for both control and inflamed tendon vasculature.

##### 4.3.4. Oximetry validation *in vivo*

For one individual mouse, it was decided to observe average  $\text{SO}_2$  as a function of time *post mortem*. A sharp decrease of vascular oxygen saturation is expected immediately after death, as previously described in chapter 3. The reason for this investigation was to provide further validation of the sensitivity of the technique to oxygen saturation *in vivo* - and to confirm that changes in  $\text{SO}_2$  observed in section 4.3.2 were not due to any other indirect inflammatory effect.

The mouse for this study was one of those which had been inoculated with  $\lambda$ -carrageenan for inflammation. After being imaged as normal, was euthanised under anaesthesia whilst still on the imaging stage. Additional data was then acquired five minutes post mortem, at which point the blood vessels were assumed to be highly deoxygenated. The average vascular  $\text{SO}_2$ , which was  $71.9 \pm 7.4\%$  before death due to inflammatory hypoxia, further decreased to  $48.2 \pm 8.2\%$  in this time, as indicated in figure 4.8. Given that no other interventions had occurred in the given time frame, it is reasonable to conclude that changes only in the vascular oxygen saturation resulted in this decrease in  $\text{SO}_2$  value as reported by the oximetry algorithm.

##### 4.3.5. Kinetic study of $\text{SO}_2$

The previous experiments were all performed when the inflammatory response caused by inoculation with  $\lambda$ -carrageenan was at its peak. It was clear from these results that as a group, the vasculature was hypoxic as compared to the controls. However, further research is required in order to ascertain whether hypoxia can be detected at lesser degrees of inflammation, as might be associated with early stages of RA. In chapter 6, minimally invasive oximetry is pursued using microendoscopic probes, which will allow for longitudinal oximetry studies in future. With this in mind, it was decided to perform a 'kinetic' study demonstrating the

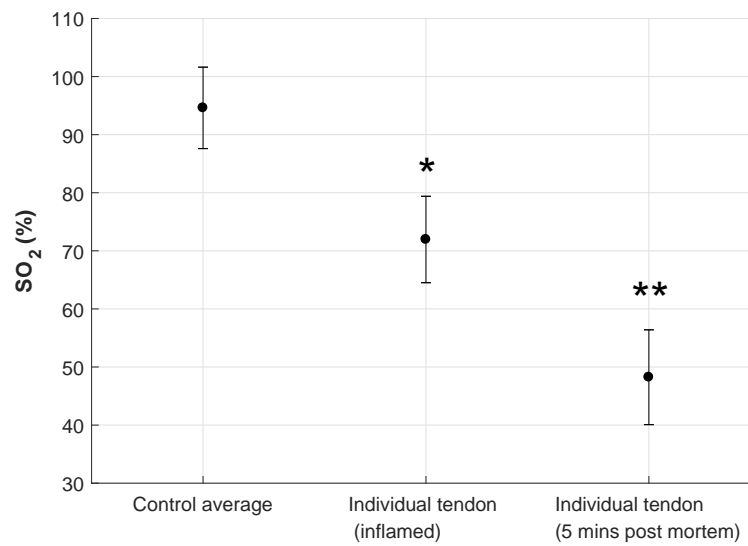


**Figure 4.8.** Comparison of overall control SO<sub>2</sub> (average over all tendons ± standard deviation), average inflamed SO<sub>2</sub> for an individual mouse, and SO<sub>2</sub> of the same tendon post mortem (both averaged over all vessels within tendon ± standard deviation). Statistically significant difference was found between controls and inflamed ( $p < 0.05$ ), and also between inflamed and post mortem tendon ( $p < 0.01$ ) - both indicated in graph. Graph reproduced from [158].

#### 4. *In vivo* oximetry study of hypoxia associated with acute inflammation

---

ability of the oximetry technique to detect milder levels of hypoxia, and whether a correlation exists between hypoxia and degree of inflammation.

As discussed previously, the inflammatory response from injection with  $\lambda$ -carrageenan peaks approximately five hours post-inoculation. For one additional mouse, imaging was performed every half hour between one and five hours post-inoculation. The assumption of this particular experiment was that there is a linear increase in inflammation (and hence hypoxia) with time once the  $\lambda$ -carrageenan has been injected. The results of this experiment are shown in figure 4.9.

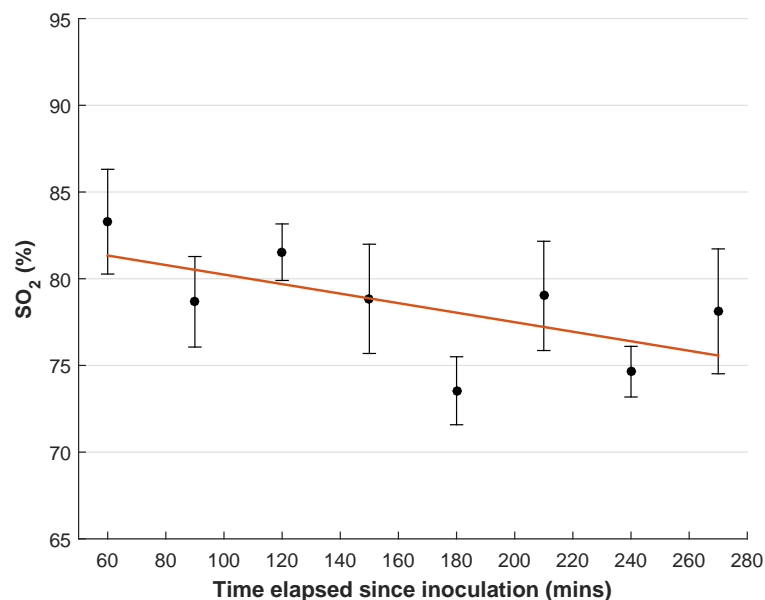


**Figure 4.9.** Kinetic analysis of  $\text{SO}_2$  as a function of increasing inflammation after inoculation with  $\lambda$ -carrageenan, mean  $\pm$  standard error,  $r = -0.63$ ,  $p = 0.095$ . Graph reproduced from [158].

As evident from the graph, there was considerable scatter between individual measurements at each time point. However, there was an overall negative linear trend in average  $\text{SO}_2$ , as expected, with Pearson correlation coefficient  $r = -0.63$ . For this correlation, the corresponding  $p$ -value was 0.095. This is not low enough to be considered statistically significant (usually defined as  $p < 0.05$ ). It may be possible that the assumption of a linear correlation between hypoxia and time since inoculation is invalid. Further, a number of vessels were analysed at

each time point, which suggests that the scatter of  $\text{SO}_2$  values about this trend reflects the natural biological variation of  $\text{SO}_2$  in the distribution of analysed blood vessels. Given that no other techniques exist to quantify localised vascular  $\text{SO}_2$  *in vivo*, it is difficult to accurately validate the variability of  $\text{SO}_2$  between individual blood vessels. However, this approach does provide evidence of a correlation between hypoxia and degree of inflammation.

#### **4.4. Potential for diagnostic classification**

In this chapter, data was acquired of vascular  $\text{SO}_2$  in murine tendon tissue, with a comparison made between healthy and inflamed tendon vasculature. As discussed in chapter 1, previous optical tests have been performed in order to make a diagnosis as to the health status of the tissue. By using the data obtained in this chapter for acute inflammation, it was decided to ascertain the potential sensitivity and specificity of diagnostic classification using vascular  $\text{SO}_2$  as a predictor. This was done by using experimentally obtained results as training data for a classification model.

##### **Classification with all data**

The data was used to train a 'decision tree' classification model, with the vascular  $\text{SO}_2$  data and  $\text{SO}_2$  variance input as training data, and assigned to a response '1' or '2' corresponding to healthy or inflamed respectively (defined as the "true class"). The  $\text{SO}_2$  variance along each vessel was input as additional predictor data due to the assumption that higher variance is associated with hypoxic data. This trained classification model was then applied to the same data. Using this model, the data was input and its class was predicted. The resulting confusion matrix is displayed in figure 4.10. In classification, a confusion matrix is used to describe the performance of a model. The top row shows the true and false

#### 4. *In vivo* oximetry study of hypoxia associated with acute inflammation

---

positive rates (TPR/FPR), and the second row shows the false and true negative rates (FNR, TNR). The TPR is the rate, or probability, of correctly making a positive diagnosis; the FPR is the probability of incorrectly making a positive diagnosis. Conversely, the FNR and TNR are the probabilities of incorrectly or correctly making a negative diagnosis. Recall from chapter 1, in classification, the true positive and true negative rates are equivalent to sensitivity and specificity respectively. From the data obtained for this project, a resulting sensitivity of 91.3% and specificity of 83.9% were obtained. It should be noted that because the same data were used to train the classification model and to compute the error rate, these values should be considered “best case” scenario. Given new data, the actual sensitivity and specificity is highly likely to be lower. In order to investigate this issue further, an additional classification model using “cross validation” was derived.

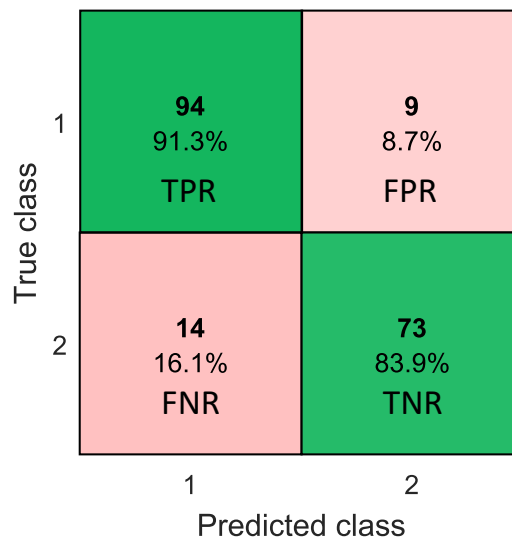


**Figure 4.10.** Confusion matrix for trained classification model using all data, with the true positive rate (TPR, also known as sensitivity) and true negative rate (TNR, also known as specificity) of the classification shown in the green cells, and the false positive rate (FPR) and false negative rate (FNR) shown in the red cells.

### Classification with cross validation

The training method of “cross validation” utilises the whole dataset by partitioning the data into divisions (also known as folds). Each division is tested individually, using all other data to train the classification model in turn. This method results in a better, more realistic estimate of the predictive accuracy of the model with new data, as compared with the previous method of “no validation”, which uses all data for training and computation of error rate [165]. An additional classification model was determined using this method, using 5 classification divisions. The data was again used to determine the classification error rate. The results of this particular test are given in 4.11, with the given sensitivity and specificity reducing to 77.7% and 64.4% respectively.

True class	1	<b>80</b> 77.7% TPR	<b>23</b> 22.3% FPR
	2	<b>31</b> 35.6% FNR	<b>56</b> 64.4% TNR
		1	2
		Predicted class	

**Figure 4.11.** Confusion matrix for trained classification model using cross-validation technique, with the true positive rate (TPR, also known as sensitivity) and true negative rate (TNR, also known as specificity) of the classification shown in the green cells, and the false positive rate (FPR) and false negative rate (FNR) shown in the red cells.

Although still much better than a random probability, these results suggest that given the  $SO_2$  of an individual blood vessel, it is unlikely to be able to accurately predict whether the tissue is healthy or inflamed. This result is not altogether

surprising, considering the heterogeneity of localised  $\text{SO}_2$  observed between individual vessels within individual animals. Further,  $\text{SO}_2$  naturally varies within the vasculature due to distribution of oxygen to tissue. For any potential future diagnostic capability, it would be preferable to consider the vasculature as a whole. In that case however, the advantage of having a localised oximetry technique is made redundant, and would likely give similar outcomes in terms of sensitivity and specificity to bulk probe and DOS techniques.

### 4.5. Conclusions

In this chapter, the multispectral imaging system and oximetry technique was applied to a first *in vivo* study of localised vascular  $\text{SO}_2$  in the mouse tendon. Comparing the  $\text{SO}_2$  of control vasculature and vasculature with inflammation, hypoxia was successfully detected and quantified. As a proof of concept of localised vascular oximetry *in vivo*, the results show that the technique was successful in detecting hypoxia associated with acute inflammation. For the 12 mice chosen for the comparative study of  $\text{SO}_2$ , the statistical power of the test was determined to be 0.7. This value was calculated using the determined values for  $\text{SO}_2$  of control and inflamed vasculature. The statistical power is the probability of correctly rejecting the null hypothesis when it is false. A greater number of mice may have increased the statistical power of the experiment, however in the interest of ethics and for an initial proof-of-concept, this number of mice was considered to be adequate.

A kinetic study was also pursued, in which vascular  $\text{SO}_2$  was observed as a function of time post-inoculation with the inflammation-inducing  $\lambda$ -carrageenan. Whilst not quite statistically significant, the determined negative linear correlation suggests a link between hypoxia and degree of inflammation. The tool provided by the multispectral oximetry technique will enable this link to be investigated in more detail with longitudinal oximetry studies.

#### 4. *In vivo* oximetry study of hypoxia associated with acute inflammation

---

During live preview of many of the image acquisition sessions, the flow and movement of blood within the microvasculature was evident, including that of individual red blood cells. Unfortunately, due to the sequential nature of the imaging system, imaging and oximetry of these individual red blood cells was not possible. If oximetry of individual red blood cells were to be of biological interest, snapshot multispectral imaging systems such as IRIS [105] could potentially be utilised for this application. However, adaptation of current IRIS systems for imaging of multiple wavebands in the visible blue region of the EM spectrum would be necessary, and the loss of resolution associated with image replication on a single detector may also present a challenge for imaging of the microvasculature and single cells.

Future work involving longitudinal studies are expected to be obtainable with minimally invasive oximetry involving microendoscopic probes. The invasive nature of the surgery required for the experiments reported in this chapter made repeated measurements unfeasible. The capability to perform longitudinal studies presents many advantages. More realistic models for RA can be employed, such as collagen-induced arthritis (CIA) which is considered the “gold standard” [166]. Like RA, CIA induces an immune response involving auto-antibodies. This model takes course over a number of weeks, as opposed to hours such as with carrageenan-induced paw oedema. Longitudinal oximetry studies of CIA may thus provide new information as to the link between hypoxia and rheumatoid arthritis.

As discussed in section 4.4, based on the data presented in this chapter, the use of localised vascular oximetry for diagnosis of early RA is questionable due to the local variations found in  $\text{SO}_2$  within the microvasculature. Further work regarding the application of localised vascular oximetry should perhaps focus on the study of the mechanisms of inflammation and hypoxia; for example, where specifically in the joint the hypoxia originates and how it affects disease progression. In this way, the advantages of access to localised  $\text{SO}_2$  distribution will be fully utilised.

## 5. Oximetry study of vasculature in the rat dorsal spinal cord *in vivo*

---

**Summary:** In this chapter, an experiment is described in which a basic multispectral microscope was employed to image the dorsal spinal cord vasculature in the rat. This was a collaborative experiment: the setup of this MSI system, and acquisition of the data, was performed by Lewis E. Mackenzie (formerly of the Imaging Concepts Group) and a collaborating research group in the Department of Neuroinflammation at University College London. The resulting raw data was supplied for the subsequent oximetry analysis described in this chapter. Venous  $\text{SO}_2$  was measured in the spinal cord of control rats, and those with a model for multiple sclerosis known as experimental autoimmune encephalomyelitis. Partial work in this chapter has been published in *Physiological Measurement* [167].

### 5.1. Background

In addition to arthritic disease such as rheumatoid arthritis, auto-immune inflammatory disease can also affect the brain and spinal chord. Multiple sclerosis (MS) is an example of such a disease, affecting upwards of 120,000 people in the UK alone [168]. In MS, damage to the insulating sheaths surrounding nerve fibres occurs, in a process known as demyelination. This results in impairment of brain and spinal cord function, leading to a range of disabilities and increased

## 5. Oximetry study of vasculature in the rat dorsal spinal cord *in vivo*

---

morbidity. Davies et al. (2013) have previously reported hypoxia in the spinal cord grey-tissue of rats affected by experimental auto-immune encephalomyelitis (EAE) [7]. EAE is a murine model which replicates the associated pathological features of MS, such as inflammation and demyelination - it is the most commonly used model for study of the disease [169]. The study by Davies et al. demonstrated that the degree of hypoxia in spinal cord tissue was correlated with severity of EAE, and suggested that hypoxia plays a crucial role in the pathogenesis of MS. However, it is not known how EAE affects vascular oxygen saturation. Further information regarding the mechanisms and progression of EAE may be gained by the study of localised  $\text{SO}_2$  in these vessels, specifically that of the spinal cord dorsal vein and tributary venules. Additionally, by making interventions such as changes to inspired oxygen ( $\text{FiO}_2$ ), the physiological response of vascular  $\text{SO}_2$  in EAE rats may be compared to healthy rats. Assessing changes in  $\text{SO}_2$  as a result of  $\text{FiO}_2$  intervention is an established method for testing the sensitivity of oximetry techniques [170].

As with the tendon, the spinal cord is not optically accessible. As such, there are only limited studies in which the  $\text{SO}_2$  dynamics of the rat spinal cord have been investigated. In 2013, Figley et al. employed a commercial two-wavelength photoacoustic tomography (PAT) system to study  $\text{SO}_2$  dynamics in the spinal cord dorsal vein during hypoxia [171]. The authors used a window chamber to access the vasculature, and reported a temporary decrease in venous  $\text{SO}_2$  during hypoxia. Lesage et al. (2009) employed optical imaging to compare neuronal activation in the spinal cord in control rats and those with spinal cord injuries. They found that the haemodynamic response to electrical stimulation was reduced in injured spinal cords, and reported a change in the relative concentration of oxygenated and deoxygenated haemoglobin. However, no absolute  $\text{SO}_2$  values were reported. Sharma et al. (2011) [172] also reported a study of the same haemodynamic response induced by electrical stimulation, instead using non-imaging light-reflectance spectroscopy. Changes in haemoglobin concentration were also

reported, again without relating these values to absolute oxygen saturation. Due to the probe-based technique, accurate localisation of measurements was not possible. Clearly, there is scope for a robust technique with the ability to image and simultaneously measure localised oxygen saturation in spinal cord vasculature *in vivo*.

In this chapter, rat dorsal spinal cord veins were studied using a custom MSI system and a multispectral oximetry algorithm. Largely similar to the algorithm described in previous chapters, modifications were made due to differences in the optical light paths, related to the distinct illumination scheme of this separate MSI system. The system was used to measure venous  $SO_2$  in anaesthetised rats, during a range of induced oxygenation states by changing the fractional of inspired oxygen ( $FiO_2$ ). The calibration-free oximetry algorithm allows for the first localised absolute measurement of oxygen saturation in blood vessels of the spinal cord in the rat. Although applied to the rat spinal cord here, this system was designed to be cost-effective, accessible and transferable for a range of oximetric applications.

### 5.2. Experimental setup

A primary aim of this project was to demonstrate vascular oximetry with high accuracy, using a custom MSI system comprised primarily of “off-the-shelf” components. Due to its accessibility, such a system would be highly transferable for a range of vascular oximetry applications.

In previous chapters of the thesis, oximetry of the microvasculature was described, in which highly absorbing wavelengths in the visible blue region were utilised. These blue wavelengths are necessary for providing sufficient contrast of the smallest capillaries, which can be less than  $10\ \mu\text{m}$  in diameter. The dorsal vein and tributary venules are much larger in calibre than capillaries in the

## 5. Oximetry study of vasculature in the rat dorsal spinal cord *in vivo*

---

microvasculature, with diameters approximately 80  $\mu\text{m}$  on average. As such, the blue wavelength regime utilised in previous chapters (410 nm - 450 nm) is unsuitable due to excessive absorption. Instead, a range of wavelengths in the green-red region were chosen to be more suitable for this specific application - previously introduced and assessed for oximetry accuracy in chapter 2, section 2.8. The six wavebands chosen for imaging were 546 nm, 560 nm, 570 nm, 584 nm, 590 nm and 600 nm. These wavebands provide close to optimal transmission for oximetry in the dorsal spinal cord tributary veins. Wavelengths above 600 nm are unsuitable due to the relatively weak absorption of light by haemoglobin in this region, resulting in low contrast and sub-optimal optimal transmission.

Referring to the extinction coefficients of haemoglobin, the 546 nm, 570 nm and 580 nm wavebands are isosbestic. The remaining wavebands, 560 nm, 590 nm and 600 nm provide sensitivity to  $\text{SO}_2$ . In figure 5.1, theoretical transmission profiles of an 80  $\mu\text{m}$  diameter vessel are shown for both the visible blue region of the EM spectrum, and this new green-red regime. Clearly, the transmission profiles  $T(\lambda)$  saturate at the blue wavelengths for blood vessels as large as 80  $\mu\text{m}$ , making oximetry unachievable. However, good contrast between wavebands in the green-blue regime indicate that high accuracy oximetry is possible, with  $0.1 < T < 0.7$  for all wavebands. As previously described in chapter 2, transmissions in this range result in minimal photometric error [144].

A schematic of the imaging system developed for this work is shown in figure 5.2. The specifications of the system are summarised in table 5.1. Due to the relatively large size of the rat body, sufficient working distance between the objective and the imaging plane was required, such that the spinal cord could be accessed for surgery prior to imaging. Further, it was required that the imaging system be portable.

Illumination was provided by a white LED (MWWHL3, *Thorlabs*), which was controlled by a 3-channel driver (DC4100, *Thorlabs*). Light from the LED was

## 5. Oximetry study of vasculature in the rat dorsal spinal cord *in vivo*

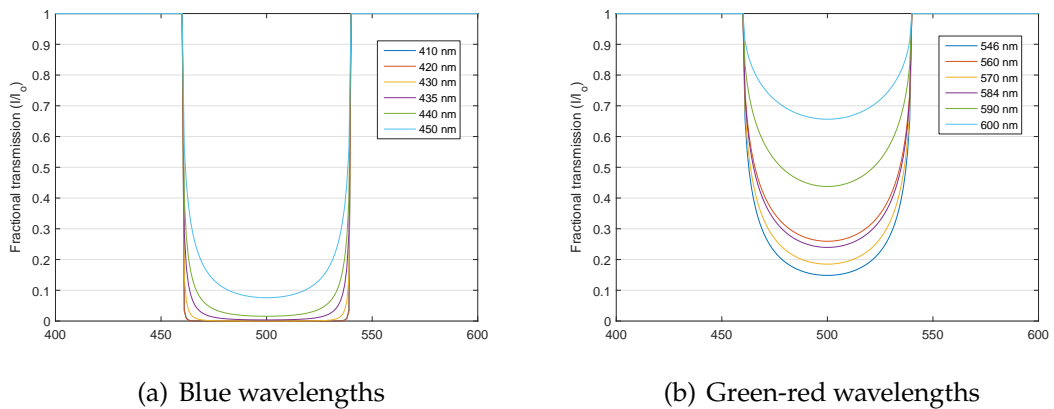


**Figure 5.1.** Comparison of theoretical transmission profiles for 80  $\mu\text{m}$  vessel at 100%  $\text{SO}_2$ , for blue wavelengths (410 nm - 450 nm) and green-red wavelengths (546 nm - 600 nm)

**Table 5.1.** Specifications of multispectral imaging system

	<b>Specifications</b>
<b>Mode</b>	Brightfield
<b>Wavelengths</b>	546 nm, 560 nm, 570 nm, 584 nm, 590 nm, 600 nm
<b>Spectral resolution <math>\Delta\lambda</math></b>	8 nm
<b>Magnification</b>	6.4X
<b>Field of view</b>	3.69 mm $\times$ 2.47 mm
<b>Spatial Resolution</b>	0.88 $\mu\text{m}$
<b>Sampling rate</b>	45 sec (6-waveband acquisition)

## 5. Oximetry study of vasculature in the rat dorsal spinal cord *in vivo*

approximately collimated by a lens of focal length 40 mm (COP-5A, *Thorlabs*). An additional lens with focal length 100 mm (LA1509, *Thorlabs*) was implemented as a condenser lens. Spectral discrimination was provided by an LCTF (VIS-7-HC-20, *Varispec*), providing electronically-controllable switching of wavebands, with spectral full-width at half maximum of 8 nm. A single reflex lens (SLR, AF Nikkor  $f/1.8$ ) with focal length of 50 mm was used as the objective, allowing for finite conjugate imaging. The position of this SLR could be translated along the z-axis for adjustment of focus. A linear polariser (LPVISE200-A, *Thorlabs*) was also introduced to the illumination path, crossed with the inherent linear polarisation of the LCTF. The purpose of this orthogonal polarisation configuration was to null specular reflections from the object. Unlike diffuse reflection, specular reflection will retain its original polarisation. The effect of this polarisation configuration means that in the oximetry analysis, back-reflected light can be omitted from the analytical model of optical transmission. This is further described in section 5.4.

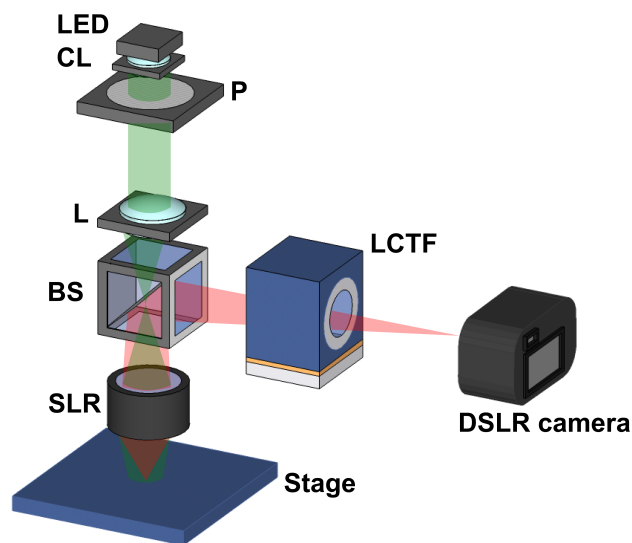


**Figure 5.2.** Schematic of multispectral microscope, with illumination path shown in green and imaging path in red. LED: light emitting diode; CL: collimating lens; P: linear polariser; L: condenser lens; BS: beamsplitter; LCTF: liquid crystal tunable filter. Image replicated from [167].

For image capture, a digital SLR camera (D300s, *Nikon*) was used, with a CMOS

## 5. Oximetry study of vasculature in the rat dorsal spinal cord *in vivo*

---

detector of  $4288 \times 2800$  pixels. For the configuration shown in 5.2, the field of view was approximately 3.69 mm by 2.47 mm, relating to a magnification of 6.4, and corresponding to  $0.88 \mu\text{m}/\text{pixel}$ . This camera generated 14 bit RGB NEF (RAW) images which were converted to greyscale TIFF images before oximetry analysis. As the images would be acquired at three colour channels, it was necessary to determine the optimum channel for each waveband in terms of SNR. For example, for an image acquired at 600 nm, the signal through the blue channel would be low. It was determined that for  $580 \text{ nm} \leq \lambda \leq 600 \text{ nm}$ , the red channel provided the highest signal. For  $546 \text{ nm} \leq \lambda \leq 570 \text{ nm}$ , the green channel provided higher signal and would be used for these wavebands. For each imaging session, image exposure time for each waveband was adjusted in order to ensure sufficient signal and to avoid image saturation. The greyscale conversion from these channels involved subtraction of the respective dark current channel. Once this initial image processing had been carried out, multispectral oximetry analysis could then be performed normally as with greyscale CCD images. A custom LabVIEW interface (developed by Lewis E. Mackenzie) was used to control the LED, the spectral filtering using the LCTF, and image acquisition by trigger of the camera.

### 5.3. Image acquisition

In total, nine adult female Dark Agouti rats (average weight of 180 g) were imaged with the MSI system: four control rats (Rats 1, 2, 3 and 4) and five with EAE (Rats 5, 6, 7, 8 and 9). In order to access the dorsal vein, a laminectomy was performed under anaesthesia, delivered by means of 2% isoflurane in room air. A laminectomy is the surgical removal of the lamina, which is part of the vertebra covering the spinal canal. The dorsal aspect of the lumbar vertebral segment L1 was then removed, exposing the vein for imaging. Once the surgery had been completed, the level of isoflurane was reduced to 1.5% for the remainder of the experiment, which included the imaging.

## 5. Oximetry study of vasculature in the rat dorsal spinal cord *in vivo*

---

As with the oximetry work in the mouse tendon, motion artifacts can pose an issue for sequential multispectral imaging in living animals. In this case, to reduce motion caused by the heart-beat and breathing, the spinous process rostral to the exposed cord was clamped in place using a modified haemostatic clamp. Surgical sutures were used in order to reduce the weight-load on the rat ribcage. This strategy reduced motion sufficiently for multispectral imaging.

For control rats and also those with EAE, a specific sequence of inspired oxygen was followed. At each oxygenation state, three series of multispectral images were taken of the scene. This strategy, previously implemented by MacKenzie et al. (2016) [82], results in changes of  $SO_2$  which are clearly distinct from normal physiological variation. As such, validation of oximetry can be performed using the control rats. Further, as well as comparing  $SO_2$  values in EAE rats with controls at baseline normoxia, the physiological response of EAE rats to the same  $FiO_2$  interventions can also be assessed. The  $FiO_2$  sequence was as follows: baseline normoxia (“normoxia 1”) for ten minutes; hyperoxia for ten minutes; return to normoxia for five minutes (“normoxia 2”); and two states of increasing hypoxia for five minutes each (“hypoxia 1” and “hypoxia 2” respectively). The corresponding values of  $FiO_2$  for these states is shown in table 5.2.

**Table 5.2.** Oxygenation states and corresponding  $FiO_2$  values for multispectral imaging sequence

Oxygenation state	$FiO_2$ (%)
Normoxia 1	21
Hyperoxia	100
Normoxia 2	21
Hypoxia 1	18
Hypoxia 2	15

#### 5.4. Oximetry analysis

The preliminary image processing and preparation for oximetry analysis remained largely the same, as described in detail in chapter 2. Vessel tracking of vessels within the multispectral data sets, calculation of transmission profiles and determination of vessel diameters was all performed as previously described. As with all previous analysis, a ratio was calculated of the light transmitted through the blood vessel, and the intensity of light that would have been scattered from the centre of the vessel centre, had the vessel been absent (this is performed with the linear fit across the vessel as described previously). In this manner, although the specific optical properties of the spinal cord are not known, the ratio of intensity values ( $I/I_0$ ) is insensitive to the precise characteristics of the spinal cord, and also to variations in source intensity with time. Minor modifications to MATLAB code was made for estimation of diameter, to compensate for the difference in magnification of the imaging system from that used previously. Hence, the scaling factor to convert from diameter in pixels to actual value in microns was changed.

However, it was necessary that the actual oximetry algorithm itself be updated, taking into consideration the illumination scheme of the new imaging system. In previous chapters, an assumption of only single-pass light transmission through the blood vessel was made. This was shown to be valid due to the nature of the annular illumination configuration, in which the central field of view was not directly illuminated. For that illumination scheme, no back-reflected light or light which had been doubly absorbed by a vessel would be imaged. However, the above assumptions are not automatically valid for this imaging system. As described in the previous section, the imaging system employed full-field illumination, with the field of view being directly illuminated with approximately uniform intensity. This configuration has been described in the literature. It has been shown that for the case of full-field illumination the transmission will be a combination of single-pass, double-pass and back-scattered light [136, 137]. As

## 5. Oximetry study of vasculature in the rat dorsal spinal cord *in vivo*

---

the linear polariser was crossed with the linear polarisation introduced by the LCTF, back-scattered light was neglected from the analysis. As with the tendon, the spinal cord tissue has low levels of pigmentation and the relative magnitudes of the single- and double-pass components are expected to have low variability between and within spinal cords.

In order that both the single-pass and double-pass component of the intensity signal can be considered in the analysis, they were incorporated separately into the expression for optical transmission  $T(\lambda)$ . In Smith et al. (2000), an optical model was described in which both of these components were considered [99], the basic form of which is:

$$T(\lambda) = \alpha \exp(-\varepsilon(\lambda)cd) + \beta \exp(-2\varepsilon(\lambda)cd) \quad (5.1)$$

where  $\alpha$  and  $\beta$  are the fractions of light transmitted in single- and double-pass respectively. As with previous experiments, it is possible that reductions in contrast due to factors other than changes in oxygen saturation may occur, for instance such as due to small overlying layers of tissue. The contrast reduction factor  $K$ , as described in chapter 2, was thus retained, as were the wavelength-dependent reduced scattering coefficients  $\mu'(\lambda)$  of oxygenated and deoxygenated haemoglobin. However, the  $SO_2$ -dependence of the reduced scatter coefficient was not implemented. The final optical model for light transmission was:

$$T(\lambda) = \left( \alpha 10^{-C_{HbT}(\lambda)d[(\epsilon_{HbO_2}(\lambda) - \epsilon_{Hb}(\lambda))SO_2 + \epsilon_{Hb}(\lambda)] + \mu'(\lambda)d} + \beta 10^{-2C_{HbT}(\lambda)d[(\epsilon_{HbO_2}(\lambda) - \epsilon_{Hb}(\lambda))SO_2 + \epsilon_{Hb}(\lambda)] + 2\mu'(\lambda)d} \right) (1 - K) + K \quad (5.2)$$

An important distinction of this imaging system is the fact that an LCTF was used in order to provide spectral discrimination. The nominal bandwidth of the LCTF is 8 nm, although the actual bandwidth increases with wavelength. This is larger than that of the AOTF used in previous chapters, which is approximately 2 nm.

## 5. Oximetry study of vasculature in the rat dorsal spinal cord *in vivo*

---

This means that for any of the transmitted wavebands, the extinction coefficient of the central wavelength only is likely to vary from the effective extinction coefficient for the waveband in its entirety. In order to minimise error in the oximetry algorithm, these effective extinction coefficients were calculated. The wavelength-dependence of the LCTF transmission band is approximately gaussian, with the central wavelength at its peak. By normalising the area underneath this transmission intensity spectrum to unity, the effective extinction coefficients could be determined by integrating the coefficients at each individual wavelength over all wavelengths within this normalised transmission spectrum. For reference, the effective extinction coefficients used within this chapter are shown in table 5.3.

**Table 5.3.** Effective extinction coefficients for LCTF transmission wavebands. Original data from Prahl, 1999 [53]

Waveband (nm)	HbO <sub>2</sub> (cm <sup>-1</sup> /M)	Hb (cm <sup>-1</sup> /M)
546	48527	51145
560	33763	52893
570	45164	45005
584	33977	33933
590	15598	27699
600	3632	15421

## 5.5. Results and discussion

### 5.5.1. Multispectral images

Figure 5.3 presents a representation of multispectral images of a control rat at normoxia, obtained with the imaging system. The large central vein is the dorsal vein, which lies on the dorsal surface of the spinal cord along the rostral-caudal axis. As evident from the image, numerous tributary veins are visible. The central vein is too large for oximetry analysis due to low optical transmission obtained at all wavelengths used. Instead, the smaller tributary veins on either side of the dorsal vein were assessed for oximetry purposes. As evident from the example

## 5. Oximetry study of vasculature in the rat dorsal spinal cord *in vivo*

---

image, the venules within the field of view possessed varying characteristics, some of which precluded them from analysis. If the vessels were either too small or too large in diameter, or too close to an adjacent vessel to obtain an accurate line profile, they could not be accurately analysed for oximetry purposes. The following inclusion criteria were applied to all vessels in order to ascertain whether or not they should be analysed:

1. Vessels with diameter between approximately 50  $\mu\text{m}$  and 130  $\mu\text{m}$ ; vessels outwith this region resulted in transmission values either too low or too high for accurate oximetry.
2. Vessels with a clear transverse line profile, at least three times their diameter. This was necessary in order that the profile is free of adjacent vessels which would likely result in errors of optical transmission calculation and subsequently introduce systemic error
3. Vessels approximately constant in the  $z$  axis - such that they do not lose contrast they move deeper into tissue, or taper due to curvature of the spinal cord tissue.

In terms of the oximetry analysis, the resulting fits of the optical model of transmission to the experimentally determined transmission profiles were good, with resulting  $\text{SO}_2$  approximately constant along the vessels analysed. Figure 5.4 shows an example of optical transmissions  $T(\lambda)$  determined along a vessel section, and the resulting  $\text{SO}_2$  profile.

### 5.5.2. Changes in inspired oxygen

In order to validate the sensitivity of the oximetry technique to changes in venous oxygen saturation, the control data was first analysed. As the state of inspired oxygen was varied, it was expected to see a corresponding change in venous  $\text{SO}_2$  as compared to the baseline value at normoxia. The measured dorsal venous  $\text{SO}_2$

## 5. Oximetry study of vasculature in the rat dorsal spinal cord *in vivo*

---

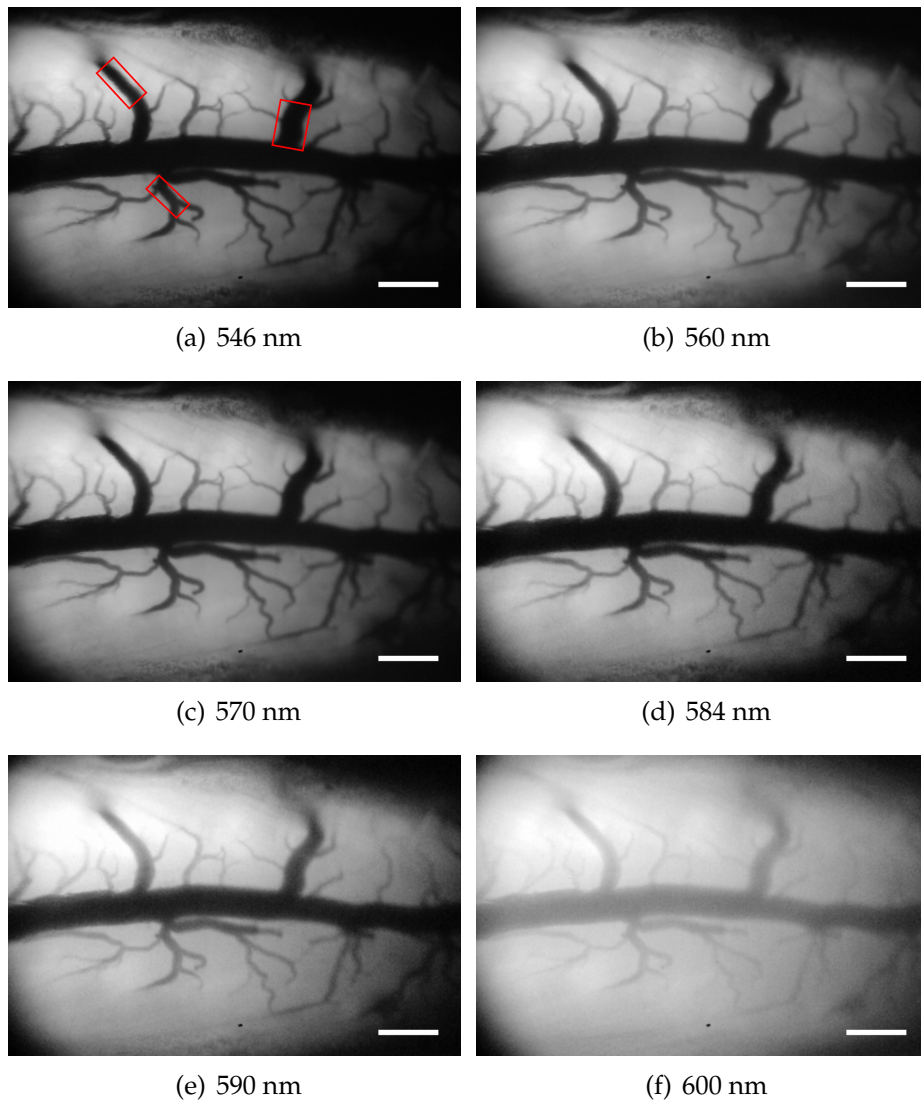


**Figure 5.3.** Examples of multispectral images of control rat dorsal spinal cord. The main dorsal vein lies in the centre on the dorsal surface of the spinal cord, with numerous visible tributary veins joining the larger vessel. Regions of interest for  $\text{SO}_2$  analysis are indicated in red on figure 5.3(a); in focus vessels with clearance on either side are required for determination of intensity profiles and  $\text{SO}_2$ . The scale bars represent  $500 \mu\text{m}$ .

## 5. Oximetry study of vasculature in the rat dorsal spinal cord *in vivo*

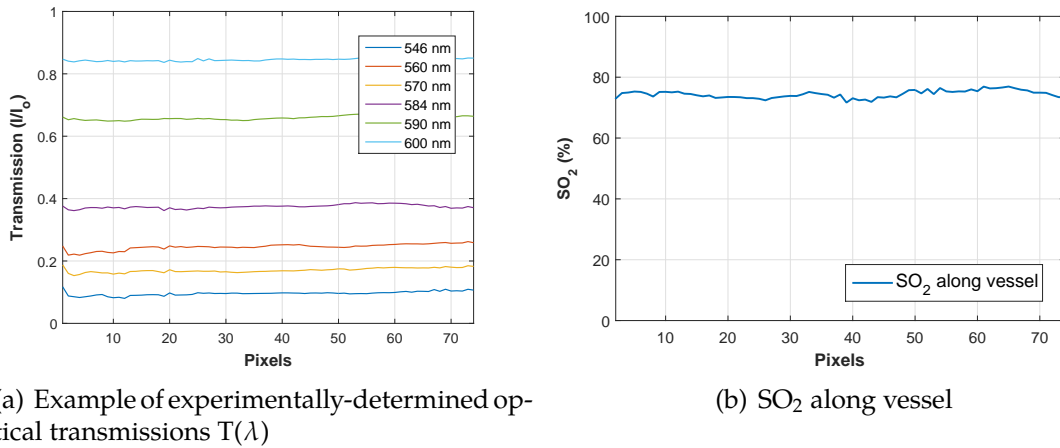


**Figure 5.4.** Example of optical transmissions  $T(\lambda)$  and  $SO_2$  along vessel - high SNR images resulted in consistent optical transmissions determined along vessels and hence  $SO_2$  profiles.

of all control rats across each state of inspired oxygen is depicted in figure 5.5, with actual values given in table 5.4. Three repeated measurements were taken at each rat, and for each state of inspired oxygen. The data for the “hypoxia 2” state is omitted for Rat 1, as it died before this oxygenation state. The differences in average  $SO_2$  between consecutive  $FiO_2$  states were all statistically significant ( $p < 0.05$ , pairwise  $t$ -test). Further, changes between normoxia 1 and hyperoxia; hyperoxia and normoxia 2; and normoxia 2 and hypoxia 1 were all highly significant ( $p < 0.01$ ).

**Table 5.4.**  $SO_2$  measurements for individual control rats

	Average rat $SO_2 \pm$ standard deviation (%)					Change ( $p$ -value)
	Rat 1	Rat 2	Rat 3	Rat 4	Average	
Normoxia 1 (21% $FiO_2$ )	74.6 $\pm$ 0.1	53.1 $\pm$ 0.5	65.8 $\pm$ 6.6	77.9 $\pm$ 1.9	67.8 $\pm$ 10.4	n/a
Hyperoxia (100% $FiO_2$ )	90.5 $\pm$ 0.3	65.2 $\pm$ 1.93	86.1 $\pm$ 8.3	90.6 $\pm$ 2.3	83.1 $\pm$ 11.6	<0.01
Normoxia 2 (21% $FiO_2$ )	72.2 $\pm$ 6.4	51.4 $\pm$ 2.1	68.1 $\pm$ 4.7	78.0 $\pm$ 0.2	67.4 $\pm$ 10.9	<0.01
Hypoxia 1 (18% $FiO_2$ )	39.6 $\pm$ 12.7	36.9 $\pm$ 6.2	57.7 $\pm$ 7.2	69.4 $\pm$ 0.7	50.9 $\pm$ 15.5	<0.01
Hypoxia 2 (15% $FiO_2$ )	N/A	12.2 $\pm$ 4.7	13.8 $\pm$ 6.00	61.5 $\pm$ 3.4	29.2 $\pm$ 24.6	<0.05

## 5. Oximetry study of vasculature in the rat dorsal spinal cord *in vivo*

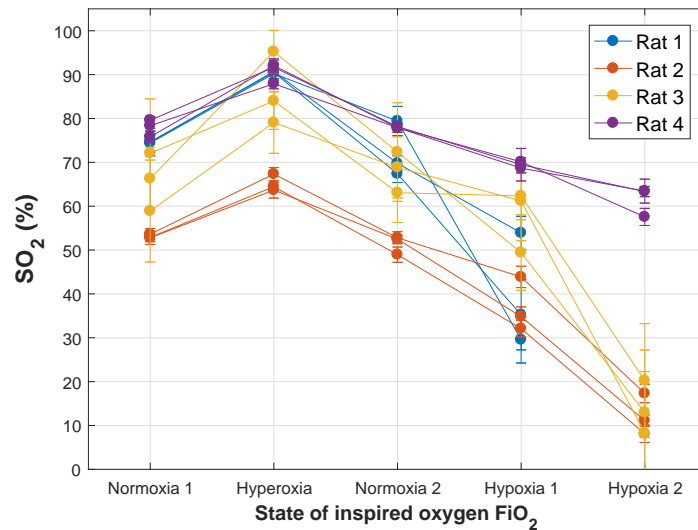


**Figure 5.5.** Results for control dorsal venous SO<sub>2</sub>, presented as average for individual multispectral acquisitions (3 per rat)  $\pm$  standard deviation along each individual vessel

Figure 5.6 shows the average values from the above data in table 5.4. As evident from the data, physiologically plausible values for average venous SO<sub>2</sub> were produced. Normal venous SO<sub>2</sub> values usually lie within 65% - 75% [173]. The average values for the two measured normoxia states were  $67.8 \pm 10.4\%$  and  $67.4 \pm 10.9\%$  respectively, in good agreement with expected SO<sub>2</sub>.

In order to further validate the changes in venous oxygen saturation, measurements simultaneously acquired with a pulse oximeter collar were analysed and the average results for each oxygenation state are also given in figure 5.6. This data was acquired by continuously measuring the arterial SO<sub>2</sub>, with the collar placed around the neck of the rat. The changes in venous SO<sub>2</sub> observed throughout the experiment were strongly correlated with changes in arterial SO<sub>2</sub>, as measured by the pulse oximeter. Comparing the pulse oximeter SO<sub>2</sub> values to venous SO<sub>2</sub> values reported for each image at the specific time-point, the calculated Pearson correlation coefficients  $r$  were 0.74, 0.79, 0.98 and 0.88 for each control rat respectively ( $p < 0.01$ ).

It is noted that there was considerable variation in baseline normoxia values for

## 5. Oximetry study of vasculature in the rat dorsal spinal cord *in vivo*

these control animals, with reported venous  $\text{SO}_2$  ranging from 53% to 78% - which is the cause for the relatively large standard deviation of the average normoxia 1 measurement (10.4%). We did not find a significant correlation between this baseline normoxia  $\text{SO}_2$  and baseline arterial  $\text{SO}_2$ . The origin of this variation is thought to be physiological. Some variation is expected between rats due to potential differences in depth of anaesthesia and the temperature of the exposed spinal cord, both of which can affect blood oxygen saturation.

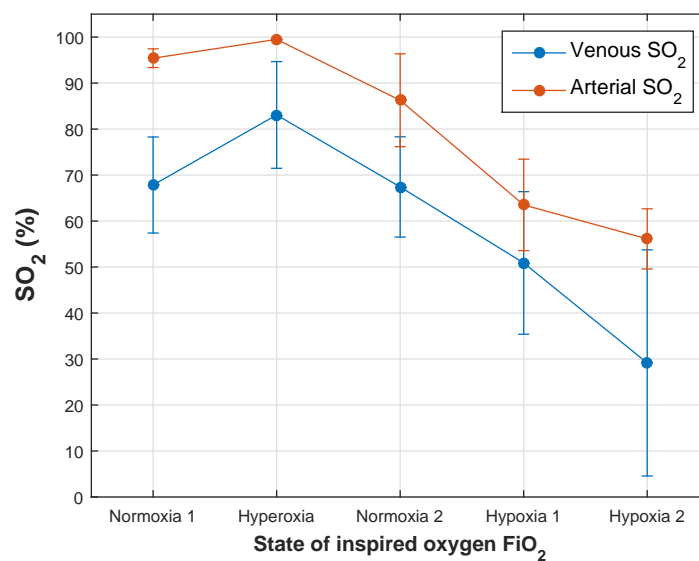


**Figure 5.6.** Results for dorsal venous  $\text{SO}_2$ , as produced by the MSI oximetry algorithm, and arterial  $\text{SO}_2$  recorded simultaneously with pulse oximeter collar (mean  $\pm$  standard deviation)

### 5.5.3. Repeatability of measurements

An important issue related to the measurement of oxygen saturation is the repeatability of the system. Clearly, comparing the reported  $\text{SO}_2$  values for different rats or vessels is not a good indicator of repeatability, as local variations are expected between rats and even between individual vessels. In order to quantify the repeatability of the system, the three repeated measurements of  $\text{SO}_2$  for each given vessel at baseline normoxia were assessed. By comparing measurements from the

## 5. Oximetry study of vasculature in the rat dorsal spinal cord *in vivo*

same vessel, physiological variations are expected to be minimum. The average standard deviation of repeat measurements across all vessels and animals was  $\pm 2.28\%$ . This deviation was much lower than the changes in  $\text{SO}_2$  resulting from changes in  $\text{FiO}_2$  as indicated in table 5.4, indicating sufficient repeatability over individual vessels for measuring changes in  $\text{SO}_2$ . Further, it supports the assumption made in the previous section that differences in measurements of baseline  $\text{SO}_2$  are physiological in origin and not due to inaccuracies within the imaging system or oximetry technique.

### 5.5.4. Comparison of control and EAE vasculature

The venous  $\text{SO}_2$  measurements for individual EAE rats are presented in figure 5.7, with numerical values given in table 5.5. Data for the “hypoxia 2” state of rat 8 is omitted due to its death after the “hypoxia 1” oxygenation state. For EAE rats there was also a spread in baseline normoxia values; the variation between rats was greater than the variation between control measurements. Baseline normoxia values for EAE rats varied between 31.4 % and 72.0 %, giving a standard deviation between rats of 15.1%.

**Table 5.5.**  $\text{SO}_2$  measurements for individual EAE rats

	Average rat $\text{SO}_2 \pm$ standard deviation (%)					
	Rat 5	Rat 6	Rat 7	Rat 8	Rat 9	Average
Normoxia 1 (21% $\text{FiO}_2$ )	65.3 $\pm$ 1.5	72.0 $\pm$ 5.5	47.2 $\pm$ 2.6	48.1 $\pm$ 1.8	31.4 $\pm$ 1.0	52.8 $\pm$ 15.1
Hyperoxia (100% $\text{FiO}_2$ )	80.3 $\pm$ 5.5	81.1 $\pm$ 2.5	64.9 $\pm$ 3.0	71.4 $\pm$ 10.5	50.5 $\pm$ 0.7	69.6 $\pm$ 12.6
Normoxia 2 (21% $\text{FiO}_2$ )	70.2 $\pm$ 7.0	84.6 $\pm$ 4.3	60.8 $\pm$ 4.3	54.4 $\pm$ 1.6	33.6 $\pm$ 5.6	60.7 $\pm$ 18.1
Hypoxia 1 (18% $\text{FiO}_2$ )	54.1 $\pm$ 1.6	63.1 $\pm$ 7.9	52.5 $\pm$ 5.5	26.0 $\pm$ 6.2	15.7 $\pm$ 3.0	42.3 $\pm$ 13.3
Hypoxia 2 (15% $\text{FiO}_2$ )	33.3 $\pm$ 2.7	38.3 $\pm$ 7.0	36.5 $\pm$ 2.6	N/A	5.2 $\pm$ 1.0	28.3 $\pm$ 14.5

The overall average results from table 5.5 are presented in figure 5.8, with the average control values also shown for comparison. These values are summarised

## 5. Oximetry study of vasculature in the rat dorsal spinal cord *in vivo*

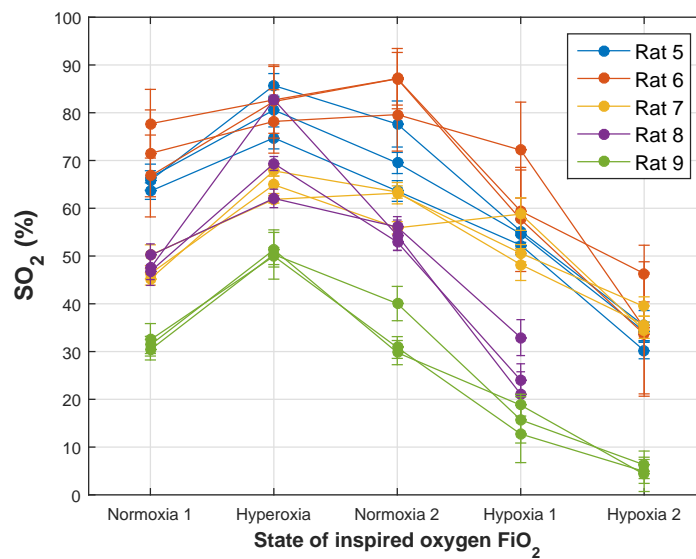


**Figure 5.7.** Results for EAE dorsal venous  $SO_2$ , presented as average for individual multispectral acquisitions (3 per rat)  $\pm$  standard deviation along each individual vessel

again in table 5.6, in which the results of a pairwise  $t$ -test between control and EAE measurements are shown for each oxygenation state. For “normoxia 1”, “hyperoxia”, and “hypoxia 1” oxygenation states, the values for EAE  $SO_2$  are significantly less than controls, with  $p$  values  $< 0.01$  respectively. As evident from the figure and table, there is less of a difference between the  $SO_2$  of EAE rats and controls at “normoxia 2”. Although the average EAE result is less than the control average, it is not significantly different ( $p = 0.25$ ). The reason for this could be due to be a slower response of the inflamed vasculature to return to normoxic baseline levels in the 5 minutes between cessation of hyperoxic  $FiO_2$  and imaging again at normoxia. The average decrease in  $SO_2$  between “hyperoxia” and “normoxia 2” was  $\sim 16\%$  for control rats, but only  $\sim 9\%$  for EAE. The average values for the “hypoxia 2” state, comparing control and EAE rats are not significantly different, with values of  $29.2 \pm 24.6\%$  and  $28.3 \pm 14.5\%$  respectively, giving a  $p$  value of 0.93. It is possible that the strong level of hypoxia induced by very low  $FiO_2$  influences vascular  $SO_2$  to a much greater extent than hypoxia associated with EAE-induced inflammation.

## 5. Oximetry study of vasculature in the rat dorsal spinal cord *in vivo*

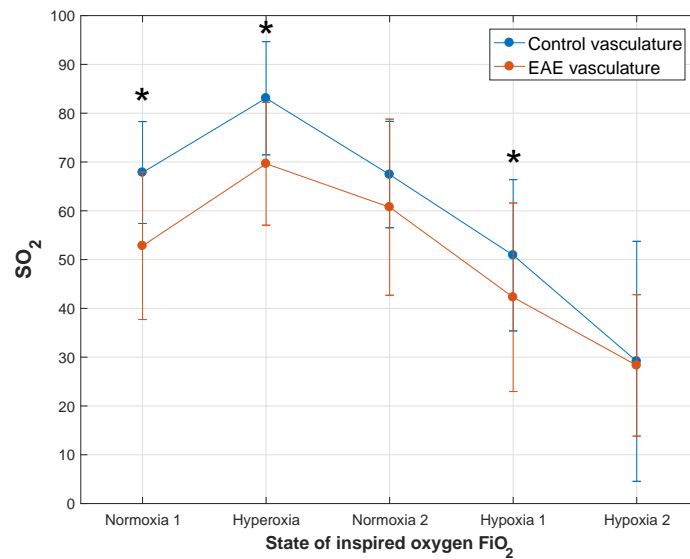


**Figure 5.8.** Comparison of average dorsal venous SO<sub>2</sub>, presented as mean ± standard deviation of values for each rat. Asterisks indicate oxygenation states for which a statistically significant difference was found between control and EAE ( $p < 0.01$ ).

**Table 5.6.** Comparison of average SO<sub>2</sub> values (± standard deviation) for control and EAE rats with results of paired *t*-test between values

Oxygenation state	Control SO <sub>2</sub> (%)	EAE SO <sub>2</sub> (%)	<i>p</i> value
Normoxia 1 (21% FiO <sub>2</sub> )	67.8 ± 10.4	52.8 ± 15.1	<0.01 *
Hyperoxia (100% FiO <sub>2</sub> )	83.1 ± 11.6	69.6 ± 12.6	<0.01 *
Normoxia 2 (21% FiO <sub>2</sub> )	67.4 ± 10.9	60.7 ± 18.1	0.25
Hypoxia 1 (18% FiO <sub>2</sub> ) *	50.9 ± 15.5	42.3 ± 19.3	<0.01 *
Hypoxia (15% FiO <sub>2</sub> )	29.2 ± 24.6	28.3 ± 14.5	0.93

### 5.5.5. Assessment of vessel diameter

In order to assess the effect of vessel diameter on reported  $\text{SO}_2$  measurements, if any, the diameter values for individual vessels were compiled. The averages for each control rat are summarised in figure 5.7. A pairwise  $t$ -test between all diameter values at consecutive oxygenation states was performed - the results of which are also given in the table. In effect, this test was looking for a significant change in diameter with changes in  $\text{SO}_2$ . The results indicate that there was no relationship between measured  $\text{SO}_2$  and associated vessel diameter for consecutive oxygenation states. Consequently, the significant changes in  $\text{SO}_2$  found for each rat at each subsequent oxygenation state (see figure 5.4) indicate that the reported  $\text{SO}_2$  is independent of diameter within the range of diameters measured.

**Table 5.7.** Vessel diameter measurements for individual control rats

	Average vessel diameter $\pm$ standard deviation ( $\mu\text{m}$ )				Change ( $p$ -value)
	Rat 1	Rat 2	Rat 3	Rat 4	
Normoxia 1 (21% $\text{FiO}_2$ )	104.5 $\pm$ 0.9	87.7 $\pm$ 0.6	59.5 $\pm$ 1.4	100.5 $\pm$ 1.1	n/a
Hyperoxia (100% $\text{FiO}_2$ )	108.1 $\pm$ 0.6	89.8 $\pm$ 1.8	59.3 $\pm$ 1.4	103.0 $\pm$ 3.3	0.89
Normoxia 2 (21% $\text{FiO}_2$ )	105.5 $\pm$ 1.6	87.6 $\pm$ 0.7	57.9 $\pm$ 5.00	97.7 $\pm$ 1.3	0.81
Hypoxia 1 (18% $\text{FiO}_2$ )	107.0 $\pm$ 0.7	86.0 $\pm$ 0.7	60.8 $\pm$ 1.7	99.4 $\pm$ 1.4	0.88
Hypoxia 2 (15% $\text{FiO}_2$ )	N/A	81.7 $\pm$ 0.6	61.7 $\pm$ 1.3	99.3 $\pm$ 0.2	0.34

As was done in chapter 4, the individual  $\text{SO}_2$  measurements for each sample are plotted as a function of measured diameter in figure 5.9. The measurements for each rat are clustered around a small range of diameters (in  $\times$ ) due to the fact that for most measurements, only one vessel was studied repeatedly for all oxygenation states: resulting in a range of  $\text{SO}_2$  values for approximately the same vessel diameter. The Pearson correlation coefficients and statistical significance

## 5. Oximetry study of vasculature in the rat dorsal spinal cord *in vivo*

for each set of measurements are also given in table 5.8. As apparent from the table, only measurements from two of nine rats analysed demonstrated a significant correlation between measured diameter and reported  $\text{SO}_2$ . Further, of the other correlations calculated, there was a mix of negative and positive correlations. Considering these inconsistencies, it was inferred that measured correlations were unlikely to be due to any systematic effect or error. Interestingly, the two correlations which were significant were within the control group. This agrees with results in the previous chapter 4, in which there was a significant correlation between diameter and  $\text{SO}_2$  for the control group only. Whilst for the mouse inflammation study a negative correlation was found, the two significant correlations here were positive. However, there is evidence to suggest that some regulatory mechanism which normally occurs in control animals is disrupted with inflammation and its related hypoxia.

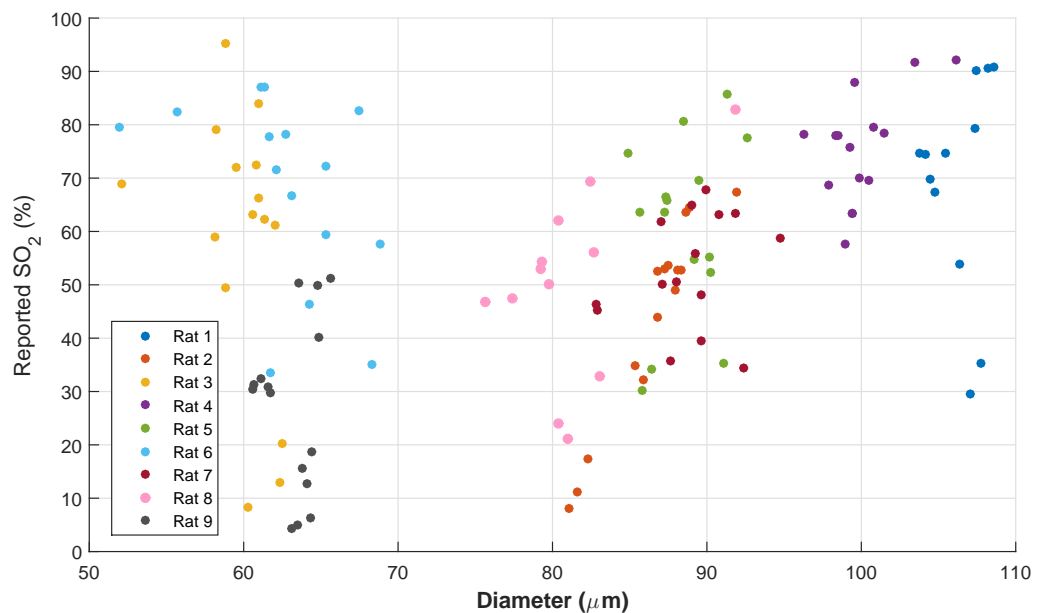


**Figure 5.9.** Reported  $\text{SO}_2$  as function of measured diameter, shown as average values for each oxygenation state for each rat.

**Table 5.8.** Pearson correlation coefficients  $r$  and corresponding statistical significance of correlation between diameter and venous  $\text{SO}_2$  for each rat.

	Rat ID	$r$	$p$ value
<i>Control</i>	1	0.05	0.88
	2	0.96	0.01 *
	3	-0.35	0.21
	4	0.55	0.04 *
<i>EAE</i>	5	0.21	0.45
	6	-0.44	0.11
	7	0.25	0.36
	8	0.49	0.11
	9	0.07	0.81

### 5.5.6. Experimental oximetry validation

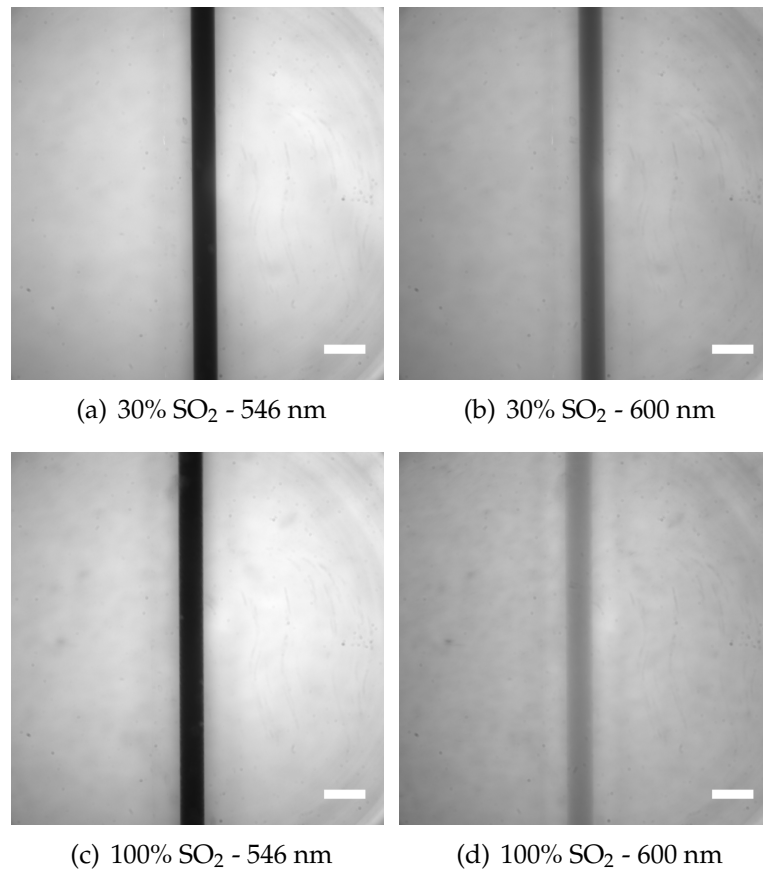
The multispectral imaging system used for the work in this chapter is distinct from that used throughout the other chapters of this thesis. In order to validate the sensitivity of the imaging system to varying levels of oxygen saturation, a phantom representing a blood vessel was imaged. The setup of this phantom was identical to that described in chapter 3, section 3.4 - defibrinated horse blood of specific oxygenations were inserted into a 150  $\mu\text{m}$  FEP capillary. As previously, specific oxygen saturation was achieved by the addition of sodium dithionite to whole blood as described in Briley-Saebø & Bjørnerud (2000) [153]. As with the previous validation of the SC-laser imaging system, the capillaries were placed on a Spectralon background, index-matched with PBS and subsequently imaged. The following  $\text{SO}_2$  values were achieved and imaged: 30%, 40%, 60%, 72%, 86% and 100%. The  $\text{SO}_2$  was verified using a clinical blood gas analyser (BGA).

Figure 5.10 shows example images of the basic phantom at 30% and 100%  $\text{SO}_2$  (as measured with the BGA), imaged at 546 nm and 600 nm. As 546 nm is isosbestic, the optical transmission for both oxygenations shown is equal, and this is reflected in the similar contrast of the phantom in 5.10(a) and 5.10(d). Similarly, as 600 nm is oxygen-sensitive, the optical transmission varies between the two oxygenations

## 5. Oximetry study of vasculature in the rat dorsal spinal cord *in vivo*

---

shown, with vessel contrast different in 5.10(b) and 5.10(d). This is shown quantitatively in figure 5.11 which shows measured optical transmissions from these two oxygen saturations for all six wavebands.



**Figure 5.10.** Example images of vascular phantoms at 546 nm and 600 nm, at two distinct SO<sub>2</sub> levels (30% and 100%). Scale bar represents 200  $\mu$ m.

The raw phantom data was processed with the oximetry algorithm, and initially produced unusual results, with reported SO<sub>2</sub> values saturating across the phantom at 100% for all oxygen saturation values. This unusual result, not previously encountered with the “real” vessel data, suggested some incompatibility between the optical model (assuming a combination of single- and double- pass transmission) and the physical setup of the blood vessel phantom. The plastic FEP, being transparent, should in theory not contribute to or influence measurements of optical transmission. It was considered that the concentration of haemoglobin

## 5. Oximetry study of vasculature in the rat dorsal spinal cord *in vivo*

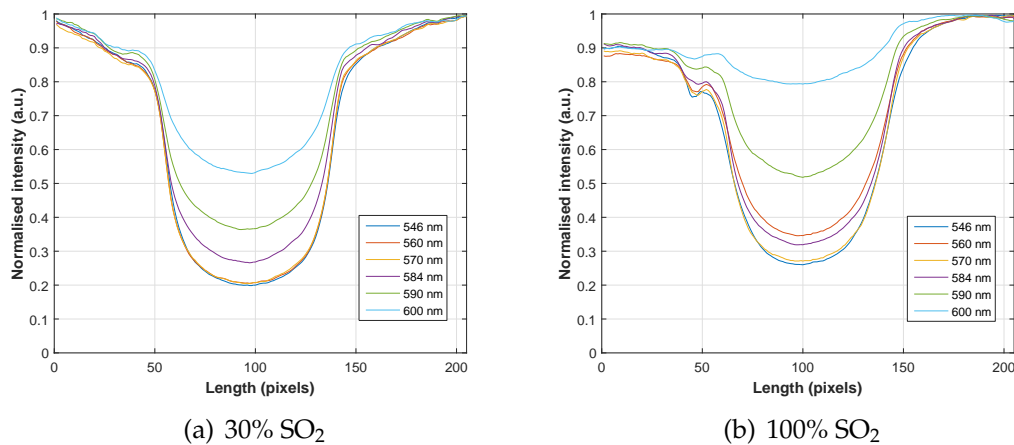


**Figure 5.11.** Comparison of intensity profiles over blood vessel at 30% and 100% SO<sub>2</sub> (as measured with BGA), illustrating distinct optical transmissions.

in this artificial setup may vary significantly from the “standard” value used for *in vivo* analysis. In order to compensate for this, the parameter of haemoglobin concentration was allowed to vary in the least-squares fitting process, from 50% to 150% of the usual value. This seemed to improve the results, with determined oxygen saturation values shown in figure 5.12.

As evident from the figure, although there was an increasing linear trend as expected, there was an over-estimation of SO<sub>2</sub> values as compared to BGA values for all data points under approximately 85%. As discussed in the *in vitro* validation section of 3, validation of absolute SO<sub>2</sub> values remains highly challenging due to the lack of comparative techniques. Clinical BGAs result in precise measurements of SO<sub>2</sub> ( $\pm 2\%$ ). However, it is difficult to gauge whether the insertion of whole blood into narrow capillaries results in re-oxygenation of blood vessels - this may explain the over-estimation resulting from the algorithm. An alternate method of confirming blood SO<sub>2</sub> once it is within the phantom would provide more confidence, however no such other localised “gold-standard” techniques currently exist.

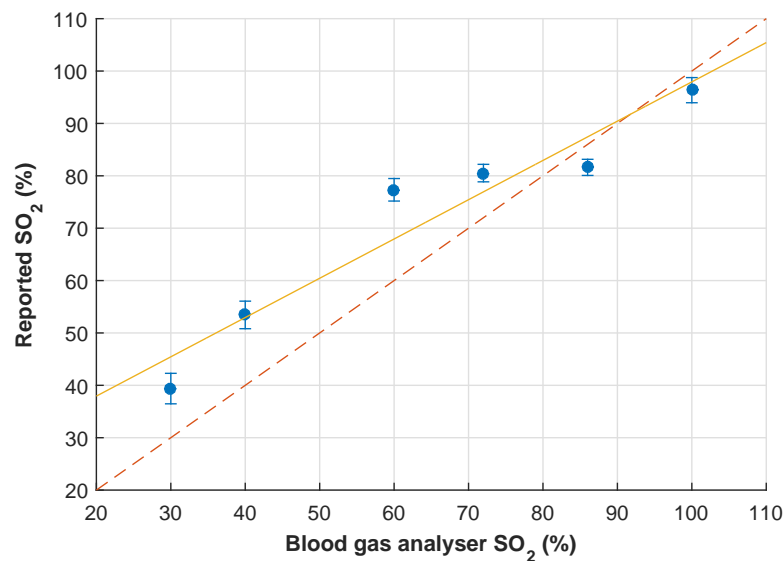


**Figure 5.12.** Validation of SO<sub>2</sub> results for the basic multispectral imaging system and oximetry technique. Linear fit shown in yellow ( $y = 0.75 \cdot x + 23$ ,  $R^2 = 0.92$ ) and 1:1 agreement shown as dashed red line.

### 5.6. Conclusions

In this chapter, a cost-effective, accessible multispectral imaging system was designed and successfully employed for the study of venous SO<sub>2</sub> in the rat dorsal spinal cord. Importantly, the application of the multispectral oximetry algorithm to alternate applications was clearly demonstrated. It was successfully shown that the vasculature of EAE rats was hypoxic compared to controls. In this work, all rats with EAE were of maximum EAE disease model severity, at EAE score 9. Future work related to dorsal spinal cord oximetry could involve determination of correlations between venous SO<sub>2</sub> and EAE score. Further, Hyperbaric oxygen therapy has been reported as a treatment for MS, although its routine use is not recommended due to lack of clinical evidence supporting its efficacy [174]. Further oximetry studies of affected tissue in EAE rats with treatment of such therapy could provide more clinical evidence as to its mechanisms and potential clinical effect.

## 5. Oximetry study of vasculature in the rat dorsal spinal cord *in vivo*

---

As with the results for the previous oximetry study of tendon tissue presented in chapter 4, hypoxia associated with inflammation was successfully quantified. Interestingly, in both cases, results indicate that inflammation is associated with a more heterogeneous distribution of vascular  $\text{SO}_2$ , with higher variability between individual measurements found in inflamed vessels than in controls. These results suggest that the extent of hypoxia within the affected tissue of any individual animal may not be equal in all locations. In terms of using hypoxia as a potential biomarker for disease-related inflammation, and for correlating hypoxia with disease grade, this should be taken into consideration. With heterogeneous  $\text{SO}_2$  within the tissue, it would perhaps be more appropriate to average over individual measurements for potential diagnostic purposes.

The results from the phantom validation of this imaging system and algorithm were promising, showing an expected linear trend - however with an offset of reported  $\text{SO}_2$  for phantoms with lower BGA values. As described in previous chapters, future research is required into alternate methods for accurate deoxygenation of blood. Compared to the “single-pass” analysis performed with the previous imaging system (described in chapter 3), the light paths in this case are more complicated due to the combination of double-pass and single-pass illumination. Further refinement of the algorithm for this light configuration may improve absolute  $\text{SO}_2$  accuracy.

Whilst the system described in this chapter successfully acquired high quality images for oximetry analysis, it does present some limitations. The use of a white LED for the illumination source restricts the range of wavelengths that could potentially be used for image acquisition. For example, the low intensity of the LED below  $\sim 540\text{ nm}$  means that imaging at the highly-absorbing blue wavelengths (410 nm - 450 nm) would likely result in low SNR. Swapping the white LED for a blue LED with stronger signal in this region of the spectrum would be feasible, however the transmission efficiency of the LCTF also decreases in the blue. This limitation, coupled with the low magnification of the object SLR

## 5. Oximetry study of vasculature in the rat dorsal spinal cord *in vivo*

---

lens, means that imaging of the microvasculature is unlikely to be possible with the current imaging system. However, for analysis of larger vessels such as those analysed in this chapter, the imaging system and oximetry technique present a unique capability for robust estimation of localised  $\text{SO}_2$  *in vivo* for a range of applications.

## 6. Minimally invasive oximetry

---

**Summary:** In this chapter, progress made towards extending the multispectral oximetry technique to minimally invasive imaging is described. Incorporation of a miniature, microendoscopic probe to the imaging system is performed, combined with a custom-made triplet fibre illumination setup to retain approximately annular illumination. An assessment of image quality is then described, followed by preliminary oximetry *in vitro* and *ex vivo*.

### 6.1. Introduction

As described in the previous chapters of this thesis, multispectral microvascular oximetry was successfully demonstrated using a multispectral microscope and oximetry algorithm. The technique was applied *in vivo* to tendon microvasculature in mice, and also for measurement of oxygen saturation in the rat dorsal spinal cord. In both cases, surgical removal of tissue was necessary in order to gain optical access to the blood vessels. The imaging objective used for the experiments performed in chapters 3 and 4 was a standard reflective objective; while suitable for the imaging of superficial or exposed tissue, non-invasive optical access to deeper tissue is clearly infeasible due to extensive attenuation of light. For this purpose, minimally invasive imaging appeared to be a potential alternative to invasive surgeries. As discussed in chapter 1, microendoscopic lenses

## 6. Minimally invasive oximetry

---

currently available can provide images at high optical resolution and minimal disruption to tissue - with diameters less than 0.5 mm. To date, vascular oximetry has been predominantly applied to studies in the retina, and as such, the use of microendoscopic probes has not been explored within the field. However, the combination of microendoscopy and multispectral imaging for localised vascular oximetry provides an opportunity for broader applications in deep tissue, and is an area which has yet to be thoroughly investigated.

The number of related studies in the literature is limited. In 1994, Hoper et al. presented a study incorporating a larger endoscope ( $\varnothing = 1.9$  mm) employed for spectrophotometry of albino rabbit retina [175]. In this study, the authors utilised a beamsplitter to split detected white light: 30% was imaged by a camera, and the other 70% was focused onto a spectrophotometer, consisting of a rotating filter disk and photomultiplier tube, for photometric measurements in the region of 502-628 nm. The authors did achieve relatively localised measurements of HbO<sub>2</sub> - however, as the spectral measurement was derived from the entire field of view of the endoscope, a low optical resolution of just 2 mm was demonstrated. Additionally, the wavelengths used for these measurements would have precluded smaller capillaries from the analysis, due to the associated lower extinction coefficients of Hb in the region. The authors optimistically stated that the combination of microendoscopy and spectrophotometry would open a new field of investigation, however there has been a scarcity of related studies in the intervening years; with microendoscopy being utilised more prevalently in fluorescence and multi-photon imaging studies as described in section 1.7.3.

In this chapter, progress is reported of extension to the previously described multispectral microscope with microendoscopes for minimally invasive imaging. By utilising the multispectral techniques and optical oximetry model in conjunction with a microendoscopic probe, it was hoped to gain access to optically inaccessible, deep tissue. Whilst not entirely non-invasive, the nature of the system described in this chapter will allow for longitudinal, repeatable measurements of localised

vascular oximetry in a range of applications. Specifically for the study of rheumatoid arthritis (RA), oximetry studies of microvascular hypoxia in mouse models of RA would be achievable, allowing the same vasculature to be studied over extended time frames. Such longitudinal studies promise to provide localised  $\text{SO}_2$  information which is inaccessible using current bulk oximetry techniques.

### **6.2. Incorporation of microendoscope to multispectral imaging system**

In this section, the incorporation of a microendoscope to the multispectral imaging system is described. Specifically for work in which mouse and rat models will be employed, it is desirable to use as small a probe as possible in order to minimise potential tissue disruption and damage.

A triplet lens microendoscope, as described in section 1.7.2, was acquired for the purposes of this work (GT-IRLS-035-50-20-50-NC *Grintech*). The microendoscope consisted of a long relay lens of NA 0.2, between two identical shorter lenses of NA 0.5, which acted as the imaging and coupling lens respectively. The custom-made GRIN lens triplet had a diameter of  $350\ \mu\text{m}$ , and was surrounded by a metallic sheath for robustness, giving a total outer diameter of  $500\ \mu\text{m}$ . The probe was specified to have a working distance of  $100\ \mu\text{m}$  in air at  $450\ \text{nm}$ , and a physical length of  $9.7\ \text{mm}$ . In order to acquire images, the microendoscope was coupled to the reflective objective of the multispectral imaging system, according to the diagram depicted in figure 6.1.

The probe was held by a small clamp (Micro V-Clamp, *Thorlabs*) secured to an XYZ stage (MT3 XYZ Translation Stage, *Thorlabs*) for accurate placement of the microendoscope. In practice, this setup was achieved by localising the microendoscope to the centre of the field of view of the microscope, and adjusting z-focus

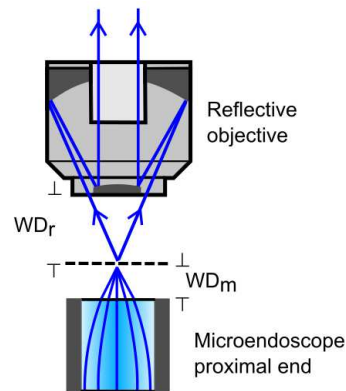


**Figure 6.1.** Illustration of light paths for microendoscope correctly coupled to objective (not to scale), with  $WD_r$  and  $WD_m$  the working distances of the reflective objective (7.8 mm) and microendoscope (100  $\mu\text{m}$ ) respectively.

such that the surface of the microendoscope was in sharp focus. The microendoscope was then offset in the  $z$ -axis by  $-100\ \mu\text{m}$  using a micrometer gauge, equal to its working distance in air. The  $z$ -focus of the reflective objective could also be adjusted, giving an additional degree of freedom. Once the microendoscope was in place, the position of the object could be adjusted independently, using an additional XYZ stage as in chapter 3.

### 6.2.1. Triplet fibre illumination

For minimally invasive oximetry, it was desired to retain approximately annular illumination, as described in chapters 3 and 4 for the previous proof-of-concept work. Direct illumination through the microendoscope was first considered. However, as previously discussed, the working distance of the triplet lens microendoscope was 100  $\mu\text{m}$ . For efficient coupling of the microendoscope to the reflective objective for imaging, the focal plane of the objective must be coincident with the focal plane of the microendoscope. However, this presented problems in terms of propagating illumination from the objective through the microendoscope. As described in chapter 3, a central obscuration in the illumination occurs beyond the focal plane due to the primary mirror of the objective. As the microen-

doscope was aligned in the centre of the field of view of the objective, coupling the illumination into the microendoscope would not be feasible. It would be possible to use an additional lens to offset the illumination focus, as in chapter 3. This would allow a focal spot to be propagated through the probe; however this would result in direct illumination of the field of view. Replicating the annulus of illumination at the distal end of the probe would not be trivial.

An alternative illumination technique was proposed, involving three multi-mode (MM) optical fibres secured about the circumference of microendoscope at approximately equal spacing. Instead of directly illuminating the object through the microendoscope, illumination from the AOTF would be coupled into these optical fibres and delivered about the field of view. In keeping with the previous assumptions made, this technique would still allow for elimination of directly back-reflected light, as well as double-pass illumination. As with the imaging system described in chapter 3, the same assumptions could then be made for the oximetry model of optical transmission. The overall setup is depicted in figure 6.2. The beamsplitter previously utilised was replaced with a mirror. The laser speckle reducer (LSR) was retained; without it, some degree of coherence and laser speckle was found to remain after propagation through the optical fibres.

Multi-mode optical fibre of core diameter  $50\ \mu\text{m}$  was employed for the purposes of illumination (FG050UGA, *Thorlabs*). This fibre had cladding diameter  $125\ \mu\text{m}$  and overall outer coating diameter of  $250\ \mu\text{m}$ . The geometry of the illumination is depicted in figure 6.3. It is known that in fibre optics, the numerical aperture  $\text{NA} = \sin(2\alpha)$ , in which  $2\alpha$  is the maximum acceptance angle. This means that light emerging from the distal end of the fibre will diverge at a maximum of this angle. The low fibre NA of 0.22 ensured that no direct illumination from the fibre would overlap with the field of view. For a working distance of  $100\ \mu\text{m}$ , this results in an illumination spot of  $45\ \mu\text{m}$  diameter.

## 6. Minimally invasive oximetry

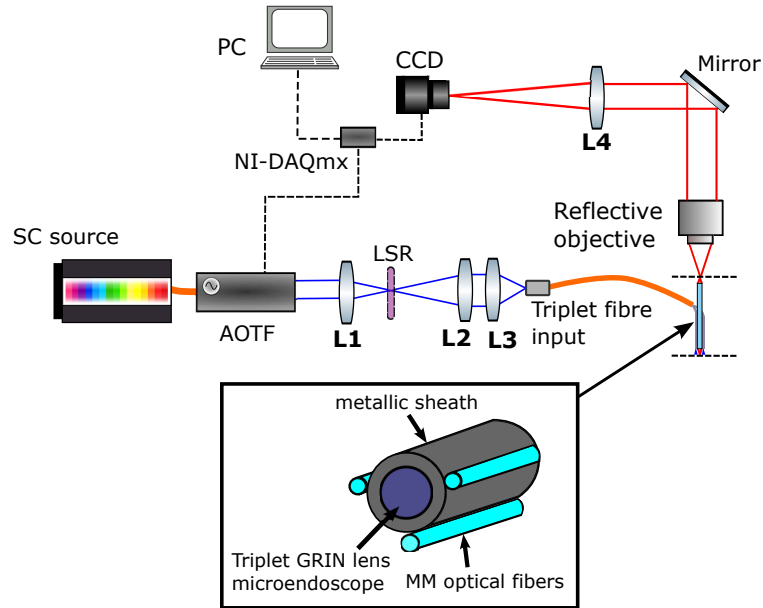


**Figure 6.2.** Schematic of setup for minimally invasive oximetry, in which a triplet set of optical fibres was affixed around the imaging microendoscope for illumination. Illumination path is shown in blue, imaging path in red.

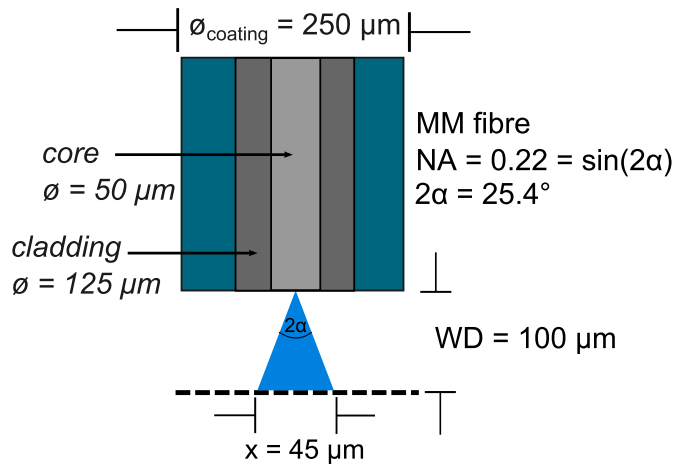


**Figure 6.3.** Geometry of individual fibre illumination output. Situated adjacent to the microendoscope, the small NA ensures that the fibre output 100  $\mu\text{m}$  away from the surface of the fibre (the working distance of the probe) will not directly illuminate the field of view.

## 6. Minimally invasive oximetry

---

In order to maximise the coupling efficiency of illumination from the AOTF into the optical fibres, it was decided to construct a custom setup involving the assembly of all three fibres into a single fibre optic connector. Off-the-shelf components such as 1-3 fan-out fibres do exist, however they are unsuitable due to the fact that they are supplied in thick patch cables and thus difficult to work with in terms of securing the distal ends to the microendoscope. Additionally, by using a custom-made fibre setup, the fibres could be as long or short as necessary in order to suit the specific application. "Connectorizing" optical fibre involves carefully cleaving the end such that it is flat, and stripping the coating from the fibre so it can be secured within an SMA connector ferrule and patch cable - using fibre optic epoxy, a stainless steel crimp sleeve and plastic boot. The epoxy is cured over 24 hours. The fibres must then be polished for efficient coupling of light. This is routinely performed for the assembly of single fibre systems; *Thorlabs* provide a useful guide for the connectorizing and polishing of optical fibre in this manner [176].

For assembly of three fibres within an individual connector ferrule, it was necessary to calculate the minimum inner diameter required to accommodate three individual fibres each of cladding diameter  $125\ \mu\text{m}$  (the larger diameter coating is first stripped). For three circles within a larger circle, Descartes' circle theorem ([177]) states that:

$$\frac{3}{r^2} + \frac{1}{R^2} = \frac{1}{2} \left( \frac{3}{r} - \frac{1}{R} \right) \quad (6.1)$$

where  $r$  and  $R$  are the radii of the smaller and larger circles respectively. This gives:

$$R = \frac{1}{3}(3 + 2\sqrt{3})r = 2.15r. \quad (6.2)$$

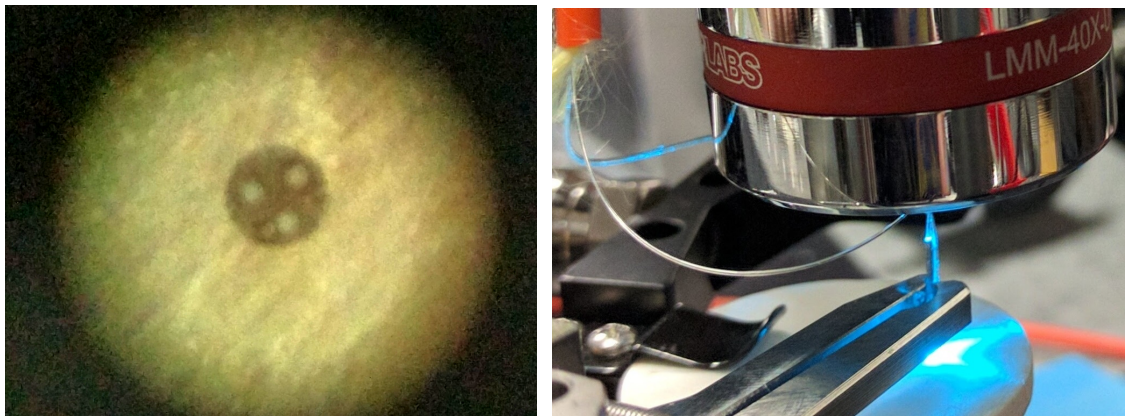
Thus for three fibres of diameter  $125\ \mu\text{m}$ , a connector ferrule of minimum inner diameter  $267.33\ \mu\text{m}$  is required. With this requirement, a ferrule of inner diameter  $270\ \mu\text{m}$  was acquired (SMA905, *Thorlabs*). The fibres were assembled as described in [176], inserting three fibres instead of one. With some practice, this technique worked as expected. A magnified image of a successfully assembled fibre triplet

## 6. Minimally invasive oximetry

**Table 6.1.** Specifications of multispectral imaging system

	<b>Specifications</b>
<b>Mode</b>	Transmission
<b>Wavelengths</b>	410 nm, 420 nm, 430 nm, 435 nm, 440 nm, 450 nm
<b>Spectral resolution <math>\Delta\lambda</math></b>	2 nm
<b>Magnification</b>	40X
<b>Field of view</b>	80 $\mu\text{m}$ diameter
<b>Spatial Resolution</b>	1 $\mu\text{m}$
<b>Sampling rate</b>	2 sec (6-waveband acquisition)

in a connector ferule is depicted in figure 6.4(a). The final issue was securing the loose distal ends of the fibres around the microendoscopic probe. This was performed using UV-cured epoxy (*Norland adhesives*) and tweezers for accurate placement of fibres. UV-curable epoxy was used as it can be easily removed with hot water in the event of a misplaced fibre, and to allow for subsequent re-use of the microendoscope. Figure 6.4(b) shows a completed assembly held in place beneath the reflective objective. The specifications of the imaging system are summarised in table 6.1.



(a) Magnified photograph of three fibers at proximal end of connector (b) Distal end of fibre triplet and microendoscope, held in place with micro v-clamp

**Figure 6.4.** Photographs of assembled fibre triplet for multispectral illumination, at both proximal and distal ends.

Whilst the relatively long working distance of the objective (7.8 mm) allowed for significant clearance, the sharp angle at which the fibres must bend towards the

microendoscope resulted in loss of light through optical fibre leakage, and this is evident in figure (6.4(b)). The patch cable was secured above the objective in an attempt to minimise this issue, however some loss of light seems an inevitable consequence of this illumination configuration. With all wavebands 410 nm - 450 nm switched on, the total AOTF output power was approximately 4.7 mW as measured by a power meter. After propagation through the fibres, the light detected from the distal ends of the fibres had diminished to approximately 10  $\mu$ W.

### 6.3. Assessment of image quality

#### 6.3.1. Basic Zemax model

In order to perform a basic assessment of image quality with the microendoscopic imaging system, it was first desired to quantify expected aberrations using a Zemax optical model. Chromatic aberration was of particular interest, as significant focal shift over the wavelength range would be problematic for sequential multispectral imaging. This would result in defocus of individual wavebands. It is known that GRIN lenses can be associated with significant chromatic aberration [127]. It was set out to investigate the extent of chromatic aberration over the waveband region implemented for oximetry of the microvasculature, between 410 nm and 450 nm. Additionally, an assessment of off-axis aberrations was also required.

Due to the proprietary nature of the *Grintech* microendoscope lenses, specific parameters for designing an accurate model of the custom-built triplet probe were not available. Instead, a more basic model was developed in Zemax, such that the model replicated properties such as physical length of the GRIN lenses, and correct working distance (100  $\mu$ m) of the probe at the nominal wavelength of 450 nm.

## 6. Minimally invasive oximetry

---

In Zemax, GRIN lenses are divided into a series of thin slices, each interpreted as a thin lens. Thus, rays are traced using Snell's law and the refractive index  $n(r)$  at the ray's intersection with the slice. The thickness of each slice is defined as a parameter  $\Delta T$  in Zemax. Higher ray-tracing accuracy is achieved with smaller values of  $\Delta T$ , but increases computational demand. A value of  $100\ \mu\text{m}$  for  $\Delta T$  was used for the model implemented in this chapter. For the glass type, the Zemax surface "gradient 5" was used, having a feature which allows for consideration of dispersion properties of the medium. This surface has the following form, where  $n(r)$  is its base index of refractions:

$$n(r) = n_o + (N_{r2})r^2 + (N_{r4})r^4 + (N_{z1})z + (N_{z2})z^2 + (N_{z3})z^3 + (N_{z4})z^4 \quad (6.3)$$

where  $r = x^2 + y^2$ , the radial distance from the centre of the lens.

A base refractive index of 1.52 was chosen for the three constituent lenses (the typical refractive index of crown glass), with  $N_{r2}$ ,  $N_{r4}$ ,  $N_{z1}$  and  $N_{z2}$  set as variables to be optimised by the Zemax merit function. For simplicity, the higher order coefficients  $N_{z3}$  and  $N_{z4}$  were fixed at zero. The imaging and coupling lenses were known to be  $0.572\ \text{mm}$  each, with the lower NA relay lens  $8.56\ \text{mm}$  in length, so these parameters were also fixed. For a point source set  $100\ \mu\text{m}$  away from the proximal end of the microendoscope, the merit function was defined to minimise the RMS spot size of the PSF at  $100\ \mu\text{m}$  away from the distal end of the probe, for a wavelength of  $450\ \text{nm}$ . From the optimisation process, parameters were determined and these are indicated in table 6.2. It should be noted that the true parameters of the microendoscopes used in this thesis may be different to those employed for this ray-tracing model. However, due to the unavailability of the exact parameters, this basic model was expected to give a best estimate of expected optical performance and aberrations resulting from the use of a triplet GRIN lens microendoscope for imaging.

The resulting model is shown in a 2D layout diagram in figure 6.5. Three input

## 6. Minimally invasive oximetry

**Table 6.2.** Parameters used for generation of Zemax optical model of microendoscope

	Glass	$\Delta T$	n0	$N_{r2}$	$N_{r4}$	$N_{z1}$	$N_{z2}$	$N_{z3}$	$N_{z4}$
Imaging lens	GTLIVIS	0.1	1.52	-4.449	15.796	4.816	-5.523	0.000	0.000
Relay lens	GTLIVIS	0.1	1.52	-0.655	0.045	0.252	$-8.46 \times 10^{-4}$	0.000	0.000
Coupling lens	GTLIVIS	0.1	1.52	-4.449	15.796	4.816	-5.523	0.000	0.000

point sources were considered and are shown in the figure; one on-axis central point source, and two off-axis point sources at  $(0, 40 \mu\text{m})$  and  $(0, -40 \mu\text{m})$  respectively. The value of  $40 \mu\text{m}$  offset was chosen as it is approximately half the field of view of the microendoscope. Recalling the discussion in chapter 1, section 1.7.2, the field of view can be defined as:

$$\text{FOV} \approx \varphi \left( \frac{l_{IL}}{l_{RL}} \right) \quad (6.4)$$

where  $l_{IL}$  and  $l_{RL}$  are the pitch lengths of the imaging lens and relay lenses respectively. For pitch lengths of 0.23 and 1, this results in a conservative estimate of FOV around  $80 \mu\text{m}$ . Consideration of these off-axis point sources allows for the evaluation of expected off-axis aberrations for this triplet microendoscope setup, by observation of the respective point spread function (PSF).

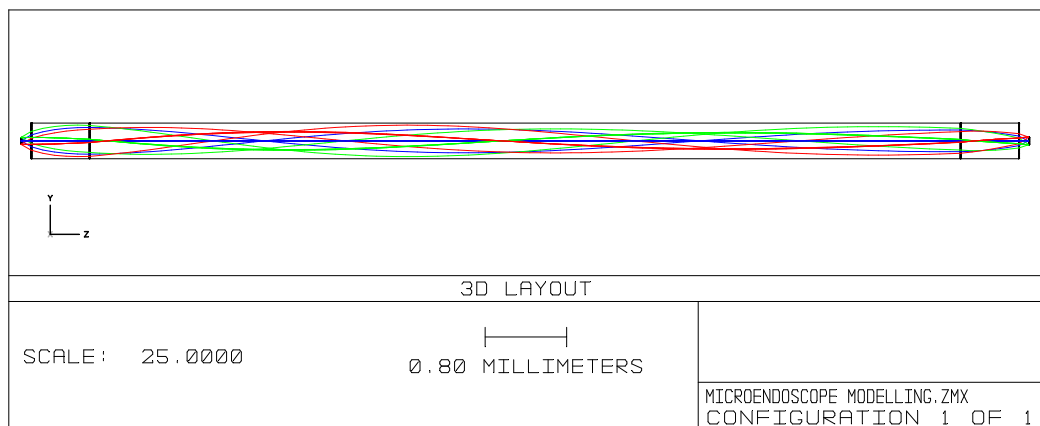


**Figure 6.5.** Illustration of Zemax microendoscope model with on-axis ( $y = 0 \mu\text{m}$ , blue) and off-axis ( $y = \pm 40 \mu\text{m}$ , green and red) input rays

This model was used to generate an assessment of chromatic aberration by plotting

## 6. Minimally invasive oximetry

---

the focal shift as a function of wavelength. This is shown in 6.6, with a reported maximum value of  $-2.52 \mu\text{m}$ . In conjunction with additional aberration introduced by the imaging lens of the microscope (not included in the model), the focal shift is likely to be slightly larger than this value. However, over the 40 nm wavelength range, even if slightly under-estimated, the extent of the focal shift is not expected to be prohibitively large for sequential multispectral imaging.

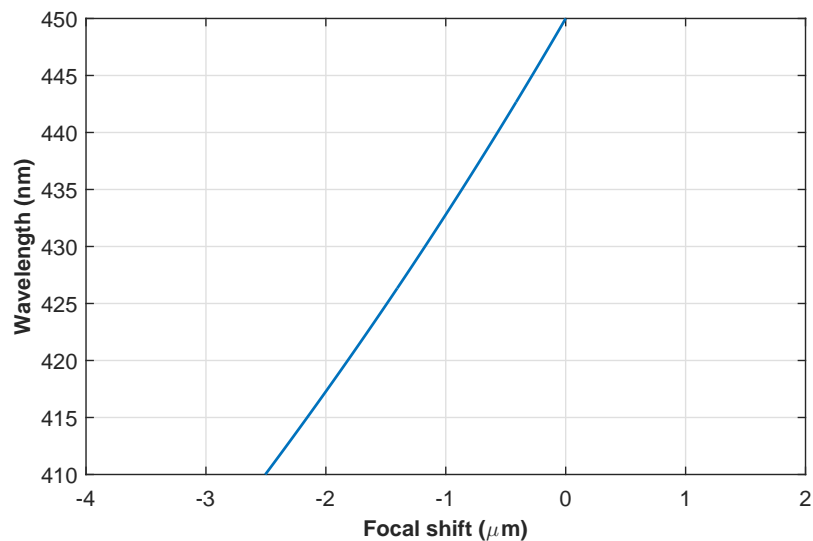


**Figure 6.6.** Results from Zemax model depicting chromatic focal shift with wavelength for triplet lens microendoscope, maximum focal shift  $2.52 \mu\text{m}$

A PSF spot diagram was then generated for all three field components (on and off-axis respectively) for defocus from  $-4 \mu\text{m}$  to  $+4 \mu\text{m}$  in  $2 \mu\text{m}$  increments. This is shown in figure 6.7. For the on-axis point source, the PSF at zero defocus retained its radially symmetric form, with the focal spot of the 450 nm wavelength being in best focus as expected. The RMS spot size of this PSF was reported to be  $1.24 \mu\text{m}$  diameter (including all three input wavelengths). This is in general agreement with measurements made by other groups reporting lateral optical resolution of  $1\text{-}2 \mu\text{m}$  in probes of near 0.5 NA [42]. However, as clearly evident from the graph, the off-axis point sources result in asymmetrical PSFs caused by off-axis aberrations. Analysis of the Zernike polynomial coefficients for the off-axis field revealed the primary optical aberrations to be predominantly spherical

## 6. Minimally invasive oximetry

aberration, coma and astigmatism. The characteristic “comet” shape of the coma aberration is clearly visible for the off-axis field components at negative defocus. Correction of optical aberrations is possible using techniques such as adaptive optics [178]; however this topic is not addressed in this thesis.

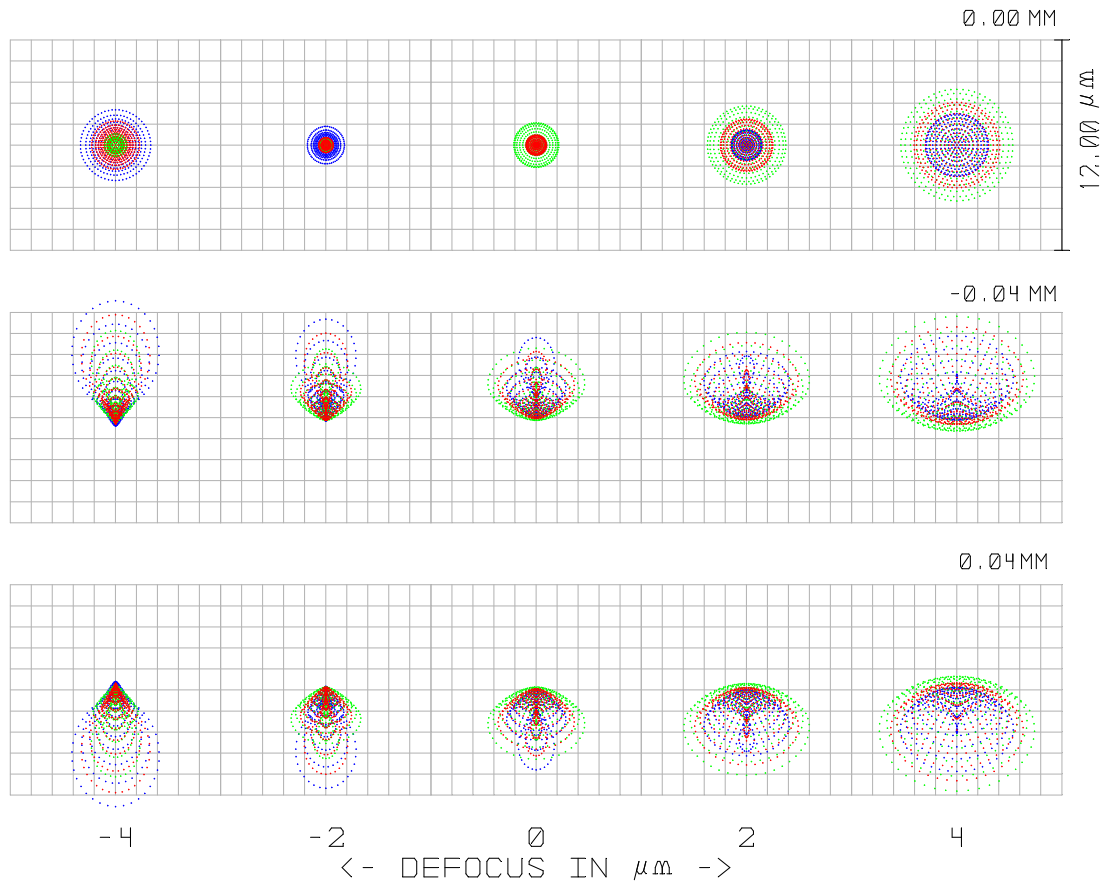


**Figure 6.7.** Zemax plot of PSF spot diagram through focus for three wavelengths: 410 nm (green), 430 nm (red) and 450 nm (blue).

### 6.3.2. Resolution and contrast modulation

In order to empirically assess the resolution of the imaging system as a whole, a resolution target (USAF 1951) was placed in the imaging plane of the system and imaged with transmission illumination. This was provided by diffuse LED light of central wavelength 530 nm underneath the target. The resulting image is shown in figure 6.8. Of the visible groups within the target, element two of group nine

## 6. Minimally invasive oximetry

---

is the smallest resolvable feature, which is  $0.87\ \mu\text{m}$  in width. Recalling that the Rayleigh criterion for optical resolution is defined as the smallest distance between two resolvable features, the actual resolution was determined to be approximately  $1.74\ \mu\text{m}$ . In terms of imaging of the microvasculature, the smallest capillaries are approximately  $10\ \mu\text{m}$  in diameter. Hence, the resolution of the minimally invasive imaging system was deemed sufficient to resolve these vessels of interest.

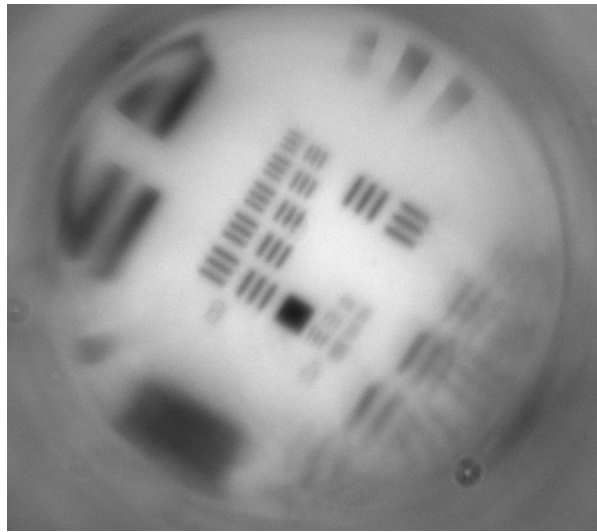


**Figure 6.8.** Image of USAF resolution target through microendoscope. Group 9 Element 2 is the smallest resolvable feature at  $0.87\ \mu\text{m}$ .

Another issue that was of interest was the contrast modulation provided by the microendoscope of the image of a knife-edge (sharp boundary between dark and light area in image). This test was previously performed for the multispectral microscope as described in section 3.3.

As evident in figure 6.9, the expected vignetting associated with microendoscopic imaging is present. The contrast modulation  $C_m$  was calculated, as in chapter 3, as  $C_m = (I_H - I_L)/(I_H + I_L)$ , where  $I_H$  and  $I_L$  are high and low reference intensities respectively. For this test, a comparison was made between transmission illumination and fibre triplet illumination. The maximum contrast modulation (as measured in the centre of the field of view) was found to be approximately 0.52 for transmission illumination with an LED ( $\lambda = 530\ \text{nm}$ ,  $\Delta\lambda$  (FWHM) = 33 nm), and

## 6. Minimally invasive oximetry

---

increased to 0.61 for the fibre triplet illumination. These values were significantly decreased as compared to the  $C_m$  of the imaging system with no microendoscope (0.9 as described in chapter 3); however this was to be expected due to the aberrations introduced by the GRIN lens. The difference in contrast modulation with illumination type was thought to be due to the narrower bandwidth of the AOTF through the optical fibre as compared to the green LED. Lower chromatic aberration was thus associated with the fibre illumination. For both cases, the contrast appeared to fall off towards the edges of the microendoscope due to expected vignetting. A line profile taken across the field of view of this grid target image is shown in figure 6.10, and clearly depicts this fall-off in intensity and contrast.

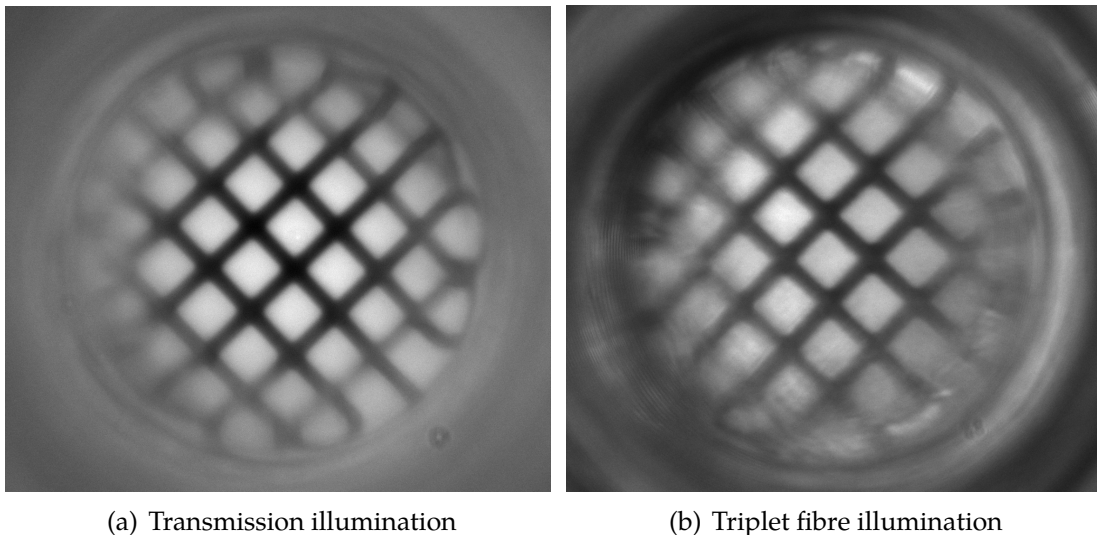


**Figure 6.9.** Comparison of 20  $\mu\text{m}$  grid target images through microendoscope, with transmission illumination and fibre triplet illumination

Errors may arise due to the fact that contrast loss is not constant over the field of view. It is expected that loss of image contrast introduced by the microendoscope may be compensated for by the contrast parameter  $K$  of the optical oximetry model. For microvasculature which is analysed across the field of view, the value of  $K$  would be expected to increase radially with decreasing contrast. In the current form of the optical oximetry model, the  $K$  parameter is allowed to vary across the vessel, and in theory should be able to compensate for this variation.

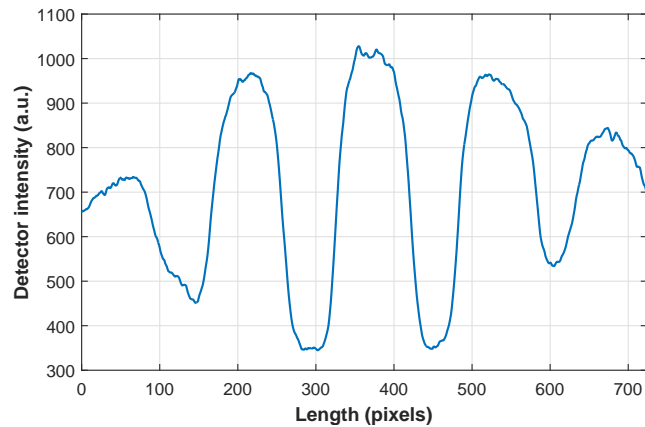


**Figure 6.10.** Line profile across 20  $\mu\text{m}$  grid target imaged through microendoscope. Note the decrease in contrast towards the edges of the field of view.

However, as discussed in chapter 2, higher values of  $K$  are associated with a higher uncertainty in  $\text{SO}_2$  due to increased photometric error. Also, as previously mentioned, increased optical aberration is associated with objects imaged off-axis through microendoscopy. As such, it was decided to consider only the central region of the FOV, which was in good focus. In practice this effectively reduced the usable FOV for oximetry purposes, but still remained sufficient for imaging of the small microvascular vessels.

### 6.4. *Ex vivo* minimally invasive oximetry

Following the development of the combined microendoscope and multispectral imaging system, it was possible to perform initial *ex vivo* imaging of the vasculature and an assessment of associated oximetry results. In chapter 3 for *ex vivo* oximetry validation, the tissue was placed in a chamber through which a nitrogen flow was delivered to prevent re-oxygenation. Cessation of this flow resulted in oxygenation of the vasculature by air, which was detected by the bulk microscope. Unfortunately, a nitrogen gas supply was unavailable at the time of this minimally invasive work. Consequently the *ex vivo* experiment performed for

## 6. Minimally invasive oximetry

---

the bulk microscope in chapter 3 could not be repeated with the adapted setup for microendoscopy. In order to provide a preliminary assessment of the ability of the system to resolve  $\text{SO}_2$  in *ex vivo* microvasculature, a repeatability study was performed on an intact mouse tendon. Superficial vessels were exposed as before, such that they would re-oxygenate in air. The vasculature was then imaged through the microendoscope at multiple scenes within the tendon, with the assumption that all microvasculature would be oxygenated. An example of an image of the microvasculature, which was acquired with all six wavebands switched on, is shown in figure 6.11.

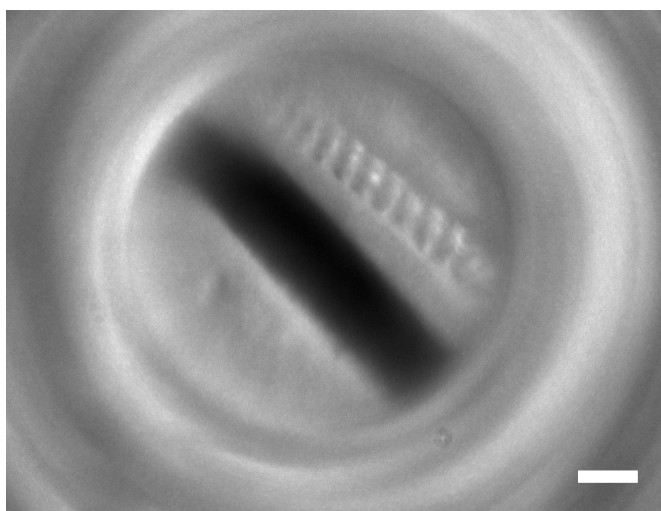


**Figure 6.11.** Example image of *ex vivo* microvasculature through microendoscope, illuminated with adjacent fibre triplet (410 nm-450 nm bands all switched on). Scale bar represents 20  $\mu\text{m}$ .

A group of 9 multispectral datasets were acquired at different scenes, and were analysed for oximetry using the algorithm previously employed. It was chosen to analyse only sections of the vessel within the central region of the microendoscope, as discussed above. An initial assessment of image quality determined that for the exposure times previously utilised with the bulk microscope (100 ms for 410 - 440 nm, 200 ms for 450 nm), the signal intensity was not adequate in this case due to the loss of light through the optical fibres. Measurement of transmitted light intensity with a power meter determined that only approximately 10  $\mu\text{W}$

## 6. Minimally invasive oximetry

---

was being propagated through the fibres. This low intensity was likely caused by a combination of poor coupling of light into the fibres as a result of suboptimal polishing. In addition, further light may have been lost through leakage as discussed previously.

As such, exposure time was increased to 1 s for all wavebands in order to achieve higher image intensity. The results of the analyses are displayed in table 6.3, which displays resulting  $\text{SO}_2$  (average  $\pm$  standard deviation) along the vessel, and corresponding contrast factors  $K$  and goodness of fit  $R^2$ . As evident from the figure, the quality of these initial results were poor; although the average  $\text{SO}_2$  for all vessels was determined to be 99%, there was a large uncertainty of  $\pm 11\%$  comparing individual vessels. There was general agreement in the value of contrast factor  $K$ , determined as  $0.228 \pm 0.004$ . However, overall the goodness of fit for all vessels was poor, resulting from the low SNR of individual multispectral images. Using the same quality criteria employed in chapter 4, accepting only those vessels with  $R^2$  value  $\geq 0.9$ , none of the results presented here would be of sufficient goodness of fit.

**Table 6.3.** Results of multiple multispectral measurements for oximetry with microendoscopic imaging

Dataset #	$\text{SO}_2$ (%)	$K$	$\eta$	$R^2$
1	$98 \pm 10$	$0.20 \pm 0.01$	1	0.63
2	$105 \pm 8$	$0.20 \pm 0.01$	1	0.15
3	$111 \pm 10$	$0.15 \pm 0.01$	1	0.52
4	$109 \pm 16$	$0.21 \pm 0.01$	1	0.16
5	$112 \pm 26$	$0.23 \pm 0.02$	1	0.29
6	$100 \pm 41$	$0.27 \pm 0.01$	1	0.03
7	$92 \pm 44$	$0.28 \pm 0.01$	1	0.11
8	$90 \pm 49$	$0.22 \pm 0.01$	1	0.11
9	$78 \pm 55$	$0.29 \pm 0.02$	1	0.02
<i>mean</i>	$99 \pm 11$	$0.23 \pm 0.04$		

In order to investigate the nature of these poor oximetry results, individual multispectral images were assessed. Figure 6.12 demonstrates transverse intensity

## 6. Minimally invasive oximetry

profiles across a vessel imaged through the microendoscope at all six multispectral wavebands. As clearly evident from the intensity profiles in figure 6.12(a), there was a loss of overall signal intensity with decreasing wavelength. The background-subtracted signal levels are shown in the  $y$ -axis. Further, as also shown in the figure, once the profiles were normalised to maximum intensity signal, it was not possible to discriminate between wavelengths. For 12-bit images where the maximum signal level is  $2^{12} - 1 = 4095$ , at low baseline ( $I_o$ ) signals, changes in oxygen saturation may not result in a large change in detected intensity signal  $I$  within the vessel. For example in this case, the  $I_o$  value was approximately 50 greyscale intensity units for the 410 nm waveband. Using a theoretical model of light transmission (as described in chapter 2) for a  $10\ \mu\text{m}$  vessel at  $K=0.2$ , a change in oxygenation from 0% to 100% oxygenation would result in a change of optical transmission from approximately 0.3 to 0.24. For an  $I_o$  of only 50, this translates to a change in greyscale level at  $I$  of only 3; much lower than the variability caused by noise. As such, wavelength-dependent changes in intensity caused by changes in microvascular oxygenation were not expected to be resolvable for this case.

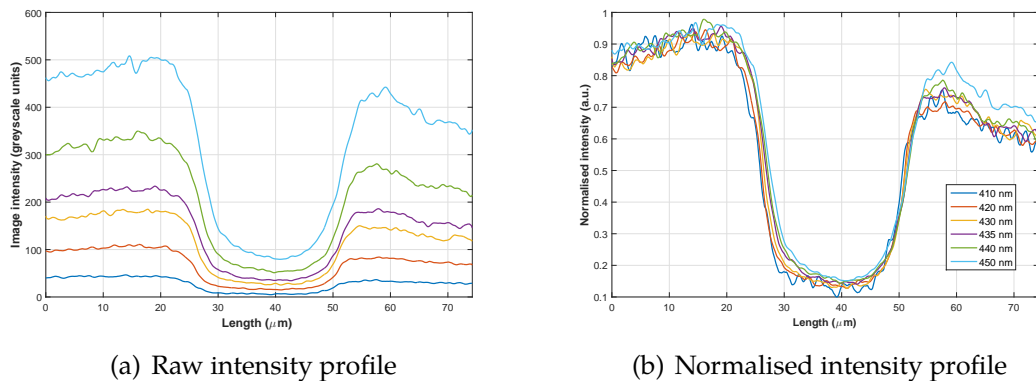


**Figure 6.12.** Waveband-dependent intensity profiles across capillary.

### 6.5. *In vitro* validation

Following the initial *ex vivo* results which raised concerns about signal intensity, it was set out to perform an *in vitro* validation. The aim was to fabricate a blood

## 6. Minimally invasive oximetry

---

vessel phantom using whole horse blood in FEP tubing, on a background of spectralon as previously described in chapter 3. It was assumed that the high albedo of spectralon would allow for higher diffusion of light towards the field of view and hence the CCD, resulting in improved SNR as compared to the *ex vivo* results. As with the previous *in vitro* validation work described in chapter 3, the smallest available FEP was of inner diameter 50  $\mu\text{m}$ . For this validation work, an attempt was made in order to fabricate narrow capillaries by using a dual-stage glass micro-pipette puller ("PC-10", Narishige). These were successfully fabricated with a small length at the end of the pulled glass capillary measuring approximately 5  $\mu\text{m}$  in diameter and placed against a background of spectralon. In previous *in vitro* validation experiments, PBS was used for index matching with the capillary wall so that it did not contribute to the transverse line profiles. For these narrow pulled glass capillaries, the walls were not of significant width and as such index matching was not required. These capillaries showed promise as a more realistic phantom for the small vessels of the microvasculature; allowing for capture of multispectral images at the blue wavelengths used for previous *in vivo* imaging. An example image of one such capillary filled with defibrinated horse blood is shown in figure 6.13.

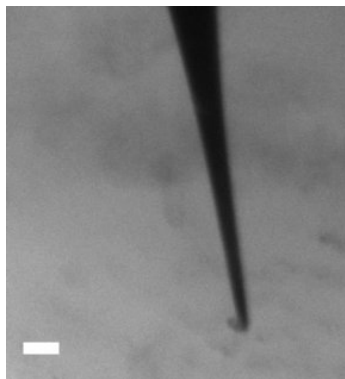


**Figure 6.13.** Image of pulled micro-pipette filled with defibrinated horse blood, on spectralon background; micropipette tip measured approximately 5  $\mu\text{m}$  in diameter. The scale bar represents 10  $\mu\text{m}$ .

Unfortunately, it was difficult to reproducibly fill these small diameters with blood of varying oxygenations; the small capillaries often shattered under the pressure

## 6. Minimally invasive oximetry

---

required to fill the tips with blood. Further, on the occasions that it was possible to successfully fill the capillaries, preliminary measurements made with the bulk microscope found determined  $\text{SO}_2$  to be approximately 20% greater than expected  $\text{SO}_2$  as determined by the BGA. It was thought that delivery of deoxygenated blood into these small capillaries may have resulted in re-oxygenation from the expected values.

Due to the difficulties associated with the micro-pipettes, it was decided to retain the 50  $\mu\text{m}$  FEP for *in vitro* validation of the minimally invasive multispectral system. As vessels of this size are too absorbing of wavelengths between 410 nm and 450 nm, the green-red wavelength regime previously utilised for *in vitro* imaging was implemented once more. The intensity output by the AOTF for these wavelengths was also expected to be higher than in the blue region, further improving SNR.

### 6.5.1. FEP phantoms with green-red wavelengths

As performed for the *in vitro* validation of the bulk microscope in chapter 3, blood-filled FEP capillaries of varying oxygenation were imaged against a spectralon background, covered with a drop of saline for index-matching to the capillary walls. Variation of the oxygen saturation was achieved as before with sodium dithionite, and the resulting oxygenation was validated with a blood-gas analyser. An example of a resulting multispectral image is shown in figure 6.14, with an overlay of  $\text{SO}_2$  along the analysed region of the vessel in the central region of the microendoscope. As evident from the image, the 50  $\mu\text{m}$  capillary occupies a large portion of the central FOV of the microendoscope, where optical aberrations are at a minimum.

As discussed in the previous section, the normalised intensity profiles obtained for the *ex vivo* imaging were indistinguishable from each other due to low SNR. The same results obtained for FEP phantoms *in vitro* at high and low oxygen

## 6. Minimally invasive oximetry

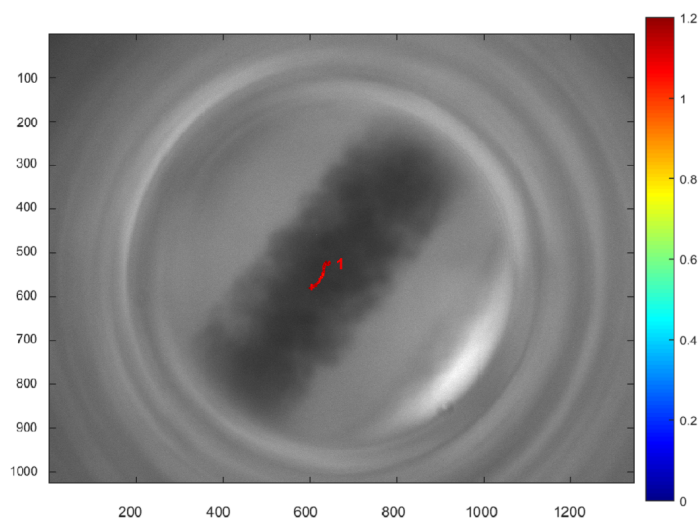


**Figure 6.14.** Image of 50  $\mu\text{m}$  FEP phantom through microendoscope, acquired at 546 nm.

saturation are shown in figure 6.15. In contrast to the previously obtained results, higher absolute signal was observed *in vitro* and hence sufficient discrimination of line profiles and optical transmission with wavelength. In addition, these profiles varied as expected with decreasing oxygenation.

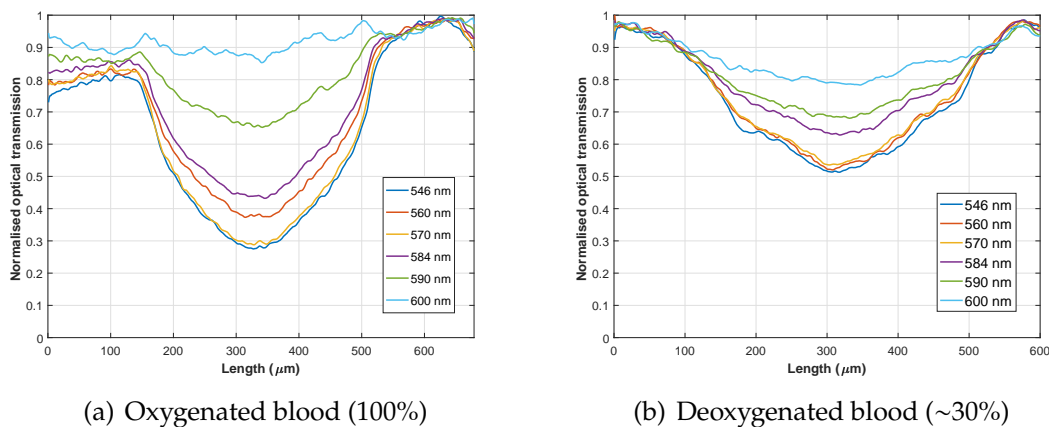


**Figure 6.15.** Waveband-dependent, normalised intensity profiles of phantom imaged through microendoscope at high and low oxygenations

For both vessels from which these line profiles were obtained, the determined  $\text{SO}_2$  is illustrated in figure 6.16. Evidently, the oximetric capability of the imaging system is retained whilst imaging through the microendoscope; for oxygenations

## 6. Minimally invasive oximetry

---

determined by the BGA as 98% and 30.3%, the obtained measurements were in good agreement at  $103 \pm 1.4\%$  and  $26.6 \pm 1.5\%$  respectively. From these results obtained over the green-red visible EM region (546 nm - 600 nm), it can be assumed that for smaller vasculature, oximetry will also be possible using the more highly absorbed blue wavelengths - provided the signal intensity is sufficiently high. For these results, the goodness of fit  $R^2$  values were 0.98 and 0.99 for oxygenated and deoxygenated phantoms respectively; a significant improvement over the results obtained previously for the *in vivo* measurements.

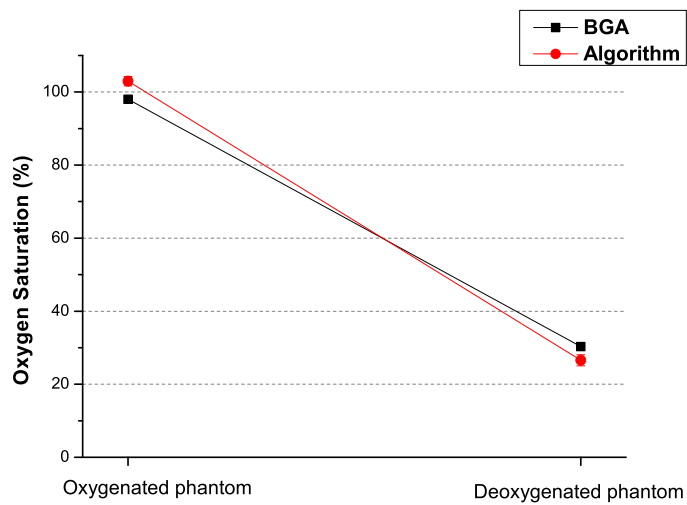


**Figure 6.16.** Obtained  $SO_2$  for microendoscopic imaging of *in vitro* phantom at distinct oxygenations.

## 6.6. Conclusions

In this chapter, adaptations made to the multispectral imaging system from minimally invasive imaging was described. The incorporation of a GRIN lens microendoscope and triplet fibre illumination scheme were successfully achieved, allowing for multispectral imaging in optically inaccessible tissue. Indirect illumination, as previously delivered in the work described in chapters 3 and 4, was retained through the fibre illumination scheme.

## 6. Minimally invasive oximetry

---

With this modified multispectral imaging system, minimally invasive imaging of tendon microvasculature was performed in *ex vivo*, in oxygenated murine tendon microvasculature. Reported oximetry confirmed  $\text{SO}_2$  of the vasculature, albeit with high standard deviation along the vessels analysed, and poor goodness of fit values resulting from poor SNR. Investigative *in vitro* experiments demonstrated improved SNR and waveband-dependent intensity profiles, however it was clear that improvements must be made to the illumination for robust oximetry to be achievable.

The work performed in this chapter highlighted some challenges associated with the use of microendoscopes for vascular imaging. A critical issue for future *in vivo* work will be minimising the integration times required to acquire images with adequate SNR. Motion is often associated with imaging *in vivo* due to e.g. breathing of the animal, but can be minimised by adequately securing the tissue as described in section 4. However, even minor movements would be expected to cause significant motion artifacts over the course of a one second exposure.

Future work pursuing microendoscopic oximetry will require significant improvement of illumination intensity in order to reduce required exposure time. There are several potential methods of achieving this, which due to time restraints were not attempted as part of this thesis. Improvement of coupling efficiency between the AOTF output and proximal optical fibre connector could help to reduce loss of light. This could potentially be achieved at additional optical polishing steps using smaller grit polishing sheets, and increasing the fill-factor of the fibre surfaces with respect to the illumination focal spot. Minimising the length of optical fibre which would also help to reduce optical attenuation. Another potential solution would be to use higher NA optical fibres, such that the illumination delivered from the distal end of the fibres is delivered in closer proximity to the field of view. Finally, an alternative solution would be to employ a more intense tunable illumination source in place of the supercontinuum and AOTF. This could include, for example, a pulsed laser source and optical parametric oscillator (OPO)

## 6. Minimally invasive oximetry

---

which can provide highly intense illumination. However, care must be taken not to exceed the optical damage threshold irradiance of the fibres.

Additional practicalities were considered for future *in vivo* imaging. The microendoscope has a blunt edge, and access to tendon tissue *in vivo* would require a small perforation to be made prior to insertion of the probe. Incorporation of the microendoscope and fibre system within a hypodermic needle would allow for much easier access to deeper tissue. The need to perform a preliminary perforation in the skin before insertion of the probe would be eliminated, and increase the ease with which the probes could be used in practice. Over the course of the experiments performed in this chapter, it was found that handling and cleaning of the triplet probes would often result in one of the smaller GRIN lenses becoming detached from the rest of the probe and sheath. The microendoscopes were rendered unusable in this case. In the next chapter, further work with microendoscopes is explored with a singlet GRIN lens microendoscope. This singlet probe, while not as long as the triplet probe and with slightly reduced optical properties, promised to be more robust for integration and multiple use within an imaging system.

Finally, additional investigations will be required in future to study the effect that contact pressure and potential tissue disruption may have on blood oxygen levels. It is clearly pertinent that the measurement does not affect the oxygen state within the tissue, if the technique is to be robust. Provided the vasculature is not ruptured however, it is reasonable to expect that there will not be significant changes to microvascular oxygenation. At least for the preliminary *ex vivo* investigations performed in this chapter, no localised rupture of vessels and displacement of blood was observed through imaging with the microendoscope. As with the “invasive” *in vivo* experiments described in previous chapters, it also remains necessary to ensure that penetration of the probe through tissue does not expose the vasculature to oxygen in air.

## 6. Minimally invasive oximetry

---

Despite the aforementioned challenges, the preliminary setup and experiments described in this chapter demonstrate the clear capacity for the use of microendoscopic imaging for vascular oximetry. In future this may be applied to a range of *in vivo* applications in the tendon and beyond.

## 7. Fluorescence microendoscopy for experiments in immunology

---

**Summary:** In the final chapter of this thesis, further modifications to the imaging system are described in which multi-channel, minimally invasive fluorescence imaging was achieved. The capacity to perform localised fluorescence microscopy allows for many potential applications in the study of inflammation through the imaging of transgenic, fluorescent cell lines, and fluorophore-conjugated antibodies. In this chapter, an experiment is described in which small, localised volumes of antibodies were introduced adjacent to the field-of-view. Localised binding of these antibodies with T cells in the murine lymph node was observed. This was performed in *ex vivo* tissue, and binding was validated with flow cytometry as the gold standard; successfully demonstrating new capability for a variety of immunological imaging applications.

### 7.1. Introduction

In the previous chapter, incorporation of a minimally invasive microendoscope to the multispectral imaging system was described, and applied to oximetry. In the final part of this thesis, multispectral and minimally invasive imaging was utilised for an alternative application, specifically multi-channel fluorescence microendoscopy in combination with localised cellular labelling with fluorophore-

## 7. Fluorescence microendoscopy for experiments in immunology

---

conjugated antibodies. In order to frame the context of the experiments performed in this chapter and the motivation, a brief introduction to basic aspects of immunology will first be given.

The immune system provides whole body surveillance, allowing recognition and removal of infectious agents such as viruses and bacteria, transformed (cancerous) cells as well as damaged or aged cells. Immune surveillance relies on cells of the immune system circulating between the blood and lymphatic systems. The lymphatic system comprises lymphatic capillaries that drain into lymph nodes; the lymph nodes act as the organising point of the immune system, where cells of the immune system called lymphocytes, sense and respond to information about the regional environment conveyed by cells known as dendritic cells. Lymphocytes consist of three main sub-populations including B cells, T cells and NK cells [179]. B cells are associated with adaptive immunity and are responsible for producing antibodies (antigen-specific proteins). T cells are involved in cell-mediated immunity, and can be further defined as either helper T cells or cytotoxic T cells. The general purpose of all these cells is to recognise and destroy foreign bacteria and viruses. Given the important role these cells play in the immune system, there is great motivation for the study of these cells and their roles in immune-related disease.

It is first necessary to be able to correctly identify cells and their sub-populations with a high degree of specificity. This is widely performed using *monoclonal* antibodies, which can be used to identify certain types of cells with high specificity. These are antibodies produced from a single clone of cells, consisting of identical molecules and reacting with only one epitope on an antigen (the epitope is the region on an antigen that is recognisable by the immune system). “Clusters of differentiation” (e.g. CD2, CD4 etc) have been allocated in order to define the specificity of the various clones [179]. For example, T cells are assigned CD3+, meaning that a specific monoclonal antibody (anti-CD3, or  $\alpha$ -CD3) will bind to all T cells. More specifically, helper T cells are also CD4+, whilst cytotoxic T cells are

CD8+ [180]. This means that  $\alpha$ -CD4 antibody will bind to helper T cells but not to cytotoxic T cells, and vice versa for  $\alpha$ -CD8. By utilising fluorophore-conjugated antibodies as cell-specific labels, it is possible to identify cell populations of interest. This is commonly performed with techniques such as fluorescence-activated cell sorting (FACS), also known as flow cytometry, which can validate successful labelling of fluorophore-conjugated antibodies to these cells [181]. Flow cytometry is considered as the gold standard, classifying cells *in vitro* based on their light scattering and fluorescence properties. The identification of T cell subtypes and the quantification of their number is essential in the diagnosis and monitoring of immunodeficiencies [179]. However, by imaging these cells and their interactions directly in real time *in vivo*, numerous potential applications exist for the study of immune related cellular events.

### 7.2. Background and motivation

The central aim of the work discussed in this chapter was development of a technique to image T cells in the murine lymph node (LN) and observe, in real time, the binding of locally delivered fluorophore-conjugated antibodies. Observation would be made possible by using multi-channel fluorescence microscopy. The lymph node is of interest as it is a major site of T lymphocytes, with high concentrations of the cells present. Interactions between dendritic cells and lymphocytes represent the first step in initiation of an adaptive immune response, and the generation of immunological memory, providing enhanced responses to previously encountered infectious agents and forming the basis of vaccination. However, in some disease states, the immune system makes the wrong decision, for example ignoring a cancerous cell and allowing establishment of a tumour, or activating in response to a self protein, resulting in autoimmune diseases such as diabetes or arthritis [182].

As such, the visualisation and study of antibody binding to T cells in the lymph

## 7. Fluorescence microendoscopy for experiments in immunology

---

node may allow for a greater understanding of the immune response, and its behaviour in autoimmune disease such as RA. Localised delivery ensures that specific cells in the observed environment have access to the labelled antibody, which is not always the case with a systemic, intravenously administered antibody. This also offers an advantage of using very small amounts of antibody in a local tissue, minimising risks of toxicity from the fluorophore conjugate - which suggests that this approach has potential to translate into imaging human tissue *in vivo*. Finally, the opportunity to administer drugs that may enhance or block cell responses would allow for mechanistic studies of molecules that control initiation of the adaptive immune response. Using a minimally invasive method to access these cells provides the potential to perform longitudinal studies of the site of injection over days, which is not possible using *ex vivo* techniques such as FACS. Cellular events that can be observed include the study of proliferation, migration of cells and rate of antibody attachment.

Validation and analysis of antibody-labelling of cells in deep tissues has been previously performed *in vivo* by invasive means (e.g. skin-flap surgery [183]) or *ex vivo*. For the case of *ex vivo* analysis, the labelled cells in the area of interest are analysed post mortem. The obvious disadvantage of such analysis is that the extraction and processing of cells provides only “snap shots of molecular and host responses at a particular time” - therefore, the study of any temporally dynamic processes is lost [184].

For non-invasive imaging, one is limited to observation of cells either on or close to the surface of the animal. For observation of cells located deeper than these superficial layers, such as those in the lymph nodes, minimally invasive techniques such as microendoscopic probes can be employed in order to access said cells for imaging [123]. For example, Yun et al (2008) demonstrated high-resolution fluorescence microscopy of dendritic cells labelled with GFP in a live mouse ear, using a 1 mm diameter GRIN lens microendoscope [44]. In 2008, Foster et al. published a study reporting local administration of antibodies, to attach to dendritic cell (DC) pop-

## 7. Fluorescence microendoscopy for experiments in immunology

---

ulations in normal and tumour tissue [185]. In this study, the DCs were labelled with an antibody known as ( $\alpha$ )-MHC-II, conjugated with a fluorophore known as allophycocyanin (APC). This antibody labels two “morphologically distinct but related antigen-presenting cells”: Langerhans Cells (LCs) in the epidermis and interstitial dermal cells (iDCs). A second antibody,  $\alpha$ CD31 was conjugated with Alexafluor (AF) 488, and also administered. AF488 is a fluorophore with excitation peak of 488 nm and emission between 515 and 530 nm. The  $\alpha$ CD31 antibody labels adhesion molecules which are highly expressed on blood vessels. These were then imaged *in vivo* using confocal fluorescence microscopy non-invasively, at depths of approximately 100  $\mu$ m in dermal ear tissue. The authors demonstrated successful imaging of positively stained cells in healthy tissue and also in the presence of a highly vascularized tumour micro-environment.

As described in the aforementioned study, localised labelling of antibodies presents significant advantages over systemic injection. Intradermal labelling of antibodies naturally means that significantly less antibody is required compared to systemic (e.g. intravascular) injection, resulting in negligible toxicity. In addition, commercially available antibody preparations are available in these small amounts. The field of view reported in this study was 800  $\mu$ m  $\times$  800  $\mu$ m. The antibody conjugates were injected “just outside of this imaging field” in a 40  $\mu$ l solution which included the antibodies, PBS and also Fc block which helped to minimise non-specific binding. The authors noted that antibody labelling of MHC-II and CD31 was efficient across the whole field of view, suggesting that the antibody conjugates diffused laterally a distance of more than 800  $\mu$ m. However, as the previous study implemented non-invasive confocal imaging, depths beyond 100  $\mu$ m were inaccessible.

In this chapter, the implementation of a multi-channel, microendoscopic fluorescence microscope is described. The imaging system is combined with a delivery system for localised delivery of fluorophore-conjugated antibodies in the vicinity of the field of view; the concept is depicted in figure 7.1. With this combined tech-

## 7. Fluorescence microendoscopy for experiments in immunology

---

nique, it will be possible to study local cellular events and interactions in real time, in deeper tissue such as lymph nodes, and in the direct vicinity of the injection site. For the specific application to be demonstrated in this chapter, LN tissue from transgenic mice will be imaged, in which the CD2 cells are positive for the DsRed (*Discosoma red fluorescent protein*) fluorophore. The cluster of differentiation CD2 is a cell adhesion molecule found on T cells and NK cells; meaning that T cells will be fluorescent if excited at approximately 557 nm, the peak excitation wavelength of DsRed; and thus should be visible by means of fluorescence microscopy. An antibody  $\alpha$ -CD4, conjugated with the fluorophore AF647 (peak excitation 647 nm) will then be delivered to the vicinity of these cells adjacent to the microendoscope. If localised labelling has been successful, any CD4+ cells (which include helper T cells, which are both CD2+ and CD4+) will become doubly fluorescent, at both 557 nm and 647 nm excitation wavelengths.

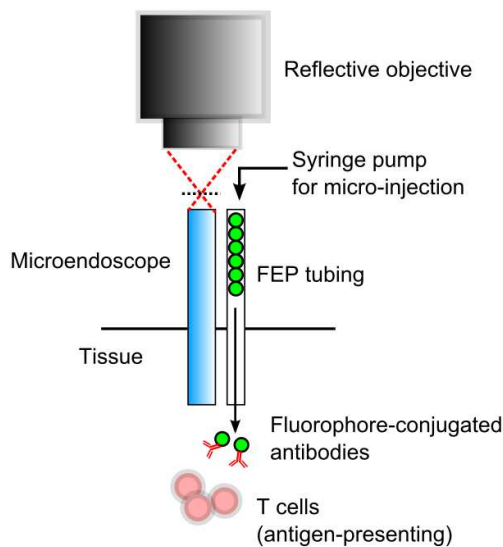


**Figure 7.1.** Illustration of setup for fluorescent microendoscopy with localised delivery of fluorescent antibodies

### 7.3. Experimental setup for minimally invasive fluorescence microscopy

#### 7.3.1. Adaptations from oximetry setup

In order to perform fluorescence microscopy with the imaging system, the most important modification to be made was the introduction of a dichroic filter, in place of the beamsplitter previously utilised for multispectral imaging. Dichroic filters act as wavelength-selective mirrors, which can, for example, transmit excitation illumination and reflect fluorescence emission. They are a necessary component for fluorescence microscopy in order to spectrally separate the excitation and emission light. For fluorescence imaging at multiple distinct bands, a multi-channel optical fluorescence filter set was obtained for this purpose (LF405/488/532/635-B-000, *Semrock*). This filter set was optimised for excitation wavelengths of 405 nm, 488 nm, 532 nm and 635 nm respectively. In conjunction with the dichroic, excitation and emission filters (also demonstrating multiple pass-bands) were introduced to reduce spectral leakage. The transmission spectra of this optical filter set is shown in figure 7.2.

Once the fluorescence filter set was implemented, a means for delivery of small volumes of fluid (such as antibodies) adjacent to the field of view was considered. It was decided that using the smallest available FEP (diameter 50  $\mu\text{m}$ ) in conjunction with a syringe pump (KDS260, *Linton Instrumentation*) would allow for this capability to be achieved. Similar to securing of optical fibres in chapter 6, the FEP was secured to the outer wall of the microendoscope with curable epoxy. The modified setup for multi-channel fluorescence microendoscopy is depicted in figure 7.3.

By using the supercontinuum and AOTF in order to supply illumination, multiple fluorescent channels could sequentially acquired. The AOTF GUI allows for

## 7. Fluorescence microendoscopy for experiments in immunology

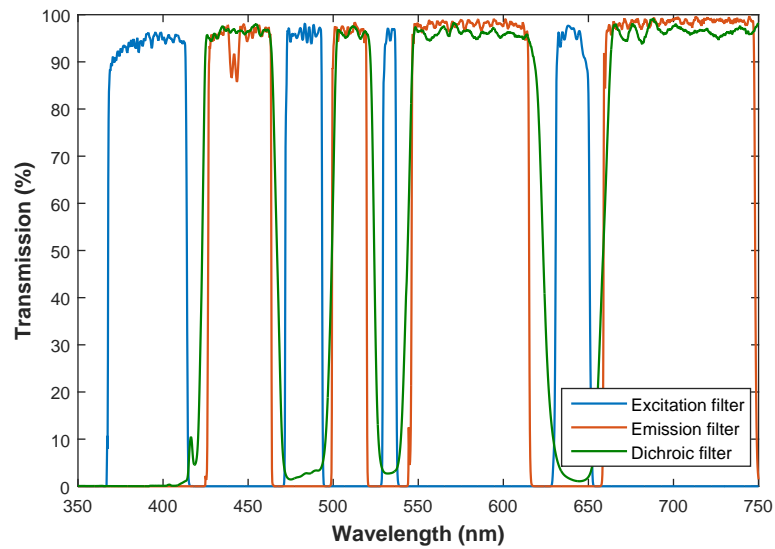


**Figure 7.2.** Transmission spectra of multi-channel optical fluorescence filter set, optimised for excitation wavelengths of 405 nm, 488 nm, 532 nm and 635 nm. (Data from Semrock, Brightline LF405/488/532/635-B-000)

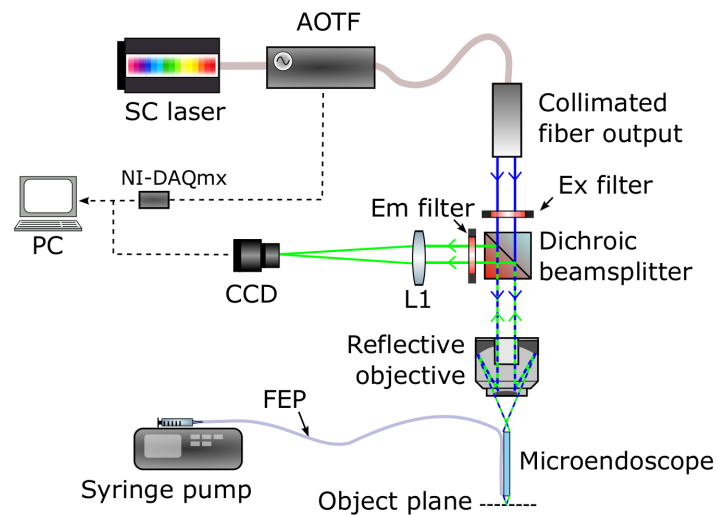


**Figure 7.3.** Schematic illustrating adaptations made to the minimally invasive multispectral microscope to allow for multi-channel fluorescence imaging. Three fluorescent bands are acquired sequentially by alternating the excitation wavelengths using the AOTF (488 nm, 532 nm and 646 nm peak wavelengths respectively). Em filter: Emission filter; Ex filter: Excitation filter.

## 7. Fluorescence microendoscopy for experiments in immunology

a total of 8 programmable channels; by setting two or three of these each to an individual fluorescent channel (central wavelength  $\pm 2$  nm), a higher level of illumination intensity could be achieved at each individual excitation channel. These channels were specified according to the diagram in figure 7.4. Channel 1 was assigned a central wavelength of 488 nm, the peak excitation wavelength of GFP and FITC fluorophores. Channel 2, with a central wavelength of 532 nm, would provide excitation for DsRed. The two remaining AOTF channels were assigned to excitation channel 3, at 645 nm and 647 nm, providing excitation for AF647. By setting the illumination in this manner, simple modifications were made to the LabVIEW GUI described in chapter 3, in order to allow for control of the sequential illumination and image capture. The process for sequential acquisition of multiple fluorescence bands is depicted in the flow chart in figure 7.5.

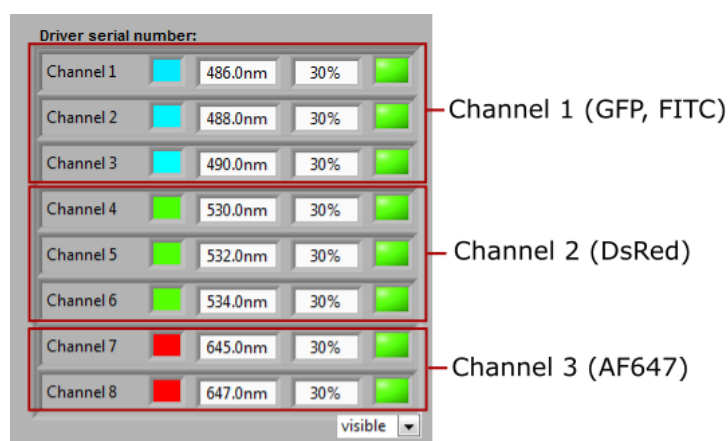


**Figure 7.4.** AOTF channels chosen for multi-channel fluorescence excitation at three central wavebands 488 nm, 532 nm and 646 nm, providing selective excitation of various fluorophores as indicated in the diagram.

For quantitative measurements of fluorescence intensity produced by various fluorophores, it was necessary to ensure that no spectral leakage of illumination from each channel was occurring through adjacent transmission bands of the excitation filter and dichroic. For example, for channel 1 with a central wavelength of 488 nm, no illumination through the 532 nm channel was desired. To verify that this was not the case, a spectrometer was used to measure the spectral output of each channel individually, as transmitted through the excitation filter and

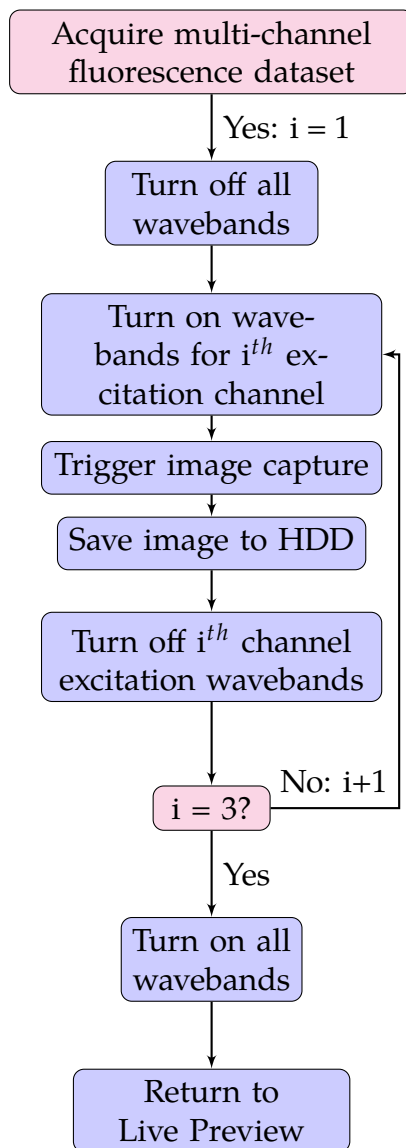


**Figure 7.5.** Simplified flow chart for multi-channel fluorescence acquisition in LabVIEW (3 channel dataset). The wavelengths used for each excitation channel are illustrated in figure 7.4.

## 7. Fluorescence microendoscopy for experiments in immunology

---

dichroic filter. The results are shown in figure 7.6, in which the spectra, measured individually, are shown on the same axes and normalised for intensity. No spectral leakage was observed.

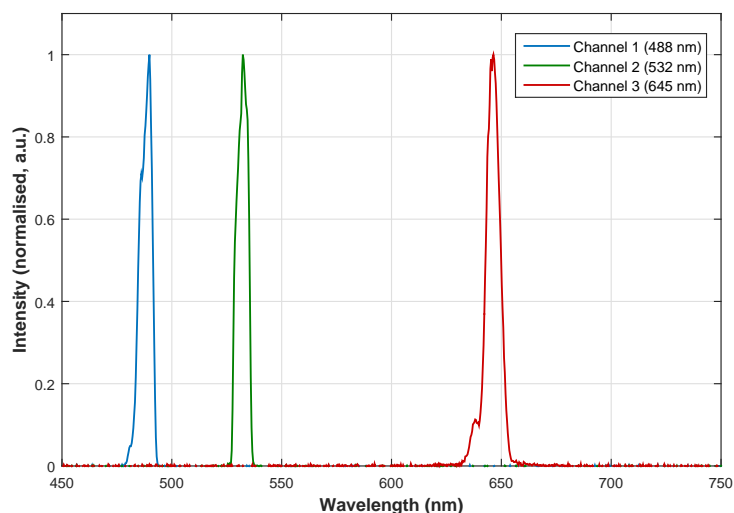


**Figure 7.6.** Composite graph of individual channels for fluorescence excitation as measured by a spectrometer and normalised for intensity. This graph demonstrates the spectral bandwidth of excitation and also that no crosstalk or leakage exists between the three channels.

In addition, the intensity of each individual channel was measured by a power meter, as transmitted through the microendoscope. For excitation channels 1, 2 and 3, the output as measured by a power meter was determined to be  $170\ \mu\text{W}$ ,  $191\ \mu\text{W}$  and  $310\ \mu\text{W}$  respectively. The increased intensity with wavelength is expected due to the spectral output of the supercontinuum and AOTF. These intensities show a marked improvement as compared to those measured through the optical fibres in the previous chapter (which amounted to approximately  $10\ \mu\text{W}$  in total).

For the experiments performed in this chapter, an alternative microendoscopic probe was used to that employed in chapter 6 (1050-002183, *Inscopix*). The previous *Grintech* probes consisted of a triplet GRIN lens encased in a metallic sheath, with a lens diameter  $350\ \mu\text{m}$  and total outer diameter of  $500\ \mu\text{m}$ . In contrast, the

## 7. Fluorescence microendoscopy for experiments in immunology

---

**Table 7.1.** Specifications of multispectral imaging system

	<b>Specifications</b>
<b>Mode</b>	Multi-channel Fluorescence
<b>Excitation Wavelengths</b>	488 nm, 532 nm, 646 nm
<b>Emission bands</b>	503 nm-518 nm, 550 nm-613 nm, 663 nm-743 nm
<b>Spectral resolution <math>\Delta\lambda</math></b>	~5 nm excitation
<b>Magnification</b>	40X
<b>Field of view</b>	80 $\mu\text{m}$ diameter
<b>Spatial Resolution</b>	1 $\mu\text{m}$
<b>Sampling rate</b>	1.5 sec (3-channel acquisition)

Inscopix probe consisted of a singlet GRIN lens and no metallic sheath. The nominal NA was also 0.5 for finite conjugate imaging, so the optical resolution was expected to be similar to that of the *Grintech* probes. The outer diameter was also 500  $\mu\text{m}$ , however with no metallic sheath increasing the diameter, the lens itself was slightly larger than Grintech's, allowing for higher light throughput due to fewer optical surfaces, and larger field of view. The specifications of the imaging system are summarised in table 7.1.

### 7.4. Validation of system

Before attempting to perform fluorescent microscopy of cells *ex vivo*, it was decided to image fluorescent microsphere beads. By imaging these beads with known dimension and spectral properties, a qualitative assessment of the image quality could be obtained. For this experiment, "Flash Red" beads (660 nm peak excitation, 690 nm peak emission) and "Envy Green" beads (525 nm peak excitation, 565 nm peak emission) were utilised. They were of similar dimension, at 0.96  $\mu\text{m}$  and 1.01  $\mu\text{m}$  diameter respectively. Channel 2 (as defined in figure 7.4) would be used for excitation of Envy Green, and channel 3 for Flash Red.

A small solution of Envy Green, Flash Red and methanol was produced (approximately 1:1:5 by volume), of which a 10  $\mu\text{L}$  droplet was pipetted on to a microscope

slide. Once the methanol had evaporated, a dried sample of mixed fluorescent microspheres remained on the surface of the slide. This microscope slide could then be imaged through the microendoscope.

An example of acquired multi-channel fluorescent images are shown in figure 7.7. False colour was applied to both channels in order to produce a multi-colour image, and the channels were normalised for intensity. The normalisation was necessary as the fluorescence intensity was greater for the Envy Green microspheres than for Flash Red. However, it became clear that significant chromatic aberration was present, caused by the difference in emission wavelengths of Envy Green and Flash Red microspheres. If the red beads were in sharp focus, the green beads were out of focus, and vice versa, as evident in figure 7.7(a). A corrected image was produced by manual refocusing of the imaging system between two sets of spectral images (approximately 5  $\mu\text{m}$ ), allowing for a composite image to be produced with both microspheres in focus. For this corrected image, a qualitative assessment of image quality was generally positive; in the centre of the field of view, the spherical beads were clearly visible, with aberrations occurring towards the edge of the field of view, as previously indicated in chapter 6. Additionally, as evident from the corrected image in figure 7.7(b), no significant autofluorescence produced by the microendoscope itself was detected; background intensity in figure 7.7(a) was produced by out of focus fluorescent microspheres. Due to the small dimensions of these microspheres (approximately equal to the spatial resolution of the imaging system at  $\sim 1 \mu\text{m}$ ), the chromatic aberration was not expected to be as evident *ex vivo*, where cells are on the order of 10  $\mu\text{m}$ .

### 7.5. Visualisation of T cells *ex vivo*

Following *in vitro* imaging of fluorescent microspheres, it was aimed to visualise T cells within intact lymph node tissue *ex vivo*. The lymph nodes used for imaging were dissected from transgenic hCD2 DsRed mice; meaning that T cells (CD2+)

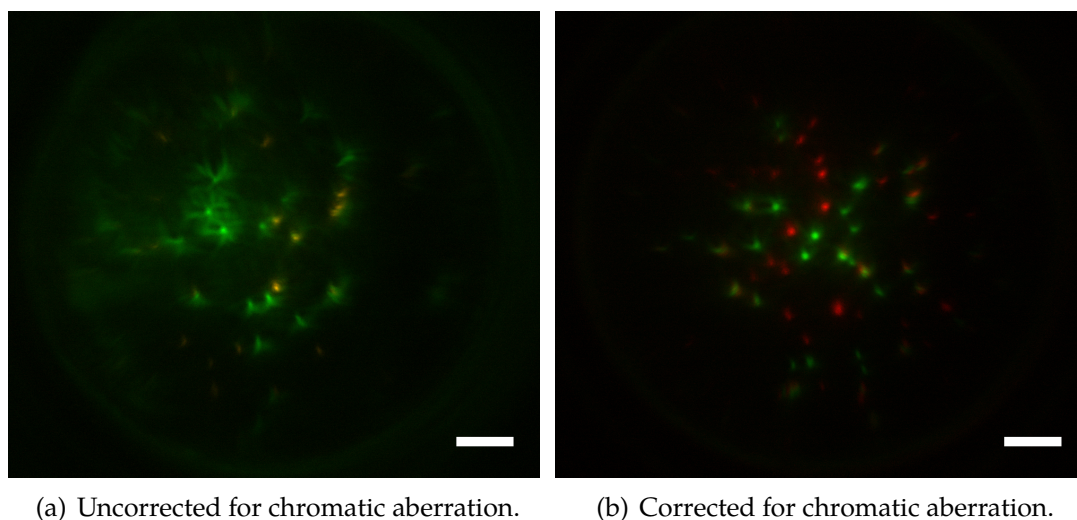


**Figure 7.7.** Multichannel false-colour images of fluorescent beads (Envy Green and Flash Red) through microendoscope, background-subtracted and normalised for intensity. Scale bars represent 20  $\mu\text{m}$ .

would fluoresce if illuminated with DsRed excitation wavelengths. Once these cells have been localised with the imaging system, they could be identified by a strong signal at channel 2 (532 nm providing strongest excitation for DsRed) but also a weaker signal at channel 1 due to less efficient excitation of DsRed at 488 nm. As there is no overlap between the emission spectra of DsRed and of the channel 3 output, no signal would be expected from DsRed+ cells through this channel.

### 7.5.1. Demonstration of fluorescence microendoscopy - T cells

As a demonstration of the imaging technique and successful binding of locally delivered antibody, two intact inguinal lymph nodes were placed on a microscope slide, and positioned on the stage of the imaging system. A drop of PBS was delivered to prevent the lymph nodes from drying out. A small incision was made to the surface of each lymph node with a scalpel, and the microendoscope was brought into contact with the lymph node tissue. For each scene, three images were acquired sequentially at each fluorescent channel. Background signals were

## 7. Fluorescence microendoscopy for experiments in immunology

---

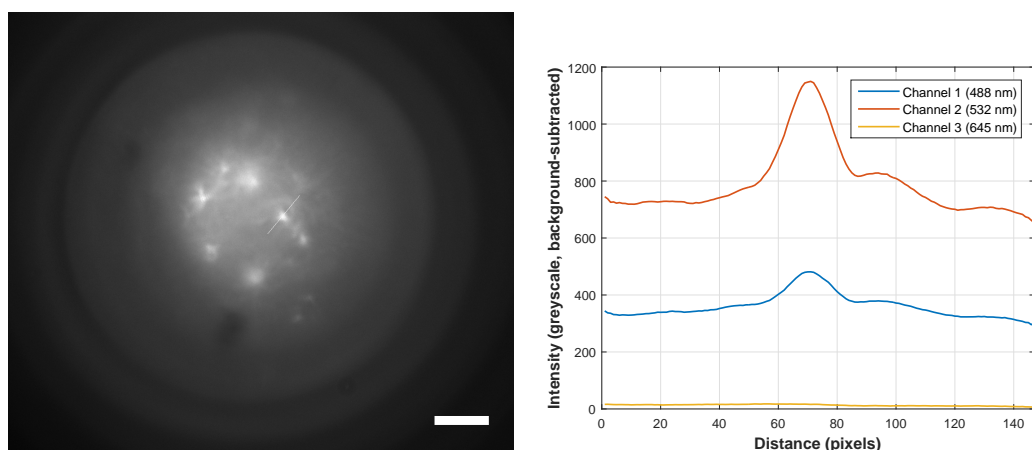
also acquired and subtracted from these images (as described in chapter 3 for the multispectral data sets).

Image 7.8 shows an example of the obtained results; 7.8(a) is an image successfully acquired of a group of T cells within the lymph node - the specific image was acquired at channel 2 (532 nm excitation). The cells were identifiable due to their round shape, dimension (approximately 10  $\mu\text{m}$  diameter) and spectral response. This response is depicted in figure 7.8(b), in which the intensity profile across a T cell is shown for each channel. A clear peak is observed from 532 nm excitation, corresponding to strong DsRed emission within the T cell. Clearly evident also is the weaker signal and peak due to excitation at 488 nm at the same spatial location. As expected, for this T cell there was no visible signal from channel 3, excitation at 645 nm. However, as shown in figure 7.8(a), a background signal outwith the T cells was present, most likely caused by the fluorescence of out of focus cells. As the system is not confocal, out of focus light is not rejected and will contribute to image intensity. This increased background signal is also evident in both channels 1 and 2 of figure 7.8(b), with the central peaks emerging from an elevated baseline level as compared to the zero intensity signal measured at channel 3.

### 7.5.2. Demonstration of localised delivery of fluorophore-conjugated antibody

Following visualisation of T cells, a solution of antibody  $\alpha\text{CD4}$  (0.2 mg/mL) in PBS was created (1:8 by volume respectively). This solution was delivered in a volume of 20  $\mu\text{L}$  by means of a syringe pump connected to FEP tubing adjacent to the microendoscope, as shown above in figure 7.3; corresponding to an approximate total of 4  $\mu\text{g}$  of  $\alpha\text{CD4}$  delivered to tissue in the vicinity. This antibody, which binds to CD4+ cells (including T helper cells), was conjugated with the fluorophore AF647 (peak excitation and emission wavelengths of 647 nm and 665 nm respectively). Following localised delivery of this antibody, if binding has been

## 7. Fluorescence microendoscopy for experiments in immunology



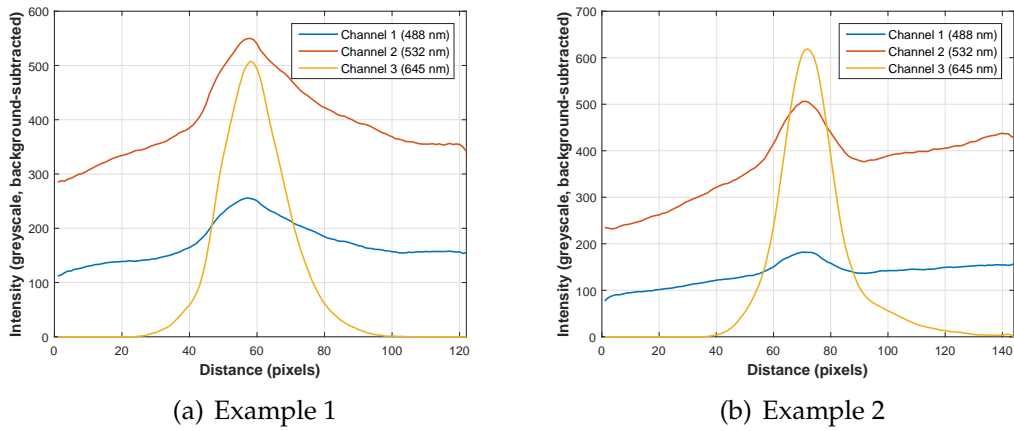
(a) Image of DsRed T cells (viewed at 532nm excitation channel) (b) Intensity profile across cell at three channels

**Figure 7.8.** Preliminary imaging of DsRed T cells with corresponding intensity profiles. Intensity profiles show no signal at third channel (645 nm excitation) as expected. The scale bar in 7.8(a) represents 20  $\mu\text{m}$ .

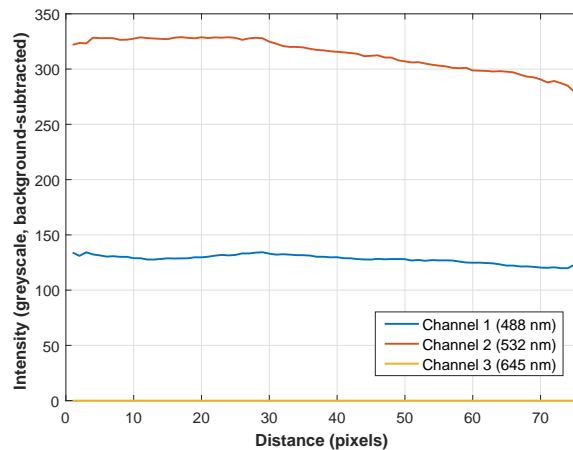
successful it was expected that an increase in the signal intensity produced from T helper cells within the field of view would be observed at channel 3. These cells remain DsRed+ and as such were expected to be doubly fluorescent.

Figure 7.9 depicts two examples of intensity profiles, acquired from T cells over three channels, as with the previous image. A strong peak had appeared at channel 3, localised to the same spatial position as the DsRed fluorescence. This could be presumed as due to successful binding of  $\alpha\text{-CD4}$  to these cells. A lack of background signal in channel 3 was evident, with the peak falling to zero outside the cell - unlike the DsRed fluorescence from channels 1 and 2. This suggests that binding was localised to the surface at which the antibody had been delivered; with no background fluorescence contributing to the signal at this channel. Further, as a negative control test, figure 7.10 shows intensity profiles from an area with no visible cells in focus. As evident from the figure, there is no signal observed in channel 3, indicating no non-specific binding of AF647. There remains a weak background signal in channels 1 and 2 from out of focus tissue.

## 7. Fluorescence microendoscopy for experiments in immunology



**Figure 7.9.** Intensity profiles demonstrating positive labelling of DsRed T cell with fluorophore AF647 on  $\alpha$ -CD4. Line profiles are intensities across labelled T cell at each fluorescent channel.



**Figure 7.10.** Intensity profiles from the tissue in an area with no visible cells, providing a negative control. Non-specific binding of AF647 is not present, as indicated by the lack of a signal from the respective excitation channel 3. Weak background fluorescence signal is evident in channels 1 and 2, likely from out of focus unlabelled T cells as described previously for figure 7.8.

### 7.6. Validation of localised AB labelling

In the previous section, a qualitative assessment of antibody binding to T cells was performed and determined to be successful. In order to validate this result and quantify the extent of the binding within the tissue, flow cytometry was employed. As mentioned earlier in the chapter, flow cytometry is considered the “gold standard” technique for classification of cells in this manner, and it can provide quantitative statistics regarding the proportion of cells in a sample which have been labelled with specific fluorophore-conjugated antibodies.

For this experiment, eight individual hCD2 DsRed lymph nodes were labelled as described in section 7.5.2. They were then processed further for flow cytometry analysis. This involved mechanical disruption of the tissue with a cell scraper and addition of PBS and EDTA to form a single cell suspension. The suspensions were then passed through a filter (100  $\mu\text{m}$  pore nitex membrane) in order to remove clumps and debris. This was followed by conventional staining of cells with addition fluorophores; 0.125  $\mu\text{L}$  of eFluor 450 (peak excitation 405 nm, peak emission 450 nm) on MHC+ cells, and 0.5  $\mu\text{L}$  PE-Cy7 (peak excitation 496 nm, peak emission 785 nm) on CD4+ cells. MHC+ cells include other cells found in the lymph node, such as B cells and dendritic cells. PE-Cy7 was added as an additional label for CD4+ cells - so that a quantification of the percentage of total T helper cells that have been labelled with AF-647 using the localised technique could be obtained. For clarity, a summary of all considered cell types and the respective fluorescence expected from these fluorophores is displayed in table 7.2.

The eight samples were then processed by the flow cytometer (MACSQuant Analyzer 10). Each cell is individually processed and the amount of fluorescence detected for each cell across a number of fluorescence channels is measured. This is achieved with a number of dichroic filters and photo multiplier tubes. The results obtained through flow cytometry are plotted with each cell representing

## 7. Fluorescence microendoscopy for experiments in immunology

**Table 7.2.** Summary of cell types and positive detection of various fluorophores expected

		DSRed	eFluor 450	PE-Cy7	AF 647
<b>MHC+</b>	B cells (MHC+)	X	✓	X	X
	Dendritic cells (MHC+, CD4-)	X	✓	X	X
<b>CD2+</b>	T helper cells (CD4+)	✓	X	✓	✓
	Other CD2 cells i.e. NK (CD4-)	✓	X	X	X

**Table 7.3.** Total detected counts from lymph node flow cytometry data, of which a portion were classified as single cells through preliminary gating

Sample	Total counts	Single cell counts
LN 1	229271	149072
LN 2	344817	213121
LN 3	586236	437537
LN 4	947861	669684
LN 5	186254	125957
LN 6	1597216	1043812
LN 7	1499124	993821
LN 8	667870	482626

an individual point on the graph. Initial processing is performed in order to isolate signal from single cells from debris and dead cells; this is done by plotting individual counts as a function of forward scatter against side scatter. By a process known as “gating”, events with low forward scatter and high side scatter are excluded, leaving only single cells for further analysis. For the eight samples analysed, the number of total detected counts, of which there were a total number of cells detected, are given in table 7.3.

Further analysis of cells could then be performed, by observing the amount of fluorescence detected for each cell at various channels. The spatial location of the cell’s point on the graph is determined the intensity of fluorescence detected by the channels assigned to the X and Y axes. For example, if the channel used to detect DsRed fluorescence is assigned to the Y axis, and a channel detecting eFluor 450 is assigned to the X axis, cells which are DsRed+ will be located at

## 7. Fluorescence microendoscopy for experiments in immunology

higher values on the Y axis. This is illustrated in figure 7.11, in which all single cells are plotted. The large cluster towards the top of the graph at higher intensity values on the Y axis were positive for DsRed, and thus would include all CD2+ cells. The second cluster to the right of the graph has lower intensity values on the Y axis and as such are DsRed-, but are higher on the X axis; thus those particular cells were MHC+ cells such as B cells and dendritic cells. By drawing gates around these clusters, a quantification of the total number of CD2+ cells and MHC+ cells was obtained.

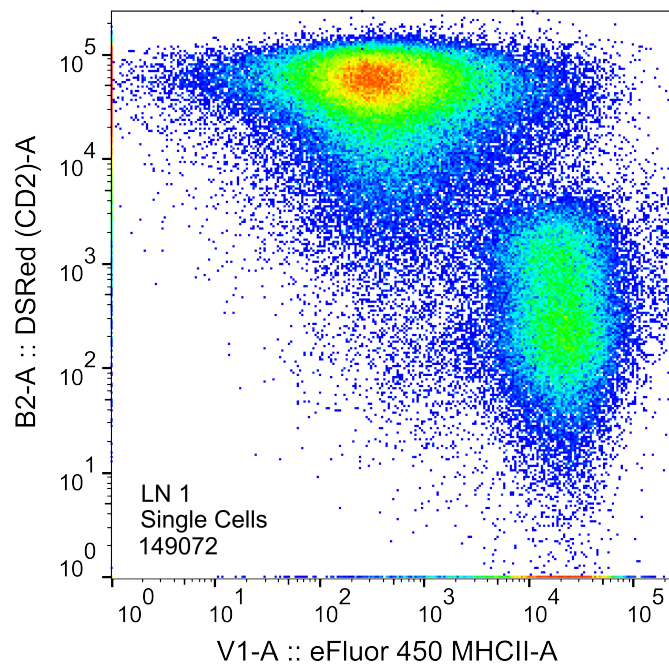


**Figure 7.11.** Example of flow cytometry plot, with total single cell counts shown on DsRed (B2) and eFluor 450 (V1) channels. Two distinct populations are evident, with DsRed+ CD2 cells (T cells) in the upper portion, and eFluor450+ MHC cells (B cells and Dendritic cells) clustered to the right of the plot.

Figure 7.12 depicts several examples of flow cytometry results; the same total number of cells as in figure 7.11 are shown, however the X axis has now been assigned to the PE-Cy7 channel. As such the cell counts have been rearranged on the graph. Recalling PE-Cy7 was labelled to all CD4+ cells, those cells which are positive for both DsRed and PE-Cy7 would consist of all T helper cells. The cluster depicted on the upper right of each graph represents this group of cells,

## 7. Fluorescence microendoscopy for experiments in immunology

and a further gate was applied to quantify the number of these cells. By using cells within this gate (e.g. as a subset of all cells), further analysis was performed by then changing the X axis to the channel detecting AF647 fluorescence. These results are shown in figure 7.13. As all cells now displayed on each graph are T helper cells, the fraction of these cells which were successfully labelled using the localised FEP delivery technique were measured.

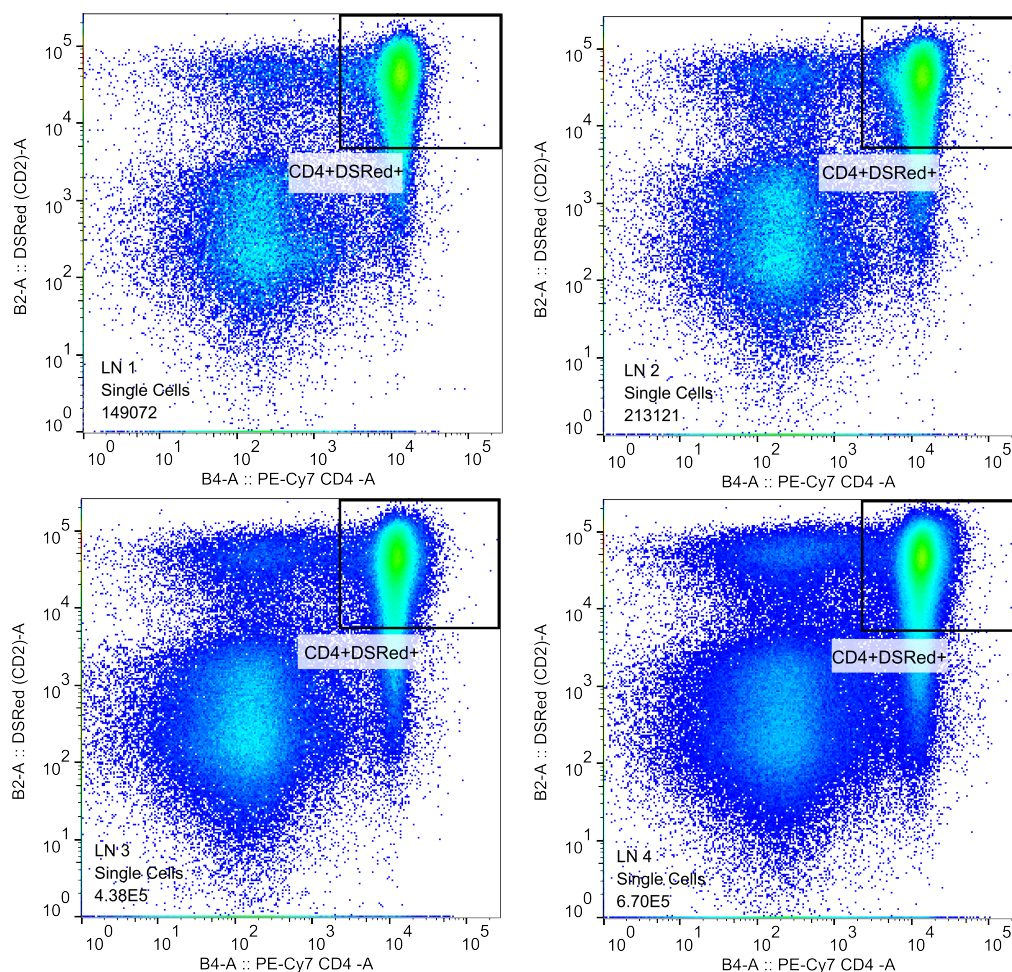


**Figure 7.12.** Total single cell counts shown with DsRed and PE-Cy7 channels; gating for DsRed+ and PE-Cy7+ (CD4+) counts shown in upper right corner of plot

The statistics of all analysed LN tissue are given in table 7.4. As a percentage of all CD4+ cells to which the locally delivered antibody could be attached, detected AF647+ counts averaged at  $7.6\% \pm 3.7\%$ . This relatively low degree of binding was to be expected as only cells in the vicinity of the microendoscope and FEP

## 7. Fluorescence microendoscopy for experiments in immunology

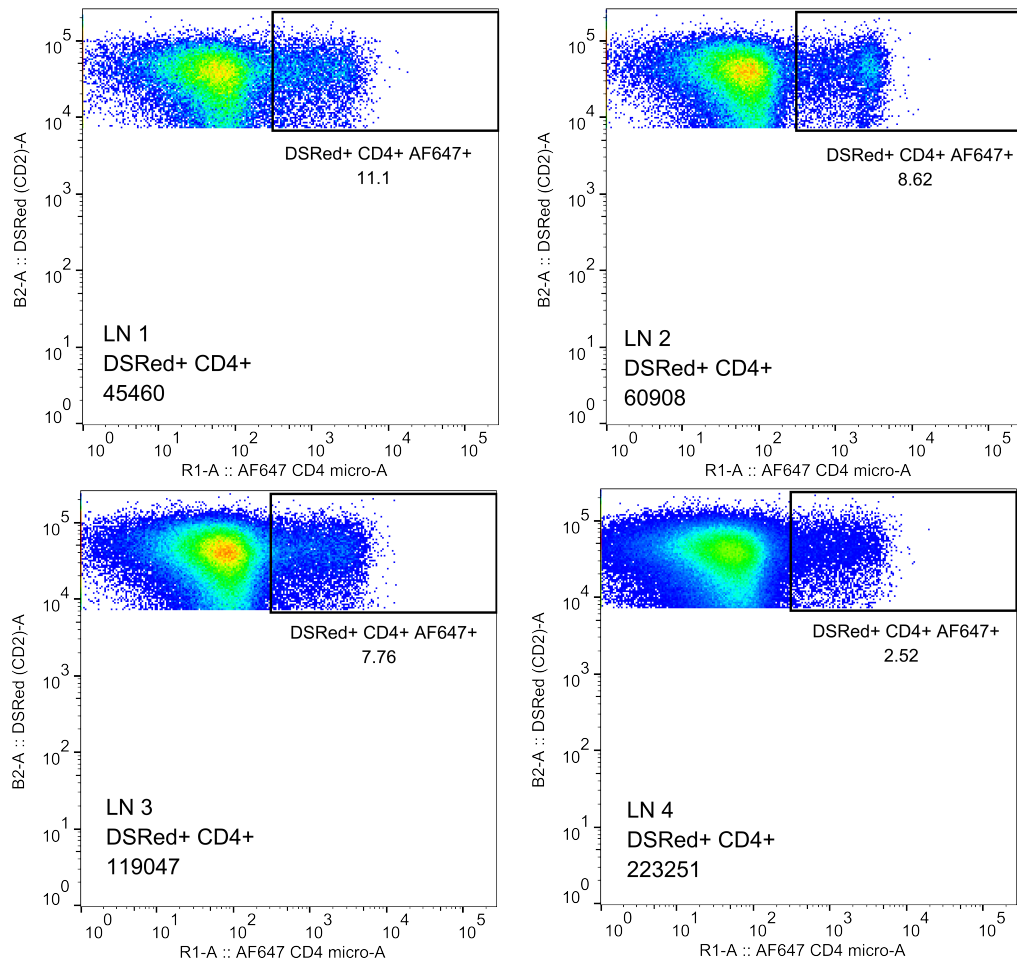


**Figure 7.13.** Cell data gated for DSRed+ and CD4+ cell counts (from figure 7.12), showing final gate for subset AF647+ cells in upper right corner of plot

## 7. Fluorescence microendoscopy for experiments in immunology

**Table 7.4.** Statistics from gated analysis of lymph node flow cytometry data

Sample	DSRed+		CD4+		AF647+	
	Count	% of Total	Count	% of DsRed+	Count	% of CD4+
LN 1	98518	66.09	45460	46.14	5061	11.13
LN 2	139651	65.53	60908	43.61	5253	8.62
LN 3	276508	63.20	119047	43.05	9243	7.76
LN 4	467693	69.84	223251	47.73	5626	2.52
LN 5	92983	73.82	42984	46.23	6144	14.29
LN 6	693850	66.47	353230	50.91	19230	5.44
LN 7	654259	65.83	336308	51.40	17610	5.24
LN 8	340112	70.47	178578	52.51	10000	5.60

tubing had been exposed to the AF647 antibody. However, it is clear that binding consistently occurred for each of the eight test samples considered in this experiment.

A final assessment was performed in order to confirm that non-specific binding was negligible. The plot in figure 7.14 shows the same data as in figure 7.13, however the gates for DsRed+ and CD4+ have not been applied, and all single cell counts are shown. In order to verify that non-specific binding had not occurred, it was expected to see minimal counts that are positive for AF647 but negative for DsRed (as AF647 is only expected to label DsRed+ CD4+ T cells). As evident from the figure, there was minimal non-specific binding of AF647 as expected. This further indicated successful, specific binding of AF647-conjugated  $\alpha$ -CD4 to the cells of interest.

### 7.7. Two-photon microscopy

As evident from the previous section, the microendoscopic imaging system in combination with minimally-invasive delivery of fluorophore-conjugated antibodies was successful. Localised labelling of DsRed T cells with AF647 was demonstrated and validated with flow cytometry. However, an important issue

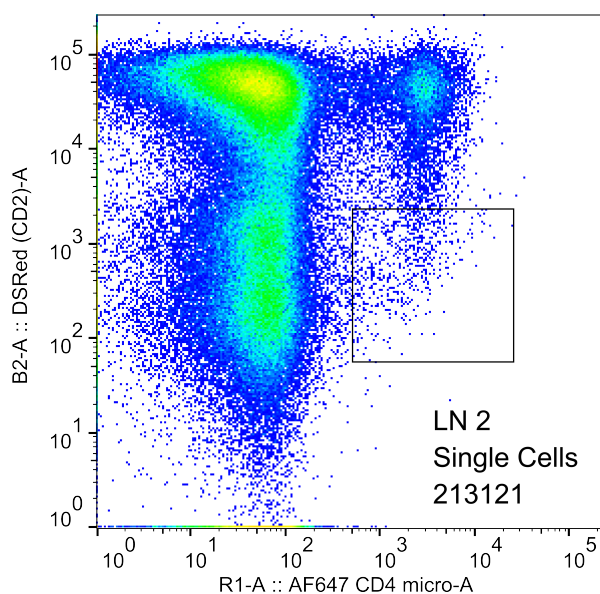


**Figure 7.14.** Cell data showing single cells for DsRed and AF647 channels. The black box highlights the minimal non-specific binding of AF647 for DsRed negative cells, further validating successful labelling of DsRed+ CD4+ cells.

regarding image quality arose from the preliminary multispectral fluorescence imaging. As the imaging system developed for this work was not confocal, out of focus light is not rejected. As such, background signal from out of focus fluorescence is captured, reducing contrast for in-focus cells of interest.

In order to minimise this issue and improve image quality for this application, a preliminary experiment was carried out, using a commercial two-photon (2P) microscope, in which the microendoscope and microfluidic system were incorporated. Two-photon microscopy involves simultaneous absorption of two photons of wavelength  $\lambda$ , resulting in excitation of the molecule of interest at a wavelength  $\lambda/2$ . It is useful as longer wavelengths are capable of penetrating deeper into tissue than of shorter wavelength photons. As two-photon microscopy involves excitation of the focal plane only, background signal is suppressed. It was attempted to determine whether image quality could be improved for this specific application.

A multiphoton laser scanning microscopy system (MPLSM) was employed for

## 7. Fluorescence microendoscopy for experiments in immunology

---

this brief qualitative experiment. The system is comprised of a multiphoton microscope (LSM7 MP, Zeiss), with Ti-sapphire femtosecond laser and optical parametric oscillator for tunable infrared illumination. The microendoscope stage and holder (Thorlabs Micro-V Clamp) was first set up on the microscope stage, after which the microendoscope and FEP delivery system was added such that the focal plane of the 2P microscope was coincident with the focal plane of the singlet GRIN lens at the working distance of (100  $\mu\text{m}$ ). A 40X objective was used for this purpose. As before, intact hCD2 DsRed+ LN tissue was dissected and imaged with the 2P microscope. As with the fluorescence microscope demonstrated previously in this chapter, three distinct channels were obtained at green, red and far-red channels. Preliminary imaging was performed using the previous hCD2 DsRed lymph node tissue as before. A two-photon image of fluorescent cells within the lymph node was obtained, and an example of a composite image is shown in figure 7.15. As evident from the image, background fluorescence was reduced - which an improvement images with the previous system, such as in figure 7.8. Further, as the three channels are captured simultaneously, temporally dynamic processes between cells are expected to be observable.

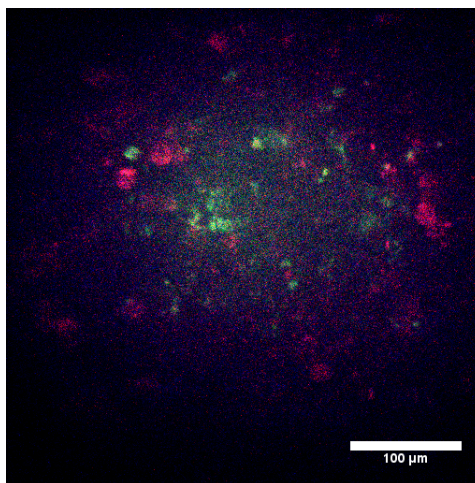


**Figure 7.15.** Composite two-photon microendoscopic image of DsRed LN tissue, acquired over three channels at 850 nm excitation

However, upon delivery of AF647-conjugated  $\alpha\text{CD4}$  (at the same volume and

concentration as before), no increase in signal in the far-red was detected, indicating that no localised binding of the antibody to the T cells were observed. As measured previously with flow cytometry, it is known that only a relatively small percentage of cells within the lymph node were labelled with the antibody. It is possible that due to the narrower imaging plane, no observable T cells within the field of view had bound to the  $\alpha$ CD4. This was a preliminary test of the system, and optimisation of the FEP placement adjacent to the microendoscope would likely address this issue. It is worth noting that as a technique, two-photon microscopy is more involved and costly than basic single photon imaging systems. For development of a transferable technique, the image quality provided by the original technique using standard fluorescence microscopy and multi-channel acquisition may be adequate for a range of applications. A potential compromise would also be to incorporate the microfluidic delivery system to a standard one-photon confocal imaging system.

### 7.8. Conclusions

In this chapter, an investigation into fluorescence microendoscopy was pursued. A multi-channel fluorescence microscope, in conjunction with a microendoscope, was developed and employed for minimally invasive imaging of intact murine lymph node tissue. Initial testing and validation of the system showed no spectral leakage between the distinct fluorescent channels. Minor chromatic aberration was observed for *in vitro* imaging of multicolour fluorescent microspheres, however the effect of this was determined to be minimal over the larger size of cells *ex vivo*. However for improvement of image quality in future, computational imaging techniques involved with increasing depth of focus could be advantageous, potentially allowing for computational selection of the ideal focal plane at the channel of interest [186]. Although out of focus fluorescence decreased the contrast of fluorescent cells within the imaging plane, T cells could be clearly resolved and the

## 7. Fluorescence microendoscopy for experiments in immunology

---

expected spectral intensities were measured over the three fluorescent channels. Alternative techniques such as two-photon or confocal microendoscopy could be employed in future for improved fluorescent image quality, as have previously been explored for alternative microendoscopic applications such as in the murine brain and kidney [45, 187].

The capability of the imaging system to detect localised binding of fluorophore-conjugated antibodies was also tested, and determined to be successful as validated by flow cytometry. This is a positive development, with the potential for this technique extending to a range of applications associated with the study of immune-related cellular events. Typically, antibodies are delivered for animal studies by means of intravascular injection. Intravascular delivery of antibodies results in cellular effects which may be observed *in vivo*, but it is often unclear as to whether the observable effect within the cells is a direct response to the antibody, or whether it is a secondary response caused by an unknown intermediary reaction. By achieving localised delivery of antibodies and real-time observation of the response *in vivo*, cellular responses can be confirmed as being a direct result of antibody delivery. There is also less toxicity associated with localised delivery of fluorophores as compared to their systemic delivery [185]. Many potential applications exist for this technology, with a large number of monoclonal antibodies and fluorophores available for a range of target cells and wavelengths.

## 8. Conclusions and future work

---

**Summary:** In this chapter, a concluding discussion is presented regarding the work undertaken as part of this thesis. The primary aim of this thesis was the development and application of a custom multispectral imaging system and oximetry algorithm. The results described in this thesis have demonstrated progress made towards this goal, and are summarised and discussed in this chapter. In addition, some potential future work arising from the experiments undertaken in this thesis are also discussed.

In this thesis, a range of work was undertaken, broadly related to the concept of optical biopsy *in vivo*. For this chapter, the work undertaken is considered as three general topics, which will be summarised and discussed briefly in this chapter.

1. Multispectral imaging for oximetry, and its applications
2. Minimally invasive imaging with incorporation of microendoscopes
3. Fluorescence microendoscopy for cellular imaging

Some important conclusions to be taken from this work are presented, as are suggestions for potential future work, which would build upon the techniques and applications addressed in this thesis.

### 8.1. Multispectral imaging system for oximetry

As discussed in chapter 1, a variety of inflammatory diseases are associated with a local hypoxic environment. The main motivation of this thesis was the development of an oximetric system allowing for access to deep tissue such as the tendon, which is affected by rheumatoid arthritis. The system would ideally be minimally invasive, allowing for repeated studies over a period of time in order to allow for the study of inflammatory disease models. Overall, significant progress was made towards this goal, with successful proof of concept work and initial oximetry studies which investigated the extension of the multispectral technique to minimally invasive imaging.

Chapters 2 and 3 covered the considerations given to the physical principles of  $\text{SO}_2$  quantification, and the development of initial system itself. The novel introduction of annular illumination with the use of a reflective objective provided single-pass transmission and elimination of directly back-scattered light. Further, the contrast reduction factor was capable of compensating for decreases in contrast whilst retaining correct  $\text{SO}_2$ , as demonstrated in chapter 3.

To the best of the author's knowledge, this was the first direct measurement of localised vascular hypoxia associated with inflammation. The standard deviation of results within the various scenes and fields of view revealed the capillary network to be heterogeneous, with a range of  $\text{SO}_2$  values found within the environment. This heterogeneity seemed to increase for inflamed tissue, with standard deviations increasing in both the inflamed murine tendon, and the rat EAE model experiments in which the oximetry algorithm was applied to previously acquired multispectral images. This was expected as the vascular network associated with inflammation is thought to be dysfunctional [18]. With the technique described in this thesis, localised  $\text{SO}_2$  values can be achieved and measured directly.

It remains challenging to assess the accuracy of obtained  $\text{SO}_2$  values *in vivo* with

## 8. Conclusions and future work

---

a great degree of certainty. Due to the fact that no alternative methods exist for the measurement of localised oxygen saturation, there is no “gold standard” technique with which to compare the results obtained in this work. As demonstrated in chapter 3, vascular phantoms can be used in an attempt to validate results, by using blood *in vitro* and deoxygenating it with the use of sodium dithionite. However, as previously discussed, this alters the osmolarity of blood and hence its optical properties - introducing a systematic error in the validation. Changes in oxygenation may also occur between measurement of  $\text{SO}_2$  with a clinical blood gas analyser, and its delivery into a narrow capillary and assembly into a vascular phantom for imaging. However, overall, general agreement was found between expected and obtained  $\text{SO}_2$  throughout the validation experiments presented in this thesis. In addition, the average of baseline venous  $\text{SO}_2$  values in chapter 5 was found to be  $67.8 \pm 10.4\%$ ; well within range of the expected value of approximately 70%. Further, the repeatability of measurements made on individual capillaries was low, within 2-3%. An analytical assessment of the potential errors was addressed in chapter 2, and in conclusion, it seems appropriate to assert that an uncertainty of vascular  $\text{SO}_2$  in the range of  $\pm 5\%$  is expected. Future work relating to this issue would investigate alternate methods of deoxygenation, which do not affect the optical properties of the blood itself - such as the bubbling of nitrogen through blood.

In addition to extension of the technique to minimally invasive imaging (discussed in section 8.2), future work relating to oximetry *in vivo* could explore the potential for snapshot multispectral imaging systems. As described in chapter 1, techniques exist for the replication of images at different spectral bands, such as with the “image-replicating imaging spectrometer” (IRIS). The application of snapshot spectral imaging to oximetry would allow for the study of individual blood cells. In many of the “live previews” observed during the undertaking of *in vivo* experiments in chapter 4, single red blood cells were resolvable and observed to be flowing through capillaries. Single cell oximetry with sequential imaging

was infeasible due to the movement of the cells within the field of view during the course of image acquisition. The hemodynamics of desaturation *in vitro* has been previously described using snapshot techniques [188], and extending this to *in vivo* applications could allow for the observation of deoxygenation of cells as they propagate through capillaries. The high resolution demonstrated in this thesis would need to be retained; for an IRIS system, as the images are all acquired on one detector, this naturally places restrictions on the resolution at which each individual image may be represented. Larger detectors, or the use of a lower number of simultaneous spectral bands, may provide a solution if this avenue was to be explored.

### **8.2. Minimally invasive *in vivo* oximetry**

Following successful demonstration of multispectral oximetry *in vivo*, extension of the technique to minimally invasive imaging was investigated. As described in chapter 6, a GRIN microendoscope was incorporated into the imaging system, and illumination was delivered by means of a custom-fabricated fibre triplet. The central goal of this work was to develop a system which could replicate the image quality and SO<sub>2</sub> quantification previously demonstrated, whilst allowing for minimally invasive access to the tissue. This additional capability was desirable due to the longitudinal studies which could be explored using such a minimally invasive technique. For example, in chapter 4 an acute model of inflammation was studied in mice, and whilst hypoxia was detected, the technique was invasive. For more accurate studies of rheumatoid arthritis, a number of models exist which take course over a period of weeks [166]. Future work employing this technique to such models has the potential to reveal information such as where hypoxia originates within the joint affected, and at what point in the disease progression the hypoxia becomes detectable. Beyond rheumatoid arthritis, the technique could be applied to a number of alternative applications, for example such as in

EAE models of multiple sclerosis.

However, a number of issues were encountered during this work, and ideally should be addressed prior to *in vivo* work. The central concerns were associated with inherent optical aberrations caused by the GRIN lens, which reduce contrast and image quality, and also low SNR as a result of poor levels of illumination and hence light reaching the detector. As discussed in chapter 6, optimisation of the fibre illumination could increase the levels of light within the field of view. Alternatively, illuminating directly through the microendoscope may provide greater levels of light than the ancillary fibres. With this method, the annular illumination would be lost and modifications of the algorithm, similar to those made for the rat imaging in chapter 5, would be necessary in order to achieve accurate  $\text{SO}_2$  values. It also appeared to be the case that triplet GRIN lenses are prone to becoming detached from within the protective metallic sheath. In a number of cases, it was necessary to replace the probes due to this issue which prevented an image from being relayed through the microendoscope. In chapter 7, the triplet microendoscopes were replaced with a singlet lens. Although triplet GRIN lenses can be of a greater length than singlet lenses due to the lower NA relay lens in the triplet setup, for this work both probes were of similar length (9.8 mm and 9.6 mm respectively). It was determined that similar image quality could be achieved with the singlet lens, and it proved to be more robust for repeated measurements and experiments. As such, for future work relating to microendoscopy, singlet lens microendoscopes would be recommended based on these observations.

### **8.3. Fluorescence microendoscopy for immunology**

The final aspect of this thesis was involved with the application of microendoscopic lenses to fluorescence microscopy. Although applicable to a range of applications, the specific target within this work was the imaging of fluorescent

## 8. Conclusions and future work

---

T helper cells within the murine lymph node; an important constituent in the function of the immune system and in inflammatory disease. For the study of such diseases, where the mechanism of progression is not yet understood, the ability to observe cellular interactions to a high degree of localisation provides exciting potential applications for gaining information which is currently inaccessible. The localised delivery of fluorophore-conjugated antibodies, successfully demonstrated in chapter 7, also allows for real time observations of interactions between cells. These observations may provide insight into the mechanism of the immune system, and how it changes in the presence of certain inflammatory diseases.

Alternative potential targets for imaging exist, such as autofluorescence produced by “flavin adenine dinucleotide” (FAD) and “nicotinamide adenine dinucleotide” (NADH) within tissue. FAD and NADH are molecules associated with redox reactions in oxygen metabolism [61]. The levels of FAD and NADH fluorescence in tissue can indicate metabolic activity, a high degree of which is typically associated with higher levels of oxygen [189]. This could potentially be another target for imaging and quantification of localised oxygen levels within tissue affected by inflammatory disease.

### 8.4. Concluding remarks

Overall, significant progress was made in this thesis relating to the application of optical imaging techniques to the study of the vasculature and biological tissue. Future work remains to be explored, such as longitudinal oximetry experiments of disease models. However, the work produced in this thesis demonstrated a new technique and a successful proof of concept of vascular oximetry in inflammatory disease. The application of vascular oximetry to microendoscopy was previously not an area which had been explored in the literature, and potential applications in a variety of diseases are in abundance. The techniques described in this thesis

## 8. Conclusions and future work

---

may lead to a greater level of knowledge regarding the mechanisms of hypoxia and inflammatory disease, increasing our understanding of these diseases, ultimately leading to the benefit of affected patients.

# Bibliography

- [1] T. Wang and J. V. Dam, "Optical biopsy: a new frontier in endoscopic detection and diagnosis," *Clinical Gastroenterology and Hepatology*, vol. 2, no. 9, pp. 744–753, 2004.
- [2] R. Alfano and Y. Pu, "Optical biopsy for cancer detection," in *Lasers for Medical Applications*, ch. 11, pp. 325–367, Woodhead Publishing, 2013.
- [3] L. M. Almond, J. Hutchings, C. Kendall, J. C. C. Day, O. a. C. Stevens, G. R. Lloyd, N. a. Shepherd, H. Barr, and N. Stone, "Assessment of a custom-built Raman spectroscopic probe for diagnosis of early oesophageal neoplasia," *Journal of biomedical optics*, vol. 17, pp. 081421–1, aug 2012.
- [4] I. Bigio and J. Mourant, "Optical Biopsy," in *Encyclopedia of Optical Engineering*, pp. 1577–1593, Marcel Dekker Inc., 2003.
- [5] J. Lorenzo, *Principles of Diffuse Light Propagation*. World Scientific Publishing, 2012.
- [6] H. K. Eltzschig and P. Carmeliet, "Hypoxia and inflammation.," *The New England journal of medicine*, vol. 364, no. 20, pp. 1976–1977, 2011.
- [7] A. L. Davies, R. a. Desai, P. S. Bloomfield, P. R. McIntosh, K. J. Chapple, C. Linington, R. Fairless, R. Diem, M. Kasti, M. P. Murphy, and K. J. Smith, "Neurological deficits caused by tissue hypoxia in neuroinflammatory disease," *Annals of Neurology*, vol. 74, no. 6, pp. 815–825, 2013.
- [8] D. Symmons, G. Turner, R. Webb, P. Asten, E. Barrett, M. Lunt, D. Scott, and A. Silman, "The prevalence of rheumatoid arthritis in the United Kingdom: new estimates for a new century.," *Rheumatology*, vol. 41, pp. 793–800, jul 2002.
- [9] H. R. Schumacher, F. Pessler, and L. X. Chen, "Diagnosing early rheumatoid arthritis (RA). What are the problems and opportunities?," *Clinical and experimental rheumatology*, vol. 21, pp. S15–9, 2003.
- [10] J. Rindfleisch and D. Muller, "Diagnosis and management of rheumatoid arthritis.," *American Family Physician*, vol. 72, no. 6, pp. 1037–1047, 2005.
- [11] Y. W. Song and E. H. Kang, "Autoantibodies in rheumatoid arthritis: Rheumatoid factors and anticitrullinated protein antibodies," *Q J Med*, vol. 103, pp. 139–146, 2009.

- [12] F. C. Arnett, M. Edworthy, Steven, D. A. Bloch, D. J. McShane, J. F. Fries, N. S. Cooper, L. A. Healey, S. R. Kaplan, M. H. Liang, H. S. Luthra, T. A. Medsger, D. M. Mitchell, D. H. Neustadt, R. S. Pinals, J. S. Schaller, J. T. Sharp, R. L. Wilder, and G. G. Hunder, "The american rheumatism association 1987 Revised Criteria for the Classification of Rheumatoid Arthritis," *Arthritis and Rheumatism*, vol. 31, no. 3, pp. 315–324, 1988.
- [13] B. Harrison, D. Symmons, E. Barrett, and A. Silman, "The performance of the 1987 ARA classification criteria for rheumatoid arthritis in a population based cohort of patients with early inflammatory polyarthritis," *Journal of Rheumatology*, vol. 25, no. 12, pp. 2324 – 2330, 1998.
- [14] D. Aletaha, T. Neogi, A. J. Silman, J. Funovits, D. T. Felson, C. O. Bingham, N. S. Birnbaum, G. R. Burmester, V. P. Bykerk, M. D. Cohen, B. Combe, K. H. Costenbader, M. Dougados, P. Emery, G. Ferraccioli, J. M. Hazes, K. Hobbs, T. W. Huizinga, A. Kavanaugh, J. Kay, T. K. Kvien, T. Laing, P. Mease, H. A. Ménard, L. W. Moreland, R. L. Naden, T. Pincus, J. S. Smolen, E. Stanislawska-Biernat, D. Symmons, P. P. Tak, K. S. Upchurch, J. Vencovský, F. Wolfe, and G. Hawker, "2010 Rheumatoid arthritis classification criteria," *Arthritis and Rheumatism*, vol. 62, no. 9, pp. 2569–2581, 2010.
- [15] H. Ye, Y. Su, R. Li, J. Zhao, X. Liu, Y. Mei, Z. Zhang, J. Guo, L. Bi, X. Liu, G. Wang, J. Liu, X. Leng, F. Gu, L. Sun, Q. Zou, Y. Fang, Q. Jiang, and Z. Li, "Comparison of three classification criteria of rheumatoid arthritis in an inception early arthritis cohort," *Clinical Rheumatology*, vol. 35, no. 10, pp. 2397–2401, 2016.
- [16] S. Konisti, S. Kiriakidis, and E. Paleolog, "Hypoxia—a key regulator of angiogenesis and inflammation in rheumatoid arthritis.," *Nature Reviews: Rheumatology*, vol. 8, pp. 153–62, mar 2012.
- [17] K. Lund-Olesen, "Oxygen tension in synovial fluids.," *Arthritis and rheumatism*, vol. 13, no. 6, pp. 769–776, 1970.
- [18] P. Taylor and B. Sivakumar, "Hypoxia and angiogenesis in rheumatoid arthritis.," *Current Opinion in Rheumatology*, vol. 17, pp. 293–8, may 2005.
- [19] A. H. Hielscher, A. D. Klose, A. K. Scheel, B. Moa-Anderson, M. Backhaus, U. Netz, and J. Beuthan, "Sagittal laser optical tomography for imaging of rheumatoid finger joints.," *Phys. Med. Biol.*, vol. 49, no. 7, pp. 1147–1163, 2004.
- [20] a. K. Scheel, M. Backhaus, a. D. Klose, B. Moa-Anderson, U. J. Netz, K.-G. a. Hermann, J. Beuthan, G. a. Müller, G. R. Burmester, and a. H. Hielscher, "First clinical evaluation of sagittal laser optical tomography for detection of synovitis in arthritic finger joints.," *Annals of the rheumatic diseases*, vol. 64, no. 2, pp. 239–245, 2005.

- [21] C. D. Klose, A. D. Klose, U. Netz, J. Beuthan, and A. H. Hielscher, "Multiparameter classifications of optical tomographic images," *Journal of biomedical optics*, vol. 13, no. 5, p. 050503, 2015.
- [22] A. H. Hielscher, H. K. Kim, L. D. Montejo, S. Blaschke, U. J. Netz, P. A. Zwaka, G. Illing, G. A. Müller, and J. Beuthan, "Frequency-domain optical tomographic imaging of arthritic finger joints," *IEEE Transactions on Medical Imaging*, vol. 30, no. 10, pp. 1725–1736, 2011.
- [23] A. Rajaram, S. Ioussoufovitch, L. B. Morrison, K. St Lawrence, T.-Y. Lee, Y. Bureau, and M. Diop, "Joint blood flow is more sensitive to inflammatory arthritis than oxyhemoglobin, deoxyhemoglobin, and oxygen saturation," *Biomedical Optics Express*, vol. 7, no. 10, p. 3843, 2016.
- [24] J. D. Ingle and S. R. Crouch, *Spectrochemical Analysis*. Prentice Hall, 1988.
- [25] S. L. Jacques, "Optical properties of biological tissues: a review," *Physics in Medicine and Biology*, vol. 58, no. 14, pp. 5007–5008, 2013.
- [26] V. V. Tuchin, *Tissue Optics: Light Scattering Methods and Instruments for Medical Diagnosis*. SPIE Press, 2nd ed., 2007.
- [27] M. Fox, *Optical Properties of Solids*. No. 12, 2001.
- [28] J. T. Walsh, "Basic Interactions of Light with Tissue," in *Optical-Thermal Response of Laser-Irradiated Tissue* (A. J. Welch and M. J. C. van Gemert, eds.), ch. 2, Springer Science, 2nd ed., 2011.
- [29] V. Ntziachristos, "Going deeper than microscopy: the optical imaging frontier in biology," *Nature Methods*, vol. 7, no. 8, pp. 603–614, 2010.
- [30] M. Friebel, J. Helfmann, U. Netz, and M. Meinke, "Influence of oxygen saturation on the optical scattering properties of human red blood cells in the spectral range 250 to 2000 nm," *Journal of Biomedical Optics*, vol. 14, no. 3, p. 034001, 2009.
- [31] E. Smith and G. Dent, *Modern Raman Spectroscopy: A Practical Approach*. Wiley Publishing, 2005.
- [32] H. Brunner, A. Mayer, and H. Sussner, "Resonance Raman scattering on the haem group of oxy- and deoxyhaemoglobin," *Journal of molecular biology*, vol. 70, pp. 153–6, sep 1972.
- [33] S. Asher, "Resonance Raman spectroscopy of hemoglobin," *Methods in enzymology*, vol. 76, 1981.
- [34] H. Abramczyk, B. Brozek-Pluska, J. Surmacki, J. Jablonska-Gajewicz, and R. Kordek, "Raman 'optical biopsy' of human breast cancer," *Progress in biophysics and molecular biology*, vol. 108, pp. 74–81, jan 2012.
- [35] C. Krafft, B. Belay, N. Bergner, and B. Romeike, "Advances in optical biopsy

- correlation of malignancy and cell density of primary brain tumors using Raman microspectroscopic imaging," *Analyst*, vol. 137, pp. 5533–5537, 2012.
- [36] H. Lui, J. Zhao, D. McLean, and H. Zeng, "Real-time Raman spectroscopy for in vivo skin cancer diagnosis.," *Cancer research*, vol. 72, pp. 2491–500, may 2012.
- [37] P. Meyer and J. Dworkin, "Applications of fluorescence microscopy to single bacterial cells," *Research in Microbiology*, vol. 158, no. 3, pp. 187–194, 2007.
- [38] M. Wang, F. Tang, X. Pan, L. Yao, X. Wang, Y. Jing, J. Ma, G. Wang, and L. Mi, "Rapid diagnosis and intraoperative margin assessment of human lung cancer with fluorescence lifetime imaging microscopy," *BBA Clinical*, vol. 8, no. March, pp. 7–13, 2017.
- [39] C. Zhu, G. M. Palmer, T. M. Breslin, J. Harter, and N. Ramanujam, "Diagnosis of breast cancer using fluorescence and diffuse reflectance spectroscopy: a Monte-Carlo-model-based approach," *Journal of biomedical optics*, vol. 13, no. 3, pp. 1–29, 2009.
- [40] B. W. Pogue, S. Gibbs-strauss, P. a. Valdés, K. Samkoe, W. Roberts, and K. D. Paulsen, "Review of Neurosurgical Fluorescence Imaging Methodologies," *IEEE Journal of Selected Topics in Quantum Electronics*, vol. 16, no. 3, pp. 493–505, 2010.
- [41] L. E. Cuevas, N. Al-Sonboli, L. Lawson, M. A. Yassin, I. Arbide, N. Al-Aghbari, J. B. Sherchand, A. Al-Absi, E. N. Emenyonu, Y. Merid, M. I. Okobi, J. O. Onuoha, M. Aschalew, A. Aseffa, G. Harper, R. M. A. de Cuevas, S. J. Theobald, C. M. Nathanson, J. Joly, B. Faragher, S. B. Squire, and A. Ramsay, "LED fluorescence microscopy for the diagnosis of pulmonary tuberculosis: A multi-country cross-sectional evaluation," *PLoS Medicine*, vol. 8, no. 7, 2011.
- [42] J. Jung, A. Mehta, E. Aksay, R. Stepnoski, and M. Schnitzer, "In vivo mammalian brain imaging using one-and two-photon fluorescence microendoscopy," *Journal of neurophysiology*, vol. 92, no. 5, pp. 3121–3133, 2004.
- [43] R. P. J. Barretto, B. Messerschmidt, and M. J. Schnitzer, "In vivo fluorescence imaging with high-resolution microlenses.," *Nature methods*, vol. 6, pp. 511–2, jul 2009.
- [44] P. Kim and M. Puoris'haag, "In vivo confocal and multiphoton microendoscopy," *Journal of biomedical optics*, vol. 13, no. 1, pp. 1–7, 2008.
- [45] X. Li and W. Yu, "Deep tissue microscopic imaging of the kidney with a gradient-index lens system," *Optics Communications*, vol. 281, pp. 1833–1840, 2008.
- [46] R. N. Pittman, "Oxygen Transport in the Microcirculation and Its Regulation," *Microcirculation*, vol. 20, no. 2, pp. 117–137, 2013.

- [47] J. Mortensen, S. Talbot, and J. A. Burkart, "Cross-sectional internal diameters of human cervical and femoral blood vessels: relationship to subject's sex, age, body size.," *The Anatomical Record*, vol. 225, pp. 115–124, 1990.
- [48] J. Allen and K. Howell, "Microvascular imaging: techniques and opportunities for clinical physiological measurements," *Physiological Measurement*, vol. 35, no. 7, pp. R91–R141, 2014.
- [49] S. Kulandavelu, W. Balkan, and J. M. Hare, "Regulation of oxygen delivery to the body via hypoxic vasodilation," *Proceedings of the National Academy of Sciences*, vol. 112, no. 20, pp. 6254–6255, 2015.
- [50] G. Stokes, "On the Reduction and Oxidation of the Colouring Matter of the Blood," *Proceedings of the Royal Society of London*, vol. 13, pp. 355–364, 1863.
- [51] M. Ellsworth, R. Pittman, and C. Ellis, "Measurement of hemoglobin oxygen saturation in capillaries," *Am J Physiol*, 1987.
- [52] C. S. Thom, C. F. Dickson, D. a. Gell, and M. J. Weiss, "Hemoglobin Variants: Biochemical Properties and Clinical Correlates," *Cold Spring Harbor Perspectives in Medicine*, vol. 3, no. a011858, pp. 1–22, 2013.
- [53] S. Prahl, "Optical Absorption of Hemoglobin," <http://omlc.org/spectra/hemoglobin/>, 1999.
- [54] A. Carreau, B. E. Hafny-Rahbi, A. Matejuk, C. Grillon, and C. Kieda, "Why is the partial oxygen pressure of human tissues a crucial parameter? Small molecules and hypoxia," *Journal of Cellular and Molecular Medicine*, vol. 15, no. 6, pp. 1239–1253, 2011.
- [55] J.-A. Collins, A. Rudenski, J. Gibson, L. Howard, and R. O'Driscoll, "Relating oxygen partial pressure, saturation and content: the haemoglobin-oxygen dissociation curve," *Breathe*, vol. 11, no. 1, pp. 194–201, 2015.
- [56] H. C. Berg, *Random Walks in Biology*. Princeton University Press, 1977.
- [57] H. Watchman, G. S. Walker, L. L. Randeberg, and N. E. I. Langlois, "Re-oxygenation of post-mortem lividity by passive diffusion through the skin at low temperature.," *Forensic science, medicine, and pathology*, vol. 7, pp. 333–5, dec 2011.
- [58] D. Goldman, "Theoretical models of microvascular oxygen transport to tissue," *Microcirculation*, vol. 15, no. 8, pp. 795–811, 2008.
- [59] J. Beach, "Pathway to retinal oximetry.," *Transl Vis Sci Technol*, vol. 3, no. 5, p. Article 2, 2014.
- [60] D. K. Harrison, "Optical Measurement of Tissue Oxygen Saturation," *Int J Low Extrem Wounds*, vol. 1, no. 3, pp. 191–201, 2002.
- [61] M. Siegemund, J. van Bommel, and C. Ince, "Assessment of regional tissue

- oxygenation.," *Intensive care medicine*, vol. 25, pp. 1044–60, oct 1999.
- [62] L. C. Clark, "Monitor and Control of Blood and Tissue Oxygen Tensions," *Trans Am Soc Artif Intern Org*, vol. 2, pp. 41–46, 1956.
- [63] L. C. Clark Jr. and C. Lyons, "Electrode systems for continuous monitoring in cardiovascular surgery.," *Ann. N. Y. Acad. Sci.*, vol. 102, no. Art. 1, pp. 29–45, 1962.
- [64] R. Germann, M. Haisjackl, B. Schwarz, N. Salak, E. Deusch, W. Pajk, H. J. Wolf, B. Riedmann, and W. Hasibeder, "Dopamine and intestinal mucosal tissue oxygenation in a porcine model of haemorrhage.," *British Journal of Anaesthesia*, vol. 79, no. 3, pp. 357–362, 1997.
- [65] P. Boekstegers, S. Weidenhofer, T. Kapsner, and K. Werdan, "Skeletal muscle partial pressure of oxygen in patients with sepsis," 1994.
- [66] O. Thews and P. Vaupel, "Spatial oxygenation profiles in tumors during normo- and hyperbaric hyperoxia," *Strahlenther Onkol.*, vol. 191, no. 11, pp. 875–882, 2015.
- [67] F. Jobsis, "Noninvasive, infrared monitoring of cerebral and myocardial oxygen sufficiency and circulatory parameters," *Science*, vol. 198, no. 4323, pp. 1264–1267, 1977.
- [68] J. M. Murkin and M. Arango, "Near-infrared spectroscopy as an index of brain and tissue oxygenation," *British Journal of Anaesthesia*, vol. 103, no. Supplement 1, pp. i3–i13, 2009.
- [69] R. Weissleder, "A clearer vision for in vivo imaging," *Nature Biotechnology*, vol. 19, no. 4, pp. 316–317, 2001.
- [70] H. Owen-Reece, M. Smith, C. E. Elwell, and J. C. Goldstone, "Near infrared spectroscopy.," *British journal of anaesthesia*, vol. 82, no. 3, pp. 418–426, 1999.
- [71] F. Scholkmann and M. Wolf, "General equation for the differential path-length factor of the frontal human head depending on wavelength and age," *J Biomed Opt*, vol. 18, no. 10, p. 105004, 2013.
- [72] D. T. Delpy, M. Cope, P. van der Zee, S. Arridge, S. Wray, and J. Wyatt, "Estimation of optical pathlength through tissue from direct time of flight measurement.," *Physics in medicine and biology*, vol. 33, pp. 1433–1442, 1988.
- [73] J. B. Hickam, H. O. Sieker, and R. Frayser, "Studies of retinal circulation and A-V oxygen difference in man.," *Transactions of the American Clinical and Climatological Association*, vol. 71, no. 657, pp. 34–44, 1959.
- [74] L. E. MacKenzie, A. R. Harvey, and A. I. McNaught, "Spectroscopic oximetry in the eye: a review," *Expert Review of Ophthalmology*, vol. 00, no. 00, pp. 1–12, 2017.

- [75] J. Beach, K. Schwenzer, S. Srinivas, D. Kim, and J. Tiedeman, "Oximetry of retinal vessels by dual-wavelength imaging: calibration and influence of pigmentation," *Journal of Applied Physiology*, vol. 86, no. 2, pp. 748–758, 1999.
- [76] M. Hammer, W. Vilser, T. Riemer, and D. Schweitzer, "Retinal vessel oximetry-calibration, compensation for vessel diameter and fundus pigmentation, and reproducibility," *Journal of Biomedical Optics*, vol. 13, no. 5, p. 054015, 2008.
- [77] S. H. Hardarson, A. Harris, R. A. Karlsson, G. H. Halldorsson, L. Kagemann, E. Rechtman, G. M. Zoega, T. Eysteinnsson, J. A. Benediktsson, A. Thorsteinnsson, P. K. Jensen, J. Beach, and E. Stefánsson, "Automatic retinal oximetry," *Investigative Ophthalmology and Visual Science*, vol. 47, no. 11, pp. 5011–5016, 2006.
- [78] G. Michelson, M. Scibor, and D. Schweitzer, "Intravascular oxygen saturation in retinal vessels in glaucoma," *Investigative Ophthalmology & Visual Science*, vol. 43, pp. U445–U445, 2002.
- [79] A. Geirsdottir, S. H. Hardarson, O. B. Olafsdottir, and E. Stefánsson, "Retinal oxygen metabolism in exudative age-related macular degeneration," *Acta Ophthalmologica*, vol. 92, no. 1, pp. 27–33, 2014.
- [80] M. Hammer, W. Vilser, T. Riemer, A. Mandecka, D. Schweitzer, U. Kühn, J. Dawczynski, F. Liemt, and J. Strobel, "Diabetic patients with retinopathy show increased retinal venous oxygen saturation," *Graefe's Archive for Clinical and Experimental Ophthalmology*, vol. 247, no. 8, pp. 1025–1030, 2009.
- [81] T. Choudhary, D. Ball, J. Fernandez Ramos, A. McNaught, and A. Harvey, "Assessment of acute mild hypoxia on retinal oxygen saturation using snapshot retinal oximetry," *Investigative ophthalmology & visual science*, vol. 54, pp. 7538–43, nov 2013.
- [82] L. E. MacKenzie, T. R. Choudhary, A. I. McNaught, and A. R. Harvey, "In vivo oximetry of human bulbar conjunctival and episcleral microvasculature using snapshot multispectral imaging," *Experimental Eye Research*, vol. 149, pp. 48–58, 2016.
- [83] R. Pittman and B. Duling, "A new method for the measurement of percent oxyhemoglobin.," *Journal of Applied Physiology*, 1975.
- [84] F. Delori, "Noninvasive technique for oximetry of blood in retinal vessels," *Applied Optics*, vol. 27, no. 6, pp. 1113–1125, 1988.
- [85] F. C. Delori, "Spectrophotometer for noninvasive measurement of intrinsic fluorescence and reflectance of the ocular fundus.," *Applied optics*, vol. 33, no. 31, pp. 7439–7452, 1994.
- [86] K. R. Denninghoff, R. a. Chipman, and L. W. Hillman, "Oxyhemoglobin saturation measurements by green spectral shift.," *Optics letters*, vol. 31,

- no. 7, pp. 924–926, 2006.
- [87] K. R. Denninghoff, R. a. Chipman, and L. W. Hillman, “Blood oxyhemoglobin saturation measurements by blue-green spectral shift,” *Journal of Biomedical Optics*, vol. 12, no. 3, p. 034020, 2007.
- [88] K. R. Denninghoff, D. a. Salyer, S. Basavanhappa, R. I. Park, and R. a. Chipman, “Blue-green spectral minimum correlates with oxyhemoglobin saturation in vivo.,” *Journal of biomedical optics*, vol. 13, no. 5, p. 054059, 2008.
- [89] C. Ellis, M. Ellsworth, and R. Pittman, “Determination of red blood cell oxygenation in vivo by dual video densitometric image analysis,” *Am J Physiol*, vol. 258, pp. H1216–23, apr 1990.
- [90] R. Shonat, E. Wachman, and W. Niu, “Near-simultaneous hemoglobin saturation and oxygen tension maps in mouse brain using an AOTF microscope,” *Biophysical journal*, vol. 73, no. September, 1997.
- [91] B. Sorg, B. Moeller, O. Donovan, Y. Cao, and M. Dewhirst, “Hyperspectral imaging of hemoglobin saturation in tumor microvasculature and tumor hypoxia development.,” *Journal of biomedical optics*, vol. 10, no. 4, p. 44004, 2005.
- [92] G. M. Palmer, A. N. Fontanella, G. Zhang, G. Hanna, C. L. Fraser, and M. W. Dewhirst, “Optical imaging of tumor hypoxia dynamics,” *Journal of Biomedical Optics*, vol. 15, no. 6, p. 066021, 2010.
- [93] K. Kaneko, H. Yamaguchi, T. Saito, T. Yano, Y. Oono, H. Ikematsu, S. Nomura, A. Sato, M. Kojima, H. Esumi, and A. Ochiai, “Hypoxia imaging endoscopy equipped with laser light source from preclinical live animal study to first-in-human subject research,” *PLoS ONE*, vol. 9, no. 6, pp. 1–9, 2014.
- [94] A. J. Cohen and R. A. Laing, “Multiple Scattering Analysis of Retinal Blood Oximetry,” *IEEE Transactions on Biomedical Engineering*, vol. BME-23, no. 5, pp. 391–400, 1976.
- [95] N. Sato, T. Matsumura, M. Shichiri, T. Kamada, H. Abe, and B. Hagihara, “Hemoperfusion, rate of oxygen consumption and redox levels of mitochondrial cytochrome c (+c1) in liver in situ of anesthetized rat measured by reflectance spectrophotometry,” *BBA - Bioenergetics*, vol. 634, no. C, pp. 1–10, 1981.
- [96] D. K. Harrison, S. D. Evans, N. C. Abbot, J. Swanson Beck, and P. T. McCollum, “Spectrophotometric measurements of haemoglobin saturation and concentration in skin during the tuberculin reaction in normal human subjects,” *Clinical Physics and Physiological Measurement*, vol. 13, no. 4, pp. 349–363, 1992.
- [97] D. Schweitzer, L. Leistritz, M. Hammer, M. Scibor, U. Bartsch, and J. Strobel,

- “Calibration-free measurement of the oxygen saturation in retinal vessels of men,” *Proc. SPIE, Ophthalmic Technologies V*, vol. 2393, pp. 210–218, 1995.
- [98] W. T. Knoefel, N. Kollias, D. W. Rattner, N. S. Nishioka, and a. L. Warshaw, “Reflectance spectroscopy of pancreatic microcirculation.,” *Journal of applied physiology (Bethesda, Md. : 1985)*, vol. 80, no. 1, pp. 116–23, 1996.
- [99] M. Smith, K. Denninghoff, A. Lompadó, and L. Hillman, “Effect of multiple light paths on retinal vessel oximetry,” *Applied optics*, vol. 39, pp. 1183–93, mar 2000.
- [100] J. Kaluzny, H. Li, W. Liu, P. Nesper, J. Park, H. F. Zhang, and A. A. Fawzi, “Bayer Filter Snapshot Hyperspectral Fundus Camera for Human Retinal Imaging,” *Current Eye Research*, vol. 42, no. 4, pp. 629–635, 2017.
- [101] G. Shabtay, E. Eidinge, Z. Zalevsky, D. Mendlovic, and E. Marom, “Tunable birefringent filters - optimal iterative design,” *Optics Express*, vol. 10, no. 26, p. 1534, 2002.
- [102] J. Beeckman, T. Hui, P. J. M. Vanbrabant, R. Zmijan, and K. Neyts, “Polarization Selective Wavelength Tunable Filter,” *Molecular Crystals and Liquid Crystals*, vol. 502, pp. 19–28, may 2009.
- [103] B. S. Sorg, M. E. Hardee, N. Agarwal, B. J. Moeller, and M. W. Dewhurst, “Spectral imaging facilitates visualization and measurements of unstable and abnormal microvascular oxygen transport in tumors.,” *Journal of biomedical optics*, vol. 13, no. 1, p. 014026, 2008.
- [104] C. D. Tran, “Acousto-Optic devices: Optical Elements for Spectroscopy,” *Analytical chemistry*, vol. 64, no. 20, pp. 971A–981A, 1992.
- [105] A. Gorman, D. W. Fletcher-Holmes, and A. R. Harvey, “Generalization of the Lyot filter and its application to snapshot spectral imaging.,” *Optics express*, vol. 18, pp. 5602–8, mar 2010.
- [106] M. Martin, S. Newman, J. Aber, and R. Congalton, “Determining Forest Species Composition Using High Spectral Resolution Remote Sensing Data,” *Remote Sensing of Environment*, vol. 65, no. 3, pp. 249–254, 1998.
- [107] Y. Xie, Z. Sha, and M. Yu, “Remote sensing imagery in vegetation mapping: a review,” *Journal of Plant Ecology*, vol. 1, no. 1, pp. 9–23, 2008.
- [108] V. L. Mulder, S. de Bruin, M. E. Schaepman, and T. R. Mayr, “The use of remote sensing in soil and terrain mapping - A review,” *Geoderma*, vol. 162, no. 1-2, pp. 1–19, 2011.
- [109] A. Nouvong, B. Hoogwerf, E. Mohler, B. Davis, A. Tajaddini, and E. Medenilla, “Evaluation of Diabetic Foot Ulcer Healing with Hyperspectral Imaging of Oxyhemoglobin and Deoxyhemoglobin,” *Diabetes Care*, vol. 32, no. 11, pp. 2056–2061, 2009.

- [110] S. R. Patel, J. G. Flanagan, A. M. Shahidi, J. P. Sylvestre, and C. Hudson, "A prototype hyperspectral system with a tunable laser source for retinal vessel imaging," *Investigative Ophthalmology and Visual Science*, vol. 54, no. 8, pp. 5163–5168, 2013.
- [111] K. J. Zuzak, M. T. Gladwin, R. O. Cannon, and I. W. Levin, "Imaging hemoglobin oxygen saturation in sickle cell disease patients using noninvasive visible reflectance hyperspectral techniques: effects of nitric oxide.," *American Journal of Physiology. Heart and Circulatory Physiology*, vol. 285, pp. H1183–H1189, 2003.
- [112] M. A. Calin, S. V. Parasca, D. Savastru, and D. Manea, "Hyperspectral Imaging in the Medical Field: Present and Future," *Applied Spectroscopy Reviews*, vol. 49, no. 6, pp. 435–447, 2014.
- [113] R. T. Kester, N. Bedard, L. Gao, and T. S. Tkaczyk, "Real-time snapshot hyperspectral imaging endoscope.," *Journal of biomedical optics*, vol. 16, no. 5, p. 056005, 2011.
- [114] H.-T. Lim and V. M. Murukeshan, "A four-dimensional snapshot hyperspectral video-endoscope for bio-imaging applications," *Scientific Reports*, vol. 6, no. December 2015, p. 24044, 2016.
- [115] S. Varadarajulu, S. Banerjee, B. Barth, D. Desilets, V. Kaul, S. Kethu, M. Pedrosa, P. Pfau, J. Tokar, A. Wang, L. Wong Kee Song, and S. Rodriguez, "GI endoscopes," *Gastrointestinal endoscopy*, vol. 74, pp. 1–6.e6, jul 2011.
- [116] M. E. Llewellyn, R. P. J. Barretto, S. L. Delp, and M. J. Schnitzer, "Minimally invasive high-speed imaging of sarcomere contractile dynamics in mice and humans.," *Nature*, vol. 454, pp. 784–8, aug 2008.
- [117] U. Utzinger and R. R. Richards-Kortum, "Fiber optic probes for biomedical optical spectroscopy.," *Journal of biomedical optics*, vol. 8, pp. 121–47, jan 2003.
- [118] A. Shahmoon, S. Aharon, O. Kruchik, M. Hohmann, H. Slovin, A. Douplik, and Z. Zalevsky, "In vivo minimally invasive interstitial multi-functional microendoscopy," *Scientific reports*, vol. 3, p. 1805, jan 2013.
- [119] B. Messerschmidt, "Gradient Index Optical Microsystems Visualize Living Cells in Deep Tissue," *Biophotonics International*, 2007.
- [120] J. K. Kim, W. M. Lee, P. Kim, M. Choi, K. Jung, S. Kim, and S. H. Yun, "Fabrication and operation of GRIN probes for in vivo fluorescence cellular imaging of internal organs in small animals.," *Nature protocols*, vol. 7, pp. 1456–69, aug 2012.
- [121] W. J. Smith, *Modern Optical Engineering*. McGraw-Hill, 3rd ed., 2000.
- [122] E. Acosta, C. Gomez-reino, and J. Lifiare, "Effective radius and numerical aperture of GRIN lenses with revolution symmetry," *Applied Optics*, vol. 26,

- no. 15, pp. 2952–2955, 1987.
- [123] R. P. J. Barretto and M. J. Schnitzer, “In vivo optical microendoscopy for imaging cells lying deep within live tissue.,” *Cold Spring Harbor protocols*, vol. 2012, pp. 1029–34, oct 2012.
- [124] M. J. Levene, D. a. Dombeck, K. a. Kasischke, R. P. Molloy, and W. W. Webb, “In vivo multiphoton microscopy of deep brain tissue.,” *Journal of neurophysiology*, vol. 91, pp. 1908–12, apr 2004.
- [125] C. Gomez-Reino, E. Acosta, and M. Perez, “Limitation in the Cone of Light through GRIN Lenses: Stops , Pupils and Vignetting,” *Jpn. J. Appl. Phys.*, vol. 31, pp. 1582–1585, 1992.
- [126] C. Saunter and S. Semprini, “Micro-endoscope for in vivo widefield high spatial resolution fluorescent imaging,” *Biomedical Optics Express*, vol. 3, no. 6, pp. 1274–1278, 2012.
- [127] K. Nishizawa, “Chromatic aberration of the Selfoc lens as an imaging system.,” *Applied optics*, vol. 19, pp. 1052–5, apr 1980.
- [128] R. Barretto and M. Schnitzer, “In vivo Microendoscopy for Imaging Cells Lying Deep within Live Tissue,” *Cold Spring Harbor Protocols*, pp. 1–16, 2012.
- [129] J. K. Kim, J. W. Choi, and S. H. Yun, “Optical fine-needle imaging biopsy of the brain,” *Biomedical Optics Express*, vol. 4, p. 2846, nov 2013.
- [130] R. S. Pillai, D. Lorensen, and D. D. Sampson, “Deep-tissue access with confocal fluorescence microendoscopy through hypodermic needles.,” *Optics express*, vol. 19, pp. 7213–21, apr 2011.
- [131] D. Huang, E. A. Swanson, C. P. Lin, J. S. Schuman, W. G. Stinson, W. Chang, M. R. Hee, T. Flotte, K. Gregory, C. A. Puliafito, and J. G. Fujimoto, “Optical Coherence Tomography,” *Science*, vol. 22, no. 2545035, pp. 1178–1181, 1991.
- [132] G. J. Tearney, S. a. Boppart, B. E. Bouma, M. E. Brezinski, N. J. Weissman, J. F. Southern, and J. G. Fujimoto, “Scanning single-mode fiber optic catheter-endoscope for optical coherence tomography,” *Optics letters*, vol. 21, p. 912, jun 1996.
- [133] G. J. Tearney, “In Vivo Endoscopic Optical Biopsy with Optical Coherence Tomography,” *Science*, vol. 276, pp. 2037–2039, jun 1997.
- [134] B. C. Quirk, R. a. McLaughlin, A. M. Pagnozzi, B. F. Kennedy, P. B. Noble, and D. D. Sampson, “Optofluidic needle probe integrating targeted delivery of fluid with optical coherence tomography imaging,” *Optics Letters*, vol. 39, p. 2888, may 2014.
- [135] C. D. Hanning, Alexander-Williams, and Jm, “Pulse oximetry: a practical review,” *The British Medical Journal*, vol. 311, no. August, pp. 367–370, 1995.

- [136] M. Hammer, S. Leistriz, L. Leistriz, and D. Schweitzer, "Light paths in retinal vessel oxymetry," *IEEE Transactions on Biomedical Engineering*, vol. 48, no. 5, pp. 592–598, 2001.
- [137] P. I. Rodmell, J. a. Crowe, A. Gorman, A. R. Harvey, G. Muyo, D. J. Mordant, A. I. McNaught, and S. P. Morgan, "Light path-length distributions within the retina.," *Journal of biomedical optics*, vol. 19, no. 3, p. 36008, 2014.
- [138] V. Twersky, "Absorption and multiple scattering by biological suspensions.," *Journal of the Optical Society of America*, vol. 60, no. 8, pp. 1084–1093, 1970.
- [139] M. H. Smith, "Optimum wavelength combinations for retinal vessel oximetry.," *Applied optics*, vol. 38, pp. 258–67, jan 1999.
- [140] D. J. Faber, M. C. G. Aalders, E. G. Mik, B. a. Hooper, M. J. C. van Gemert, and T. G. van Leeuwen, "Oxygen Saturation-Dependent Absorption and Scattering of Blood," *Physical Review Letters*, vol. 93, no. 2, p. 028102, 2004.
- [141] A. S. Gorman, *Snapshot spectral imaging using image replication and birefringent interferometry: Principles and Applications*. PhD thesis, Heriot-Watt University, 2010.
- [142] M. J. M. Fischer, S. Uchida, and K. Messlinger, "Measurement of meningeal blood vessel diameter in vivo with a plug-in for ImageJ.," *Microvascular research*, vol. 80, pp. 258–66, sep 2010.
- [143] R. H. Byrd, R. B. Schnabel, and G. A. Shultz, "A Trust Region Algorithm for Nonlinearly Constrained Optimization," *SIAM Journal on Numerical Analysis*, vol. 24, no. 5, pp. 1152–1170, 1987.
- [144] O. van Assendelft, *Spectrophotometry of Haemoglobin Derivatives*. Van Gorcum, 1970.
- [145] W. G. Zijlstra and A. Buursma, "Spectrophotometry of hemoglobin: Absorption spectra of rat oxyhemoglobin, deoxyhemoglobin, carboxyhemoglobin, and methemoglobin," *Comp. Biochem. Physiol.*, vol. 107B, no. 1, pp. 161–166, 1994.
- [146] J. G. Kim and H. Liu, "Variation of haemoglobin extinction coefficients can cause errors in the determination of haemoglobin concentration measured by near-infrared spectroscopy.," *Physics in medicine and biology*, vol. 52, no. 20, pp. 6295–6322, 2007.
- [147] W. Zijlstra, A. Buursma, and W. Meeuwssen-van der Roest, "Absorption Spectra of Human Fetal and Adult Oxyhemoglobin, De-Oxyhemoglobin, and Methemoglobin," *Clin. Chem.*, vol. 37, no. 9, pp. 1633–1638, 1991.
- [148] J. Dainty, *Topics in Applied Physics: Laser Speckle and Related Phenomena*. Springer-Verlag, 1975.

## Bibliography

---

- [149] G. Nadorff and F. DeWitt, "Refluxicon objectives for imaging," *Proc. of SPIE*, vol. 8486, p. 84860C, oct 2012.
- [150] M. Riedl, *Optical Design Fundamentals for Infrared Systems*. SPIE Press, 2nd ed., 2001.
- [151] G. D. Boreman, "MTF in Optical Systems," in *Modulation Transfer Function in Optical and Electro-Optical Systems*, SPIE Press, 2001.
- [152] S. L. Jacques, B. Wang, and R. Samatham, "Reflectance confocal microscopy of optical phantoms.," *Biomedical Optics Express*, vol. 3, no. 6, pp. 1162–72, 2012.
- [153] K. Briely-Saebo and A. Bjornerud, "Accurate de-oxygenation of ex vivo whole blood using sodium Dithionite," *Proc. Intl. Sot. Mag. Reson. Med*, p. 2025, 2000.
- [154] H. Maeda, K. Fukita, S. Oritani, K. Ishida, and B.-L. Zhu, "Evaluation of post-mortem oxymetry with reference to the causes of death," *Forensic Science International*, vol. 87, pp. 201–210, jun 1997.
- [155] K. R. Denninghoff and M. H. Smith, "Optical model of the blood in large retinal vessels," *Journal of Biomedical Optics*, vol. 5, no. 4, pp. 371–374, 2000.
- [156] M. Friebel, J. Helfmann, and M. C. Meinke, "Influence of osmolarity on the optical properties of human erythrocytes," *J. Biomed. Opt.*, vol. 15, no. 5, pp. 0550051–6, 2010.
- [157] J. Wang, P. Ghassemi, A. Melchiorri, J. Ramella-Roman, S. A. Mathews, J. Coburn, B. Sorg, Y. Chen, and J. Pfefer, "3D printed biomimetic vascular phantoms for assessment of hyperspectral imaging systems," *Progress in Biomedical Optics and Imaging - Proceedings of SPIE*, vol. 9325, p. 932508, 2015.
- [158] M. A. van der Putten, J. M. Brewer, and A. R. Harvey, "Multispectral oximetry of murine tendon microvasculature with inflammation," *Biomedical Optics Express*, vol. 8, no. 6, p. 2896, 2017.
- [159] J. Necas and L. Bartosikova, "Carrageenan: A review," *Veterinarni Medicina*, vol. 58, no. 4, pp. 187–205, 2013.
- [160] C. J. Morris, *Carrageenan-Induced Paw Edema in the Rat and Mouse*, vol. 225. 2003.
- [161] P. a. Flecknell and M. Mitchell, "Midazolam and fentanyl-fluanisone: assessment of anaesthetic effects in laboratory rodents and rabbits.," *Laboratory animals*, vol. 18, no. 2, pp. 143–6, 1984.
- [162] R. E. Odeh, "Critical values of the sample product-moment correlation coefficient in the bivariate normal distribution," *Communications in Statistics - Simulation and Computation*, vol. 11, no. 1, pp. 1–26, 1982.

- [163] J. B. Hickam, R. Frayser, and J. C. Ross, "A Study of Retinal Venous Blood Oxygen Saturation in Human Subjects by Photographic Means," *Circulation*, vol. 27, no. 3, pp. 375–385, 1963.
- [164] S. E. LeBlanc, M. Atanya, K. Burns, and R. Munger, "Quantitative impact of small angle forward scatter on whole blood oximetry using a Beer-Lambert absorbance model," *The Analyst*, vol. 136, no. 8, pp. 1637–1643, 2011.
- [165] H. Blockeel and J. Struyf, "Efficient algorithms for decision tree cross-validation," *Journal of Machine Learning Research*, vol. 3, no. 4-5, p. 9, 2001.
- [166] D. L. Asquith, A. M. Miller, I. B. McInnes, and F. Y. Liew, "Animal models of rheumatoid arthritis," *European Journal of Immunology*, vol. 39, no. 8, pp. 2040–2044, 2009.
- [167] M. A. van der Putten, L. E. MacKenzie, A. L. Davies, J. Fernandez-Ramos, R. A. Desai, K. J. Smith, and A. Harvey, "A multispectral microscope for in vivo oximetry of rat dorsal spinal cord vasculature," *Physiological Measurement*, vol. 38, pp. 205–18, 2017.
- [168] I. S. Mackenzie, S. V. Morant, G. a. Bloomfield, T. M. MacDonald, and J. O'Riordan, "Incidence and prevalence of multiple sclerosis in the UK 1990-2010: a descriptive study in the General Practice Research Database," *Journal of neurology, neurosurgery, and psychiatry*, vol. 85, no. 1, pp. 76–84, 2014.
- [169] C. S. Constantinescu, N. Farooqi, K. O'Brien, and B. Gran, "Experimental autoimmune encephalomyelitis (EAE) as a model for multiple sclerosis (MS)," *British Journal of Pharmacology*, vol. 164, no. 4, pp. 1079–1106, 2011.
- [170] J. Yi, W. Liu, S. Chen, V. Backman, N. Sheibani, C. M. Sorenson, A. A. Fawzi, R. A. Linsenmeier, and H. F. Zhang, "Visible light optical coherence tomography measures retinal oxygen metabolic response to systemic oxygenation," *Light: Science & Applications*, vol. 4, no. 9, p. e334, 2015.
- [171] S. a. Figley, Y. Chen, A. Maeda, L. Conroy, J. D. McMullen, J. I. Silver, S. Stapleton, A. Vitkin, P. Lindsay, K. Burrell, G. Zadeh, M. G. Fehlings, and R. S. DaCosta, "A Spinal Cord Window Chamber Model for In Vivo Longitudinal Multimodal Optical and Acoustic Imaging in a Murine Model," *PLoS ONE*, vol. 8, no. 3, p. e58081, 2013.
- [172] V. Sharma, J. W. He, S. Narvenkar, Y. B. Peng, and H. Liu, "Quantification of light reflectance spectroscopy and its application: Determination of hemodynamics on the rat spinal cord and brain induced by electrical stimulation," *NeuroImage*, vol. 56, no. 3, pp. 1316–1328, 2011.
- [173] P. van Beest, G. Wietasch, T. Scheeren, P. Spronk, and M. Kuiper, "Clinical review: use of venous oxygen saturations as a goal - a yet unfinished puzzle," *Critical Care*, vol. 15, no. 5, p. 232, 2011.

- [174] M. Bennett and R. Heard, "Hyperbaric oxygen therapy for multiple sclerosis," *CNS Neurosci Ther*, vol. 16, no. 2, pp. 115–124, 2010.
- [175] J. Höper and R. H. Funk, "A combination of microendoscopy and spectrophotometry allowing real-time analysis of microcirculatory parameters during in vivo observations.," *Physiological measurement*, vol. 15, pp. 333–7, aug 1994.
- [176] Thorlabs, "FN96A: Guide to Connectorization and Polishing Optical Fibers," 2013.
- [177] J. Lagarias, C. Mallows, and A. Wilks, "Beyond the Descartes Circle Theorem," *Mathematical Association of America, JSTOR*, vol. 109, no. 4, pp. 338–361, 2002.
- [178] W. Lee and S. Yun, "Adaptive aberration correction of GRIN lenses for confocal endomicroscopy," *Optics letters*, vol. 36, no. 23, pp. 4608–4610, 2011.
- [179] A. Hall and C. Yates, *Fundamentals of Biomedical Science: Immunology*. Oxford University Press, 2010.
- [180] J. Chan, C. Ng, and P. Hui, "A simple guide to the terminology and application of leucocyte monoclonal antibodies," *Histopathology*, vol. 12, no. 5, pp. 461–480, 1988.
- [181] L. A. Herzenberg, D. Parks, B. Sahaf, O. Perez, M. Roederer, and L. A. Herzenberg, "The history and future of the Fluorescence Activated Cell Sorter and flow cytometry: A view from Stanford," *Clinical Chemistry*, vol. 48, no. 10, pp. 1819–1827, 2002.
- [182] G. S. Firestein, "Evolving concepts of rheumatoid arthritis.," *Nature*, vol. 423, no. 6937, pp. 356–61, 2003.
- [183] M. Choi, S. J. J. Kwok, and S. H. Yun, "In Vivo Fluorescence Microscopy: Lessons From Observing Cell Behavior in Their Native Environment," *Physiology*, pp. 40–49, 2015.
- [184] S. Mitra and T. H. Foster, "In vivo optical imaging to visualize photodynamic therapy-induced immune responses," *Biophotonics and Immune Responses IV, Proc. of SPIE*, vol. 7178, pp. 71780F–71780F–8, 2009.
- [185] R. J. Cummings, S. Mitra, E. M. Lord, and T. H. Foster, "Antibody-labeled fluorescence imaging of dendritic cell populations in vivo," *J Biomed Opt*, vol. 13, no. 4, pp. 1–7, 2009.
- [186] P. Zammit, A. R. Harvey, and G. Carles, "Extended depth-of-field imaging and ranging in a snapshot," *Optica*, vol. 1, no. 4, p. 209, 2014.
- [187] J. C. Jung and M. J. Schnitzer, "Multiphoton endoscopy.," *Optics letters*,

vol. 28, pp. 902–4, jun 2003.

- [188] J. Fernandez Ramos, L. R. Brewer, A. Gorman, and A. R. Harvey, “Video-Rate Multispectral Imaging: Application to Microscopy and Macroscopy,” *Classical Optics 2014*, p. CW1C.3, 2014.
- [189] I. Georgakoudi and K. P. Quinn, “Optical Imaging Using Endogenous Contrast to Assess Metabolic State,” *Annual Review of Biomedical Engineering*, vol. 14, no. 1, pp. 351–367, 2012.